Degradation of Tungsten Components Exposed to Deuterium Plasmas in JET:

An Investigation into Component Processing, Mechanical Behaviour and Be–W Deposits.

Robert William Kerr

Wolfson College
University of Oxford

Supervisors: Prof. D.E.J. Armstrong, Prof. S. Lozano-Perez, and Dr. A. Widdowson

A thesis submitted for the degree of

Doctor of Philosophy

September 2024

Declaration

The material presented in this thesis was conducted by the author in the Department of Materials at the University of Oxford and in the Materials Research Facility at the UK Atomic Energy Authority (UKAEA). The research was supervised by Prof. David Armstrong, Prof. Sergio Lozano-Perez and Dr. Anna Widdowson. No section of this work has been submitted for the award of a degree at this or any other institution. All external sources have been acknowledged and referenced accordingly within the text, with a complete bibliography provided at the end.

This work has been carried out within the framework of the EUROfusion Consortium, funded by the European Union via the Euratom Research and Training Programme (Grant Agreement No 101052200 — EUROfusion) and from the EPSRC [grant number EP/W006839/1]. To obtain further information on the data and models underlying this paper please contact Publications-Manager@ukaea.uk. Views and opinions expressed are however those of the author(s) only and do not necessarily reflect those of the European Union or the European Commission. Neither the European Union nor the European Commission can be held responsible for them. The research used UKAEA's Materials Research Facility (MRF), which has been funded by and is part of the UK's National Nuclear User Facility (NNUF) and Henry Royce Institute for Advanced Materials.

Acknowledgements

I would like to acknowledge the many people who have helped me throughout my DPhil, whether through their technical expertise or encouragement. I owe a special thanks to my supervisors: Prof. David Armstrong, Prof. Sergio Lozano-Perez, Dr. Yevhen Zayachuk and Dr. Anna Widdowson. Their insights and guidance made it possible to bring together all the different elements of this work. I also want to thank Debbie Samaddar, my supervisor during my year in industry, whose encouragement gave me the confidence to apply for a PhD in the first place.

Within the Materials Department, I have received invaluable support from everyone in the Oxford Micromechanics Group and the Nanoanalysis Group. I would also like to thank Dr. Martin Meier and Prof. Michael Moody for their help with collecting atom probe data. And to my friends in the office–Anna, Ben, Brad, Jack, Johann, Keivan, Pedr, Robin and Shatha–thank you for the laughs, pranks, indoor cricket matches, lunch and pub trips that made every day in the department enjoyable.

I am extremely grateful to the staff and researchers in the Materials Research Facility (MRF) and the Erosion Deposition Group at the UK Atomic Energy Authority (UKAEA) for their help with my experiments. A special thanks to Kate Breach, who often gave up her weekends so that I could access a microscope; to Dr. Scott Silburn, Beth Thomas and Dr. Spyros Aleiferis at UKAEA for taking the time to analyse valuable diagnostic data; and Prof. Eduardo Alves and Dr. Norberto Catarino from the Technical University of Lisbon for running the ion beam experiments on my samples.

As part of the EPSRC Centre for Doctoral Training in Fusion Power, I was fortunate enough to visit the York Plasma Institute (YPI) each year. I am grateful to the students and staff at the YPI who made it such a welcoming experience. In particular, my sincerest appreciation goes to my cohort and those based in Oxford with me–Arun, Yorick, Cyd and Laura. I will always look back fondly on our many walks, movies, dinners, and debates as some of the highlights of my PhD.

Beyond the lab, I am grateful to those who made Oxford feel like home. To the Oriel College Chapel Choir, whose rehearsals, services, formals, games, and tours brought endless joy and laughter. To my wonderful housemates on Canal Street–Alexis, Raffy, Holly, Emre, Becky and Fred “my rock” Caso–thank you for your friendship and support over the past four years.

I am incredibly lucky to have friends who have stood by me throughout this journey–those from the University of Bristol, who supported me even when they had no idea what my research was about, and my childhood friends, who reassured me that I would not be a student forever. Most of all, I want to thank my family: my partner Alicia, my mum Katy, my dad Simon, my brother Chris, and his fiancée Sofie. Without these incredible people and all they have taught me, I would never have had the confidence to pursue a PhD.

Abstract

The mechanical behaviour and structural integrity of tungsten components, specifically Langmuir probes and lamellae from the JET divertor are evaluated both in their as-received state and after exposure during the ITER-like wall campaigns. The results reveal significant disparities in the as-received microstructures of these components. The lamellae exhibit fine grains suited for high-heat flux conditions, whereas the probes display larger equiaxed grains. Electrical discharge machining (EDM) induced cracks up to 50 μm and voids in both component types, raising concerns about the mechanical integrity of these surfaces.

Advanced characterisation techniques, including atom probe tomography and transmission electron microscopy, identified significant impurity concentrations in the as-received samples, particularly phosphorus and iron at grain boundaries, which likely contributed to embrittlement. EDM-generated cracks were shown to widen and deepen after exposure, propagating up to 1 mm into the bulk of one Langmuir probe. Additionally, some EDM-generated cracks contained embedded debris, including elements such as carbon and oxygen. This debris poses potential safety risks, including beryllium retention and associated toxicity, as well as tritium retention issues.

Exposure to deuterium plasmas induced distinct microstructural differences between the Langmuir probes placed next to tiles 3 and 6 and the lamellae taken from stacks C (rows 3, 4, 12 and 13) and D (row 12). The Langmuir probes underwent recrystallisation and void formation with an increase in hardness of up to 0.40 GPa due to cascade damage from the incident deuterium. Conversely, the lamellae were more resilient under plasma loading, with no change in hardness or signs of melting or recrystallisation.

Beryllium and beryllium oxide were found to accumulate on the surface of lamella C3, particularly near W droplets, raising concerns about droplet detachment and increased erosion rates during reactor operation. The surface of Lamella C3 also contained stratified deposits, consisting of alternating layers of beryllium oxide and sputtered tungsten, which raises concerns about impurity accumulation and its impact on component performance. This study underscores the need for further research into the effects of EDM and D-T plasma exposure on tungsten, particularly in light of the decision to transition ITER to a tungsten first wall for the nuclear operational phase.

List of Abbreviations and Symbols

APT Atom Probe Tomography

BF Bright-Field

CFC Carbon Fibre Composite

CSM Continuous Stiffness Measurement

DEMO Demonstration Reactor

DF Dark-Field

DPA Displacements per Atom

D-T Deuterium-Tritium

EBSD Electron Back-Scatter Diffraction

EDM Electrical Discharge Machining

EDX Energy Dispersive X-ray Spectroscopy

EELS Electron Energy Loss Spectroscopy

ELM Edge-localised Mode

FIB Focused Ion Beam

GB Grain Boundary

GND Geometrically Necessary Dislocations

HAADF High-Angle Annular Dark-Field

IBA Ion Beam Analysis

ILW ITER-like Wall

ITER International Thermonuclear Experimental Reactor

JET Joint European Torus

MRF Materials Research Facility

NRA Nuclear Reaction Analysis

PFIB Plasma-Focused Ion Beam

PFC Plasma-Facing Component

SEM Scanning Electron Microscopy

STEM Scanning Transmission Electron Microscopy

TEM Transmission Electron Microscopy

TKD Transmission Kikuchi Diffraction

UHP Ultra High Purity

UKAEA UK Atomic Energy Authority

Contents

Chapter 1

Introduction

1.1 Nuclear Fusion

The demand for energy has rapidly increased in recent decades, with global energy consumption rising by 53 % between 1990 and 2015 while the International Energy Agency predicts an increase of 41 % from 2015 to 2040 based on policies from 2019 [1]. The demand must be met with carbon-neutral and sustainable energy sources to mitigate the effects of climate change. Nuclear fusion is considered to be an ideal solution to these challenges due to an abundant supply of fuel, a lack of long-lived radioisotopes, and its reliability over other renewable energy sources. The conventional fuel choice for an energy-producing fusion reactor is a 50/50 mix of deuterium and tritium (D-T) due to its high fusion cross-section at lower temperatures compared to other possible fuel combinations. Moreover, the fusion reaction between D and T releases 17.6 MeV of kinetic energy carried by a helium nucleus (3.5 MeV) and a neutron (14.1 MeV), which is also a higher energy output than many other fusion reactions [2]. The fusion neutron contains most of the energy and its capture enables the generation of electricity and the breeding of more T. Lithium-based ceramics are prominent candidates for T breeding due to the $^{6}\mathrm{Li}(n,\alpha)^{3}\mathrm{H}$ reaction [3]. Recent studies have explored Helium Cooled Pebble Bed (HCPB) configurations containing lithium orthosilicates (Li_4SiO_4) and Water Cooled Lead-Lithium (WCLL) designs that use a lead-lithium eutectic alloy [4].

$$^{2}_{1}\mathrm{D} +^{3}_{1}\mathrm{T} \rightarrow^{4}_{2}\mathrm{He} +^{1}_{0}\mathrm{n} \tag{1.1}$$

The D-T reaction typically requires temperatures greater than 100 million °C which ionises the gaseous fuel mix into a charged plasma. In a tokamak, one of the leading reactor designs, the plasma is confined by magnetic fields which are produced by toroidal and poloidal coils that surround the main chamber. The International Thermonuclear Experimental Reactor (ITER), the largest experimental tokamak, is currently under construction in France. A key objective for ITER is to prove that this type of confinement can surpass the energy breakeven point. ITER hopes to achieve a fusion gain, Q of $\sim$10 [5] which is the ratio of the energy produced by the fusion reaction to the energy input required to sustain the reaction [5]. These accomplishments will help lay the groundwork for the first generation of power-producing, commercial fusion power plants, known as DEMO reactors, including the European DEMO design.

The conditions required to sustain the fusion reaction result in extreme thermal and pressure gradients within the vacuum vessel of a tokamak. This poses a particular challenge for the plasma-facing components (PFCs), not least because their failure affects the safety and the overall lifetime of a reactor. A significant focus of the fusion community is the development of advanced components designed to withstand the harsh conditions of the fusion environment. The research presented here builds upon this theme by assessing the structure of components in the as-received state and their degradation after exposure in the Joint European Tokamak (JET) during the ITER-like wall (ILW) campaigns. The parameters for JET and the estimated parameters for the ITER and European DEMO reactors are shown in Table 1.1.

Table 1.1: Comparison of parameters for JET, ITER, and EU-DEMO fusion reactors [6–9].

Parameter	**JET**	**ITER**	**EU-DEMO**
Major Radius (m)	2.96	6.2	9
Minor Radius (m)	1	2	2.38
Pulse Length (h)	0.001	0.11	1.83
Fusion Output (MW)	16	400	1793
Fusion Gain	0.63	10	36

1.2 The Joint European Torus and the ITER-Like Wall

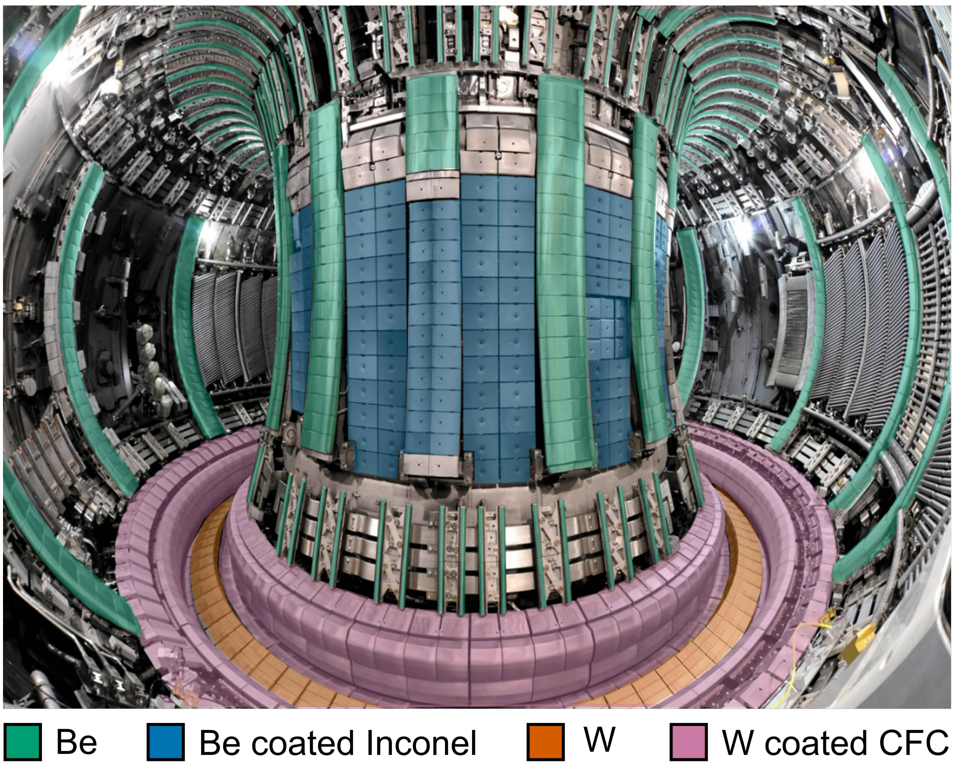

Figure 1.1: The Material Configuration of JET after the instalment of the ILW.

The JET tokamak at the UK Atomic Energy Authority (UKAEA) Culham Campus, is a crucial device for investigating material performance in a fusion environment [10]. In 2011, the carbon-based PFCs of JET were replaced with a Be first wall in the main chamber and a W divertor to mirror the material configuration of ITER [11][12]. The ensuing ILW campaigns helped develop plasma handling tools and scenarios while gathering information on in-vessel material migration [13]. The characterisation of PFCs that have been exposed in the ILW campaigns is essential for predicting the performance and longevity of components in ITER with one caveat. In recent years, it has been discussed and agreed that the Be first wall of ITER will be replaced by W before the first D-T operational phase [14][15]. The transition of materials is part of an effort to optimise the project by addressing technical challenges and managing risks related to component manufacturing, safety and operational efficiency. This shift could affect the scientific milestones planned for ITER but aims to ensure the project progresses toward its goals more effectively.

JET remains a closer approximation to ITER than most current tokamaks due to its size, plasma conditions and material configuration. The main chamber of JET, highlighted with blue and green in Fig. 1.1, is surrounded by magnetic field coils and is the region where the plasma is confined and heated. During the ILW campaigns, bulk Be tiles were the dominant material used in the high heat flux regions of the main chamber, including the upper dump plates, inner wall guard limiters and the outer poloidal limiters [16]. Be-coated Inconel is used for the inner wall cladding, the lower heat flux regions of the main chamber. The divertor sits underneath the main chamber and is highlighted in pink and orange in Fig. 1.1. It acts as an exhaust system, with surface temperatures that are typically the highest in the entire machine. The exhaust system removes impurities from the plasma and manages power loading on the first wall by directing particles and excess heat towards material surfaces called targets. There is no active cooling in the divertor and the tiles are made from W-coated carbon fibre composites (CFCs) except tile 5 which is comprised of bulk W components [17]. There were three ILW campaigns in total: ILW-1 in 2011–12, ILW-2 in 2013–14 and ILW-3 in 2015–16, with the details of each campaign listed in Table 1.2.

Table 1.2: Campaign data from JET ILW-1, ILW-2, and ILW-3 [18–23].

Campaign	Number of Discharges	Total Input Energy (GJ)	Average Input Power (MW)	Plasma time (h)		
				Total Operation	Limiter	Divertor
ILW-1	3812	150	2.2	19.0	6.0	13.0
ILW-2	4150	201	2.9	19.4	5.2	14.2
ILW-3	4420	245	2.9	23.4	4.9	18.5

JET is a pulsed device, meaning it operates in short bursts called shots or discharges where the maximum plasma duration was tens of seconds throughout ILW [24]. The loss of confinement was generally attributed to the plasma becoming unstable and having to be gradually shut down to protect the PFCs. However, the knowledge gained from JET ILW is directly applicable to ITER which is designed for pulses of up to several hundred seconds [24]. The DEMO reactors aim to achieve longer pulses, nearing two hours in the case of the European DEMO with the goal of one day building a reactor that can continuously operate in steady-state [7][25]. The vast majority of ILW pulses used a pure D fuel, which has two fusion reactions of equal probability [26][27]:

$$ {}_{1}^{2}\mathrm{D} + {}_{1}^{2}\mathrm{D} \rightarrow {}_{2}^{3}\mathrm{He} + {}_{0}^{1}\mathrm{n} \tag{1.2} $$

$$ {}_{1}^{2}\mathrm{D} + {}_{1}^{2}\mathrm{D} \rightarrow {}_{1}^{3}\mathrm{T} + {}_{1}^{1}\mathrm{p} \tag{1.3} $$

The first reaction produces a 0.8 MeV He-3 nucleus and a 2.45 MeV neutron while the second generates a 1.01 MeV T nucleus and a 3.02 MeV proton. The fusion neutron produced in D-D carries 11.7 MeV less energy and occurs less frequently than with D-T due to competing reactions. The use of D fuel may result in a smaller fusion power output but reduces neutron-induced material damage which improves safety and increases the machine lifetime. Moreover, it avoids the complexities and safety risks associated with handling T which is a low energy β emitter with a half-life of 12.3 years [21]. This afforded the JET team time to develop the plasma-handling tools and expertise required to operate the machine with a D-T fuel mix and to maximise the fusion power output. In 2021, during the D-T campaigns that followed the ILW, they achieved an energy output of 50.5 MJ over 5 s [9]. They not only proved this to be reproducible but improved on it in 2023 with an energy output of 69 MJ over 5 s, breaking records for magnetic confinement fusion [28]. This highlights the critical role of JET as a precursor to ITER. The installation of the ILW and the consistent testing of relevant plasma scenarios, even with D fuel, have resulted in plasma-material interactions, heat loads, fuel retention, erosion and deposition that closely resemble those expected in ITER. This thesis investigates the degradation of W PFCs from JET, therefore providing insights into the potential material damage that may occur in ITER.

1.3 Plasma-Surface Interactions in Tokamaks

In order to understand the practical impact of plasma-surface interactions on fusion materials it is necessary to study samples that have been exposed to the complex environment within a tokamak [29][30]. Damage mechanisms induced by one type of interaction can be significantly influenced by the simultaneous occurrence of a different kind of interaction or the presence of pre-existing damage [31][32]. These effects are particularly difficult to replicate in a laboratory setting. For example, neutron-induced damage can alter the way incident He ions interact with the material, and this effect varies with temperature, leading to unique damage profiles not captured in controlled experiments. Therefore, examining materials exposed in actual fusion environments is crucial to predict their behaviour and durability accurately.

Furthermore, PFCs in tokamaks are exposed to various kinds of plasmas, each with distinct characteristics such as density, temperature, and impurity content, which makes it difficult to explain and predict damage profiles. For instance, the interaction of high-energy D plasmas with PFCs differs significantly from that of He plasmas, both of which may create unique erosion patterns, fuel retention behaviour, or microstructural damage. Moreover, tokamak plasmas can experience transient phenomena such as disruptions and edge-localised modes (ELMs), where instabilities at the plasma edge arise due to periodic fluctuations in the edge transport barrier. PFCs in an experimental tokamak are therefore subjected to a continuously evolving environment, which is hard to reproduce anywhere else but also complicates the deconvolution of specific plasma-surface interactions during post-mortem component analysis. The following section primarily focuses on interactions relevant to W divertor components, while the selection of plasma-facing materials is discussed in Section 1.4.

1.3.1 The Effects of Neutron Irradiation

The number of neutrons was not expected to be a major issue during the JET ILW campaigns. However, there will be greater neutron fluxes and energies in ITER and DEMO. The 14.1 MeV D-T neutrons are more likely to cause transmutation, where a nucleus in the PFC absorbs a neutron and forms another element or isotope [33][34][35][36]. For W the most stable products of transmutation are H, He, Ta, Re and Os. The presence of different elements can result in the formation of precipitates or alloys that modify the component chemistry and therefore change its mechanical behaviour [37][38]. Furthermore, these elements could transmute again into other unstable nuclei that undergo radioactive decay with longer half-lives, posing a significant safety risk and limiting the lifetime of the components.

The high-energy fusion neutrons can also cause damage through collision cascades where they collide with atoms in the material and displace them from their lattice sites [39][40]. The displaced atoms can also cause other displacements, resulting in many interstitials and vacancies that can migrate and form defect clusters. The accumulation of interstitials can lead to the formation of other structures such as dislocations which are line defects caused by a misalignment in the crystal lattice, or dislocation loops which occur when interstitials form a 2D circular structure. When vacancies accumulate they can coalesce into larger voids which cause the material to swell. Neutrons are a particular concern because they are uncharged and can therefore cause transmutation and cascade damage deep in the bulk of a component. The term displacements per atom (dpa) is commonly used as a very basic measure of radiation damage and refers to the number of times an atom in the material is displaced from its lattice site. The ITER W tiles are predicted to display 0.6 dpa of neutron damage across the lifetime of the reactor [41]. A demonstration power plant such as the EU-DEMO is expected to produce around 5 dpa per fusion power year for the W first wall components [42]. Fission neutrons and ion implantation experiments have shown that $\sim$10 dpa, 2 full power years in the EU-DEMO, is enough to cause swelling in the range of 1.7–2.9 % [43] [44]. Other mechanisms of void formation include He implantation and interactions with high-energy ions, which can be further exacerbated at elevated temperatures by the accumulation of vacancies. The combined effects of neutron irradiation and these additional plasma interactions can significantly increase swelling, potentially necessitating the replacement of PFCs in a power plant every few years.

1.3.2 The Effects of Particle Loads

Other gaseous species can also cause cascade damage such as H and He, depending on their kinetic energy and the overall fluence of particles [45]. Furthermore, the elevation of surface temperatures during operation can increase the mobility of H and He atoms as well as vacancies within the lattice. This promotes vacancy coalescence, while gas atoms stabilise void formation, leading to increased swelling and potentially compromising the structural integrity of the component [46]. H and He can diffuse and become trapped in other irradiation-induced features which can lead to material hardening and embrittlement [47][48][49], these include vacancies, interstitials, defect clusters, dislocation loops, grain boundaries (GBs), precipitates and dislocations. If many features present in the component can trap H isotopes, then there will be an unnecessary increase in T retention. Beyond material embrittlement, T decays via β emission and therefore poses a safety risk through radiation exposure and contamination. Its retention in PFCs can interfere with the T recovery which is a critical step of the fuel cycle. It could also delay power generation as a commercial facility will have an operating license with a strict limit on the amount of T that can be present in the machine.

When large quantities of H and He have been implanted into the surface of a component the lattice can become saturated, leading to the formation of bubbles [50][51][52]. Their growth is extremely dependent on the temperature and defect population of the component and the kinetic energy and flux of the incident particles. Both species and their isotopes can originate from the fusion reaction or as transmutation products. H has less of a tendency to form bubbles due to its greater solubility and mobility in the material lattice. The H atoms can diffuse quickly through the material and can accumulate at defects or GBs, where they form bubbles by recombining into molecular H_2. H bubble formation therefore requires much higher concentrations than He, which typically results in different types of damage such as blistering or embrittlement [53]. Conversely, He tends to be trapped by vacancies or dislocation sites, forming stable bubbles even at lower concentrations. These bubbles can grow, causing significant swelling and potentially reducing the lifetime of the component.

Contact between the plasma and a component can not only result in cascade damage but can cause material loss through sputtering and erosion. These processes occur when high-energy particles bombard the material, removing atoms and causing morphology changes to the surface. Impurities are generated when the escaped atoms enter the plasma and radiate away some of the heat required to operate the reactor efficiently. When greater particle fluxes and heat loads are incident on the material surface, there is more significant surface degradation with the formation of voids, cracks and possibly dislodging larger pieces of material. Erosion rates are further increased by the formation of W fuzz which is caused by the bombardment of He ions on the surface of W components [54][55][56]. The fuzz forms a porous, nanostructured layer that can limit the lifespan of the component and release more W into the plasma.

Impurities, whether atoms, droplets or solid fragments, can be transported around the vessel and deposited onto the surface of other PFCs. These deposits can form uneven surface layers of mixed materials which have different properties than the original surface. Weak adhesion of these deposits and uneven thermal expansion can result in new sources of impurities and constant redistribution of material around the machine. This material can also accumulate as dust, potentially triggering a plasma disruption, interfering with diagnostic instruments and cooling systems and posing a safety risk by increasing the retention of radioactive isotopes.

1.3.3 The Effects of Thermal Loads

A key aspect in all these interactions is temperature. A large change in the temperature of the plasma or the component from one interaction to another can result in the formation of very different microstructures. Heat loads are not spatially or temporally constant which causes uneven thermal stresses and material wear. Heat loads vary across surfaces throughout the machine due to the shifting plasma position, which is influenced by changes in the magnetic field configuration as the plasma current, temperature, and magnetic fields are ramped up and down. Another factor that affects the divertor is the position of the strike point. This is the precise location where magnetic field lines intersect with the plasma-facing surface which receives much higher localised heat and particle fluxes compared to other surfaces in the divertor.

Heat loads can fluctuate during steady-state operation due to transient events. In steady-state operation, PFCs must continuously endure high temperatures. Peak stationary heat fluxes on ITER divertor components are predicted to reach 10 MW m^{-2} which can produce temperatures of up to 1800 °C at the trailing edge and 1400 °C on the surface of the component [57]. These temperatures exceed the typical recrystallisation range for W of 1000–1300 °C which might induce grain growth, making the component more brittle and susceptible to cracking [41]. Transient events such as ELMs [58][59][60] and plasma disruptions expose them to sudden, intense heat fluxes, potentially leading to localised melting or vaporisation. Models predict that the surface temperature of the W components in the ITER divertor vertical targets could increase by up to 1100 °C during an ELM in D-T operation [57][61]. This increase could be more than tripled at the edge of one of these components. Additionally, the cyclical loading from plasma pulses causes repeated thermal expansion and contraction of components, leading to significant thermal stresses [62]. These stresses can induce thermal fatigue, which over time contributes to crack formation and material degradation. As cracks propagate, they can compromise the structural integrity of the PFCs, potentially leading to failure. The concept of liquid metal flowing first walls and open-surface divertors have recently gained attention as a way of reducing material damage and extending the longevity of components [63][64]. The technology is promising but still requires considerable research and development, particularly in relation to corrosion and interference from the magnetic fields which affect the overall performance of the liquid metal systems.

Understanding and mitigating complex plasma-surface interactions and material challenges in solid PFCs is crucial for the long-term viability and safety of future fusion reactors. Laboratory-based experiments are frequently employed to simulate various aspects of the fusion environment [65]. Linear plasma devices can simulate plasma-surface interactions under controlled conditions, while electron beam facilities offer insights into radiation damage. Ion implantation is used to mimic the effects of charged particle bombardment, and neutron exposure in fission reactors provides a proxy for fusion neutron damage. Additionally, high-power lasers can simulate the thermal stresses and ablation effects experienced during intense heat loads. Each of these methods contributes valuable data, yet they cannot fully encompass the multi-faceted nature of the damage experienced in a tokamak. It is therefore extremely important to thoroughly characterise the damage in samples that have been exposed to real fusion environments. This provides critical insights that help predict how components will perform under operational conditions.

1.4 Material Selection for ITER and the JET ITER-Like Wall

Be was selected for the first wall tiles due to its impressive thermal shock resistance for transient events and high thermal conductivity of 200 $Wm^{-1}K^{-1}$ [66]. It also has a low Z number and binds strongly to O which decreases radiative power losses caused by impurities [67]. However, Be does have limitations regarding sputter resistance and a suboptimal melting point of 1287 °C [66]. In the future, Be could be used as a neutron multiplier to generate a sufficient neutron flux for lithium-containing T breeding blankets.

Carbon fibre composites (CFCs) have been widely used as PFCs in early iterations of devices such as JET and ASDEX at the Max Planck Institute for Plasma Physics in Germany [68]. CFCs have many desirable properties such as a thermal conductivity of 400–600 $Wm^{-1}K^{-1}$, and superior thermal shock and fatigue resistance compared to W [69]. In a study by T. Hirai *et al.* [70], CFC samples displayed no thermal fatigue damage up to 25 MW m^{-2} using the JUDITH I electron beam, 5 MW m^{-2} higher than the threshold for the W sample. In the case of a power-producing machine, the issues with CFCs start to outweigh their benefits due to the prompt decline of their favourable thermal properties after exposure to 14.1 MeV neutrons [71]. Moreover, CFCs are easily eroded, generating dust within the machine. They also tend to react with fuel ions at thermal energies to form hydrocarbons, which can trap T and thereby increase its retention [72]. These effects have been confirmed experimentally in JET [73] and ASDEX-Upgrade [74], where a significant decrease in fuel retention was observed when the C PFCs were replaced with W. Most present-day fusion devices use W for high-heat-flux components because of its low T retention and sputtering yield and relatively large thermal conductivity of 174 $Wm^{-1}K^{-1}$ and high melting point of 3422 °C [66]. Other devices have operated using a W divertor in addition to JET and ASDEX-Upgrade, including EAST at the Hefei Institutes of Physical Science in China [75] and WEST at the CEA Cadarache centre in France [76].

1.5 Sample Details and Thesis Objectives

The JET ILW divertor consists of a series of tiles shown in Fig. 1.2 (a) where tiles 0, 1, 3, 4, 6, 7, 8, B and C are made from CFCs with a ∼20 μm W coating and a thin Mo interlayer to separate the W and C [77]. Tile 5 is subjected to the highest heat fluxes in the divertor and therefore has a different design to the other tiles which is depicted in Fig. 1.2 (d), consisting solely of bulk W components called lamellae. The tile 5 assembly contains four stacks of lamellae, labelled A-D, with stack A closest to the inboard side and stack D on the outboard side. The divertor is toroidally divided into 96 modules, each containing 24 rows of lamellae. The first three rows of a module are slightly lower relative to the preceding module which results in shadowing from the plasma and prevents component melting. Additionally, the plasma-facing surface of each lamella is designed to prevent the formation of a leading edge. This is accomplished by machining a curve into half of the surface using electrical discharge machining (EDM). Overall, 1.4 mm of the lamella 5.9 mm width is fully shadowed, as shown in Fig. 1.3 (c). Two tile 5 modules can be seen in Fig 1.2 (d) where the lamellae in red were investigated for this thesis. The five lamellae selected for analysis were: C3 (ILW-1), C4 (ILW-3), C12 (ILW-1 & -3), C13 (ILW-3) and D12 (ILW-3).

These lamellae were chosen from different locations within the module and for different periods of exposure to see if slight variations in plasma loading would affect their microstructure and mechanical properties. The strike point is the location where magnetic field lines intersect the divertor surface, concentrating the majority of heat and particle flux in a highly localised region. This concentrated loading is typically associated with extreme thermal stresses, erosion, and material damage. The distribution of the strike point over the ILW campaigns is shown in Fig. 5.15. The strike point remained predominantly on stack C compared to the rest of tile 5, with the most significant damage likely occurring during ILW-1 and ILW-3.

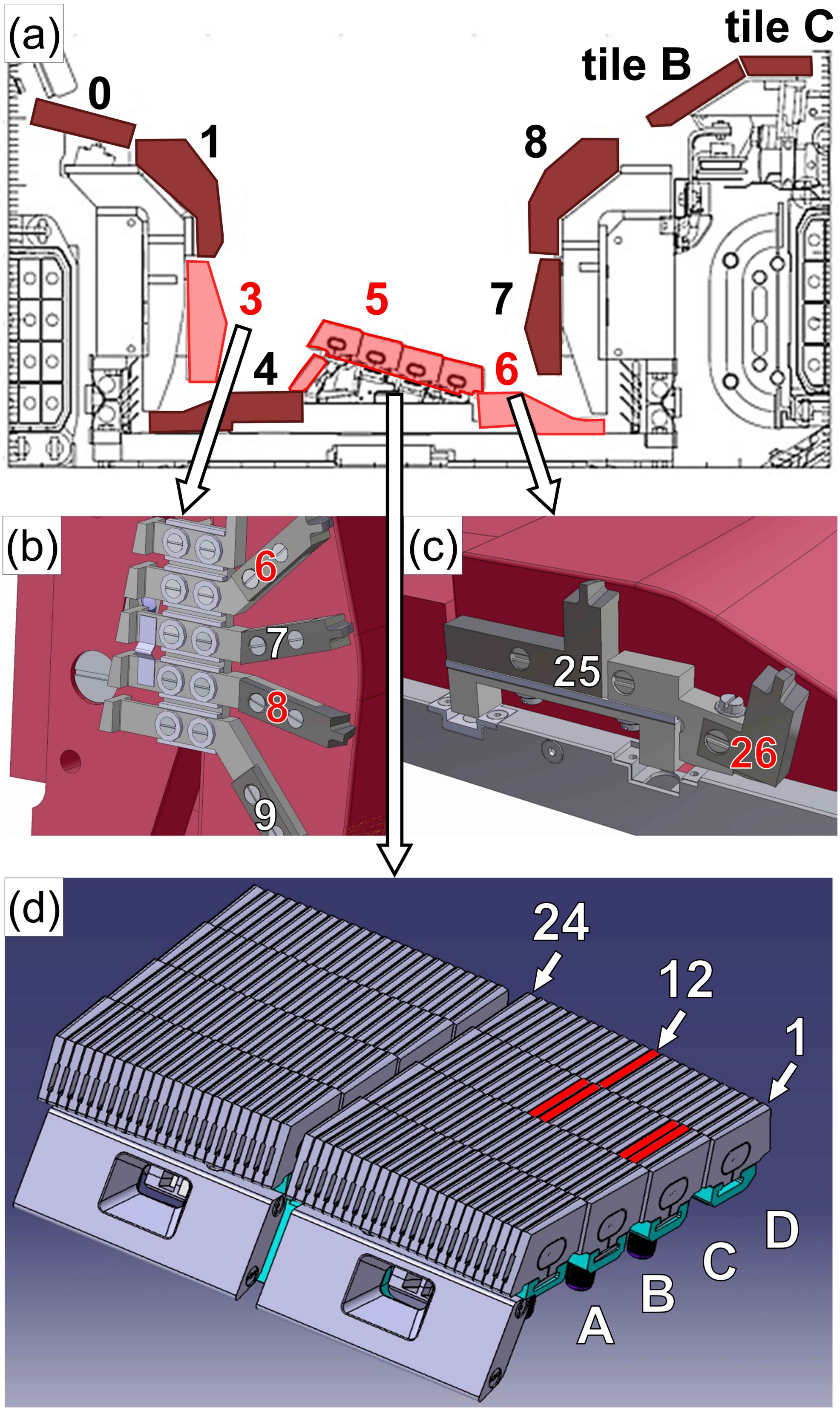

Figure 1.2: (a) A diagram showing the cross-section of the JET divertor during the ILW campaigns with the central column on the left-hand side and 3D renderings of (b) Langmuir probes 6–9 from tile 3, (c) Langmuir probes 25–26 from tile 6 and (d) two modules of lamellae from tile 5.

The analysis of lamella C3 differed slightly from the approach used for the others, as it was removed from a shadowed region of the module, where a build-up of surface deposits had occurred. This analysis forms the core of Chapter 6, which explores dust formation within the JET vessel. Initial structural and compositional characterisation of the deposits was obtained using a scanning electron microscope (SEM) and an energy dispersive X-ray spectrometer (EDX). A Ga focused ion beam (FIB) was used to observe the deposit cross-sections and to prepare samples for the transmission electron microscope (TEM). The TEM was then operated in scanning (STEM) mode to obtain micrographs of the deposits at high magnifications. These TEM samples also included the lamella surface to see how it had been modified by deposition in ways that could affect material adhesion to the surface and possible mechanisms for dust formation. Transmission Kikuchi diffraction (TKD) was used at the deposit-surface interface to detect residual stresses or grain growth induced by the temperature of the deposit. Electron energy loss spectroscopy (EELS) was performed on the TEM samples to map the distribution of low-Z number elements such as Be, C, O and N. Finally, a Xe plasma-FIB (PFIB) was used for tomography along one of the largest deposits to see how its structure changed with thickness and assess if it had modified the surface underneath it.

Characterising the structure of these deposits and the evolution of the lamella surface are essential for understanding material migration patterns, mechanisms of dust formation and the implications on fuel retention. Ultimately, this knowledge can help improve PFC design, manage fuel recycling, and optimise thermal performance, which is critical for the longevity and safety of future fusion devices. These findings represent the most detailed, high-resolution analysis of deposit structures from JET, the only modern tokamak operating with a Be first wall. Given the identical material configuration to the non-nuclear phases of ITER, similar deposit structures are expected. Consequently, these results can be confidently extrapolated to ITER, enhancing predictions of material behaviour and overall reactor performance.

A second type of bulk W component was analysed for this thesis, called a Langmuir probe. This is a type of diagnostic placed in a tokamak to measure local plasma properties such as electron temperature, density, and plasma potential. There is a high concentration of probes distributed around the divertor to help manage thermal loads. They are placed in between the tiles of adjacent modules as shown in Fig 1.2 (b) and (c), where the triangular-shaped tip protrudes into the plasma. The tip, highlighted in red in Fig. 1.3 (a), then behaves as an electrically biased electrode and records current-voltage (I-V) characteristics from the plasma.

The probe bias is varied to distinguish the ion currents from the electron currents, which allows the plasma parameters to be extracted from the I-V curve. The surface area of the tip is critical for calibration, as it determines the effective collection area for charged particles and influences the accuracy of the measurements.

This thesis includes the analysis of three Langmuir probe samples that were exposed in both ILW-1 and -2. Probes 6 and 8 were retrieved from modules 16 and 17 respectively, next to tile 3. Probe 26 was taken from module 15 near tile 6, all highlighted in red in Fig. 1.2 (b) and (c). The different sample locations allow for slight variations in plasma loading to result in distinct microstructures. In particular, probes 6 and 8 were close to the inner strike point and probe 26 was near the outer strike point, which likely resulted in high heat loads and particle fluxes. Meanwhile, the measurements recorded by the probes can theoretically offer insights into the real-time plasma conditions and contextualise the observed microstructural features.

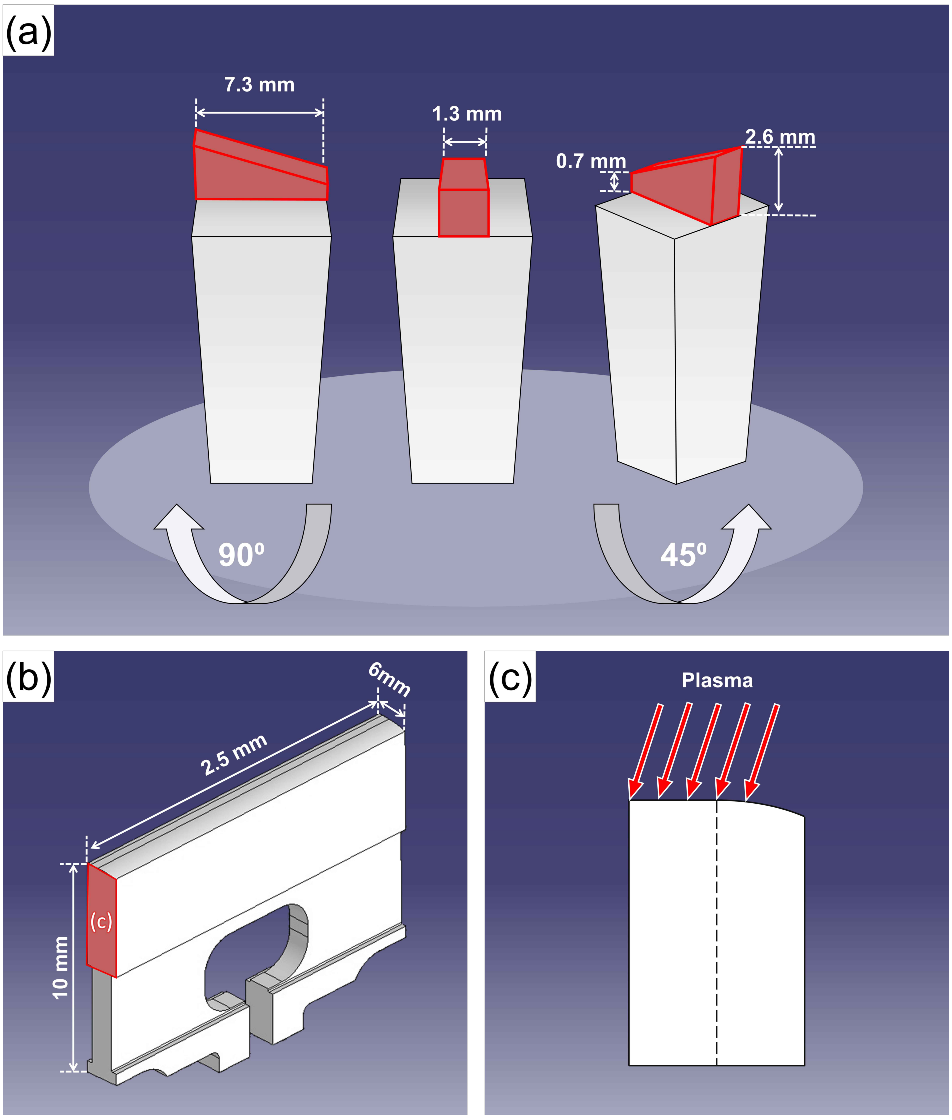

Figure 1.3: Schematics showing the structure of (a) a Langmuir probe with the triangular tip highlighted in red (b) a lamella with the cross-section highlighted in red and (c) the curved lamella cross-section which was machined with EDM with the direction of the plasma highlighted in red.

The four remaining lamellae and three Langmuir probes are investigated in Chapter 5 with an emphasis on the possible ways W components can be modified by plasma exposure. This chapter involves electron backscatter diffraction (EBSD) for microstructural analysis, to find out in which areas of the divertor have sustained sufficient temperatures to induce grain growth. Infrared (IR) camera diagnostic measurements were used to estimate the surface temperatures of the lamellae. Berkovich nanoindentation was used to locally determine where changes in elastic modulus and suspected irradiation hardening had occurred. Spherical nanoindentation was used to gain a better understanding of what mechanisms might cause these changes in mechanical properties. Ion beam analysis was performed on the Langmuir probes to see if D retention was affecting mechanical properties and void formation. The data recorded by the probes was then used to try and calculate the fluence of D ions that were incident on all the samples throughout the ILW campaigns. The chapter also addresses the limitations posed by diagnostic data from JET operations and the challenges of handling active materials.

The probes were manufactured by the same company, MGS Precision Ltd., using the same fabrication method as the lamellae, ensuring that the grade of W was comparable to that used in the ITER divertor. Although not specifically designed to withstand high heat fluxes, the probe tips needed to make direct contact with the plasma to collect measurements. Unlike the lamellae, where the JET control systems tried to keep surface temperatures below 975 °C [20], the probes were not given the same protection and likely suffered greater damage from thermal loading. Therefore, the results from these JET ILW probes represent an upper limit of potential heat damage for a W component in a modern tokamak operating with D. ITER will run with longer pulses and campaign lengths, increased thermal loads and more fusion neutrons but these findings still provide valuable insights that can be extrapolated to such a device. Moreover, these divertor samples capture the effects of simultaneous particle and thermal loading and D retention in a way that cannot be replicated using ion implantation, electron beam or high-power laser experiments.

In addition to comparing each exposed lamella and Langmuir probe to each other, a single lamella and Langmuir probe were manufactured for the ILW but not placed in the vessel so they could also be characterised. This provided a snapshot of what the components looked like before exposure and contrasting that with the exposed samples allowed conclusions to be made about recrystallisation behaviour, hardening mechanisms, and defect formation from D plasma-material interactions. In Chapter 4, the first experimental section of the thesis, the microstructure and mechanical properties of these two samples were characterised in the as-received state. The results also led to an assessment of the manufacture of the components with particular attention paid to the process of EDM, impurity content, void formation and crack initiation.

The analysis of the two as-received components included EBSD to analyse grain size and distribution across samples, checking if they had been engineered for thermal stability. Berkovich nanoindentation was performed to compare hardness and modulus between areas that were structurally unique. SEM-EDX was used to identify material that had become lodged in the surface due to the EDM process. The damage to this surface was also examined by creating cross-sections with the Xe PFIB. The Ga FIB was then used to prepare samples for TEM and atom probe tomography (APT). The TEM was operated in STEM mode to image the microstructures in the damaged layer and was paired with EDX for compositional analysis. APT was also used for compositional analysis of impurity-rich regions in both lamella and Langmuir probe samples. The cause of the damaged layer was confirmed to be EDM when it was used to cut samples from the as-received lamella and Langmuir probe components as well as a third ultra-high purity (UHP) W sample. These three samples were also heated to 900 °C and 1500 °C to check if the steep thermal gradient and intense stresses of EDM were also required to form the structures within this damaged layer.

EDM is used in nearly all W PFC shaping so it is important to fully understand what structures form during the process and how they could interact with the plasma in a fusion device. An abundance of impurities in the component can also weaken GBs, leading to a decline in mechanical performance. Moreover, these impurities could transmute from the bombardment of fusion neutrons, into unstable elements which increases the risk of radiation exposure and material degradation. Void formation can further contribute to material degradation by acting as stress concentration sites where cracks may initiate. These voids can also trap ions from the plasma such as T and Be, posing a significant health risk. If cracks are already present on the surface, it requires much less energy to propagate existing cracks than to initiate new ones, allowing for substantial crack growth. Under cyclic thermal loading in a reactor, repeated expansion and contraction can dislodge material, generating dust within the vessel. This dust presents multiple risks, including plasma contamination, which degrades performance and may lead to disruptions. Additionally, it can accelerate PFC erosion and increase T retention, compromising reactor safety. The accumulation of dust and damage further complicates machine maintenance, ultimately affecting the economic viability of fusion power by increasing the need for operational interventions.

Throughout the ILW campaigns, the vast majority of plasma pulses used a pure D fuel which has a non-zero probability of generating T in the side reaction D + D $\rightarrow$ T [1.01 MeV] + p [3.03 MeV] [21]. T is a β emitter with a half-life of 12.3 years and can be physically trapped in W samples [78] therefore the lamellae and Langmuir probes could still contain trace levels of T. Moreover, Be tiles in the main chamber are consistently eroded and Be deposits build up on the surface of the divertor which presents a risk of inhaling toxic material [13]. Therefore all experiments concerning these samples took place at the UKAEA Materials Research Facility

(MRF) and active sample preparation was completed by the MRF technicians.

1.6 Thesis Structure

This thesis is structured into seven chapters. Chapter 1 has been an introduction to the field of materials in nuclear fusion and how my research project fits into the wider discussion. Chapter 2 reviews the recent and relevant literature on the challenges of W components for fusion, providing context for the results discussed in the experimental chapters. Chapter 3 details the techniques used throughout the experiments, while the methodology itself is described in each experimental chapter. Chapter 4 presents the results obtained from the as-received components, concentrating on the distribution of grain size and hardness, the effects of impurities, and the formation of voids and cracks. Chapter 5 compares the microstructure and mechanical behaviour across the as-received samples and the components that were exposed in the JET divertor, focusing on the interactions that caused these differences. Chapter 6 characterises multiple types of deposits that formed on the plasma-facing surface of lamellae C3, identifying the distribution of deposited Be and its impact on dust formation in ITER. The thesis concludes with Chapter 7 which summarises the key findings, their limitations and implications while providing a direction for future work within the research area.

Chapter 2

Literature Review

2.1 Electrical Discharge Machining

Conventional machining techniques such as laser cutting, abrasive waterjet cutting, and diamond wire cutting are unsuitable for producing bulk W components for several reasons [79]. W has an extremely high melting point which makes laser cutting impractical due to the enormous energy requirements. Abrasive methods, such as diamond wire and waterjet cutting are inefficient and lack precision because W is hard and brittle. This brittleness also increases the risk of cracking and introduces substantial mechanical stresses. EDM removes material through electrical discharges in a contactless process, which helps mitigate common issues such as residual stress. This technique is particularly effective for working with high-strength, hard materials such as W, as it reduces the risk of damaging the material while maintaining its integrity [80]. However, the high thermal conductivity of W presents challenges, such as accelerated electrode wear, slow material removal, and reduced surface quality. Despite these limitations, EDM remains the most efficient and cost-effective method for machining W in fusion component manufacturing.

EDM can induce high temperatures, potentially introducing additional internal stresses [81]. These stresses arise from several factors: crystallographic mismatch, vacancies formed during oxidation, compositional changes and steep thermal gradients that cause differences in thermal expansion. These conditions influence void coalescence, GB sliding, and oxidation processes, which lead to the formation of intergranular cracks on the surface. Surface temperatures can vary between 8,000 and 12,000 °C, surpassing the melting point of W, which is 3,422 °C [66][82]. The effects of thermal damage are somewhat mitigated by maintaining short pulse lengths and the prompt dissipation of heat by a dielectric fluid. However, the process does typically result in a rough, re-solidified layer characterised by surface craters, voids, and cracks [83][84].

These features arise from residual stresses induced by impurities and elements diffusing from the surface into the bulk, particularly during arcing events [85][86][87]. The mechanism for void formation in steel was first proposed by Y.H. Guu *et al.* [88][89] who stated they were caused by gas bubbles that had been expelled from the molten material during solidification. Y. Zhang *et al.* [90] clarified in later studies that these gases were water vapour and H_2 from the water-based dielectric fluid. Moreover, the water vapour could induce oxidation in the metal workpiece at elevated surface temperatures. Other studies have shown that N, O, P, S, and Si are key impurities that promote GB decohesion in W and could be associated with cracking during EDM [91]. Among these, P appears to be the most detrimental to mechanical properties [92][93]. In recent years, the fusion community has placed less emphasis on impurities in W, instead focusing more on the effects of grain size, shape, degree of deformation, and dislocation density on its fracture behaviour [94–97]

2.2 Oxidation of Tungsten

W exhibits significant chemical stability at room temperature and atmospheric pressure but can gradually oxidise in the presence of moisture and O [98]. The oxidation rate sharply rises above 300 °C, even with atmospheric O levels as low as 5 ppm [99][100]. A thin oxide layer begins to form, likely comprising WO_2, $WO_{2.72}$, and $WO_{2.75}$, which restricts the diffusion of O atoms and slows the oxidation process. As temperatures exceed 500 °C, the oxide layer thickens, leading to the formation of $WO_{2.9}$, followed by the development of a bright yellow WO_3 layer on the surface. While WO_3 is the most thermodynamically stable oxide, it starts to sublimate at temperatures above 750 °C, with a significant increase in the sublimation rate beyond 900 °C.

2.3 Recrystallisation of Tungsten

Recrystallisation includes the nucleation of new, strain-free grains in a deformed microstructure which is typically followed by a period of grain growth. In W, recrystallisation begins between 1000 and 1300 °C [41], and as the grains become larger, the mechanical strength decreases and the GBs start to become brittle [94] [101–103]. The larger grains result in fewer boundaries so there are fewer barriers to dislocation movement and higher concentrations of impurities at the boundaries. In W, this increases the ductile to brittle transition temperature [104], meaning the component requires higher temperatures to become ductile and is more likely to fail via brittle fracture at low temperatures. It also affects the thermal conductivity of the sample and promotes cleaving along GBs [105]. Moreover, fewer boundaries mean fewer defect sinks which lowers radiation resistance and could enhance sputtering from the component surface. These factors could lead to early component failure in a fusion reactor where large stress fields can be caused by thermal and mechanical cycling. The rate of recrystallisation is extremely temperature-dependent, with higher temperatures expediting the nucleation and growth of new grains.

2.4 Analysis of Tungsten Components in Tokamaks

Some studies have started to characterise the microstructures produced in W components after exposure to D plasmas in a tokamak. In ASDEX Upgrade, W tiles exhibited deep and shallow cracks, likely driven by thermo-mechanical and electromagnetic stresses, particularly in high heat load regions [68]. Post-exposure analysis revealed deep cracks that propagated 15 mm deep into the W tiles, and shallow cracks forming up to 400 μm in regions experiencing repetitive cyclic thermal loads due to ELMs and other transient events. These cracks compromised the mechanical integrity of the tiles but did not cause operational failure.

At TEXTOR, W PFCs exposed to similar conditions experienced severe material changes, including melt-layer motion driven by Lorentz forces and evaporation cooling [106][107][108]. Molten W was redistributed to form large structures at the surface, leading to localised hot spots and subsequent erosion through mechanisms such as splashing and fine spraying. Additionally, significant microstructural changes, including bubble formation and recrystallisation, were observed, which degraded the power-handling capability of W.

Pintsuk *et al.* [10] investigated W lamellae from the JET ILW, showing that thermal and particle loading led to surface erosion, crack formation, and minor melting, especially in the highly loaded regions where the strike points were. Microstructural examination revealed no significant recrystallisation in these lamellae, despite surface damage such as erosion and cracks propagating up to 200 μm. Hardness measurements indicated an increase in surface Vickers hardness near the plasma-facing side, which was attributed to plasma interaction and D diffusion, though this was not sufficient to induce bulk recrystallisation.

Similarly, Spychalski *et al.* [109] used nanoindentation to investigate the mechanical properties of two W Langmuir probes, probe 5 from tile 3 and probe 26 from tile 6, that were exposed to the JET ILW-1 and ILW-2 campaigns. Their findings revealed a difference in hardness between the recrystallised probe tips (5 GPa) and the support structure (15 GPa). The elastic modulus was consistent across both regions at $\sim$260 GPa, despite localised surface modifications. The exposed probe tips experienced recrystallisation due to prolonged exposure at temperatures around $\sim$1300 °C, whereas the support structures remained unaffected. It should be noted that these samples could not be polished so nanoindentation was performed on a rough surface that had been exposed in the JET reactor, which should be considered when evaluating the changes in mechanical properties.

These studies highlight that W components in fusion environments experience varying degrees of surface modification, crack formation, and hardness changes depending on their exposure and thermal history, with recrystallisation at elevated temperatures emerging as a critical obstacle for mechanical integrity.

2.5 Deposits with the JET ITER-Like Wall

There have been numerous studies carried out on the types of deposits that form in the divertor of JET during the ILW campaigns, primarily involving energy-dispersive X-ray spectroscopy and ion beam techniques [110–122]. These investigations have identified that deposits can be categorised into mixed material layers, also called stratified deposits resulting from the continuous erosion of PFCs, and metal droplets, mostly W, Ni and Be, produced during the melting of components in the main chamber.

Be droplets, flakes and splashes likely originate from Be tiles from the first wall and Be-rich co-deposits that move within the divertor. W-rich droplets are believed to originate from W-coated carbon fibre composites (CFCs) or Langmuir probes near the lamellae, where the likelihood of melting is heightened [123]. Ni-rich droplets are thought to come from Inconel components in the main chamber, such as tiles in lower heat flux regions, which have an Inconel 625 substrate and a 7–9 μm thick beryllium coating [124]. Additional sources of Ni include the ion cyclotron resonance heating (ICRH) antennas, where both the central conductors and antenna housing are coated with Ni [125].

The mixed material layers have been shown to contain elements such as C, N, O, Ni, Mo and W, which have been linked to increased T retention [126–128]. The main constituent is Be which was continually eroded from the first wall, migrated to the divertor surface and was deposited in layers [118]. Mo is present in both the main chamber and the divertor and is used as the first mirror material in spectroscopy for plasma diagnostics [129]. Ni and Mo were both injected as part of laser blow-off (LBO) experiments to study the effects of impurities on the core of the plasma [130]. N was also injected into the vessel for disruption mitigation and plasma edge cooling which may explain why it was retained in the deposited layers [119].

There are a number of potential O sources including residual gases from when the vessel was at atmosphere, water vapour on the walls or directly injected into the plasma during operation [23][116]. Outside of the vessel, O contaminants could arise from oxidation during sample transfer and storage or from impurities in the PFCs during manufacture [131]. MGS Precision Ltd. reported 510 ppm of O and 25 ppm of C in the W powder before the lamellae were sintered, far higher than the other elements that were listed. Therefore C could also exist as an impurity from the manufacture of W components. In-vessel sources of C include residual dust from the C walls in the JET-C campaigns and the CFC substrates of the W-coated divertor tiles [122]. It is also possible for C to accumulate underneath the electron beam in an SEM/TEM and augment the amount of C recorded in an EDX/EELS spectrum [131].

2.6 Beryllium in the Fusion Environment

Be atoms are not particularly soluble in W due to differing lattice structures and electronegativities [132][133]. The solid solution is substitutional and therefore no high-W compounds form [134]. Only 5 at. % of Be is soluble in W from 2100 to 1800 °C and ~3 at. % down to 1000 °C [135]. For a W film on a Be substrate the energy of diffusion and alloy formation for a W atom in a Be matrix, is relatively low [136]. The alloy in this case is $Be_{12}W$, which is experimentally observed above 970 K [137–140]. $Be_{22}W$ can also form through the peritectic reaction, $L + Be_{12}W \leftrightarrow Be_{22}W$ [134].

In the reverse system of a Be film on a W substrate, there is a high energy barrier for an adsorbed

Be atom to diffuse into the bulk. If temperatures are sufficient to overcome this barrier then weak Be–W chemical bonds can form near the surface but not in the bulk [141][142]. Moreover, the energy barrier of desorption is smaller than the diffusion barrier, meaning there is a competition between W–Be alloy formation and Be sublimation. The alloy Be_2W is still able to form due to the large energy minima associated with the adsorption of a Be atom onto a W surface. In general, the alloy structure, $Be_{12}W$, produced by a W film on a Be substrate is more stable than Be_2W formed by a Be film on W substrate.

Be_2W has been shown to form ternary compounds Be_xWO_3 and BeWO4 when implanted with O ions at room temperature [143]. O was not able to diffuse at these temperatures so these compounds were only observed up to the implantation depth. Above 700 °C $BeWO_3$ and BeWO4 decompose, primarily favouring the formation of BeO while some W oxides form in an excess of unbound O [144]. In general, Be can diffuse through both W and Be_2W lattices, binding to any O in the system and favouring the formation of BeO over W oxides [145]. Furthermore, X-ray photoelectron spectroscopy (XPS) studies show that Be ions can diffuse through GBs in WO_2 and are mobile in WO_3 due to the diffusion channels in its structure [144]. So despite an innate resistance to W–Be alloy formation, at sufficient temperatures Be is still able to diffuse through many compounds that are likely to form at the plasma-facing surface.

In a reactor scenario, such as JET, Be impurities are likely to strike the W surface at sufficient energies to overcome any surface energy barriers and cause intermixing [146]. This can cause the formation of amorphous layers on the order of nanometres [147][148] and the formation of the aforementioned stable W–Be alloys, $Be_{22}W$, $Be_{12}W$ and Be_2W. The presence of these W–Be alloys has been shown to increase H and He retention compared to pure W surfaces [132][148–153]. These alloys are intermetallics with partial equilibrium liquid phases present at 1327 °C for Be_2W, 1507 °C for $Be_{12}W$ and 2247 °C for $Be_{22}W$ [154]. Although W PFCs are expected to have an operational temperature range of 150-1000 °C in ITER, transient events such as ELMs may cause temperature spikes which could result in ablation, melting and dust formation [155].

2.7 The Importance of Dust Production

Deposits are often a source of dust within a tokamak depending on their structure, porosity and composition. A total of ∼1 g of dust was generated during JET ILW-1 [156] but this quantity is predicted to be orders of magnitude larger in ITER where particle sizes are also expected to be greater than 150 μm [157]. Dust is detrimental in a fusion reactor for several reasons, due to potential safety hazards, radiological risks, plasma performance degradation, increased operational costs, and challenges in licensing and maintenance [131][117][116]. Dust particles, if allowed to accumulate, could exacerbate the risk of an explosion through contact with O during air ingress or water during a water leak. Dust particles can become contaminated with toxic Be or radioactive materials such as T and neutron-activated isotopes. This becomes an issue when applying for operating licenses and regulatory bodies may impose strict requirements which could impact the feasibility and economics of fusion. The generation of dust also imposes the need for thorough cleaning and specialised handling of components which is inefficient and costly. Additionally, dust degrades plasma performance through radiative power losses and increases erosion of first wall materials which reduces component lifetimes.

Chapter 3

Experimental Techniques

This chapter provides the relevant context and background, outlining the key concepts and principles that underpin the experimental techniques discussed in Chapters 4–6.

3.1 Scanning Electron Microscopy

The initial step for characterising most JET samples involved the TESCAN MIRA3 XMH SEM. SEMs converge a beam of electrons to a point with a diameter of 1 nm to 1 μm and raster said beam across the sample surface with a voltage between 0.5 and 30 kV [158]. The interaction between the electrons and the sample surface generates several signals that depend on the type of emission or scattering event. Secondary electrons (SE) are used for detailed topological imaging and are produced when the incident electrons transfer some of their energy to outer shell electrons. Backscattered electrons (BSE) provide compositional contrast and are elastically scattered electrons that interact with the atomic nuclei in the sample that are scattered back out. Characteristic X-rays determine elemental composition and are generated when the incident electrons knock out inner-shell electrons and higher-energy electrons fill the vacancy. These phenomena take place at different depths within the sample, known as the interaction volume: secondary electrons (SE) originate from the shallowest region, backscattered electrons (BSE) from a slightly deeper layer, and X-rays from the deepest region beneath the surface. The size of the interaction volume is determined by the beam energy, atomic number and density of the material. There is, however, a compromise between signal generation, resolution, sample integrity, and instrument capability when it comes to beam currents and voltages.

3.2 Energy Dispersive X-Ray Spectroscopy

An Oxford Instruments X-Max 80 detector was used for EDX analysis of the JET samples in the TESCAN SEM and analysed with the AZtec software, version 6.0 SP1. An EDX detector collects the characteristic X-rays produced at each beam position and maps the elemental composition near the surface of the sample. The beam diameter (probe size) is crucial. A smaller probe enables more localised chemical analysis but can reduce signal strength. Binning multiple pixels together can boost the signal, though this comes at the cost of resolution. Long acquisition times can reduce noise in the spectra but increase the risk of drift. Additionally, X-rays from other elements present in the vacuum chamber can introduce background noise, affecting accuracy, particularly for trace element detection.

3.3 Electron Back-Scatter Diffraction

The EBSD maps in this thesis were obtained using an Oxford Instruments NordlysNano Detector in the TESCAN SEM and analysed with the AZtec software, version 6.0 SP1. Some of the backscattered electrons undergo Bragg diffraction when they interact with the crystal lattice. These electrons are elastically scattered at certain angles that correspond to specific crystallographic planes and constructively interfere to form Kikuchi patterns. These patterns are indexed by referencing established crystallographic databases and properties such as crystal orientation, phase and strain can be mapped. The ability of the software to index the patterns and produce high-quality EBSD maps can be enhanced by optimising the probe size, dwell time, beam current and signal-to-noise ratio. Longer dwell times and higher beam currents improve pattern quality, while smaller pixel sizes increase spatial resolution, though these settings also increase acquisition time. The contrast of the patterns can be enhanced by applying a background correction and adjusting the gain settings. Pattern quality is also highly sensitive to surface finish and signal strength, requiring careful sample preparation and precise alignment with the detector.

3.4 Focused Ion Beam

An FEI Helios NanoLab, Ga FIB and a Tescan Amber X, Xe PFIB were the only FIB systems used to analyse the JET components. FIBs are a type of microscope capable of machining material at the sub-micron scale [159]. This is achieved by accelerating a beam of Ga ions toward the sample surface and focusing it to a fine diameter using a series of electromagnetic lenses. The beam is rastered over a predefined area and the incident ions then sputter atoms from the surface, removing material in a highly localised manner in a process called milling. Inelastic collisions with the atoms on the surface also produce secondary electrons which are collected to generate images. FIBs can also deposit material by decomposing a precursor gas introduced into the chamber, allowing for both additive and subtractive surface modifications. They are useful for creating micro- and nanostructures for small-scale mechanical testing. In this thesis, they were used to mill cross-sections, allowing for the investigation of sub-surface microstructures and preparing samples for techniques such as TEM and APT. FIB sample preparation can cause significant sample damage, such as surface ion implantation, amorphisation, and microstructural modifications [160]. Various techniques have been developed to lessen these damage mechanisms, including protective layer deposition, low-energy ion polishing, and cryogenic cooling. This can restrict damage layer thickness to less than a nanometre, allowing for high-resolution analysis.

Additional applications that were used in this thesis were a plasma-FIB (PFIB) and tomography [161], both of which were undertaken using the Tescan Amber X, Xenon PFIB. Instead of a beam of Ga ions, a PFIB uses a plasma source to generate a range of ion species, but a Xe beam was used in this instance. The beams are typically able to reach higher beam currents which enables faster material removal rates and covers larger areas. The increased sputtering rates and higher ion energies can result in reduced precision and potential surface damage compared to traditional FIB systems. A PFIB system was used to perform tomography on one of the JET samples. The technique involves sequentially milling thin layers from the cross-section of a sample and capturing a high-resolution SE image at each step. These images can be rendered into a 3D model, providing valuable volumetric information about the internal structure of the material.

3.5 APT Sample Preparation

The APT samples that were analysed in this thesis were prepared using standard lift-out procedures with the Helios Ga FIB [162][163]. To protect the surface from FIB damage, a Pt layer was deposited, ensuring it covered the GBs to incorporate them into the samples. A long bar was milled from the sample surface to produce multiple APT specimens, with additional Pt deposited to secure the bar to an OmniProbe nanomanipulator before it was lifted from the sample. These bars were then divided into individual wedges and fastened onto Si microposts with Pt. The wedges were sharpened to tips with radii of less than 50 nm, using annular milling at 30 kV with beam currents of 230, 80, and 24 pA followed by a polishing step at 2 kV.

3.6 Atom Probe Tomography

The samples were analysed using a CAMECA LEAP 5000 XS Atom Probe with a laser wavelength of 355 nm. Automatic detection rate control was enabled to maintain a stable W^{3+}/W^{2+} ion charge state ratio of 0.2. Tip reconstruction and compositional analysis were conducted with the IVAS software from CAMECA, running version 6.3.0.90. APT is a powerful technique, providing 3D compositional maps with a spatial resolution down to 0.2 nm in the XY plane and a sensitivity that can reach 100 atomic parts per million [164][165]. Atoms are removed from the tip of the needle-shaped sample via field evaporation and become ionised. This is achieved via a voltage pulse or a laser, with the latter used in this work. A static electric field then accelerates these ions towards a detector and the location of impact and time of flight are recorded. These measurements can then be converted into a mass-to-charge ratio for each fragment or individual ion and the exact species and starting positions are identified [166]. The key advantage of APT is its near-atomic resolution, making it well-suited for investigating the chemistry of GBs, interfaces and precipitates. It can also be used quantitatively to calculate the density of certain species and their isotopes.

However, the technique has some limitations related to sample preparation due to the presence of asymmetries, bluntness or multiple tips which can cause the sample to explode during the atom probe procedure. FIB damage can also introduce artefacts which ultimately limits the types of material that can be studied. Moreover, certain materials can be too fragile to withstand the high electric fields within the atom probe. The volume of material that can be analysed is also small, up to several hundred nanometres in the Z direction. Lastly, the user has to assign peaks in the mass spectrum to specific ions, which becomes difficult when ions have similar mass-to-charge ratios. One method of deconvolution involves natural isotope abundances which can be sufficient to resolve individual peaks. Overlapping peaks did not appear to be an issue for the analysis in this thesis particularly because the types of elemental impurities within the W components were provided by the manufacturer.

3.7 TEM Sample Preparation

The Helios FIB was also used to make TEM samples in a similar lift-out process to the APT samples [160][167]. TEM foil preparation was conducted using the following method:

A protective Pt layer was deposited, outlining the sample dimensions and 30 kV Ga ions were used to mill the surrounding material. The sample was then extracted using the OmniProbe nanomanipulator and attached to a copper grid using Pt. The sample was tilted ±1.5° to mitigate beam spread [168] while ion currents of 790 pA and 430 pA were used for thinning. Subsequent polishing steps involved a range of currents and accelerating voltages: 430 pA at 10 kV with a tilt of ±2°, 230 pA at 7 kV with a tilt of ±2°, and 230 pA at 5 kV with a tilt of ±10°. The final sample was thinned to 100 nm so that EELS and TKD were applicable and a Jeol ARM 200F TEM was used primarily in STEM mode.

3.8 Transmission Electron Microscopy

STEM imaging was performed on some of the JET components using a JEOL ARM200F with a cold field-emission gun source at 200kV accelerating voltage and the DigitalMicrograph software from Gatan, version 3.51.3720.0. EDX analysis was also performed in JEOL ARM200F with the JEOL Centurio high solid-angle EDX detector, using the Thermo Scientific Pathfinder X-ray Microanalysis software. TEMs are often used when the resolution of an SEM is insufficient, the short wavelengths of high-energy electrons allow some TEMs to achieve atomic resolution [169]. A beam of electrons is accelerated to energies of 100-400 keV to be able to pass through an extremely thin sample. The required thickness of the sample depends on the average atomic number of the material and the energy of the electrons, but a sample of less than 200 nm is typically preferred for most applications. The electrons then interact with the atoms in the material lattice as they pass through and are then focused by electromagnetic lenses to form a magnified image or diffraction pattern on a fluorescent screen or detector. The scattered electrons and X-rays that result from these interactions then provide information about the structure of the sample and composition. TEMs can operate in several modes, including STEM, bright-field and dark-field imaging, diffraction such as TKD, and spectroscopy such as EDX and EELS. This allows for a comprehensive analysis of a material structure, composition, and electronic properties at the nanoscale.

In STEM mode, the principles of TEM and SEM are combined to produce a finely focused electron beam, typically less than 5 nm in diameter, which is scanned across the sample [169]. A variety of signals are produced from each location of the beam which can be collected to produce images, diffraction patterns, and spectra with high resolution. The transmitted signal has a wide range of scattering angles based on the electron interactions with the sample. Different groupings of scattering angles can be studied in isolation to achieve various imaging modes [170].

Bright-field (BF) STEM involves electrons that are collected by an on-axis detector, where contrast is produced by differences in diffraction, mass and sample thickness. BF STEM is often used for studying phase contrast, assessing structural details and detecting light elements. Dark-field (DF) STEM captures electrons that have been scattered at angles away from the optical axis using an annular dark field (ADF) detector, which enhances the contrast of GBs, dislocations, and strain fields. High-angle annular dark-field (HAADF) STEM uses an annular detector to collect electrons scattered at large angles which provides atomic number (Z) contrast and helps distinguish heavier atoms from lighter ones. STEM mode can also be used for EDX which functions the same in a TEM compared to an SEM, with a few caveats. The interaction volume is much smaller in a TEM since the specimen is so thin which improves spatial resolution and expands analysis to nanostructured materials. The location of the EDX detector within the vacuum chamber can be a limitation, reducing the efficiency of X-ray collection to a lower level than in an SEM.

3.9 Electron Energy Loss Spectroscopy

EELS was carried out on the majority of TEM samples using a Gatan Quantum EELS detector in the JEOL ARM200F and analysed with the DigitalMicrograph software from Gatan, version 3.51.3720.0. The energy loss of the transmitted electrons after their interaction with the sample can also provide information on bonding, chemical composition and electronic structure with high spatial resolution [170]. The EELS spectrum contains a zero-loss peak where the electrons pass through the sample without losing energy and peaks of interest that arise from inelastic scattering events. Plasmon excitations, where free electrons in the sample collectively oscillate, produce energy losses up to 30 eV and can be used to distinguish different phases. Most important are the core-loss peaks where the incident electrons transfer enough energy to eject tightly bound electrons, typically from the K, L, or M shells. The energy lost by an incident electron corresponds to the binding energy of the ejected core electron, which provides detailed information about chemical bonding and elemental composition. The main advantage of EELS over EDX is its sensitivity to light elements, but the sample thickness must typically be below 100 nm, which complicates sample preparation. Interpretation can also be complicated with complex background signals and high electron doses can also damage delicate materials.

3.10 Transmission Kikuchi Diffraction

TKD was performed on one TEM sample using the Bruker Quantax EBSD system in a ZEISS Merlin Field-Emission SEM and analysed using Esprit software, version 2.0 [171]. TKD uses the same procedure as EBSD but the electrons are transmitted through the sample after elastic scattering instead of being backscattered [170]. The main advantage of TKD over EBSD is higher spatial resolution due to the smaller interaction volume which is well-suited for thin films and fine-grained microstructures. In some cases, the signal-to-noise ratio is improved in the diffraction patterns which leads to a higher success rate for pattern indexing. TKD uses higher energy electrons than EBSD which can damage certain kinds of samples and it also requires a sample thickness of less than 100 nm which is difficult to achieve consistently.

3.11 Berkovich Nanoindentation

The JET components were indented using the Nano Indenter G200 from Agilent Technologies with version 6.52 of the NanoSuite software and the iMicro Nanoindenter from KLA with the InView software. Nanoindentation is an extremely useful technique for obtaining local values of hardness and elastic modulus from the polished surface of solid samples. Berkovich tips are widely used in nanoindentation due to their self-similar geometry, meaning that their shape remains constant at all depths, which ensures a uniform strain rate during indentation. This consistency simplifies data analysis and enhances the accuracy of mechanical property measurements. The sharpness of the Berkovich tip helps to detect the precise moment when the indenter first makes contact with the material, improving the reliability of depth and load measurements. Additionally, its three-sided pyramid design requires less force to penetrate materials compared to spherical or flatter tips, making it particularly useful for probing thin films and small volumes.

The procedure involves using a sharp, Berkovich diamond indenter tip to penetrate the surface of the material. A known load, P, is incrementally applied through the Berkovich tip which causes a displacement, h, into the surface of the material. The plastic zone is the region surrounding the indenter that undergoes irreversible plastic deformation, leading to localised stress and strain that extend beyond the contact area and influence the measured hardness and mechanical response during the test. The contact area is an important variable during the indentation process and is the surface area in direct contact with the indenter. Although the 2D projection of the area of elastic contact, A, is typically used to simplify the calculations of mechanical properties while maintaining sufficient accuracy. The Oliver and Pharr method [172] was used to calculate the hardness, elastic modulus and area function for all Berkovich nanoindentation in this work. The maximum load, P_{max}, and the projected area of the hardness impression are then used to calculate the hardness, H:

$$\mathrm{H} = \frac{\mathrm{P_{max}}}{\mathrm{A}} \tag{3.1}$$

The reduced modulus E_r must be derived before calculating the elastic modulus of the sample, E. The contact stiffness, S, is determined by the gradient of the unloading segment of the load-displacement (P-h) curve which is related to E_r by the following equation:

$$S = \frac{dP}{dh} = \frac{2\beta}{\sqrt{\pi}} E_r \sqrt{A} \tag{3.2}$$

where β is a correction factor for the geometry of the tip. The values for S, β and A are known and the obtained value for E_r is then used to calculate E:

$$\frac{1}{E_r} = \frac{1-\nu^2}{E} + \frac{1-\nu_i^2}{E_i} \tag{3.3}$$

where ν is the Poisson's ratio for the material, ν_i is the Poisson's ratio for the indenter and E_i is the elastic modulus of the indenter. Accurate measurement of A is essential for precise evaluation of the material hardness and modulus. A mathematical relationship called the area function is established which accounts for the shape of the tip and links A to the penetration depth, h_c. The indentation in this work used the same polynomial as Oliver and Pharr [172] with six constants:

$$A = C_0 h_c^2 + C_1 h_c + C_2 h_c^{\frac{1}{2}} + C_3 h_c^{\frac{1}{4}} + C_4 h_c^{\frac{1}{8}} + C_5 h_c^{\frac{1}{16}} \tag{3.4}$$

The area function was obtained during the tip calibrations where at least 16 indents were placed in a well-characterised sample of fused silica each time the indenter was used. Fused silica has a known elastic modulus of 72 GPa and a Poisson's ratio of 0.17 which are used alongside the slope of the unloading segment of the $P-h$ curve to obtain a calculated E_r and an ideal E_r. The constants in the area function are then adjusted until the calculated E_r value matches the ideal.

The JET components were indented to an indentation depth of either 1 or 2 μm using the continuous stiffness measurement (CSM) mode established by Oliver and Pharr [173]. The method continuously records the stiffness throughout indentation by applying a relatively small oscillation to the force signal, while simultaneously recording the resulting amplitude and phase of the displacement.

All indents were performed at room temperature once thermal drift rates had reached an acceptable magnitude and displacement control was enabled. Indents were placed in arrays of typically more than 16 indents to ensure statistical reliability and account for potential variability in material properties. Taking an average of multiple indents reduces the impact of outliers and anomalies, leading to more accurate and representative measurements of hardness and modulus. Indents were excluded from the final analysis if they did not reach the specified depth, showed skewed imprints or were located on GBs in the optical images or EBSD maps.

The mechanical components of the system also contribute to the overall stiffness measured during indentation which is accounted for with a frame stiffness correction. This process was applied to all indents and involves subtracting the stiffness of the indenter and frame from the total measured stiffness. The stiffness of the indenter and frame is calculated during the calibration and any further deviations are adjusted by hand until the modulus-depth curves become flat. These curves only start to plateau to a constant value once at larger displacements when noise and surface roughness effects are negligible.

The main limitations of this method of indentation include the “pile-up” of material around the indenter due to significant plasticity which increases the contact area and produces an overestimation of hardness and modulus [173]. Another limitation is the indentation size effect, where hardness increases at smaller indentation depths due to the pronounced strain gradients and the need to accommodate geometrically necessary dislocations (GNDs) in response to these gradients [174][175]. Additionally, the technique is sensitive to surface roughness and requires highly polished samples to obtain reliable data [176]. The indenter tip itself can also wear over time, which can introduce errors if it is not regularly calibrated [177]. Finally, the method assumes elastic isotropy of the material, but this should not adversely affect the data in this work since W exhibits minimal deviation from isotropic behaviour [178].

3.12 Spherical Nanoindentation

Spherical Indentation was performed using a diamond tip with a radius of 2 μm to a depth of 500 nm using the Nano Indenter G200 from Agilent Technologies and analysed with the NanoSuite software, version 6.52. The amount of deformation that occurs during indentation depends on the opening angle of the indenter tip [179–184]. The strain produced by a spherical tip increases with indentation depth due to changes in the opening angle of the tip, which is not observed with self-similar geometries such as a Berkovich tip [185][186]. Therefore it is possible to extract a stress-strain curve from a single spherical indent but relies on a precise tip calibration [183][187][188].

The methodology of spherical nanoindentation has developed at quite a pace in recent years, specifically with the refinements proposed in the publication by A. Leitner *et al.* [187]. The new approach adjusts the definitions of the different deformation regimes and introduces a new method for calibrating the tip radius, using an effective contact radius that changes as the indenter penetrates the material. Their initial results appeared to match the micropillar compression tests of ultrafine-grained metals without prolonged or fastidious sample preparation. The article by A. Leitner *et al.* [187] lays out a set of equations for the new tip calibration:

$$\mathrm{A_c} = \mathrm{a_c^2} \cdot \pi \qquad (3.5) \qquad\qquad \mathrm{A_c(h_c)} = \mathrm{B_0} \cdot \mathrm{h_c^{B_1}} - \mathrm{B_2} \cdot \mathrm{h_c^2} \qquad (3.6)$$

where A_c is the contact area, a_c is the contact radius, h_c is the contact depth and B_i is a constant that is adjusted using a non-linear least square method to define the sphericity of the tip. The output from these equations is then used to calculate the stress, σ, and strain, ϵ, for every value of displacement:

$$\sigma = \frac{\mathrm{P}}{\mathrm{A_c}} \qquad (3.7) \qquad\qquad \epsilon = \frac{4\mathrm{h}}{3\pi \mathrm{a_c}} \qquad (3.8)$$

where P is the load and h is the total displacement which is found using the method outlined by Oliver and Pharr [172]:

$$\mathrm{h_c} = \mathrm{h} - 0.75 \cdot \frac{\mathrm{P}}{\mathrm{S}} \qquad (3.9)$$

where S is the stiffness and 0.75 is the geometric constant used for a spherical tip.

3.13 Ion Beam Analysis

A 2.5 MV Van de Graaff accelerator was used at the Instituto Superior Técnico, Universidade de Lisboa, Portugal which is displayed in Fig. 3.1. There were three main lines which offered various ion beam techniques including elastic recoil detection analysis (ERDA), particle-induced

X-ray emission (PIXE), Rutherford backscattering spectrometry (RBS), Nuclear Reaction Analysis (NRA), and a Nuclear Microprobe [189]. The final two techniques can both detect D by accelerating ^{3}He$^+$ ions at a sample while collecting the protons that are given off as a result of the D(^{3}He, p)^{4}He reaction. The beamline highlighted in green in Fig. 3.1 was the first to be used, housing an Oxford Microbeams Ltd. type Nuclear Microprobe with a resolution of 3×4 μm^2 and a scan amplitude of 2.6×2.6 mm^2. The Microprobe detector had a surface barrier of 200 mm^2, solid angles of 80 msr, Cornell geometry of 40$^{\mathrm{o}}$, and was covered by a 12 μm Mylar foil. Initial beamline experimental transmission conditions were optimised using a 2 MeV H$^+$ beam that was swapped to a 2 MeV ^{3}He$^+$ beam for the rest of the analysis. The Microprobe detector was calibrated using a Be target which relied on the detection of protons from the ^{9}Be(^{3}He,p$_x$)^{11}B reaction. The proton peak energies of this reaction are listed in the study by V. Foteinou *et al.* [190].

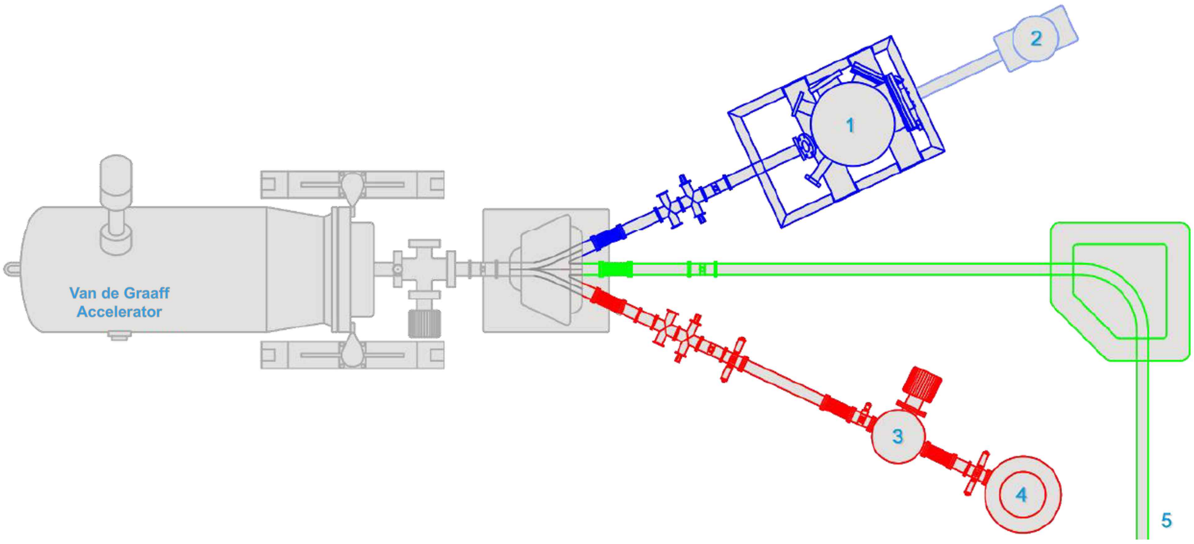

Figure 3.1: Schematic of the Van de Graaff accelerator at IST, Portugal with the JET tile analysis line in blue, the Microprobe line in green, and the RBS line in red. Chamber 1 is equipped for NRA of large samples, chamber 2 for PIXE analysis, chambers 3 and 4 for RBS, NRA and ERD (only in chamber 4), and chamber 5 for the Microprobe. Diagram created by N. Catarino [189].

Chapter 4

JET W Plasma-Facing Components in the As-Received State

4.1 Introduction

A bulk W lamella sample and a bulk W Langmuir probe sample were originally characterised in the as-received state to compare to the JET-exposed microstructures presented in chapters 5 and 6. However, once data collection was underway, it became clear that the manufacture and machining of these samples resulted in the formation of microstructural features that should be fully understood before considering the effects of plasma exposure. The manufacturing steps included sintering, hot rolling, annealing and EDM, which are widely used in the production of bulk W components, making these results applicable to the broader fusion materials community.

This chapter aims to assess how the manufacturing route has shaped the microstructure of the samples, with a particular emphasis on understanding the difference in grain morphology that was observed between the two types of component. The chapter explores the effects of these microstructural variations on mechanical behaviour, fully characterising the different regions in terms of hardness and elastic modulus and providing a reference for the JET-exposed samples.

Another goal of this chapter is to examine the changes induced by EDM, focusing on how extreme thermal gradients and impurities introduced during this process and manufacture influence the structural integrity of W components. A related objective is to investigate the role of impurities, particularly at GBs, and how they contribute to the formation of voids, cracks, and other defects.

Additionally, the chapter will investigate how the components are affected by different heat treatments and how their response compares to an ultra-high purity (UHP) W sample. These treatments attempt to replicate certain microstructural features observed in EDM such as voids and cracks. The results will establish a foundation for subsequent chapters, which will explore how Langmuir probes and lamellae behave under plasma exposure in a fusion environment.

4.2 Manufacturing Details

The UHP W sample was manufactured in the same batch as the UHP samples used in the study by M. Rieth *et al.* [191]. It had a reported purity that exceeded 99.999%, a deformation degree ∼80% and was sintered in an atmosphere of H_2.

The manufacturer of the JET components, MGS Precision Ltd., stated a component purity of 99.95%. Physical documents concerning the manufacture of the lamellae were acquired from the JET archive and contained specifications and certificates for batch and charge number, chemical composition and mechanical properties. The equivalent documents for the Langmuir probes were not found after an extensive search of the JET archive but direct correspondence with MGS Precision Ltd. confirmed that they had been manufactured using the same procedure as the lamellae. This procedure involved cold isostatic pressing of W powder at 200 MPa for 2 minutes and sintering in a H_2 furnace by Beijing Tian-Long Tungsten & Molybdenum Co., Ltd., who did not disclose the precise T-t curve. Subsequently, the lamella underwent hot rolling, detailed in Table 4.1, followed by an hour of annealing between 1150 and 1200 °C. Finally, the plasma-facing surfaces were shaped using EDM.

Table 4.1: Machining parameters used in the hot rolling of the lamella, where T and L represent rolling in the transverse and lateral directions

Pass Number	1	2	3	4	5	6
Temperature (°C)	1620	1580	1500	1420	1340	1280
Holding Time (min)	50	15	10	10	10	10
Rolling Direction	L	T	T	L	L	L

4.3 Experimental Details

The bulk, as-received lamella had been machined using EDM in the same manner as the other lamellae exposed in JET. It was then cut using a diamond saw, creating a sample to image the plasma-facing surface and another two samples to study the cross-sections parallel and perpendicular to the rolling direction. The cross-sectioned samples were polished through to 1 μm using diamond suspensions before colloidal silica was used as the final polishing step. Grain size and distribution were obtained via EBSD of the cross-sections and nanoindentation was performed to obtain sample hardness and elastic modulus. A total of 64 indents were collected to a depth of 1 μm, with the indentation axis aligned with the rolling direction of the grains. The sample containing the plasma-facing surface was of particular interest due to the surface damage that occurred during machining and the potential interactions that could occur with the plasma in the divertor. This sample was left unpolished and was examined with both a Ga FIB and Xe PFIB. The Ga FIB was also used to lift out and thin one TEM sample and nine APT samples. The TEM sample, which included a cross-section of the surface damage, was imaged in STEM mode and investigated with EDX.

One sample was cut from the bulk, as-received Langmuir probe by the MRF technicians so they could develop a recipe for active sample preparation. The remainder of the Langmuir probe was not immediately accessible therefore preliminary testing began with this smaller off-cut. The sample was polished to 1 μm with diamond suspension and colloidal silica and EBSD revealed a bimodal grain size distribution. Nanoindentation was performed to 1 μm depth using the G200 at the MRF with 15 indents placed in the fine-grained region and 25 indents in the coarse-grained region. The process was repeated using the G200 at the Department of Materials, University of Oxford, with 32 indents placed in the fine-grained region and 32 indents in the coarse-grained region. The results from both G200 machines were compared, additionally the G200 at the MRF was incapacitated from November 2021 through the end of data collection.

It was not immediately clear from which region the MRF technicians had cut the sample so another two samples were prepared in the same manner once the remainder of the Langmuir probe became available. One sample contained the cross-section of the triangular tip and part of the base while the other was cut perpendicular to this to check for any grain elongation from rolling. The preliminary results were validated by comparing the hardness and modulus values between the technician-prepared sample and the sample containing the cross-section of the tip. This was achieved with 25 indents at a depth of 1 μm in the coarse-grained regions in both samples.

EBSD maps were then collected from the two newly cut samples and the very top of the probe tip was examined in the FIB for further signs of machining damage. Six APT samples were prepared from the coarse-grained regions in the bulk of the probe and compositional analysis was carried out by Dr Martin Meier (University of Oxford) using the CAMECA LEAP 5000 XS Atom Probe. A total of 15 APT samples were prepared from both the as-received lamella and Langmuir probe. One of the Langmuir probe APT samples captured a triple point of GBs directly through its centre which is the sample that is discussed in section 4.7. More APT samples would need to be collected to obtain a reliable mean for the impurity content at the GBs, but this APT sample serves as a good indicator for the as-received W samples that are characterised in this chapter.

The EDM process was found to introduce large cracks that were frequently decorated with voids on the machined surface of the as-received lamella. There were numerous attempts at placing indents in void-dense regions to gauge their effect on mechanical properties but it was not possible using the built-in optical microscope of the G200. FIB cross-sections of the cracks showed that many of them appeared to be filled with material that produced a darker contrast in SE micrographs. To study the effect of this dark material on mechanical properties, an indent of 300 nm was placed on either side of a crack with a separation of 6 μm. The first indent of each pair was hand-placed and every pair was positioned at least 4 μm from the sample edge to minimise the effect of surface curvature on the calculated area function. This was repeated for 19 consecutive cracks that were observable in an optical microscope, over a total distance of 1.61 mm along the cross-section of the lamella.

The indentation depth of 300 nm was selected after analysing the CSM measurements from the 1 μm indent tests. It was the smallest that an indent could reasonably be before surface effects introduced appreciable scatter into the measurements. A shallow depth was desired to minimise the size of the plastic zone such that a greater proportion of this zone was occupied by dark regions which were typically less than 2 μm wide. The plastic zone radius of a 300 nm indent was calculated using the Johnson continuum elastic-plastic model [192–194], and was used by C. Robertson *et al.* similarly for austenitic stainless steels [195]. The model states $c = \sqrt{\frac{3F}{2\pi\sigma_{ys}}}$, where F is the applied load at 300 nm which was 16.1 mN and σ_{ys} is the bulk yield strength which is 750 MPa [196], yielding a plastic zone radius, c, of 3.20 μm. Hence a 6 μm separation was sufficient for the dark region to be captured in the plastic zone of at least one of the indents in each pair. After the 19 pairs of indents were placed next to the dark regions, each pair was cross-sectioned in the FIB. Indents that were placed over 2.55 μm from the boundary were excluded from the analysis. Three 5x5 arrays of 300 nm were also placed in the bulk of the sample and these hardness and modulus values were compared to those from the dark regions.

Two sets of three samples, an ultra-high purity (UHP) W sample, the as-received Lamella and Langmuir probe, were heated in a vacuum furnace to try and activate void formation at two specific temperatures. Both sets of heated samples were cut with a diamond saw to remove all EDM-ed surfaces, polished, and sealed in quartz tubes with a vacuum pressure of 1 x 10^{-6} torr. One tube was held at 900 °C for an hour, excluding ramp-up and cool-down time, to reduce W oxidation and probe impurities such as white P that can boil at temperatures as low as 280.5 °C [66]. The other quartz tube was held at 1500 °C for 24 hours, excluding ramp-up and cool-down time. This was the imposed time and temperature limit of the tube since quartz, vitreous silica, has a melting temperature of 1713 °C [66]. The samples that were held at 1500 °C all developed flaky greenish coatings which signaled the formation of WO_3. These coatings were removed from one face of each sample with P400 grit paper and the faces were then polished with diamond suspensions and colloidal silica. The surfaces of the 900 °C samples remained smooth and did not require further preparation. Three pristine samples were kept in the as-received state, cut and polished, and compared to the heat-treated samples. All nine samples were viewed in the FIB, and at least 3 cross-sections were milled in the bulk of each sample. No evidence of void formation was observed so to confirm the origin of the observed microstructural features, the three pristine samples were cut using EDM. The machine was a Charmilles Robofil 240 CC Wire EDM, with a water lubricant. Two FIB cross-sections were milled into the EDM-ed surface of each sample which was sufficient to show the formation of voids and cracks in each sample.

4.4 Starting Microstructure of Lamellae

The grain structure of the lamella is summarised in Fig. 4.1, where the rolling direction (RD) is normal to the plasma-facing surface. Fig. 4.1 (a) and (b) reveal a structure characteristic of rolled W [197][198], namely the formation of large grains that are elongated in the RD. These grains are subdivided by low- and high-angle boundaries which form due to the significant accumulation of deformation during hot rolling. The degree of subdivision across one of these grains appears to correspond with grain orientation, for instance, the green ⟨101⟩ grains display the smallest amount of misorientation compared to the other orientations. The sub-grained regions are shown at a higher magnification in Fig. 4.1 (c), using the AZtec software from Oxford Instruments for grain analysis with a grain detection angle of 2.0 °. This returned an average value of 2.1 μm for the equivalent circular diameter (ECD), with a standard deviation of 0.9 μm for a total of 250 grains with a minimum area of 1 μm^2.

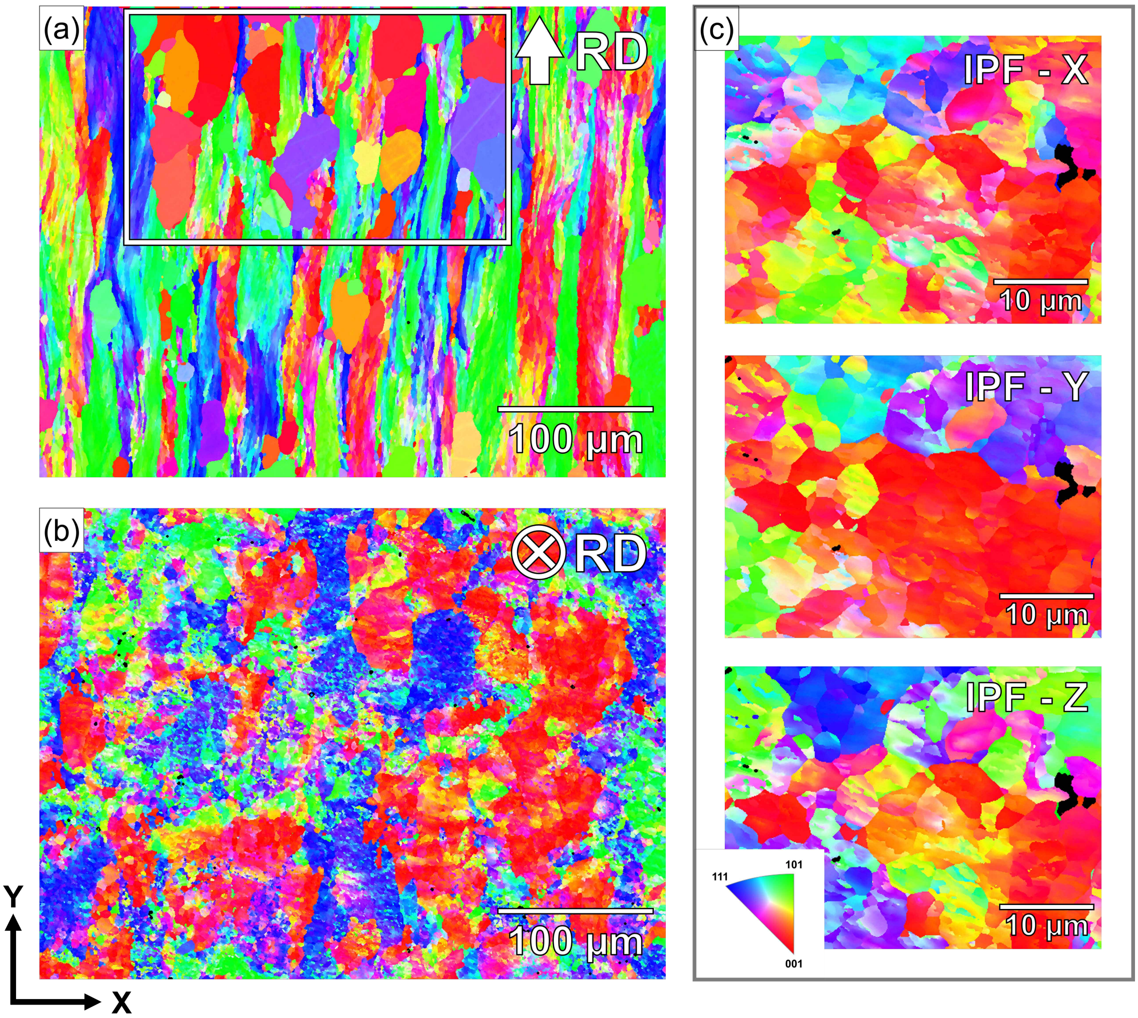

Figure 4.1: EBSD maps of the as-received lamella showing the cross-section (a) parallel and (b) perpendicular to the rolling direction (c) inverse pole figures (IPFs) for the X, Y and Z directions at higher magnification.

Conversely, Fig. 4.1 (a) shows the formation of equiaxed, recrystallised grains, highlighted in the white box, that are non-uniformly distributed throughout the sample. The average ECD value for this region was 26 μm with a standard deviation of 8 μm. A grain detection angle of 2.0 ° was used for a total of 42 grains with a minimum area of 189 μm^2. The minimum area was manually selected to stop the AZtec software from identifying artefacts as grains. The larger grains likely formed during the hour of annealing at 1150-1200 °C which did not appear long or hot enough to cause recrystallisation in all regions. The presence of small, 2 μm grains may have a pinning effect on GBs as they migrate during recrystallisation. The nucleation behaviour and mobility of GBs could also be affected by impurities, which could suppress recrystallisation and result in a more stable microstructure.

4.5 Starting Microstructure of Langmuir Probes

The manufacturer of the samples, MGS Precision Ltd., confirmed that the Langmuir probes had been manufactured using the same procedure as the lamellae and the grain structures were therefore expected to be similar. An overview of the Langmuir probe structure is shown in Fig. 4.2 which depicts a different morphology from the lamella. Most of the sample is comprised of equiaxed grains but there are some fine-grained regions, as shown in Fig. 4.2 (a) and (d), that resemble the rolled structure in the lamella. Grain analysis was performed in AZtec to find the ECD for both of these regions with a grain detection angle of 2 °. In the coarse-grained region for a minimum grain area of 50 μm^2 and a total of 1,157 detected grains, the average ECD was 24 μm with a standard deviation of 15 μm. For the 383 fine grains detected in Fig. 4.2 (d), the average ECD was 1.5 μm with a standard deviation of 1.3 μm and a minimum grain area of 50 nm.

The distinct distributions of coarse- and fine-grained regions have previously been observed in recrystallised W samples for similar annealing temperatures and periods [199][200]. In the study by A. Manhard *et al.*, the grain size increased further and the fine-grained regions were removed after another annealing step at 1,727 °C. The distribution of grains also appears to depend on purity, where a UHP sample is more likely to recrystallise fully [201]. Such a drastic difference in purity between batches is not expected from MGS Precision Ltd., particularly since the distinct microstructures of the Langmuir probes and the lamellae were reliably recreated in the exposed samples in Chapter 5. The most likely explanation is the use of a slightly different manufacturing parameter due to the different shapes and sizes of the two components. This parameter could be increased annealing time or higher temperatures during either annealing or rolling, but importantly this is a parameter that would give the probes a greater chance of recrystallisation compared to the lamellae. Furthermore, the size of the recrystallised grains in both the Langmuir probe and the lamellae were extremely similar, 24 μm and 26 μm respectively, suggesting that there may be fewer differences between the two manufacturing processes.

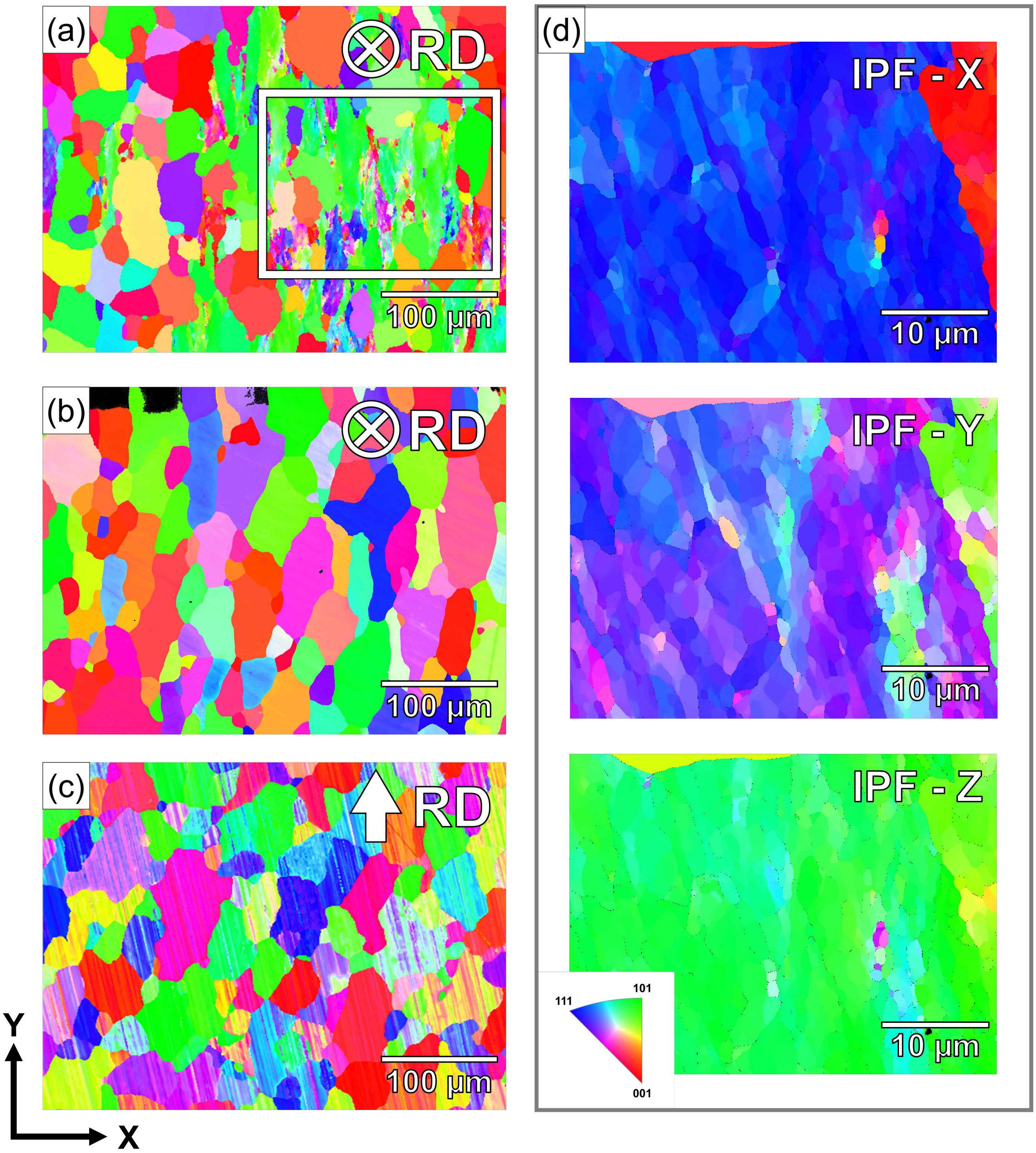

Figure 4.2: EBSD maps showing (a) the as-received Langmuir probe cut by the MRF technicians with the fine-grained region highlighted in the white box (b) a cross-section of the tip parallel to the triangular face (c) a cross-section of the base perpendicular to the triangular face (d) IPF-X,Y and Z taken from a fine-grained region.

The appearance of the fine grains was not homogeneous throughout the whole sample and they appear to be absent from Fig. 4.2 (b) and (c) which were taken from a central slice through the sample and represent the tip and the base of the probe respectively. The mapped surface in Fig. 4.2 (c) was perpendicular to the surfaces in the other EBSD maps and was unfortunately scratched during sample transfer but the pattern quality was sufficient to confirm the absence of grain elongation due to rolling.

Table 4.2: A comparison between the Langmuir probe sample that was prepared by the MRF technicians in Fig 4.2 (a) and the sample in Fig 4.2 (b) that was cut from a known region of the probe.

		Hardness (GPa)		**Modulus (GPa)**	
Sample	Number of Indents	Mean	Standard Deviation	Mean	Standard Deviation
Technician-Prepared	11	**5.2**	0.1	**380**	10
Self-Prepared	13	**5.2**	0.1	**390**	10

Berkovich nanoindentation was performed in the coarse-grained regions of the samples in Fig. 4.2 (a) and (b) to confirm an agreement in mechanical properties, proving that the technician-prepared sample originated from the same bulk probe. The results are summarised in Table 4.2, showing similar hardness and modulus values for both samples and validating the EBSD maps and subsequent nanoindentation data collected from the technician-prepared sample in Fig. 4.2 (a).

4.6 Mechanical Properties of the Lamella and Langmuir Probe Samples

An overview of the investigation into mechanical properties is presented in Table 4.3. Tests 1 and 2 were conducted using a Nano Indenter G200 where test 1 was performed at the Materials Research Facility, UKAEA and test 2 at the Department of Materials, University of Oxford. The same Berkovich tip was used across both tests and the same NanoSuite software was used for all analyses. The hardness and modulus values were consistent across both machines for the Langmuir probe sample. The difference in the mean hardness values between the two tests was negligible with a combined standard deviation of 0.3 GPa in the fine-grained region and a difference of 0.1 GPa with a combined standard deviation of 0.1 GPa in the coarse-grained region. In both cases, the difference in the means is not significantly larger than the combined standard deviations, which implies that the observed difference is not likely to be statistically significant and is within the range of what might be expected for random variation or measurement error. The difference in the mean elastic modulus values in the fine-grained region was 20 GPa with a combined standard deviation of 10 GPa and 20 GPa in the coarse-grained region with a combined standard deviation of 10 GPa. The difference in average modulus was more pronounced but was still close enough for both machines to approximate the true material properties. This highlights that nanoindentation data should not be expected to provide absolute values and should mainly be used as a tool for comparison.

When comparing the hardness values between the fine- and coarse-grained regions, there is a difference of 1.0 GPa with a combined standard deviation of 0.2 GPa in test 1 and a difference of 1.1 GPa with a combined standard deviation of 0.3 GPa in test 2. These values are only 0.1 GPa apart, far smaller than either standard deviation, and are close enough to combine into an average value of 1.1 GPa and a standard deviation of 0.3 GPa. For the elastic modulus in test 1, there was a difference of 30 GPa with a standard deviation of 10 GPa between the two regions and a difference of 30 GPa with a standard deviation of 10 GPa in test 2. The average difference in modulus is therefore 30 GPa which is a less pronounced change than the hardness, particularly when considering the combined standard deviation of 10 GPa.

Table 4.3: A table summarising the hardness and modulus data collected from both as-received lamella and Langmuir probe samples, where Berkovich indents were performed to a depth of 1 μm and a spacing of more than 25 μm

				Hardness (GPa)		**Modulus (GPa)**	
Sample	Indented Region	Number of Indents	Test	Mean	Standard Deviation	Mean	Standard Deviation
Lamella	Fine Grains	58	1	**6.8**	0.2	**440**	10
Langmuir Probe	Fine Grains	10	1	**6.3**	0.2	**420**	10
		25	2	**6.3**	0.3	**440**	10
	Coarse Grains	15	1	**5.3**	0.1	**390**	10
		25	2	**5.2**	0.1	**410**	10

The fine-grained region is likely considerably harder due to increased GB density and therefore strengthening. GBs are barriers to dislocation motion and there is a higher density of them in the fine-grained region. The plastic zone diameter is 17.2 μm for all indents [195], but the grain size is 1.5 μm in the fine-grained region, meaning that many GBs contribute to the overall hardness value. The coarse-grained region has a grain size of 24 μm which means the plastic zone will sample a few GBs at most which results in lower hardness. The small grain size will also contribute to Hall-Petch strengthening since fewer slip planes are available for dislocation movement compared to larger grains.

The as-received lamella was indented to the same depth of 1 μm but since there were fewer distinct recrystallised grains, the sample was only indented in the fine-grained regions. The indentation axis was aligned parallel to the rolling direction to lessen the effects of any rolling-induced anisotropy. The results in Table 4.3 for the fine-grained regions in test 1 show that the lamella has a slightly higher modulus than the Langmuir probe with a difference of 20 GPa and a combined standard deviation of 10 GPa. The lamella also appears to be 0.5 GPa harder than the probe with a combined standard deviation of 0.2 GPa. In the case of both modulus and hardness, the difference between samples is more than twice the combined standard deviation and is, therefore, a significant difference.

The suspected increased temperature or period of annealing for the Langmuir probe would have resulted in fewer dislocations and defects in the microstructure, which was likely responsible for the slight softening compared to the lamella. However, the lamella exhibited an average grain size of 2.1 μm in the fine regions, slightly exceeding the 1.5 μm fine grains in the Langmuir probe. This would typically be associated with grain size weakening, but considering the combined standard deviation of 1.1 μm, there appears to be a large degree of variability. The size of the fine grains may not be homogeneous across either sample and the analysis should have included EBSD maps from more locations, particularly at the locations of the indents. The reported results could be highly localised and the fine grains in the Langmuir probe could be slightly larger than in the lamella due to the difference in annealing conditions. Furthermore, the lower hardness and modulus of the probe may also be affected by some residual anisotropy in the fine grains since the original RD was not discernible, the probe could have been indented on the axis perpendicular to the RD.

4.7 Cracking and Impurities

Following the EDM step of the manufacturing process, cracks were observed on the plasma-facing side of the lamella, as depicted in Fig. 4.3. The occurrence of EDM-induced cracking in W samples has been noted in prior studies [202, 203]. Similar observations were also made for JET lamellae by Mailloux *et al.* [17], where the EDM-ed surface exhibited a roughness (Ra) of approximately 2 μm. Fig. 4.3 (a) illustrates the spacing between vertical cracks, typically tens of microns apart, with an average depth of approximately 50 μm. Successive cross-sectional images taken in the FIB confirmed that these cracks were interconnected, forming a network across the lamella surface. With a terminal length of less than 100 μm, these cracks are relatively shallow compared to those that can form during divertor operation.

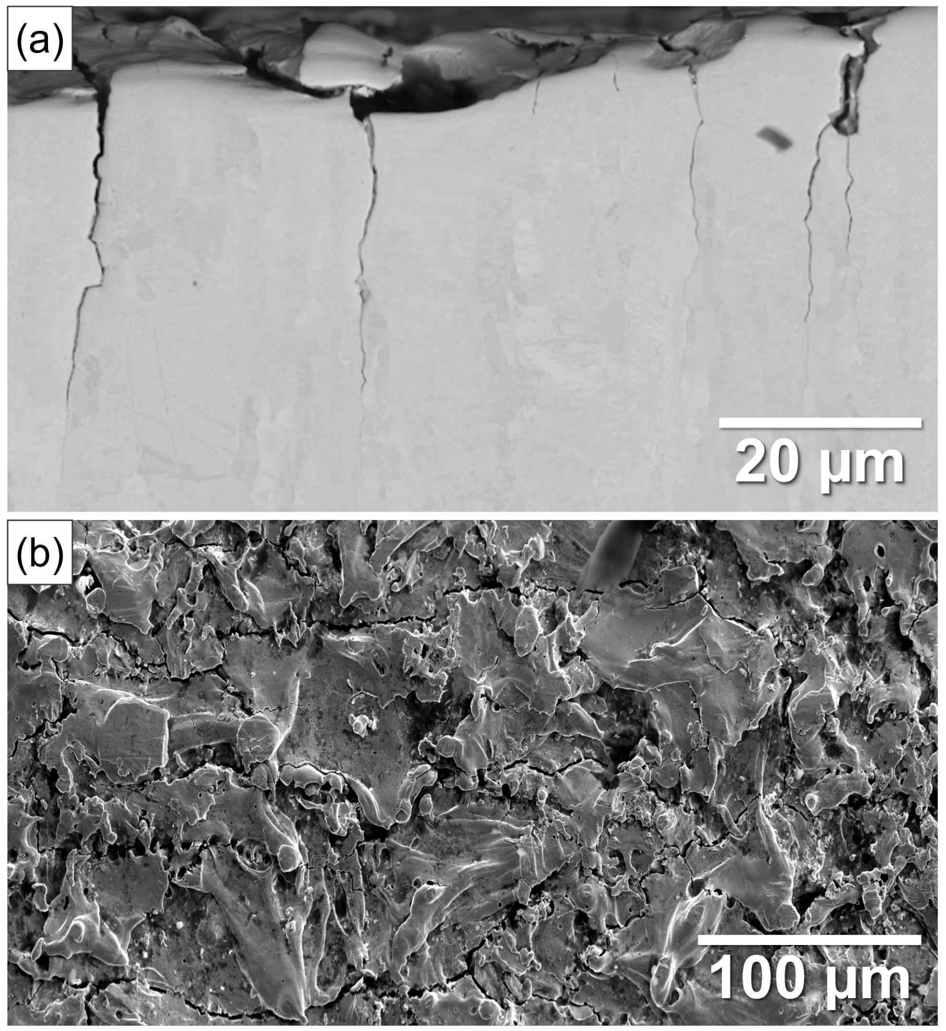

Figure 4.3: SE images of (a) Cross-sectional view of the EDM-ed top surface of the as-received lamella captured in the SEM (b) Top surface of the lamella imaged in the FIB-SEM.

In ASDEX Upgrade Div-III [68], bulk W tiles displayed a shallow crack network up to 400 μm and deep cracks up to 15 mm, caused by plasma exposure. Despite this, there was no material flaking nor a decline in plasma performance, suggesting that similar behaviour may be expected in the JET divertor. However, pre-existing surface cracks may act as stress concentration points, potentially exacerbating cracking under thermal cycling. Given comparable conditions to ASDEX Upgrade, the established crack network in the JET lamellae could lead to more severe degradation. Moreover, longer campaign durations in JET (61.6 hours [20]) compared to AS-

DEX Upgrade (2700 plasma discharges, up to 10 s each) could also intensify microstructural degradation. Increased cracking may result in material loss and dust production which could build up the T inventory, increase material erosion and impact plasma performance.

A PFIB was required to expand the observable area in the cross-sectional images, and mill away appreciably larger volumes of material. Due to high milling currents and the distinct surface roughness, achieving smooth cross-sections without curtaining was unavoidable. Nevertheless, the channelling contrast effectively differentiated grains on the order of a micron from larger recrystallised grain regions in Fig. 4.4. Cracks consistently propagated along the boundaries of larger grains, typically tens of microns in diameter, resulting in crack spacing and depth values related to grain sizes.

One factor likely influencing crack propagation around larger grains is GB misorientation. The EBSD map in Fig. 4.1 (a) reveals a trend of high-angle boundaries around the recrystallised grains. A larger misorientation angle between grains can increase diffusion at the GB [204] while GBs, in general, have proven to be preferential pathways for the migration of H and He in W [205] [206]. Enhanced diffusion at the GB could also lead to embrittlement.

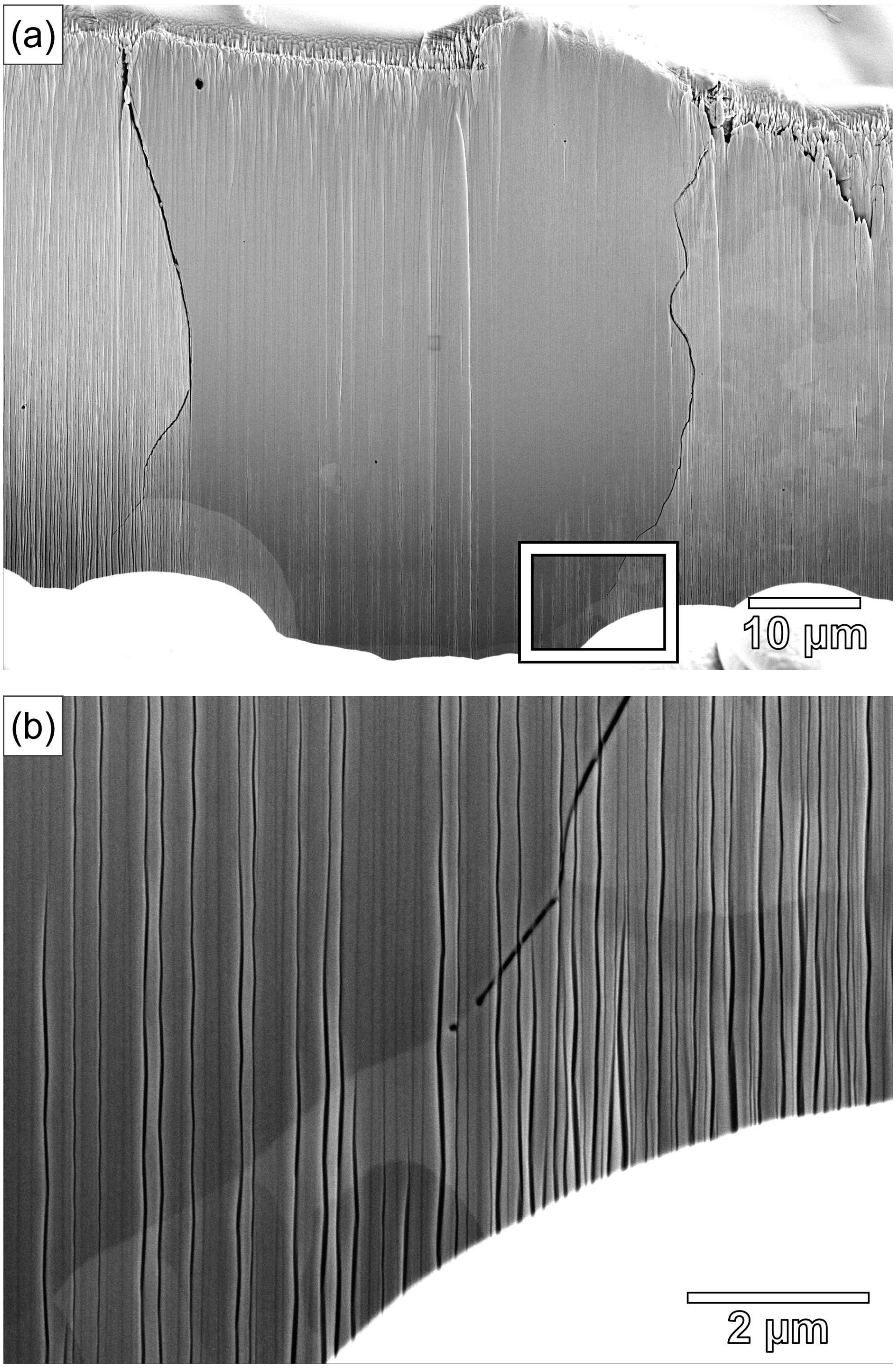

Figure 4.4: Micrographs obtained using PFIB SE imaging, (a) revealing cracks encircling prominent recrystallised grain in the as-received lamella and (b) a higher magnification image showing a void ahead of the crack tip.

The very top of the machined surface experiences greater temperatures than the underlying material, resulting in a mismatch of thermal expansion and raising internal stresses. The formation of an oxide layer could further exacerbate stress concentration and promote cracking in this region through vacancy creation and further volumetric expansion. Impurity levels could also influence crack propagation along GBs, with larger grains requiring fewer impurities for boundary saturation [91]. APT analysis was used to assess impurity segregation to GBs and their impact on fracture behaviour.

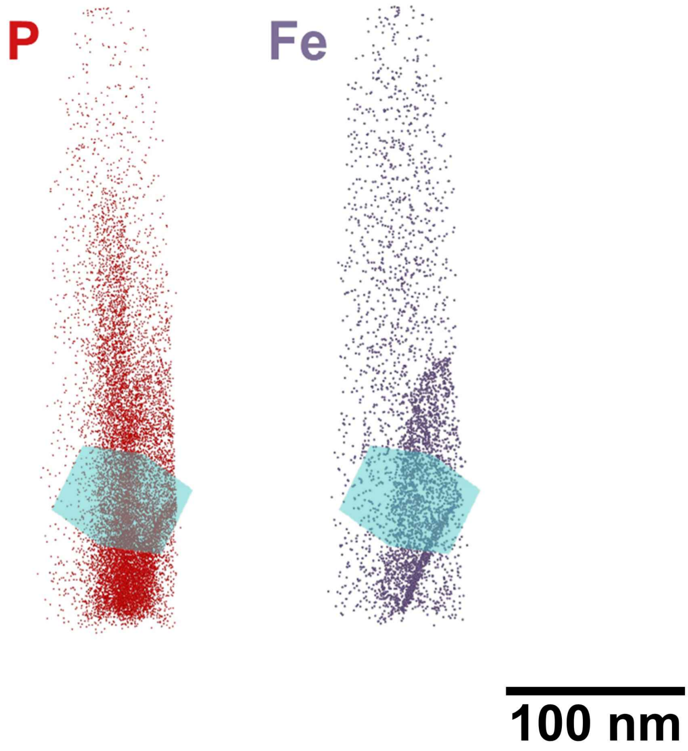

Figure 4.5: 3D reconstructions showing the distribution of P and Fe at GBs in the APT tip.

In one of the APT samples, a triple point of GBs was successfully captured, with the corresponding reconstructions presented in Fig. 4.5 and 4.6. The segregated impurities demarcate the location of the boundaries. A 1D concentration profile was drawn across one of the boundaries, highlighted in blue in Fig. 4.5, with the results depicted in Fig. 4.7. The profile featured a notable aggregation of P, Fe, Cr, and Ni, with their concentrations listed in Table 4.4.

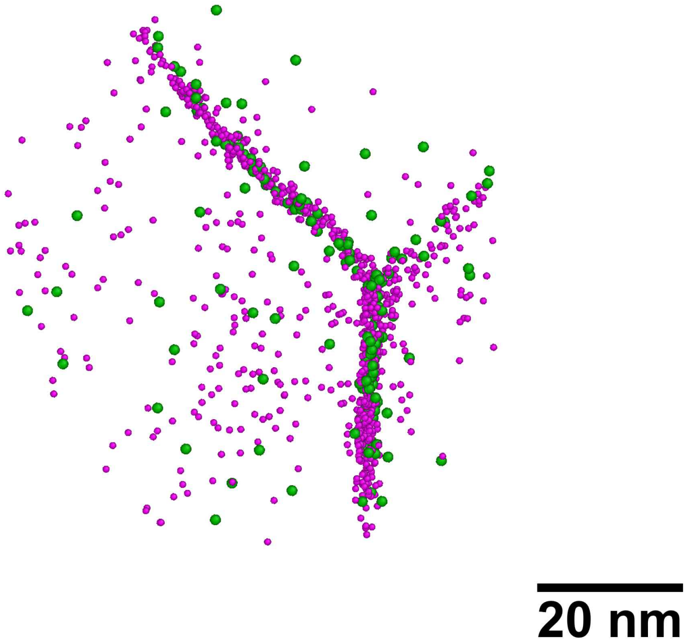

Figure 4.6: A triple point captured in a 30 nm slice of the APT dataset, viewed parallel to the Z-axis of the tip and exhibiting segregation of Fe (purple) and Ni (green).

The distribution of P and O atoms extends significantly beyond the width of the GB in Fig. 4.7, far greater than the other elements that have segregated to the boundary. P is a relatively mobile species during APT experiments [207] and can migrate as a result of the applied electric fields. The distinction between surface migration which is the artefactual movement of atoms caused by the experimental electric fields and true GB segregation is crucial for accurate analysis. This differentiation is achieved by observing crystallographic poles in the 3D reconstruction. Crystallographic poles correspond to specific atomic planes in the material that are preferentially detected more frequently due to their orientation relative to the crystallographic structure of the sample. When P atoms align with these poles in the reconstruction, it indicates that their spatial distribution reflects the actual microstructure of the material rather than artefacts from surface migration. This was observed in the analysis which confirms that the segregation of P to the GBs is a true representation of the microstructure and not an artefact of the APT experiment.

Slight oxidation of the APT sample exterior occurred during FIB preparation, as evidenced by the O spike at the sample edge in Fig. 4.7, and was likely unavoidable. There was a subtle increase in O in the vicinity of the GB, but it was not included in Table 4.3 as there was no distinct peak at the exact location of the GB. In Fig. 4.7, the O profile closely resembles that of P, with both species exhibiting an initial concentration increase of approximately 10 nm from the centre of the boundary. P and O atoms likely segregated to the GBs during manufacturing, but O may have diffused to these areas during FIB preparation.

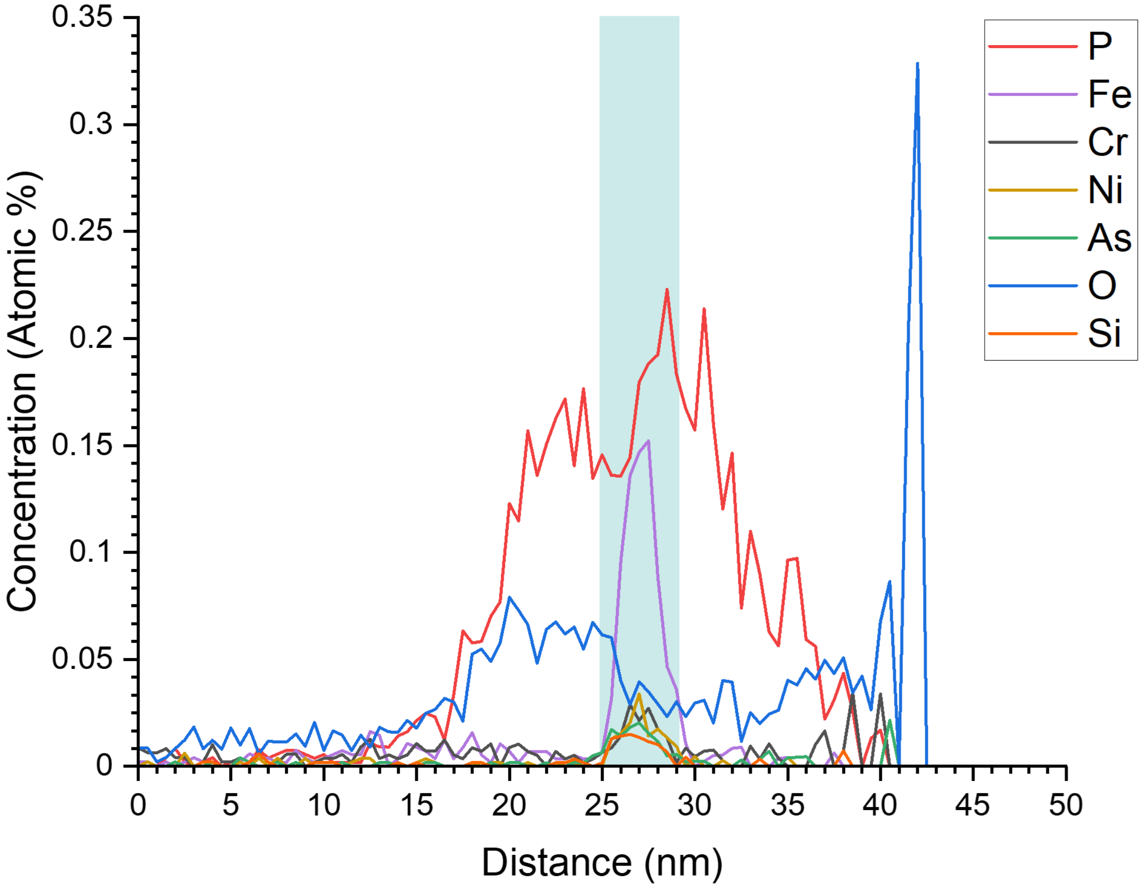

Figure 4.7: The distribution of elements across a 1D concentration profile, where the GB is highlighted in blue with a GB thickness of 4 nm.

The peak value for the O concentration near the GB and away from the edge of the sample, was ∼800 appm in Fig. 4.7. The initial bulk concentration of O in the W powder before sintering was 510 appm, as provided by Jiangxi Yaosheng Industry and Trade Development Co. Ltd.. Previous studies on polycrystalline W indicate that bulk O concentrations of 10 to 50 appm can lead to preferential segregation at GBs, which induces embrittlement, reduces the ultimate tensile strength, and increases the ductile-to-brittle transition temperature [208]. This is facilitated by the O at GBs which starts to remove carbon and other impurities from the W lattice, consequently facilitating dislocation movement and reducing yield strength.

It is also important to consider the phases that could be present at the GBs and although there is an abundance of P around the boundary, tungsten phosphide (WP) is not likely to have formed [209–211]. WP possesses metallic-like character and an orthorhombic crystal structure, but it has poor thermal stability under normal atmospheric pressure and vaporises at a temperature of 1000 °C, which was exceeded during sample rolling and annealing [212]. Extensive simulations were conducted by P. Olsson *et al.* to investigate the impact of P on W [92][93]. The findings showed that P preferentially segregates to GBs rather than the bulk and occupies lattice sites over interstitial sites. The P atoms effectively behave as negatively screened ions due to the polar nature of the P-W bond, which weakens the GB. Consequently, increased P content leads to diminished GB strength and heightened susceptibility to brittle cleavage. Additionally, J. Sun *et al.* demonstrated P incorporation into the lattice of WO_3 nanoparticles, transforming monoclinic WO_3 into an orthorhombic structure [213]. This confirms that it is energetically favourable for P to be an impurity in both WO_3 and pure W matrices.

Table 4.4: The pre- and post-manufacture concentration of impurity elements for the W powder as documented by MGS Precision Ltd. and at the GBs of the as-received Langmuir probe as determined by APT.

Impurity Element	P	Fe	Ni	Cr	As	Si
Nominal Composition (appm)	5	6	3	4	5	5
Composition at GB (appm)	2200	1500	340	290	200	150

As for the effects of Fe segregation, two W samples were exposed to a D plasma in the studies by W. Shu *et al.* [214–218], one 99.99% pure with 10 weight ppm of Mo and Fe and the other 99.95% pure with 100 weight ppm of Mo and 40 weight ppm of Fe. The plasma temperature ranged from 315 K to 1000 K and even though the experiments were designed to study blistering, interestingly large crack-like voids formed at GBs underneath the surface even in the higher purity sample. The linear plasma device likely created a temperature gradient similar to that produced during EDM, while Fe and Mo impurities may have segregated at the GBs. Mo and Fe are both transition metals so may not change bonding character as much as a group 1 or group 2 metal would but there is still a possibility that they could form covalent bonds with the W atoms in the lattice which ultimately produces GB decohesion and embrittlement [91].

4.8 Void Formation

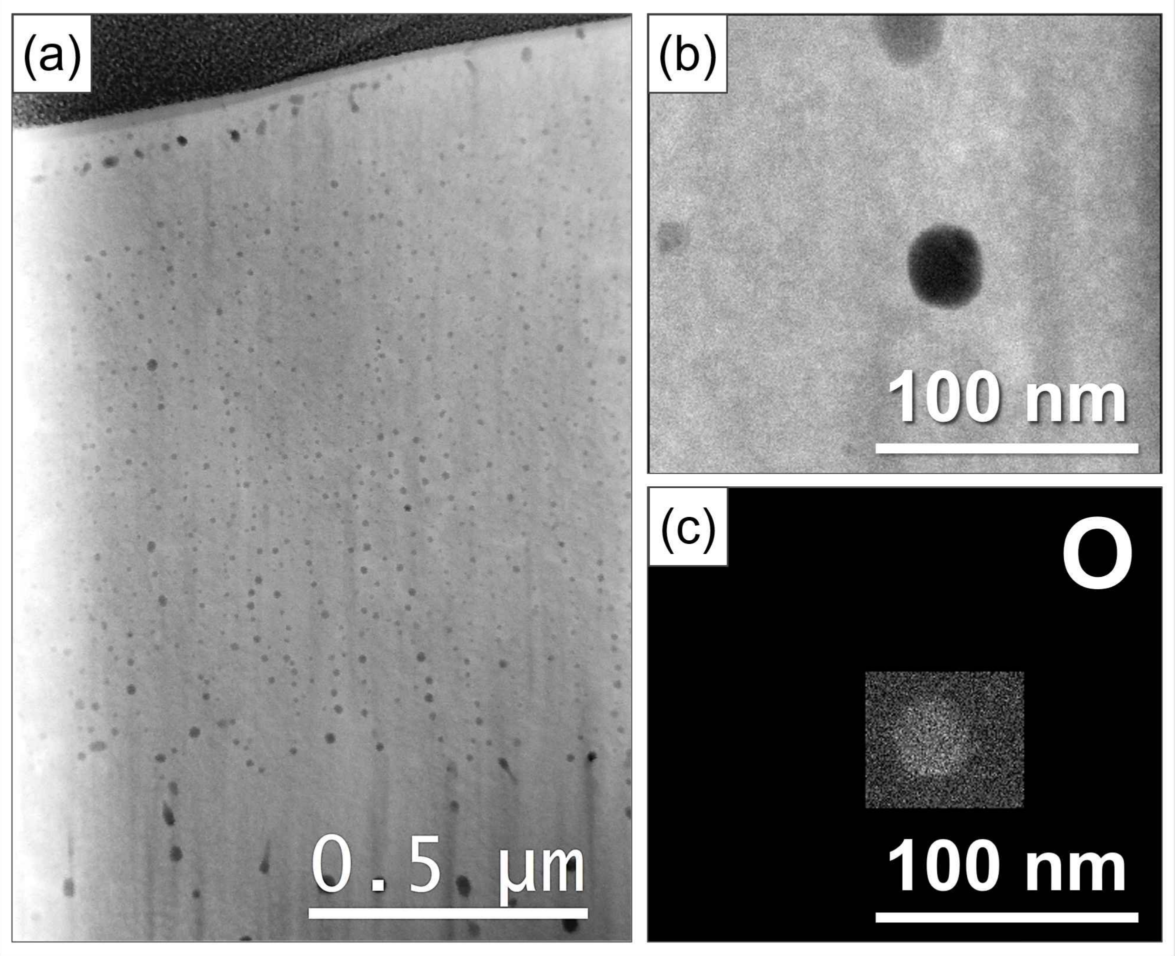

Figure 4.8: (a) STEM HAADF image revealing voids beneath the top surface of the as-received lamella (b) STEM HAADF image of the region analysed using EDX (c) EDX map of O within a void.

In addition to surface cracking, there was clear evidence of void formation beneath the lamella surface, as depicted in Fig. 4.8. These voids were not found in the bulk, the deepest region they were found in was ahead of the crack tips which penetrated up to 50 μm into the surface, shown in Fig. 4.4 (b). This indicated that the voids had also formed in the heat-affected zone produced by EDM rather than during prior manufacturing steps. They were scattered along GBs in some areas (intergranular) and were dispersed within grains, irrespective of GBs in others (intragranular), as illustrated in Fig. 4.9 (a) and (b). In both areas, there were signs of voids coalescing to form larger cavities such as Fig. 4.10, which introduces weak points where cracks could initiate under cyclical loading in JET.

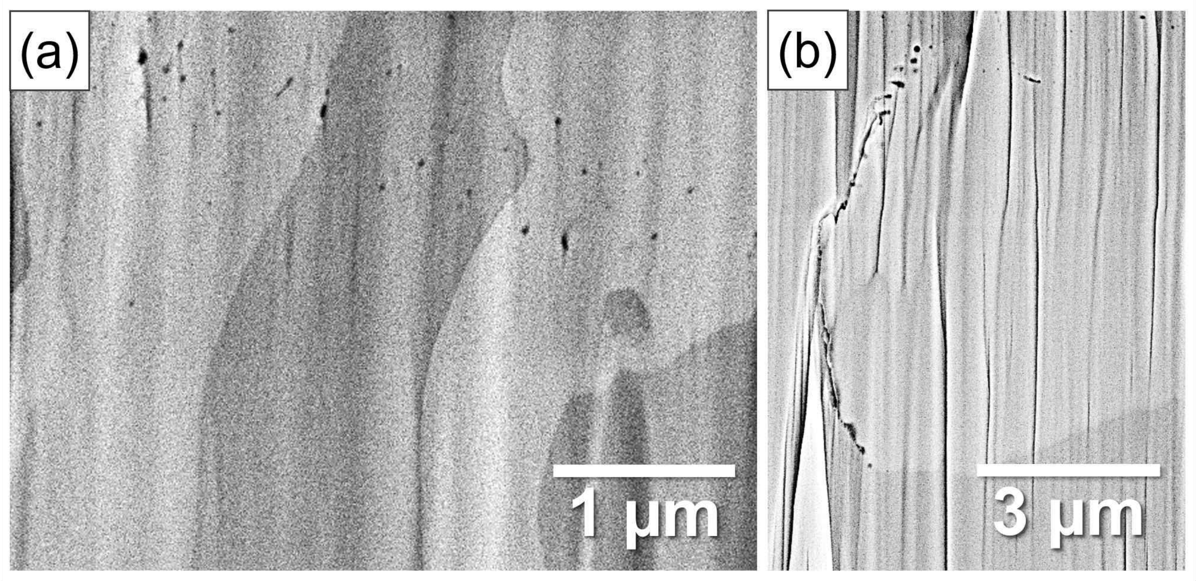

Figure 4.9: PFIB SE images from the as-received lamella reveal voids scattered (a) throughout grains (intragranular), and (b) voids aligning along GBs (intergranular).

Previous research on KSiAl-doped W wires showed void nucleation also occurring within grains and at GBs [219]. The nucleation process in KSiAl-doped samples involved diffusion-controlled mechanisms, where the K dopants boil and form subcritical bubbles which go on to migrate, collide, and coalesce. P could play a similar role to K in the lamella, given that its boiling point can be as low as 280 °C [66], leading to P gas-filled voids until the P atoms diffuse away.

Multiple EDX maps were collected from these voids in the TEM which revealed a distinct O signal, suggesting potential oxide formation on the internal surface. It is unclear whether this oxide formed when the voids themselves formed or during FIB sample preparation. The EDM of other materials has shown void formation via the expulsion of gas bubbles from the molten layers during solidification [86][88–90]. EDM typically uses a water-based dielectric fluid, which these studies have hypothesised can produce water vapour and H_2 gas bubbles. The EDM process likely produced significant amounts of water vapour, surface temperatures far above 500 °C and non-negligible electric fields, all of which have been shown to increase the oxidation of W [99][220]. The presence of this O signal suggests that the vaporisation of the dielectric fluid during EDM is a plausible mechanism for void formation. The origin of the voids is explored in greater detail through dedicated experiments in Section 4.10.

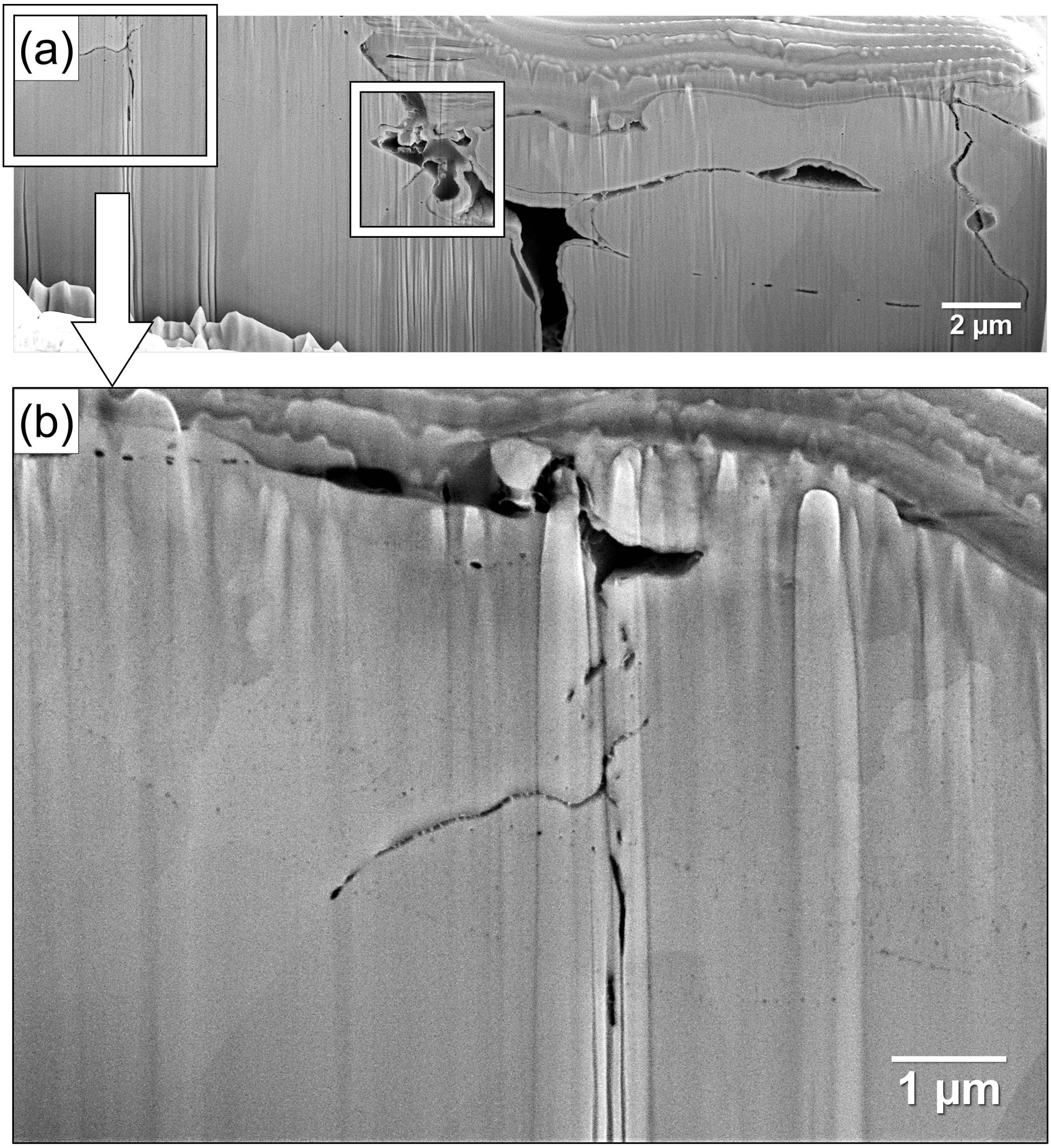

Figure 4.10: SE images of the as-received lamella in the FIB-SEM showing (a) a region of darker contrast at the top of the crack and large cavities forming within grains (b) voids coalescing at GBs.

Irrespective of their formation, the voids appear to be more susceptible to oxidation which poses further risks of component cracking during operation. It was suggested by S. Cifuentes *et al.* that cracking occurs when W is cooled from 700 °C to room temperature due to the allotropic transformation of WO_3 from the orthorhombic structure to the monoclinic structure [221]. Additionally, WO_3 starts to sublimate substantially above 900 °C [222], which could lead to the formation of more cavities and structural weak points. An in situ TEM study of W oxidation in an O atmosphere by M. Togaru *et al.* showed the formation of micro-cracks at 900 °C due to sublimation [223]. Another recent experimental study showed the significant loss of material from WO_3 sublimation at 1075 °C in the presence of water vapour and a He atmosphere [224]. Surface temperatures in the divertor of a machine such as JET are of this order of magnitude. The installation of a W lamella in this state could result in the ongoing removal of WO_3 from oxidised regions such as voids and GBs. This could increase the risk of component failure and plasma disruption.

4.9 The Effect of Debris from EDM on Mechanical Properties

Cracks and voids were observed at the GBs of the EDM-ed plasma-facing surface of the as-received Langmuir probe in Fig. 4.11 (a) and (b), respectively. Moreover, the micrographs in Fig. 4.10 (a) and 4.11 (c) highlight the formation of dark regions near cracks in both the as-received lamella and Langmuir probe. The difference in contrast likely stems from material of a different composition that originated from the EDM chamber and filled the open cracks.

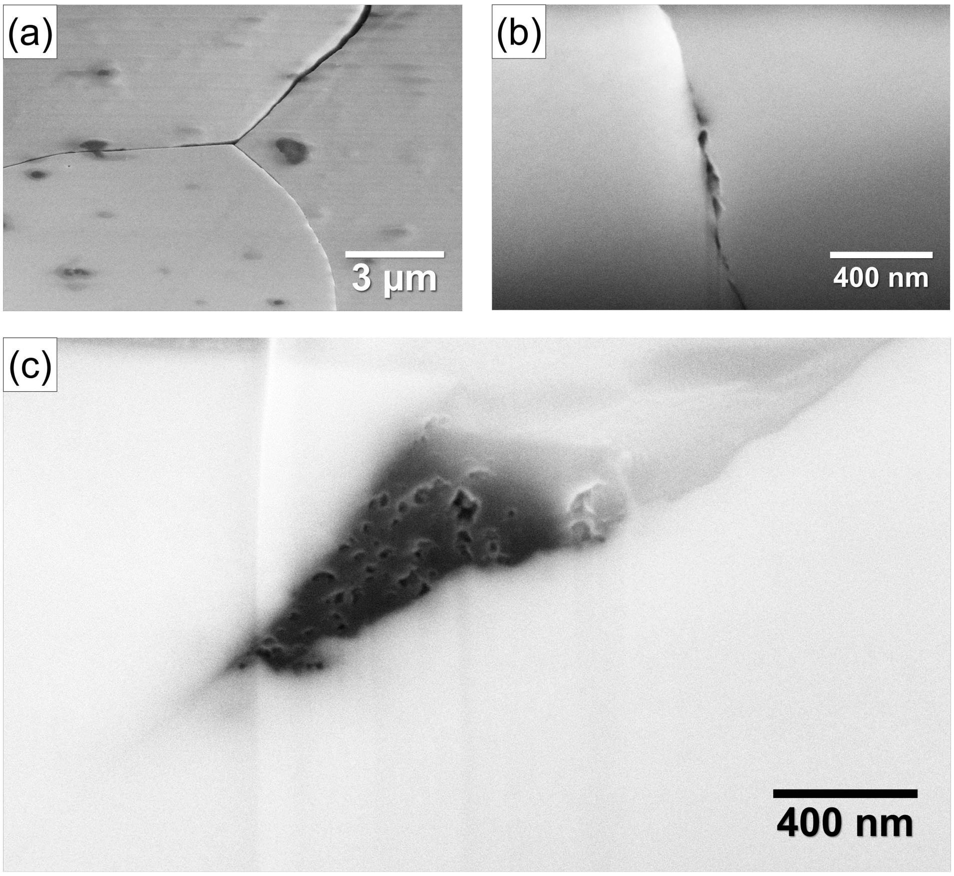

Figure 4.11: SE micrographs of the as-received Langmuir probe captured in the FIB-SEM showing (a) an intergranular crack at a triple point of GBs near the EDM-ed surface (b) a single GB where multiple voids had formed (c) debris from EDM that had filled GB crack.

A rectangular cross-section was milled in the heat-affected zone of the lamella sample, spanning multiple cracks to study the dark material using EDX. The maps in Fig. 4.12 and the point spectra in Fig. 4.13, which were taken from the locations marked in Fig. 4.12 (a), show that the dark regions are mainly enriched with C and O. The point spectra suggest that a small amount of N may also be present in these regions but N segregation was not visible overall in the EDX maps.

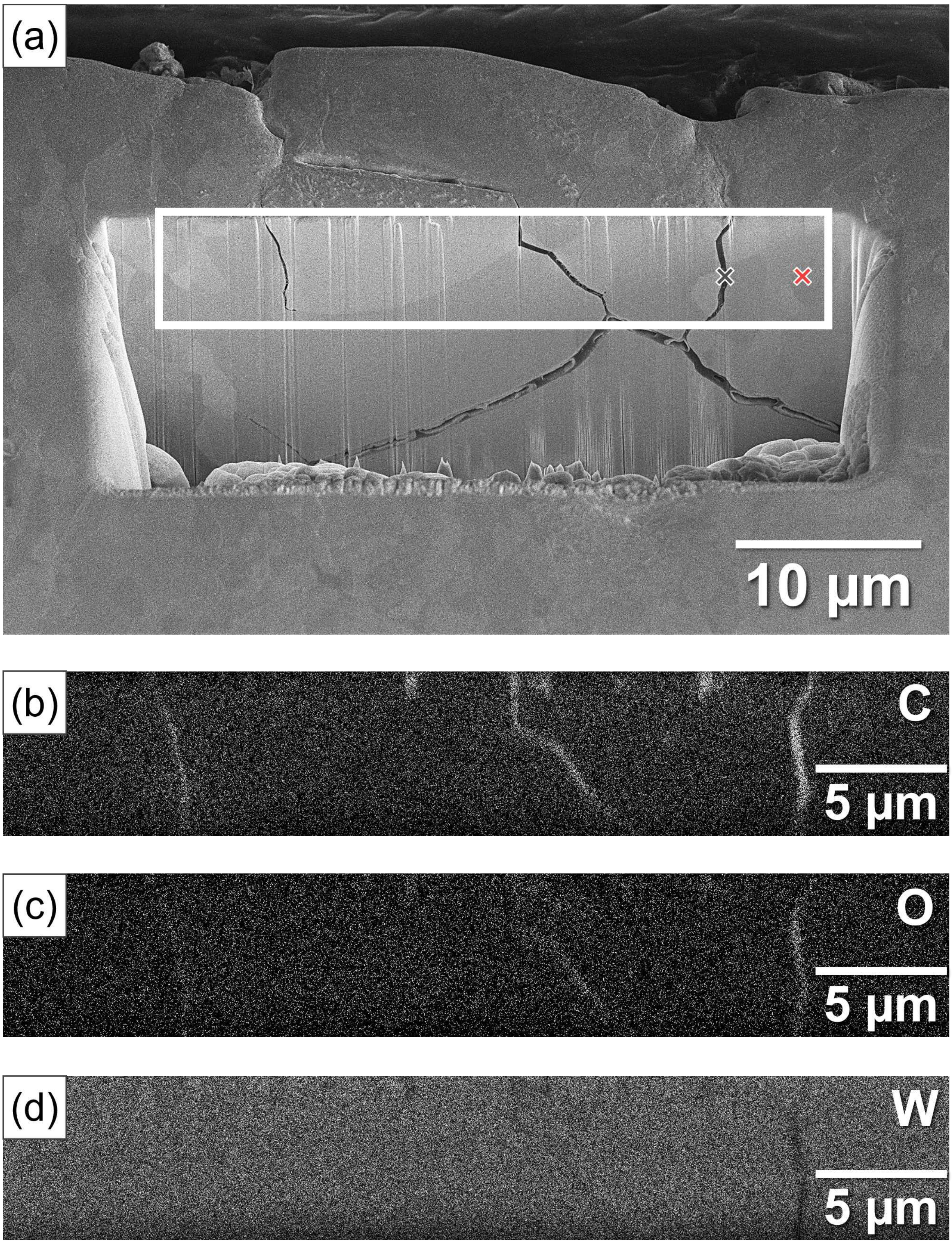

Figure 4.12: (a) FIB cross-section of the debris-filled cracks in the as-received lamella and EDX maps highlighting the segregation of (b) C, (c) O, and (d) W, in these regions.

The dark material is rich with C and O that likely originates from debris in the EDM chamber, contaminants in the dielectric fluid and the wearing of the electrode which is typically made from graphite. The width of these regions can reach nearly 2 μm in Fig. 4.14 and they appear tens of microns deep into the surface, too deep to remove by washing. To quantify how this material affects the overall toughness of the plasma-facing surface and its susceptibility to fracture, these regions were targeted using Berkovich nanoindentation.

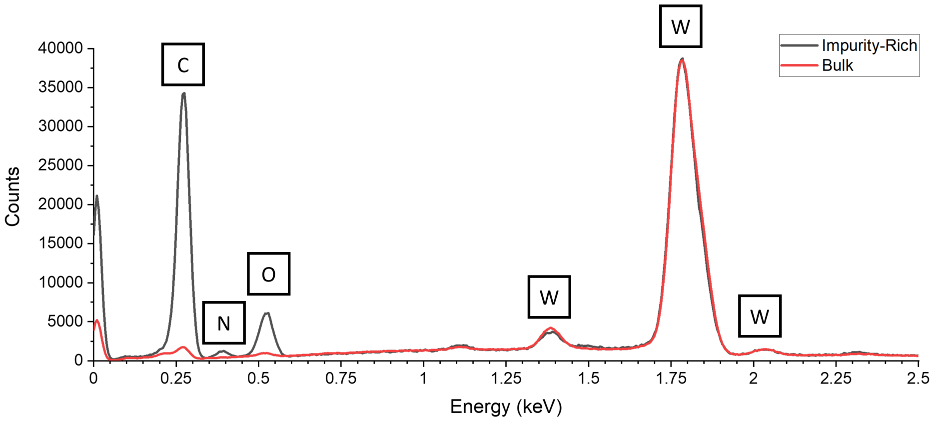

Figure 4.13: EDX point spectra taken from an impurity-rich region within the cracks (black) and the bulk (red) of the FIB cross-section in the as-received lamella, shown in Fig. 4.12

Table 4.5 summarises the mechanical data collected from the material-filled cracks near the EDM-ed surface and the bulk of the as-received lamella. The pronounced variability in the widths of these regions is most likely responsible for the large standard deviations and spread in hardness and modulus values compared to the bulk region. The shape of the dark material is determined by the shape of the crack and is therefore irregular. Each indent captures a different volume of this material in its plastic zone so they were only included in the analysis if they were within 2.55 μm from the centre of the crack. This ensured that the C and O rich material filled a significant proportion of the plastic zone.

Table 4.5: A comparison of the hardness and elastic modulus near the debris containing cracks and the bulk regions of the as-received lamella, where the Berkovich indents were performed to a depth of 300 nm

		Hardness (GPa)		**Modulus (GPa)**	
Indented Region	Number of Indents	Mean	Standard Deviation	Mean	Standard Deviation
Bulk	23	**6.9**	0.2	**390**	20
Near Crack	12	**5.4**	0.8	**280**	60

There was a 1.5 GPa difference in hardness between the two areas which is a decrease of 22% from the bulk values. Since there was far less scatter in the bulk values and the scatter in the dark material is explained, it did not make sense to combine the standard deviations. The fact that the standard deviation for the material in the crack was still only 15% of the hardness value, shows that there is a statistically significant difference. The modulus decreased by 110 GPa in the dark regions. This is a decrease of 28% from the bulk, which is a significant difference compared to the standard deviation of 21% for the dark material. Indents 20 and 22 are highlighted in Fig. 4.14, showing the analysis procedure and the appearance of the dark material in the cracks. Indent 20 returned the lowest hardness value of 4.3 GPa and indent 22 had the lowest modulus value of 180 GPa. This is likely due to the increased volume of material captured in the plastic zone of these indents compared to the others and signals that the true hardness and modulus of the dark region could be smaller if it were isolated.

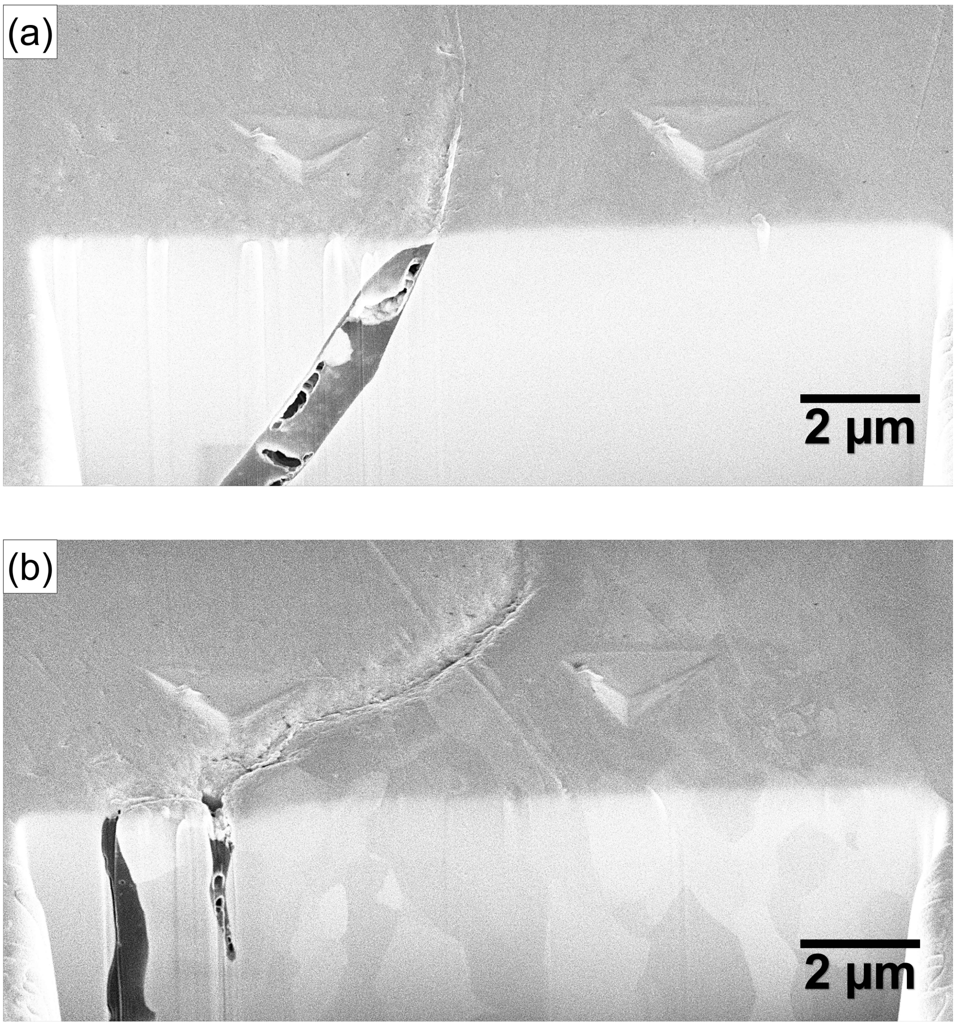

Figure 4.14: SE images showing the FIB cross-sections of indents (a) 22 and 23 (b) 20 and 21, where the impurity-rich regions were particularly wide and closer to one indent than the other.

In a reactor environment, debris that is lodged in the surface cracks can compromise the structural integrity of the component and pose safety risks. W is used in PFCs due to its high melting point and thermal conductivity. This debris certainly does not share the same resistance to thermal loads as the W component and can hinder heat transfer and cause localised hot spots. It could also crack and melt under standard operational temperatures in the divertor of JET. Sections of this material could then enter the plasma as a whole or vaporise and disrupt operations. Additionally, the material in the cracks has a different coefficient of thermal expansion from the surrounding material. At elevated temperatures, it could wedge the crack open and lower the amount of stress required for the crack to propagate deeper into the bulk. The elements in these regions could also diffuse deeper into the component and weaken other areas such as voids and GBs. High thermal and mechanical stresses could cause catastrophic failure in these weakened areas and parts of the W armour could detach. Ultimately, components with deteriorated mechanical properties may require more frequent maintenance and replacement, resulting in increased operational costs and downtime for the reactor.

4.10 Heat Treatment and Electrical Discharge Machining

An experiment was designed to compare a UHP W sample to the as-received lamella and Langmuir probe samples and confirm if the voids and cracking were linked to sample purity and certain temperatures. The first set of three samples was heated in a vacuum furnace at 900 °C for an hour, while a second set was heated at 1500 °C for 24 hours. A third, untreated set was kept for comparison and FIB cross-sections were made on all samples to look for microstructural changes in the bulk material. A selection of FIB cross-sections is shown in Figs. 4.15–17, showcasing the absence of voids or cracking in any of the samples at these temperatures. This suggests that simply heating these components to 1500 °C was not sufficient to activate any impurity boiling or diffusion-controlled mechanisms. However, it could be the case that these mechanisms occur at the more extreme temperatures that are achieved during EDM.

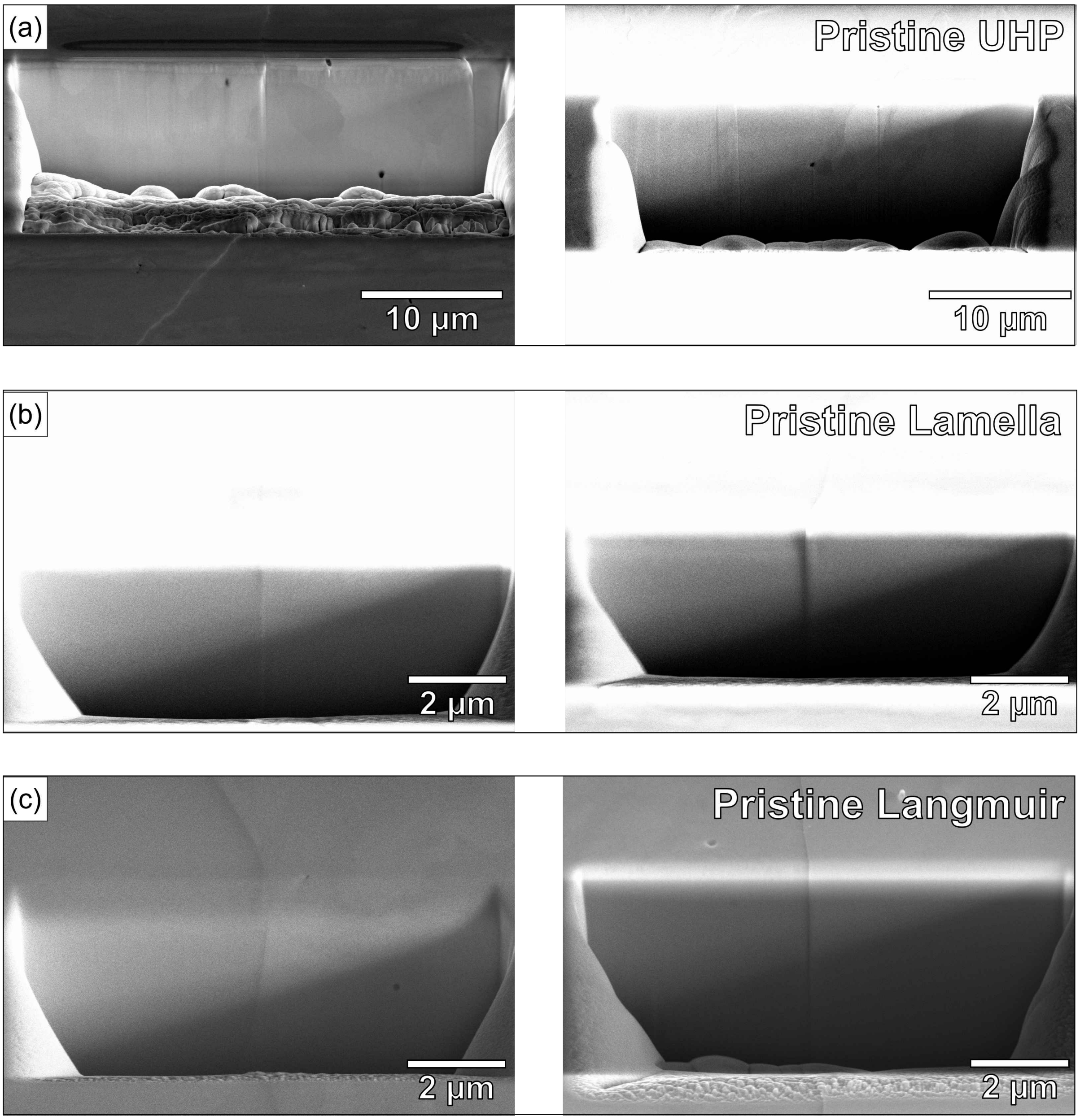

Figure 4.15: FIB cross-sections of the pristine (a) ultra-high purity W sample (b) the lamella sample and (c) the Langmuir probe sample in the as-received state.

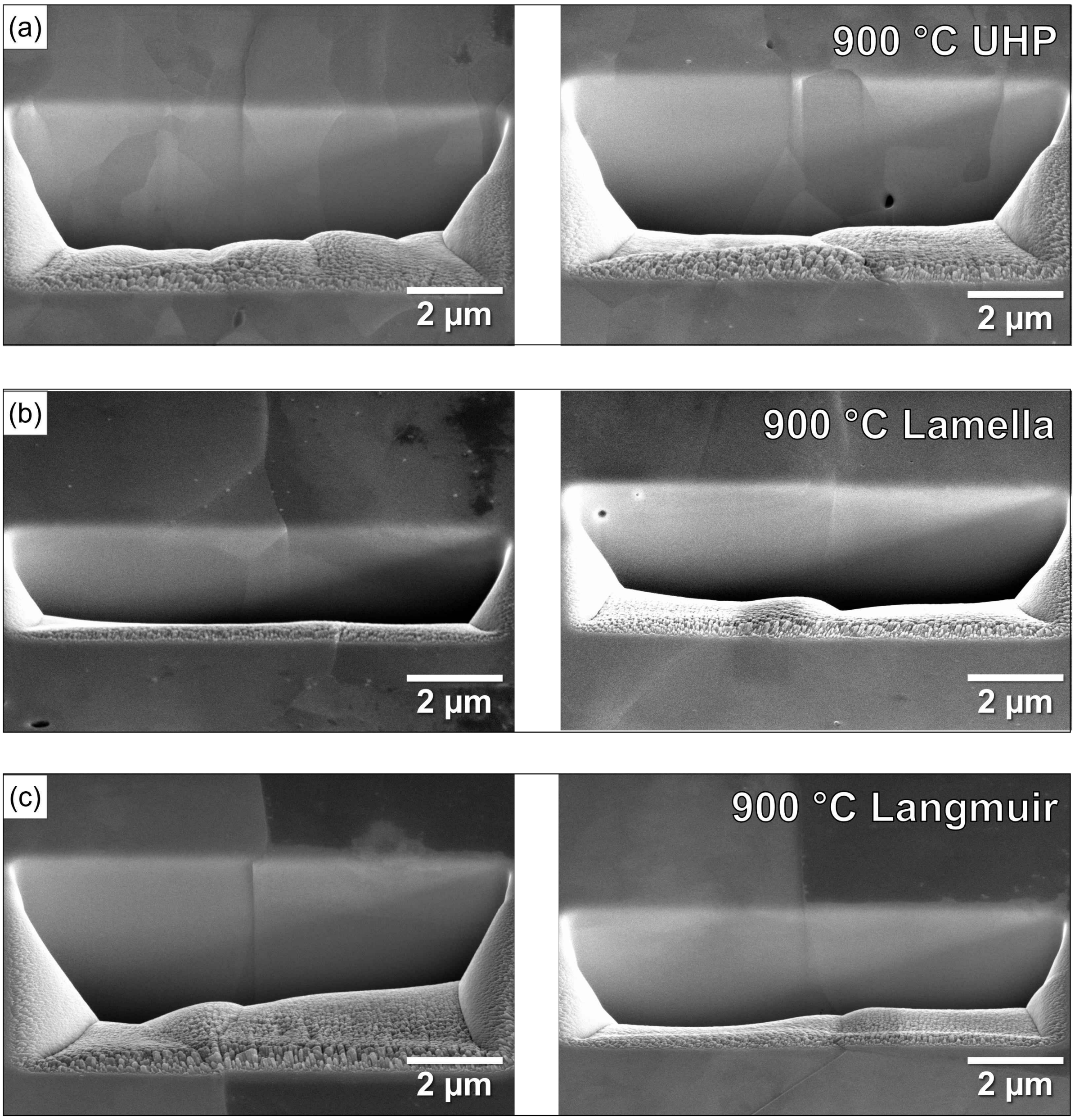

Figure 4.16: FIB cross-sections of the samples heat treated at 900 °C (a) ultra-high purity W sample (b) the lamella sample and (c) the Langmuir probe sample in the as-received state.

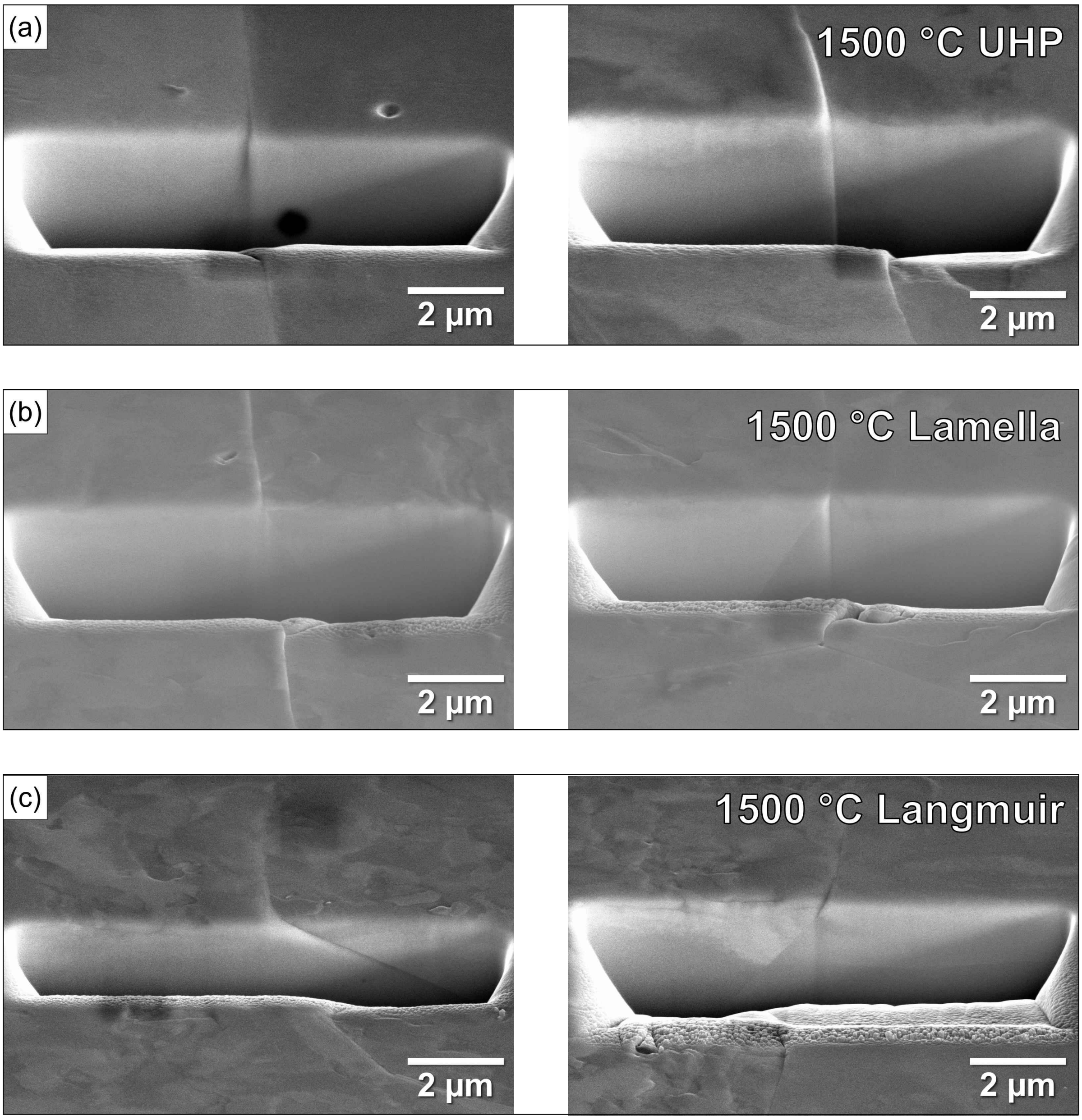

Figure 4.17: FIB cross-sections of the samples heat treated at 1500 °C (a) ultra-high purity W sample (b) the lamella sample and (c) the Langmuir probe sample in the as-received state.

Another set of three samples, including the UHP sample, the lamella and the Langmuir probe, were cut using EDM to see if voids and cracking still occurred in the 99.999% pure UHP sample. The machined surfaces were investigated using FIB cross-sections with each micrograph showing a different cross-section in Fig. 4.18. Voids and cracking were observed in all EDM-ed surfaces including the UHP W sample. The latter is the highest purity that a W component can feasibly attain. The fact that it appears the same as the other samples, shows that the voids and cracking cannot be avoided by addressing the concentration of intrinsic impurities. These impurities could still impact the overall microstructure of the EDM-ed surface, perhaps they are only required in small concentrations at GBs to influence where cracking occurs. However, these results suggest that impurities are not the primary driving force behind the formation of voids and the mechanism that involves the vaporisation of the dielectric fluid is far more likely to have occurred. This also implies that W oxide may have formed in the vicinity of the voids and cracks which could cause further embrittlement and increase erosion through sublimation. It is therefore important to address many aspects of EDM, such as the type of dielectric fluid, debris in the chamber, significant temperature gradients and the resulting thermal stresses.

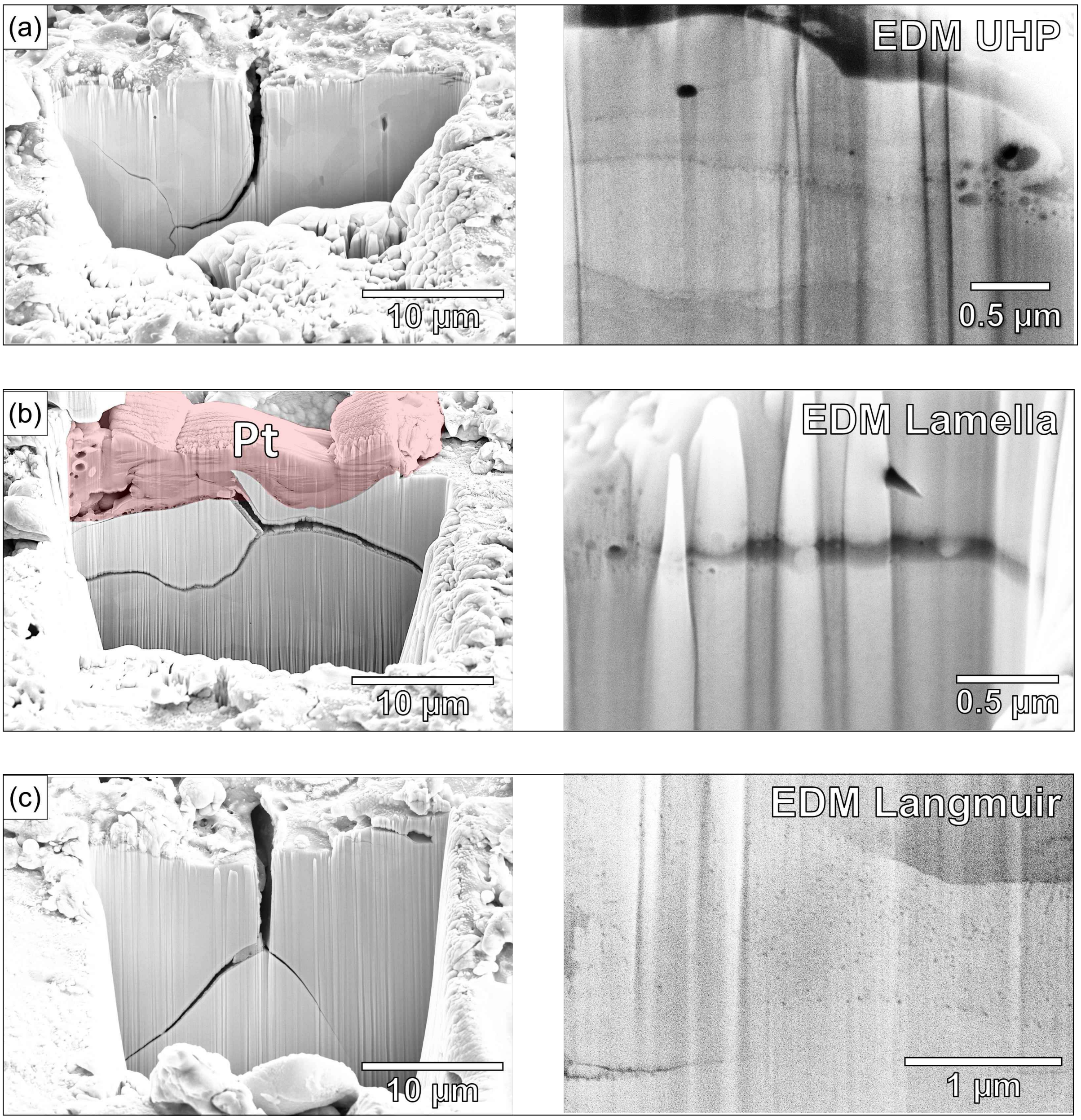

Figure 4.18: SE cross-sectional micrographs captured in the FIB-SEM from the EDM-ed surface of (a) ultra-high purity W sample (b) the lamella sample and (c) the Langmuir probe sample in the as-received state.

4.11 Conclusions

This chapter includes a detailed characterisation of as-received W lamella and Langmuir probe samples, focusing on their microstructure and mechanical properties which have been shaped by various manufacturing processes including sintering, hot rolling, annealing, and EDM. The investigation revealed that these manufacturing processes, though similar, resulted in distinct microstructural features for the Langmuir probe and lamella samples. The Langmuir probe exhibited a bimodal grain size distribution, with mainly coarse recrystallised grains and a distinct distribution of fine-grained regions. In contrast, the lamella displayed a more uniform fine-grained structure with some localised recrystallisation. This variation in grain morphology influenced the mechanical properties, with the Langmuir probe exhibiting a lower hardness and modulus in the fine-grained regions compared to the lamella. A potential difference in the manufacturing processes between the lamella and the Langmuir probe could be attributed to subtle variations in parameters such as annealing time, temperature or rolling conditions, which may have facilitated more extensive recrystallisation and grain growth in the Langmuir probe compared to the lamella. The observed grain structure of the lamella appeared to be more resistant to recrystallisation during manufacturing than the Langmuir probe. This suggests that the lamellae may also show strong resistance to recrystallisation during exposure in the JET divertor, which is explored in Chapter 5.

A network of cracks developed on the lamella surface after EDM which primarily propagated along the boundaries of larger grains, with steep thermal gradients, GB misorientation and impurity level emerging as important factors. A considerable concentration of P, Fe, and O was observed at GBs via APT which may have influenced where the cracks had formed. Voids were also observed in the heat-affected region after EDM which produced a strong O signal via EDX. The analysis also revealed that debris from the EDM chamber had become lodged in many of the surface cracks and primarily contained C and O. These regions exhibited significantly lower hardness and elastic modulus compared to the bulk material, potentially degrading thermal conductivity and compromising the structural integrity of the component.

Heat treatment experiments were performed on the UHP, lamella, and Langmuir probe samples, and revealed that temperatures up to 1500 °C were insufficient to replicate the microstructural features produced during EDM. Another set of three samples was subjected to EDM in the laboratory, where all three samples exhibited the formation of voids and cracks. These results indicated that the boiling of intrinsic impurities and subsequent diffusion-controlled processes were not driving void formation. The accepted mechanism therefore involves the vaporisation of the water-based dielectric fluid used during EDM and the melting of the component surface, which then expels gas bubbles of water vapour and H_2 during solidification. Additionally, it is theorised that the extreme thermal gradients are primarily responsible for the observed cracking. The voids likely served as pinning sites for GBs during the solidification of the EDM-ed surface, subsequently acting as stress concentrators under the steep thermal gradients. This amplification of localised stress may have facilitated crack initiation at the GBs, which explains why cracks predominantly propagated along these boundaries. Impurity content and oxidation may have further influenced crack propagation. P was the most abundant impurity in the samples which has been shown to cause embrittlement at GBs in W. Moreover, the diffusion of O may be enhanced at the boundaries compared to the grain interiors which could cause oxidation. The presence of water vapour is also likely to have caused oxidation at the voids. W oxide has been shown to start cracking during sublimation and cooling from high temperatures.

This chapter underscores the importance of understanding how the dielectric fluid, debris in the chamber and surface temperatures of the workpiece influence the development of microstructural features. These features can affect fracture mechanisms, component longevity, plasma performance, Be and T inventory, maintenance and operational costs. The impact of the voids, cracks and debris is explored further in subsequent chapters. Further investigation is warranted to explore alternative configurations of EDM or other manufacturing techniques that could minimise damage, potentially leading to more robust surface finishes for W plasma-facing surfaces. The full characterisation of the samples in the as-received state also provides a solid foundation for exploring the effects of plasma exposure on these materials in Chapter 5.

Chapter 5

Evolution of W in the JET Divertor after the ITER-Like Wall Campaigns

5.1 Introduction

JET is currently the closest machine in specification to ITER due to the ILW materials, large size for an experimental tokamak and comparable plasma conditions. The key differences between the ILW campaigns and the fusion power operational phase of ITER are fewer 14.1 MeV neutrons, and smaller thermal and particle loads which reduces the erosion and deposition of material around the machine. As an example, ITER is expected to have an auxiliary heating power of 50 MW [225] while the average input powers for ILW-1 and -2 were 2.2 and 2.9 MW, respectively [226]. However, JET is a pulsed device, meaning it operates in a series of short-duration plasma discharges, which mimics the cyclic thermal and mechanical loading on materials that will also be present in ITER.

The JET environment facilitates simultaneous heat and particle loading of components while other plasma-material interactions, such as sputtering, implantation and erosion, also occur. This results in unique microstructures that are difficult to replicate in the laboratory. Moreover, T will be used in future devices such as ITER, and if too much T becomes trapped in the first wall, operations could be halted due to licensing limitations.

The main objective of this chapter is to evaluate how and why the microstructure and mechanical properties of W components evolve when they are exposed to these D plasmas. The two types of components, lamellae and Langmuir probes, were characterised in the as-received state in

Chapter 4 to identify what microstructural changes were caused by plasma exposure. This chapter focuses on seven exposed samples shown in Fig. 5.1: four W lamellae from tile 5 and three Langmuir probes, two from tile 3 and one from tile 6.

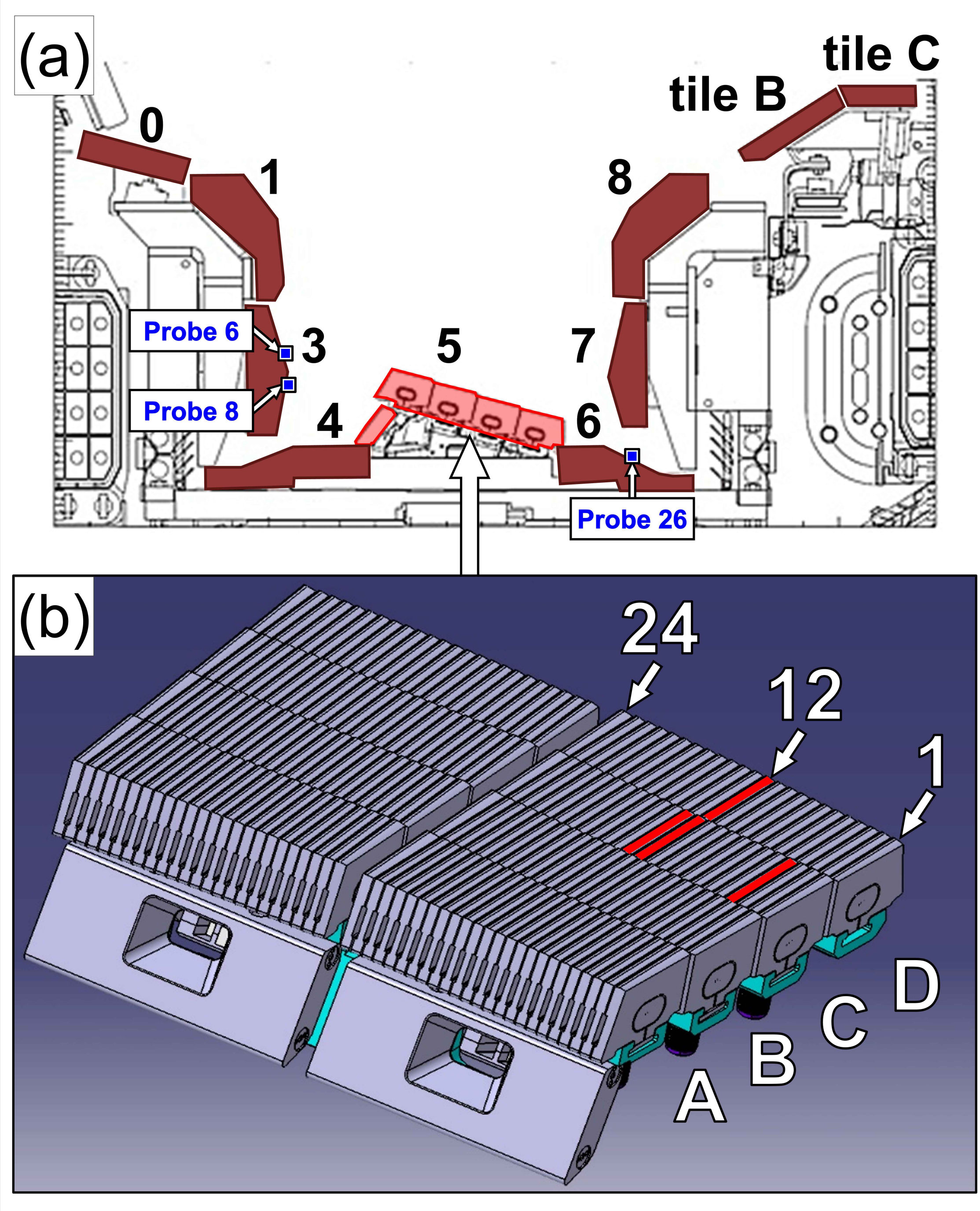

Figure 5.1: Schematic outlining the locations of the exposed W (a) Langmuir probes from tiles 3 and 6 and (b) lamellae from tile 5 in the JET divertor during the ILW campaigns.

This analysis addresses the challenges of working with active materials, using techniques such as EBSD for microstructural examination, nanoindentation to assess mechanical properties, and ion beam analysis to investigate D retention. Additionally, this chapter examines how diagnostic data from Langmuir probes and infrared (IR) cameras offer insights into plasma conditions during the ILW campaigns, while also highlighting the limitations of such data. Finally, the comparison between the JET-exposed and the as-received samples provides valuable information on recrystallisation behaviour, hardening mechanisms, and defect formation due to D plasma-material interactions. Ultimately, these findings contribute to predicting the performance and longevity of plasma-facing materials in future devices such as ITER.

5.2 Experimental Details

5.2.1 JET Lamella Experiments

Lamellae C4 and D12 were cut with a diamond saw to approximately 9×6×2 mm by the technicians at the UKAEA Materials Research Facility (MRF). Slightly larger samples of 9×6×10 mm had been cut from lamellae C12 and C13 before the start of this work and these samples were not cut down any further to reduce the amount of active waste. All four cut samples were then attached to stainless steel cylindrical blocks with a diameter of 25 mm and a height of 15 mm such that the lamellae cross-sections could be investigated. Crystalbond was used as a mounting adhesive to reduce the amount of frame compliance during nanoindentation. The cross-sections were ground flat using P2000 grit paper for a minimum of two minutes, followed by P4000 paper for a further three minutes and then they were polished using Trident 3 μm diamond polishing solution on a ChemoMet pad for another three minutes. The same methodology was applied using 1 μm diamond polishing solution and then using Master Met 2 colloidal silica polishing solution for five minutes to remove all grinding marks. The samples were rotated 90° every minute during grinding and polishing to evenly remove material from the surface, with minimal force applied since the weight of the stainless steel block provided sufficient force. They were also polished for over a minute using a wet ChemoMet with running deionised water after each polishing step. They were only rinsed with deionised water throughout the entire procedure and rinsed with methanol as the final step.

The microstructures of these lamellae were investigated using EBSD where the rolled, fine-grained regions made up the majority of the samples. This made it difficult to place one indent in a single grain, so Berkovich nanoindentation was performed to a depth of 2 μm such that many grains and boundaries would be encompassed in the plastic zone and an average hardness and modulus would be obtained. The Keysight G200 Nano Indenter was under repair at the MRF during this time and was replaced by a KLA iMicro Nanoindenter which was used for sample indentation. Repeat measurements for the as-received lamella were recorded with the iMicro to compare to the results from the other exposed samples, using an array of 60 indents. The lamellae retrieved from JET were indented and mapped with EBSD in near identical regions, within 500 μm from the exposed surface and centrally, as far from the sides of the sample as possible, to enable an accurate comparison between the samples. An array size of 30 indents was selected for lamellae C4, C12, C13, and D12 while any indent that failed to reach the set depth or had a skewed residual imprint was not included in the final analysis. One EBSD map of 300×225 μm was taken for each sample in the indented region with pixel sizes in the range of 250–554 nm. Lamellae C4 and C12 were indented while EBSD maps were collected in lamellae C13 and D12 and vice versa, hence the indents are visible in Fig. 5.6 (a) (b).

5.2.2 JET Langmuir Probe Experiments

The triangular tip of a Langmuir probe, highlighted in red in Section 1.5 Fig. 1.3 (a), is the part of the component that is subjected to the largest particle fluences, reaches the highest temperatures and can come into direct contact with the plasma during operation. This part of the probe is the most likely to show any changes in microstructure and mechanical properties due to plasma exposure. It is therefore a useful part of the probe to compare to the as-received sample and the different probe positions in the JET divertor. The triangular tips were removed from probes 6, 8 and 26 using a diamond saw and one side of each tip was mounted on a 25×15 mm cylindrical stainless steel block with Crystalbond. The opposite side of the samples, containing the cross-section of the tips, were ground flat and polished through to the colloidal silica step, following the same procedure as the lamellae.

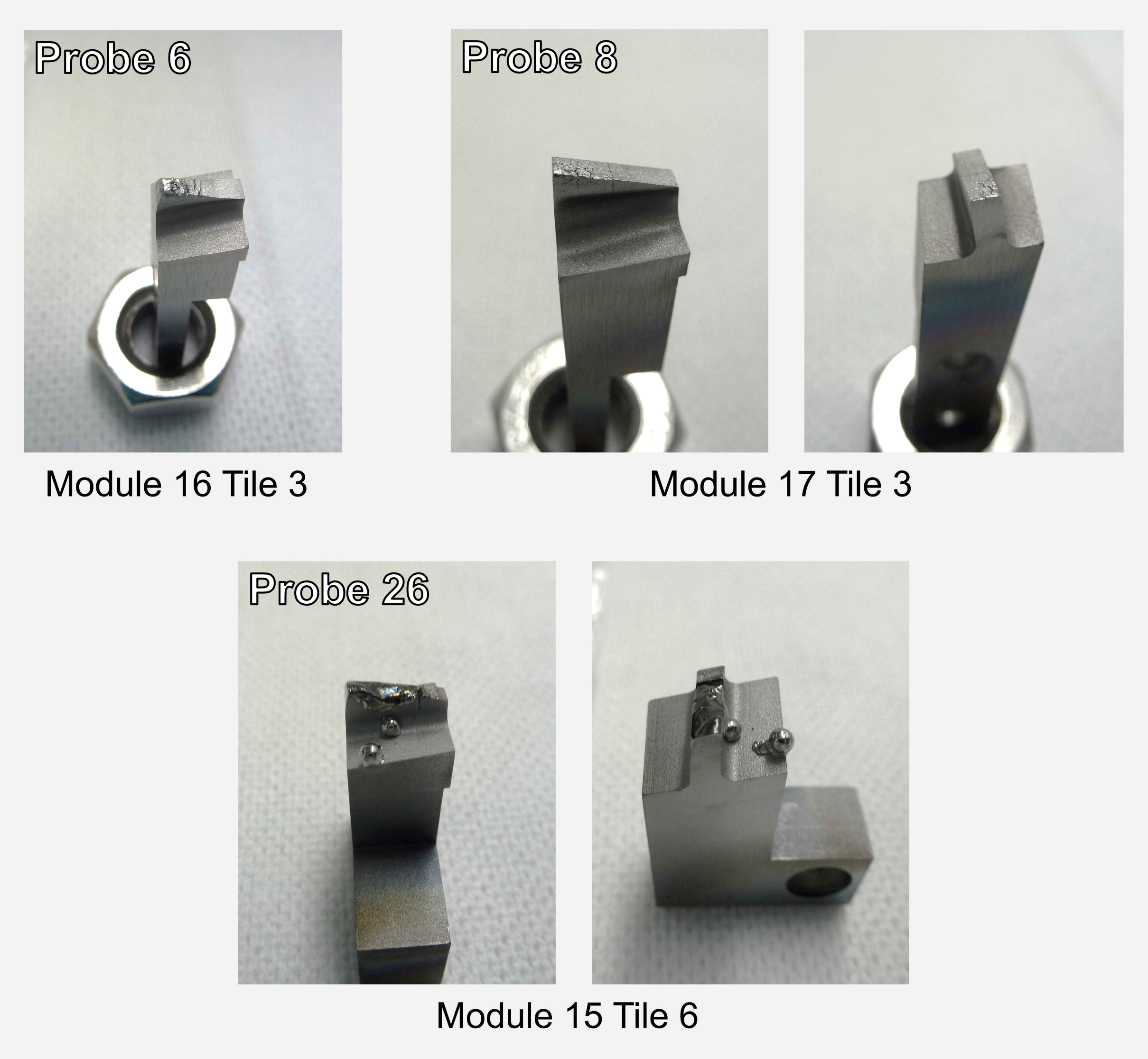

Figure 5.2: Digital photographs of probes 6, 8 and 26 once they were removed from JET after ILW-1 & -2 and before sample preparation.

Initial examination of the probes involved using a TESCAN Mira3 XMH SEM equipped with an Oxford Instruments NordlysNano EBSD Detector. SE images were taken for the cross-sections of all the probe tips and from the top surface of probes 8 and 26, which had not been obscured by Crystalbond. These top surfaces would have been exposed to even more extreme particle and thermal loads than the cross-sections. The cross-sectional SE images of probe 26 also revealed the formation of large voids on the order of tens of microns, along GBs near the exposed surface. A series of FIB trenches were milled near these boundaries to study void size and distribution. EBSD maps were also collected from regions of interest on the cross-section of each probe tip using the AZtec software from Oxford Instruments with grains defined as continuous boundaries with a misorientation angle exceeding 10°. The EBSD maps provided specific sites on each probe to target with Berkovich nanoindentation.

Probe 26 and the as-received probe were indented using the Keysight G200 Nano Indenter at the MRF before November 2021. After that, the instrument was out of operation for maintenance throughout the remainder of the data collection period. The as-received probe hardness and modulus values for the coarse-grained regions are from the same data set collected in Chapter 4. In the case of probe 26, an array was placed in a recrystallised grain, site 2 in Fig. 5.10 (c), near the exposed surface with a surface normal close to the $\langle 101 \rangle$ direction. The array contained 36 Berkovich indents with an indent depth of 1 μm and a spacing of 25 μm. The differences in mechanical properties between the as-received sample and probe 26 were attributed to plasma exposure. To investigate these differences further and produce stress-strain curves, spherical indentation was carried out on both samples.

A total of 30 spherical indents were placed at site 2 of probe 26, in the same $\langle 101 \rangle$ grain as the Berkovich indents with a spacing of 15 μm. EBSD was then used to place 29 individual indents, originally 30 but one indent failed, in separate coarse grains that were close to the $\langle 101 \rangle$ orientation in the as-received probe. The crystal orientation was kept approximately the same between samples to reduce the effects of any radiation-induced anisotropy. This was also a factor in selecting spherical indentation since the tip is self-similar, tip rotation does not affect the residual imprint, and greatly simplifies data collection. The tip had a radius of 2.0 μm but was only used to an indentation depth of 0.5 μm and a depth-to-radius ratio (a/R) of 0.25. At larger ratios, the stress and strain distributions become more complex and the approximation for the contact radius starts to break down [227].

During the repair of the Keysight G200 Nano Indenter, a KLA iMicro Nanoindenter was used to obtain micro-mechanical data probes 6, 8, 26 and the as-received probe. It was important for the instrument to be consistent across all the samples to facilitate a fair comparison. All probe cross-sections were indented to a depth of 1 μm with a spacing of 25 μm to make sure the parameters were identical. The number of indents at each site was optimised to make the most of the available equipment time. For probe 6 there were: 25 indents at site 1, 25 at site 2, 52 at site 3, and 50 at site 4. For the other probes, there were: 41 indents at site 1 of probe 8, 25 at site 1 of probe 26, and 25 indents paced in the coarse grains of the as-received probe. These locations are laid out in Figs. 5.8-5.10 in Section 5.6 and were sufficiently distanced from the sample edge so they were unaffected by any curvature of the surface.

Before the experiments in this thesis began or any samples were cut and polished, the exposed surfaces of the three Langmuir probes were subjected to Microprobe analysis at IST, Portugal by A. Widdowson, E. Alves, and N. Catarino, which is mentioned in the study by R. Kerr *et al.* [228]. The results from this investigation are displayed in Fig. 5.12 and showed that D was detected on the top surface of all three samples, 6.2×10^{15} at/cm^2 on probe 6, 22.5×10^{15} at/cm^2 on probe 8 and 22.9×10^{15} at/cm^2 on probe 26. To determine if D retention was influencing the mechanical properties measured after ILW-1 and 2, the cross-sections of the Langmuir probes were examined at IST, Lisbon using ion beam analysis (IBA).

Three elemental maps of D were recorded from both probe 8 and probe 26 using the Oxford Microbeams data acquisition software (OMDAQ) [229] with the Microprobe in scanning mode. The maps were compared to a W sample containing ∼4% D and showed that there were nearly undetectable levels of D in the two JET samples. The Microprobe was exchanged for another beamline which housed the NRA detector and could achieve larger beam sizes. The NRA detector was positioned at a scattering angle of 135° with a 2000 μm thick active layer and a 75 μm thick Mylar stopping foil. The sample manipulator could analyse surfaces of over 150 mm^2 which has been used to study large samples such as JET divertor tiles [230]. Probes 6, 8, and 26 were all separately placed in the chamber, shown in Section 3.13 Fig. 3.1 and were analysed using the Ion Beam Analysis DataFurnace (NDF) code [231].

5.3 Issues with Active Sample Preparation

All JET-exposed Langmuir probes and lamellae potentially contained trace amounts of T and Be and were considered too active for handling in a standard laboratory. Due to the radioactive and toxic safety risks posed by these samples, technicians at the MRF had to cut and polish them in a glovebox. After examining the initial EBSD maps of the Langmuir probes, it became apparent that the microstructure presented in the images was not as expected. Fig. 5.3 (a) presents a low-magnification EBSD map, where GBs are visible, but a substantial percentage of points in the grain interiors cannot be indexed. Subsequent higher-magnification mapping, as illustrated in Fig. 5.3 (b-d), resolved this issue. These higher-magnification maps revealed a cell or subgrain structure across the sample surfaces. This substructure likely explains the observed limitations in indexing Kikuchi patterns. The larger pixel size at lower magnifications resulted in sampling multiple orientations within a single measurement, leading to ambiguous diffraction patterns.

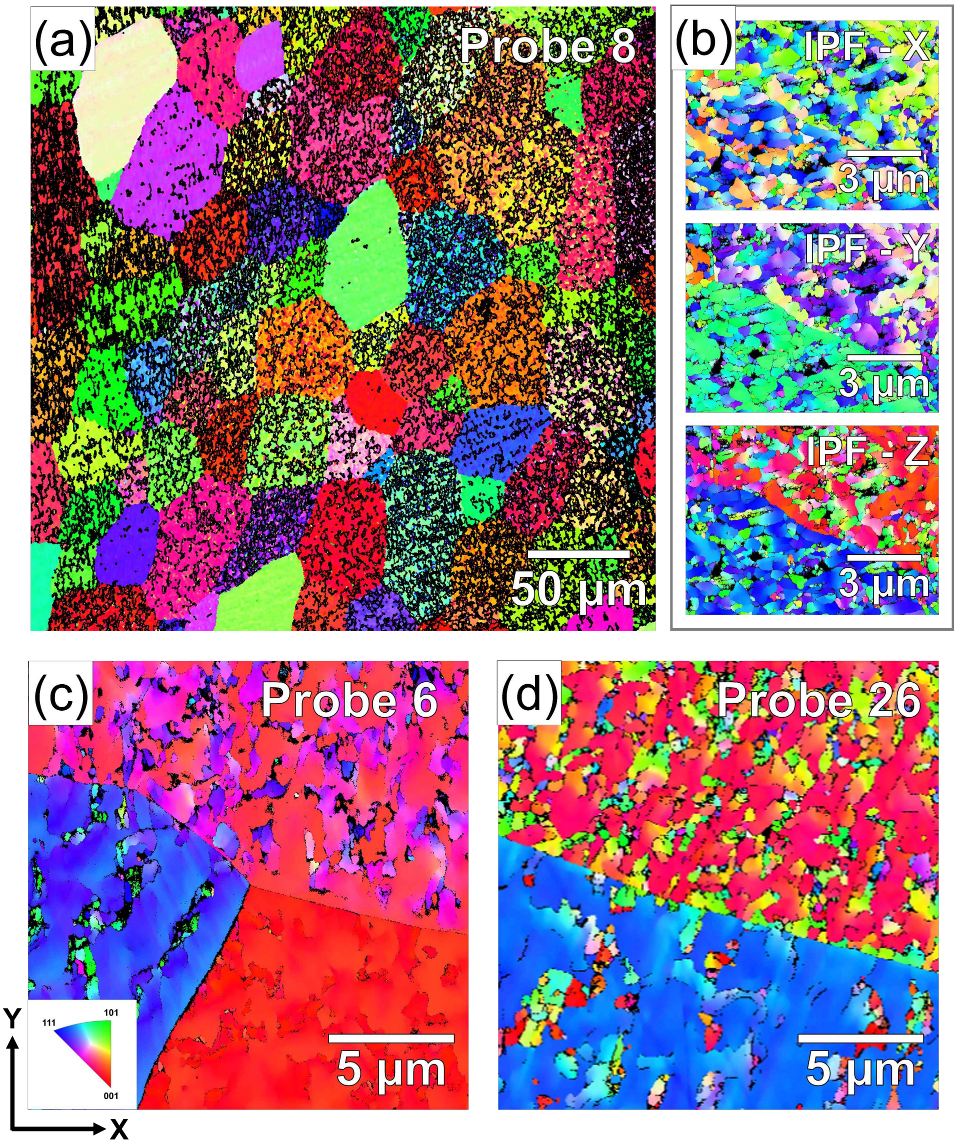

Figure 5.3: EBSD maps showing the artefacts generated during active sample preparation (a) overview of grain structure in probe 8 with a pixel size of 0.10 μm (b) IPF-X, Y and Z maps of probe 8 at higher magnification with a pixel size of 0.01 μm (c) high magnification map of probe 6 with a pixel size of 0.025 μm (d) high magnification map of probe 26 with a pixel size of 0.05 μm.

During plastic deformation, dislocations are generated and interact, forming tangled networks that increase internal energy and hinder further deformation. To mitigate this, dislocations rearrange into ordered, low-energy subgrain structures through a process called polygonisation, where the number of active slip systems is locally reduced [232]. These subgrain boundaries are characterised by small misorientations between adjacent subgrains, ultimately reducing the overall strain energy in the material. In cold working, the term "subgrain" is typically replaced with "cell" where the cells are smaller and less defined. Despite the different terminologies, both boundaries are essentially dislocation networks that transform during deformation from thick walls that contain many dislocations dipoles (pairs of dislocations with the opposite sign) to thin walls associated with misorientations.

The body-centred cubic (BCC) structure of W has fewer slip systems than face-centered cubic (FCC) structures which leads to higher internal stresses and encourages dislocations to rearrange into subgrains at lower temperatures. W also has a melting point of 3422 °C which gives rise to high stability at elevated temperatures and strong resistance to dynamic recovery. As a result, dislocations do not easily annihilate or rearrange during deformation and high densities of dislocations accumulate. Well-defined subgrain structures then form to reduce the energy, even at higher temperatures [233].

One study achieved a 500 nm thick surface layer of ultra-fine grains in pure polycrystalline W by introducing dislocations into the surface using P400 grinding paper before annealing the samples [234]. Perhaps without the annealing step, the samples would be more disordered and resemble the surface of the Langmuir probes. It is therefore proposed that a thin layer dense with dislocation networks, was produced during the grinding of the Langmuir probes and was not successfully removed in subsequent polishing steps. This hypothesis was seemingly confirmed by a series of FIB cross-sections that were made on the surface of probe 26 displayed in Fig. 5.4. Channelling contrast was sufficient to show that the dislocation-dense subgrain region only extended 500 nm from the surface, similar to the study by H. Wang *et al.* [234].

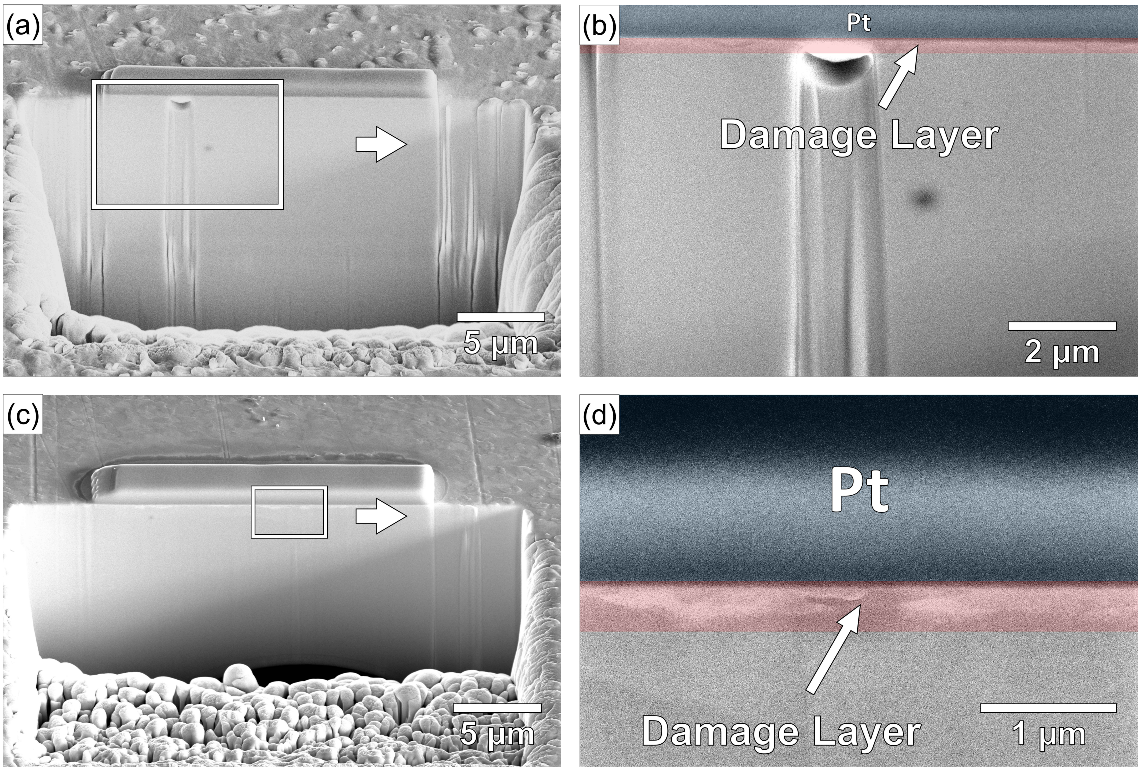

Figure 5.4: FIB cross-sections showing the thickness of subgrain layer (a) first cross-section at low magnification (b) first cross-section at high magnification (c) second cross-section at low magnification (d) second cross-section at high magnification.

Beyond the first few hundred nanometres beneath the surface of probe 26, the FIB cross-section appeared consistent in contrast and brightness with no indication of subgrain formation. The grains of probe 26 had grown by an order of magnitude while it was in the JET divertor, which is discussed in Section 5.6. The formation of cells and subgrains can be observed as part of the recovery stage of recrystallisation but they are intermediate structures and are not stable enough to withstand the nucleation and growth of strain-free grains which are lower in stored energy. Since grain growth had occurred, it is unlikely that any cells or subgrains would remain in the sample and therefore these structures were indeed an artefact of sample preparation.

The EBSD maps may not have had the desired percentage of indexed Kikuchi patterns but the true grain sizes of the exposed probes were still visible. In terms of the nanoindentation data, the plastic zone diameter was ∼17.2 μm for all 1 μm indents in W, as stated in section 4.5. Since the layer of cells and subgrains is less than 500 nm, it should not significantly impact the hardness and modulus measurements for the Langmuir probes. The presence of the rolled, fine-grained structure in the lamellae meant it was nearly impossible to observe the dislocation-dense subgrain layer that appeared in the Langmuir probes. The percentage of Kikuchi pattern indexing in the EBSD maps was sufficient to check for signs of recrystallisation. Furthermore, a greater indentation depth of 2 μm was used for the lamellae because of the fine-grained structure. This also meant that the subgrain layer occupied an even smaller proportion of the plastic zone than in the case of the probes and the hardness and modulus values would remain unaffected.

Active sample preparation required the use of a glovebox, which severely restricted hand maneuverability so a better surface finish may not have been achievable. Moreover, re-polishing the samples would have taken a significant amount of time to schedule and execute at the expense of experiment time which had been substantially affected by the COVID-19 pandemic. A decision was made that the main conclusions from these results were not compromised and further sample preparation was not required.

5.4 JET Diagnostics and Plasma Conditions During the ITER-Like Wall Campaigns

Two sets of codes were developed to link the plasma conditions during exposure to the observed changes in microstructure and mechanical properties. The first analysis was developed by Dr.

Scott Silburn at UKAEA to utilise data from infrared (IR) camera diagnostics. The second code was developed by Beth Thomas and Dr. Spyros Aleiferis at UKAEA to use the data collected by the Langmuir probes during the ILW campaigns.

5.4.1 Surface Temperature Calculations from IR Camera Data

IR camera systems in JET are integral to monitoring the temperature and heat flux on PFCs [235][236]. These cameras operate in the mid-infrared range (3-5 µm) and capture thermal radiation emitted by surfaces within their view. They have a maximum sampling frequency of up to 20 kHz which allows for the study of fast plasma phenomena such as ELMs. The data collected is converted from raw signals into calibrated temperature profiles, considering the emissivity of the materials. The IR setup in JET includes four scientific CMOS cameras, positioned to observe plasma-facing regions in the divertor. They were concentrated on the lamellae of the central tile and therefore did not collect any usable data for the Langmuir probe samples. Through a combination of direct in-vessel calibration techniques, which utilise a heated grey body source for precise measurements, and software tools for data acquisition and non-uniformity correction, these systems allow detailed, real-time thermal analysis during fusion experiments. Together, these infrared diagnostics offer detailed insights into the temperature distribution and heat dynamics in the JET divertor, contributing valuable data for optimising PFC performance under extreme conditions.

Sources of uncertainty are linked to the use of W components which can result in low emissivity that varies with wavelength, leading to an underestimation of surface temperatures [237]. Reflections from surfaces within the environment can introduce measurement artefacts and cause an overestimation of the surface temperature [238]. Additionally, the degradation of target material surfaces or detector mirrors due to material deposition and erosion processes can impair temperature measurements [239]. Furthermore, intense radiation could adversely affect the refractive properties of optical components, potentially distorting measurements. Finally, parasitic bremsstrahlung radiation is emitted when electrons are deflected during collisions with ions in the plasma [240]. When the bremsstrahlung signal is superimposed on the thermal signals originating from the PFCs, it overestimates the assessed surface temperature values. Beyond these environment-specific factors, the fundamental limit imposed by diffraction restricts the maximum attainable spatial resolution, setting an inherent boundary on the level of detail that can be resolved. Unfortunately, there was insufficient time to develop advanced image-processing techniques to compensate for all of these phenomena.

IR camera data from the KL9B and KL9A/KLDT sightlines was used to calculate the time in seconds that the lamellae plasma-facing surfaces spent between 400 °C and 1300 °C, in increments of 20 °C. This was used to produce histograms of surface temperatures for each lamella in Fig. 5.7 and Fig 6.2 with bin sizes of 100 °C and 20 °C, respectively. The analysis only included a pulse if the outer strike point position was situated on tile 5 for over 20% of the heating window. Data below 300 °C was omitted due to reduced reliability, while the upper limit of surface temperature detection was 1300 °C. The IR cameras were also prone to saturation at high temperatures and in these cases, a lower bound of 700 °C was implemented, likely causing a slight underestimation of the overall surface temperatures. The campaign lengths were inputted as the first and last pulse number of each campaign. The sample locations were defined by s-coordinates which is a coordinate system in millimetres that poloidally traces the divertor surface with the origin at the inner corner of tile 0 [20][241]. The code outputs the total time in seconds where the maximum temperature was within the s-coordinate range. Uncertainties arise due to missing data during some pulses and some samples will have more data missing than others but this was not anticipated to significantly skew the results. The data quality appeared satisfactory after removing obvious anomalies, though lacking thorough validation.

5.4.2 Deuterium Fluence Calculations from Langmuir Probe Measurements

The measurements from the three Langmuir probes under investigation in this chapter, along with data from the closest tile 5 probe to each of the four lamellae, were analysed to quantify the particle loads experienced by the samples in the JET divertor. The fluence numbers and the amount of available pulse data are included in the mechanical properties discussion in Table 5.1 of Section 5.5 and Table 5.3 of Section 5.6. The code derives the fluence of D^+ ions from the electron density and temperature measurements. It checks if the strike points are close enough to a specific location of interest with s-coordinates that are provided by the user. The overall percentage of available data is calculated and the gaps in location data are filled with additional data from EFIT [242] (an equilibrium reconstruction code at JET used to locate the strike points). The integrated fluence is computed for the region of interest for time intervals when the strike point is within the specified s-coordinate range. The code then identifies dry runs or aborted pulses so they can be excluded from the analysis and categorises pulses into specific experimental campaigns based on their pulse number. Finally, it compiles the percentage of available data, the fluence values for each valid pulse and the cumulative fluence organised by ILW campaign.

The fluence is calculated assuming that all particles detected by the Langmuir probe are D^+ ions. In reality, while the majority of detected particles are D^+ ions, a significant fraction consists of other ionised gas species present in the divertor for plasma control. These species have different masses, charges, and velocities compared to a D^+ ion, all of which influence the fluence calculation. The total fluence is derived from the ion density and the thermal velocity of the incident ions. Heavier ions have lower thermal velocities than lighter ions at the same temperature. The calculation assumes that the incident particles are the lighter D^+ ions. This assumption could lead to an underestimation of the fluence value, as heavier ions have lower thermal velocities and contribute less to the detected current, making them underrepresented in the fluence estimation. Conversely, ions with higher charge states generate larger currents for the same ion flux, which increases the calculated ion density and fluence. The fluence values presented in this chapter therefore do not represent the absolute fluence but offer a value that can be compared across different samples.

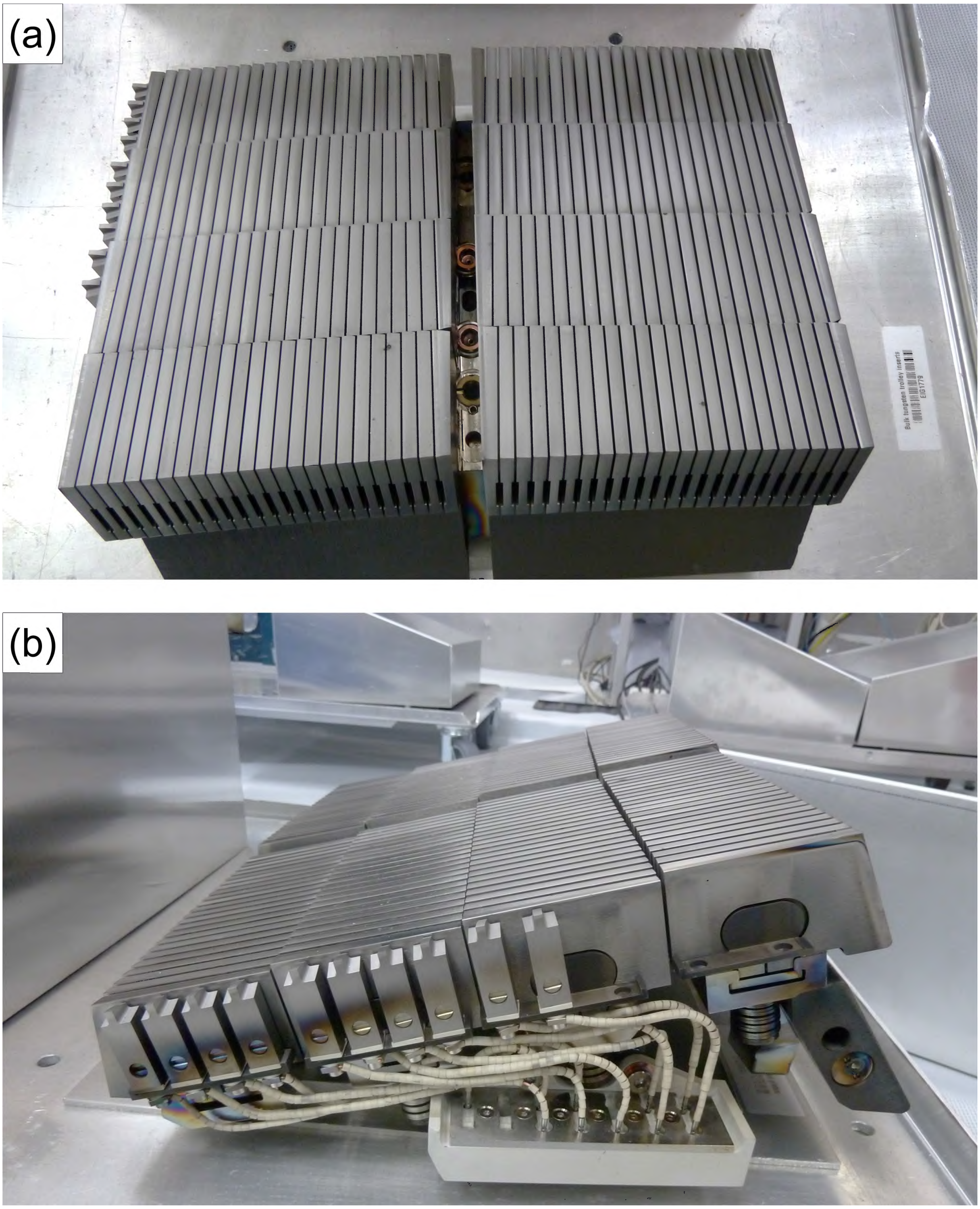

Figure 5.5: Digital photographs of a tile 5 module of lamellae (a) from a top-down view (b) from a cross-sectional view, showing the location of the tile 5 Langmuir probes.

5.5 The Effects of Deuterium Plasma Exposure on JET Lamaellae

Once lamellae C4, C12, C13, and D12 were mounted and polished, their cross-sections were mapped using EBSD in the same region which was located in the centre of the sample, next to the exposed surface. The maps are displayed in Fig. 5.6 and show no sign of recrystallisation for the four samples. Grain size analysis was not performed for the exposed lamellae since the grain size did not appear to change after exposure and subgrain formation remained a possibility. Each EBSD map represents a 2D slice of a component that is 62 mm in length [243], therefore recrystallisation might have occurred in other regions. Localised temperature variations can stem from material inhomogeneity where defects, impurities, or grain sizes are not evenly distributed throughout the component. However, the starting microstructure of the as-received samples in Chapter 4 did not appear to have any defects or artefacts that were too large. In general, W has an extremely high thermal conductivity which helps create a uniform temperature distribution even though the components were not actively cooled.

Differences in temperatures can also be caused by non-uniformities in heat flux due to geometric shadowing or strike point position. The lamellae are symmetric along the length of the component, in the poloidal direction, but are asymmetrical in the toroidal direction as the surface curves downward on one side. This was done so that 1.4 mm of the 5.9 mm lamella width is completely shadowed and prevents the formation of a leading edge [243][244]. The mapped and indented region was over 1.9 mm from the shadowed region where the heat flux should be near its peak and the mechanical data would not be influenced by edge effects. The surface temperature would, however, fluctuate along the length of the samples due to the strike point position on stacks C and D, summarised in Fig. 5.15. Ultimately, the lamellae were assumed to be unaffected by recrystallisation due to the surface temperatures recorded by the IR cameras in Fig. 5.7. If active sample preparation had not been an issue, it would have been beneficial to evaluate more cross-sections.

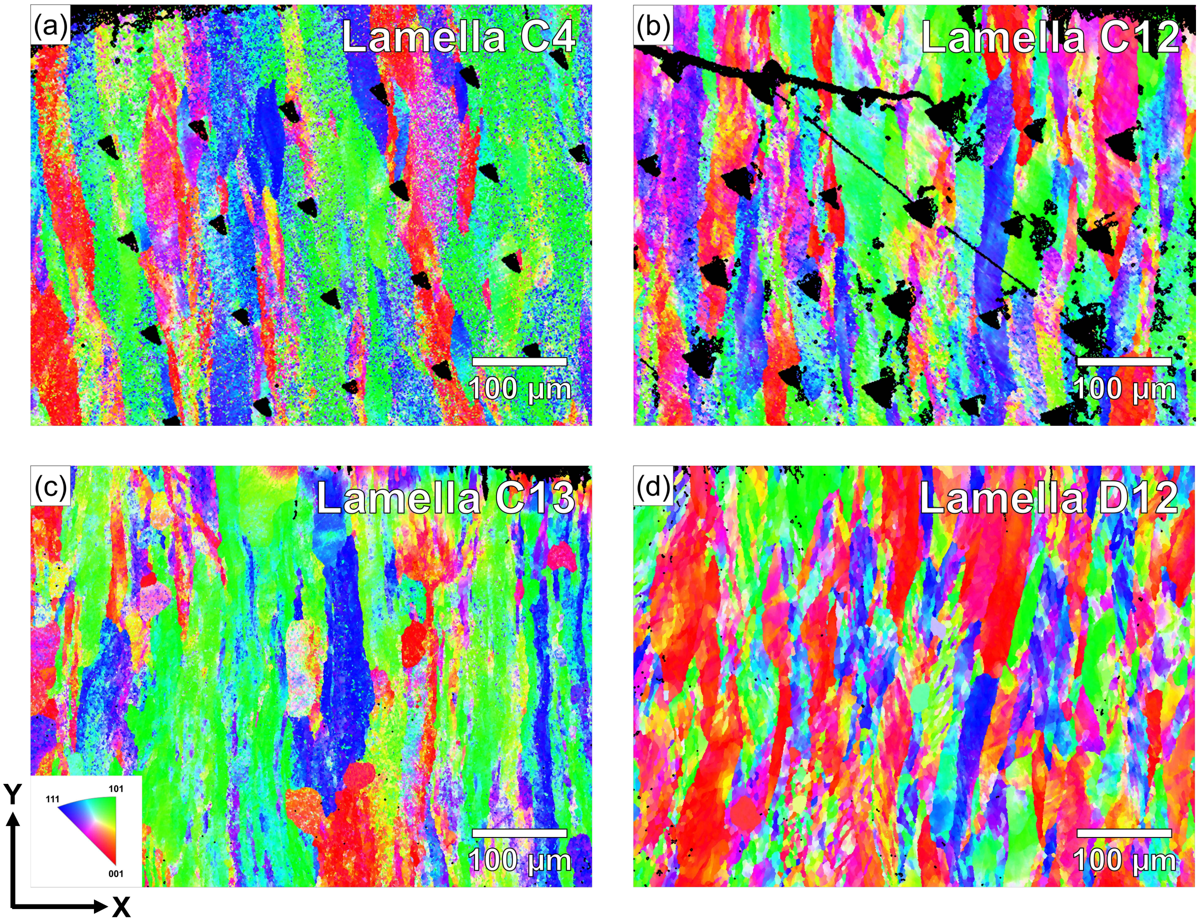

Figure 5.6: EBSD maps from the cross-sections of lamellae (a) C4 (b) C12 (c) C13 (d) D12, taken just below the exposed surface in the centre of each sample.

Nanoindentation of lamellae C4 and C12 was performed while the EBSD maps were collected for lamellae C13 and D12 and vice versa, hence the Berkovich indents visible in Fig. 5.6 (a) and (b). The results can be seen in Table 5.1 which includes estimates for the D^+ fluence incident on the lamellae surfaces as determined by the Langmuir probes neighbouring tile 5. All indents were performed to a depth of 2 μm because the grains were too small to indent individually. In anticipation of potential anisotropic effects post-exposure, the plastic zone is also large and can sample as many crystallographic orientations as possible to obtain a representative average. The maximum plastic zone size was estimated using the method proposed by C. Robertson *et al.* [195], taking an indent from lamella C13 with the highest hardness which had an applied force of 537 mN at 2 μm and returned a plastic zone radius of 18.5 μm. The as-received lamella had an average ECD of 2.1 μm and assuming no change in grain size after exposure, a perfectly hemispherical plastic zone should sample ∼2770 grains at an indentation depth of 2 μm.

Table 5.1: A table comparing the fluence, hardness and elastic modulus data for the as-received lamella and lamellae C4, C12, C13, and D12

iMicro				**Hardness (GPa)**		**Modulus (GPa)**	
Lamella	Available Data	Fluence (D^+/m^2)	Number of Indents	Mean	SD	Mean	SD
As-Received	N/A	N/A	36	**6.1**	0.3	**430**	20
C4 (ILW-3)	97.3%	7.6×10^{23}	30	**6.0**	0.2	**430**	10
D12 (ILW-3)	95.5%	9.3×10^{23}	19	**6.1**	0.2	**460**	10
C13 (ILW-3)	97.5%	1.0×10^{24}	22	**6.2**	0.4	**410**	20
C12 (ILW -1 & -3)	94.0%	3.8×10^{24}	13	**5.9**	0.2	**420**	10

Overall there was only a difference of 0.3 GPa between lamella C12 and C13 which had the smallest and largest hardness averages, respectively. The standard deviations of these hardness values were large, ranging from 0.2 to 0.4 GPa, so a difference of 0.2 GPa does not suggest a quantifiable change in hardness between the samples. In the case of the as-received lamella, its hardness value fell in the middle of the range of exposed values, implying that D plasma exposure did not cause a statistically significant change in hardness for the tile 5 lamellae.

In terms of the modulus, lamella D12 had a value of 460 GPa which was 30 GPa higher than the as-received lamella. The maximum standard deviation was 20 GPa which may suggest that this was a statistically significant difference, but it was not accompanied by a change in hardness. The appearance of a larger modulus is more likely an error due to a poor frame stiffness correction as the modulus vs. depth curves do not completely plateau to a horizontal line (see APPENDIX A). This was not identified at the time of analysis and could not be addressed after the fact but should not affect the hardness measurement. Of the remaining samples, there was only a difference of 20 GPa between lamella C13 and the as-received, the smallest and largest values. This is the same magnitude as the standard deviation for the as-received lamella and suggests that D plasma exposure did not impact the modulus values. It was therefore not possible to establish a relationship between the D fluence and the mechanical properties of the lamellae after exposure.

The variability in the mean values and the standard deviations for both hardness and modulus likely stems from a large spread of grain sizes since the coefficient of variation was 44% for the as-received lamella. The EBSD maps of the as-received lamella in Chapter 4 and the JET-exposed lamellae in Fig. 5.6 visually confirm that grain size is not uniformly distributed across the samples. Consequently, no two indents will capture the same proportion of GBs in their plastic zone which gives rise to different contributions of boundary hardening, the likely cause for the discrepancies in both hardness and modulus values. GBs behave as barriers to dislocation motion which then alter stress and strain fields during indentation. In smaller grains, dislocation movement is more constrained due to the increased presence of GBs. Other factors to consider are variations in the composition of the GBs across the samples and irradiation-induced anisotropy such that different crystallographic orientations have different mechanical properties. Individual indents were also checked close to the exposed surface and deep in the bulk for differences in hardness and modulus but no such pattern could be established.

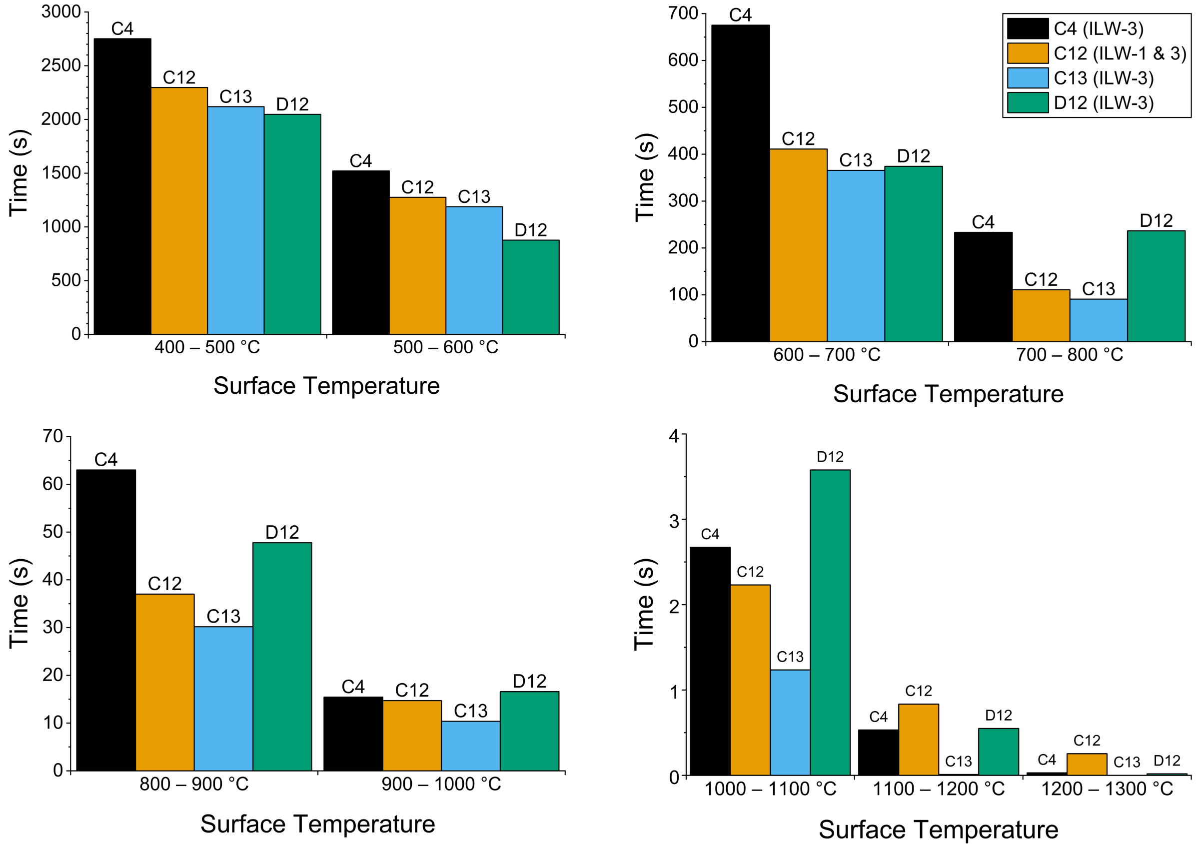

Figure 5.7: Histograms showing the duration of time in seconds that the surfaces of lamellae C4, C12, C13 and D12 were in the temperature range of 400–1300 °C with a bin size of 100 °C.

The surface temperature data from the IR camera system shown in Fig. 5.7, was initially intended to contextualise any property changes after the lamellae were exposed. However, the values for grain size, hardness, and modulus remained unchanged by the plasma. Despite this, the surface temperatures can still offer insights into the exposure conditions that resulted in an absence of recrystallisation and grain growth. The fusion community has researched at great length the response of W components to different starting microstructures, temperatures and periods of heat treatment. In one study the W samples had a rolled microstructure akin to the JET lamellae where one W sample showed signs of recrystallisation after heating at 1200 °C for an hour and another recrystallised after 3115 hours at 1100 °C [245]. All four JET-exposed lamellae spent less than 0.5 s at temperatures between 1200 and 1300 °C, less than 1 s between 1100–1200 °C and less than 4 s between 1000–1100 °C which was not long enough for new crystals to nucleate. It is assumed that all the lamellae spent the vast majority of time below 400 °C and the discrepancies in the total times displayed in the histograms were accounted for at temperatures below 400 °C.

The plasma control systems of JET had a trip level at a lamella surface temperature of 975 °C, at which point the auxiliary power is turned off, the plasma current is ramped down and the strike points are moved away, ultimately terminating the plasma [20]. There might have been exceptions to this but there was an overall budget for higher temperatures to protect the mechanical properties of the W components. This method of surface temperature monitoring appeared to be sufficient for a real-time protection system as surface temperatures only exceeded 1000 °C for a few seconds. These temperatures above 1000 °C are likely due to the time required for the plasma control system to execute these processes, perhaps during an inter-ELM period but particularly during ELMs since the transient events occur on very short timescales. The maximum surface temperature for each lamella was recorded during the occurrence of an ELM as follows: C4 $>$ 1243 °C, C12 $>$ 1299 °C, C13 $=$ 1121 °C, D12 $>$ 1260 °C, where the greater than sign signifies that the IR camera was saturated, making the temperature a lower bound.

Lamella C12 was placed in the JET divertor for the longest period, for both ILW-1 & -3 and a total of 31.5 hours of divertor operation [19]. The remaining lamellae were exposed in the JET divertor for a total of 18.5 hours in ILW-3. The longer exposure time of lamella C12 likely provided more opportunities for ELMs, hence why it spent more time between 1100–1300 °C than the other samples. Given that it was exposed to an additional campaign compared to the other lamellae, it was unexpected that this was not the case between 400–1100 °C. These results make more sense when taking into consideration the radial position of the outer strike point which is accompanied by higher temperatures and heat loads. Generally, the outer strike point spent most of ILW-1 on tile 5 where the lamellae are positioned and most of ILW-3 campaign on tile 6 [20]. The outer strike point remained on stack C longer than any other stack in both

ILW-1 & -3, highlighted in Fig. 5.15 (b), JET data previously shown by G. Pintsuk *et al.* [10]. This can be seen for lamella C4 which spent the most time in the temperature range of 400 to 900 °C but fails to explain why lamella D12 spent the most time between 900–1100 °C than the other lamellae.

Another factor to take into consideration is the lamella number which represents the toroidal position, since heat loads are non-uniformly distributed along the module [10][246]. The first three lamellae (1-3) in a module are shadowed from the plasma by the adjacent module to help prevent component melting [18][247] and the heat loading gradually increases across the module with a maximum typically between lamellae 22-24. This distribution of heat appeared to affect C12 and D12, which spent more time between 1100–1300 °C and 900–1100 °C respectively. However, this effect cannot have been that pronounced if lamella C4 spent the most time in the 400–900 °C temperature range, far more time than the few seconds that lamellae C12 and D12 spent above 900 °C. The study by G. Pintsuk *et al.* investigated lamella C23 from the highest loaded part of tile 5 after ILW-1 which showed no observable change in grain size but some EDM crack growth [10]. This confirms that temperature increased with lamella number and that surface temperatures remained below the recrystallisation range for W. Moreover, the EDM cracks in lamella C23 only propagated a further $\sim$150 μm [10] compared to the 15 mm cracks observed in ASDEX-Upgrade [68]. Ultimately showing that the bulk W components in JET were better suited for plasma loading.

The period of exposure for W components in the JET divertor is far shorter than that of a commercial reactor, the first ITER divertor will be exposed to 2500 hours of divertor operation [5]. Lamella C12 was exposed for 18.5 hours of divertor operation during ILW-3 and spent a total of 0.254 s above 1200 °C. Under the assumption that component failure could occur after exposure at 1200 °C for one hour due to significant recrystallisation, lamella C12 would be able to endure nearly 30 years of JET operation. Although this extrapolation appears to be quite optimistic, the energy output of ITER will far exceed the ILW campaigns. The following section investigates the Langmuir probe samples during these campaigns with microstructures that resemble ones that could form in ITER.

5.6 The Microstructural Evolution of the JET Langmuir Probes

The Langmuir probes were exposed in ILW-1 and -2 and exhibited observable microstructural changes depending on their placements in the JET divertor. Probe 8 showed the least damage, the grain size shown in Fig. 5.8 (c) appeared to be unchanged from the as-received Langmuir probe and channelling contrast in the SEM showed that this was consistent across the whole cross-section. The only feature differentiating it from the as-received sample was the growth of the EDM-induced cracks on the exposed surface which were originally $\sim$50 μm in length. These can be seen in Fig. 5.8 (a) where the largest crack propagated over 1 mm into the bulk from the exposed surface, which is a substantial increase from the $\sim$200 μm cracks that formed on W lamella C23 [10]. This indicates that the loading conditions on probe 8 were more extreme than those on lamella C23 which may have been exacerbated by the slight differences in starting microstructure. It is also unknown whether cracking would have been initiated in either sample if cracks were not already present after EDM. IR cameras could not be used to estimate the temperatures of the Langmuir probes due to the positioning of camera sightlines. But the other two samples, probes 6 and 26, were associated with some degree of recrystallisation, suggesting they were exposed to higher temperatures than probe 8. This seems to confirm that the small EDM-induced cracks can propagate deep into the bulk even if the surface of the component remains below recrystallisation temperatures.

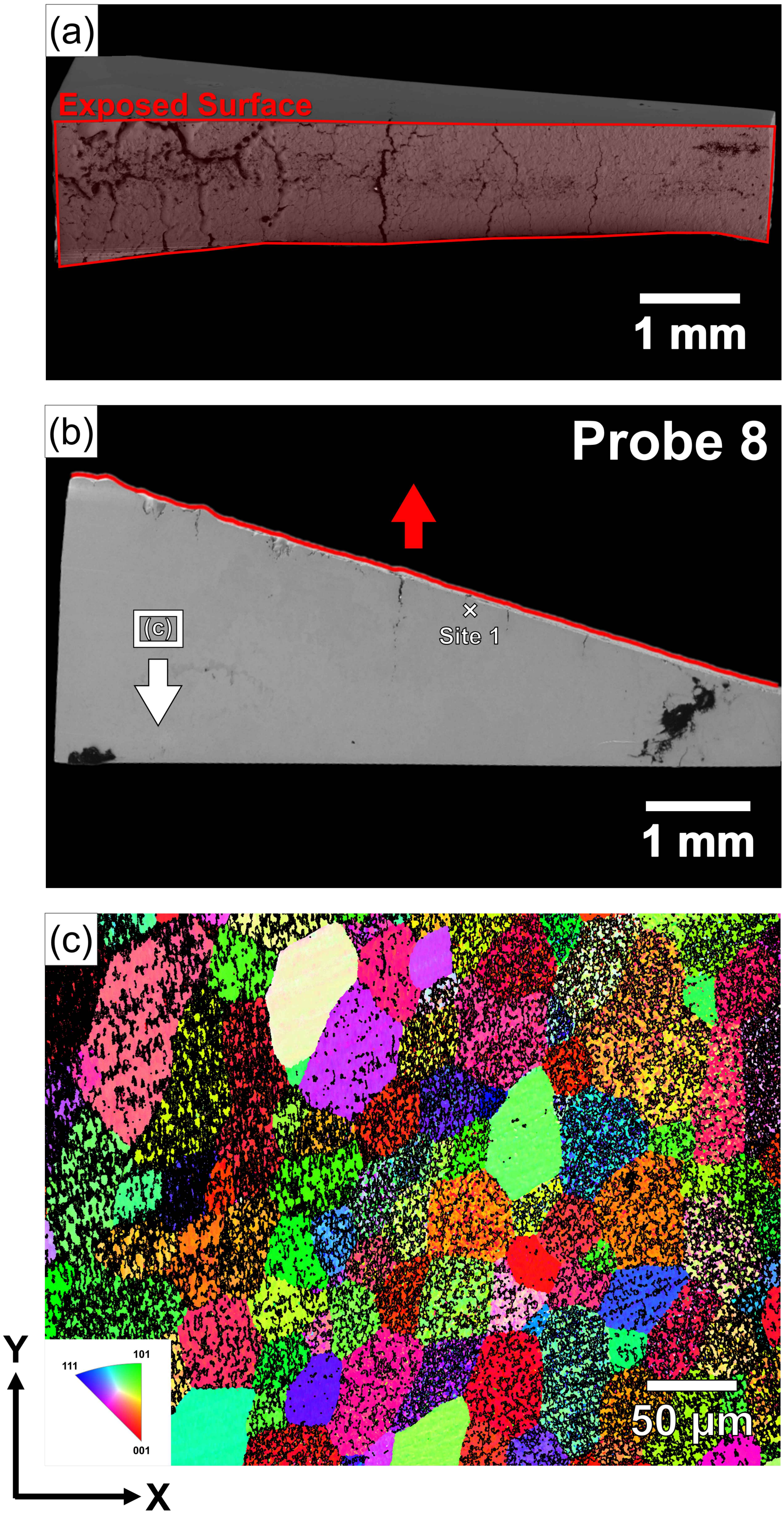

Figure 5.8: A schematic of probe 8 showing (a) SE image of the exposed surface (b) SE image of the cross-section with the indented region at site 1 and black residue from copper tape that was placed in the bottom corners (c) EBSD map from the cross-section with substandard indexing caused by active sample preparation.

A possible explanation for this crack growth likely stems from the pulsed nature of JET which results in significant cyclical thermal stresses even below 1100 °C. The EDM cracks can act as stress concentration points when the component is placed in the divertor. The residual stresses that are caused by machining can also promote crack propagation, especially when surface temperatures are not high enough to cause annealing during operation. The largest crack extends across the width of the exposed surface in Fig. 5.8 (a) and nearly halfway down the cross-section of the tip in Fig. 5.8 (b). The probe tip could conceivably split in half if it had been exposed for more time in the vessel, which could not only release W dust into the divertor but could risk losing key diagnostic information about the plasma. Furthermore, Langmuir probes could be used to help control target heat fluxes in ITER [248], meaning it would be a significant loss if they broke in that environment.

The EBSD map in Fig. 5.9 (b) shows the very top of probe 6, which extends into the plasma and should therefore experience the highest temperatures across the sample. This is confirmed by the presence of the recrystallisation front which is the boundary where the larger annealed grains meet the original, deformed microstructure. The recrystallisation front is the result of a large temperature gradient that forms due to the hot plasma making contact with the top of the sample and a heat sink at the bottom of the probe which is attached to the vessel wall. The fact that the whole tip did not recrystallise suggests that probe 6 did not remain within the recrystallisation temperature range for as long as probe 26, likely due to the location of the inner strike point. A microscopic overview of probe 26 can be seen in Fig. 5.10 where the grains have grown from 23.5 μm to over a millimetre and were so large that a reliable average could not be obtained from the EBSD maps in Fig. 5.10 (c). The substantial recrystallisation and grain growth of the Langmuir probe compared to the lamellae was attributed to the protrusion of the probes beyond the armour materials. The probes must also be in regular contact with the plasma to take measurements during a pulse which leads to higher heat loads and greater surface temperatures. A study investigating the effects of leading edges in JET ILW-1 by J. Coenen *et al.* showed similar grain growth when a test lamella was deliberately raised into the plasma [249].

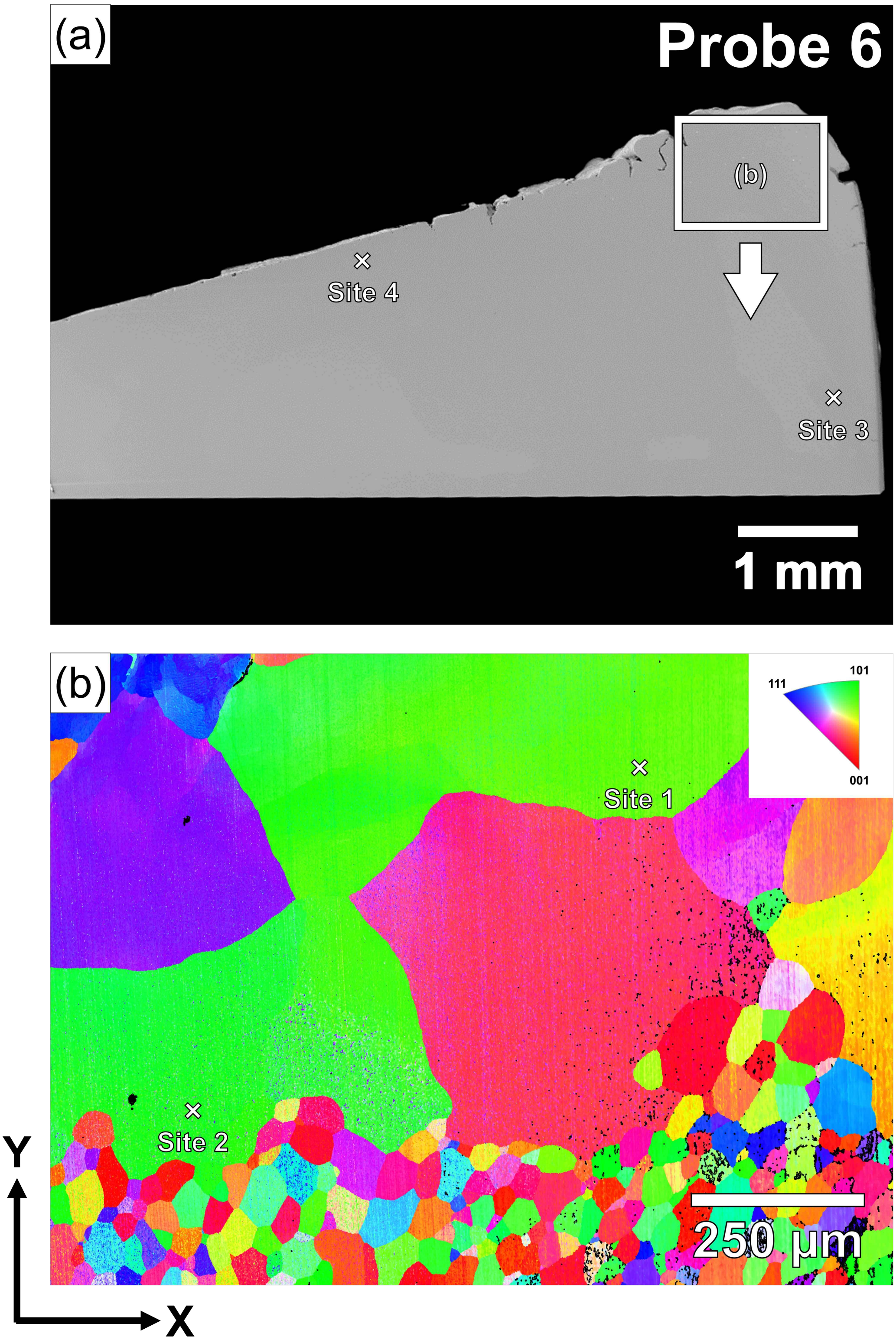

Figure 5.9: A schematic of probe 6 showing (a) SE image of the cross-section with the indented regions at sites 3 and 4 (b) EBSD map from the recrystallisation front with the indented regions at sites 1 and 2, where variations in surface finish and pixel size affected the number of points that could be indexed.

A small part of probe 26, to the right of Fig. 5.10 (b), became detached due to a large crack that had formed during exposure which grew across the whole sample during polishing and led to brittle fracture. The formation of that crack and the vertical crack that remains visible in Fig. 5.10 (b), are likely due to repeated exposure to elevated temperatures, resulting in recrystallisation, deformation, creep damage and fatigue [202]. The exposed surface in Fig. 5.10 (a) and highlighted in red in (b) appears to have melted and the crack network that was generated during machining was covered by melt layers. This indicates that temperatures at the exposed surface exceeded 3422 °C, the melting point of W [233]. However, the temperature was not uniform over the entire component as the warping and melt damage appeared to be localised near the exposed surface. The large increase in grain size suggests that even the lower section of the probe 26 tip likely reached temperatures above 1200 °C for a duration close to an hour.

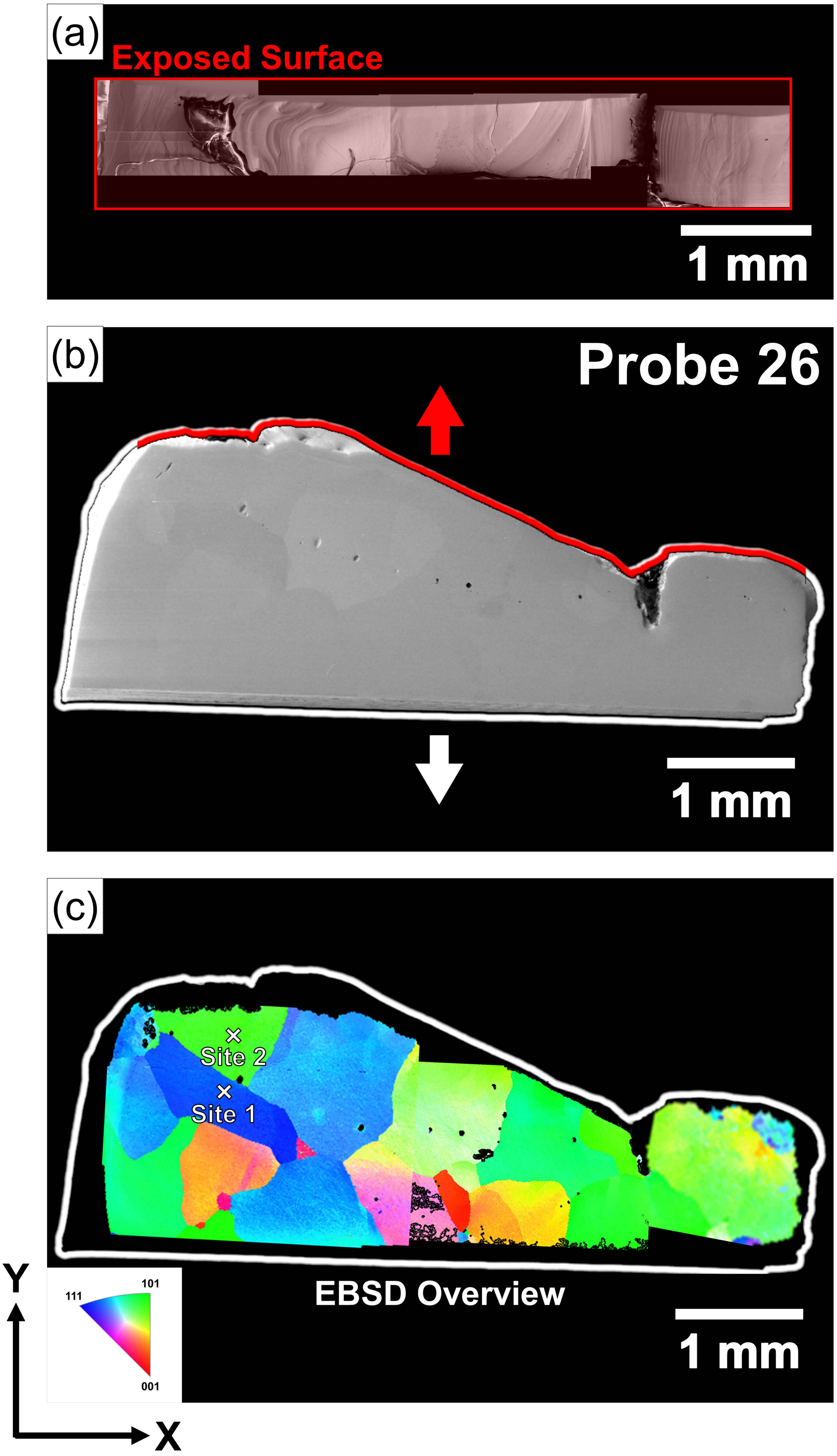

Figure 5.10: A schematic of probe 26 showing (a) combined SE images of the exposed surface (b) SE image of the cross-section (c) combined EBSD maps to provide an overview of the cross-section with the sample outlined in white and the indented regions at sites 1 and 2.

These elevated temperatures may have been caused by off-normal events such as major disruptions or transients, but are more likely due to steady-state operation. This is based on the assumption that most major disruptions move upwards, away from the divertor and the strike point was positioned near probe 26 for an extended duration (Fig. 5.15) [228]. In-vessel images taken between the first and second campaigns showed that melting occurred during ILW-2, consistent with the 20 GJ of energy deposited on tile 6 during ILW-2, compared to 5.5 GJ in ILW-1 [250].

In addition to the melt damage present in probe 26, plasma exposure also resulted in the formation of voids which can be seen in Fig. 5.11. These voids formed in the vicinity of GBs in the top half of the tip closest to the exposed surface. They ranged from sub-micron sizes up to 50 μm, similar to those observed in the TEXTOR tokamak [106]. In the TEXTOR samples, voids were thought to be associated with the evaporation of W at nucleation sites such as GBs or impurity clusters [107][108]. The melt damage on the exposed surface suggests that the voids likely formed in a molten region of probe 26. If gas bubbles were also present then the voids could have formed via the same mechanism as those observed after EDM where gas was expelled during solidification [86] [88–90].

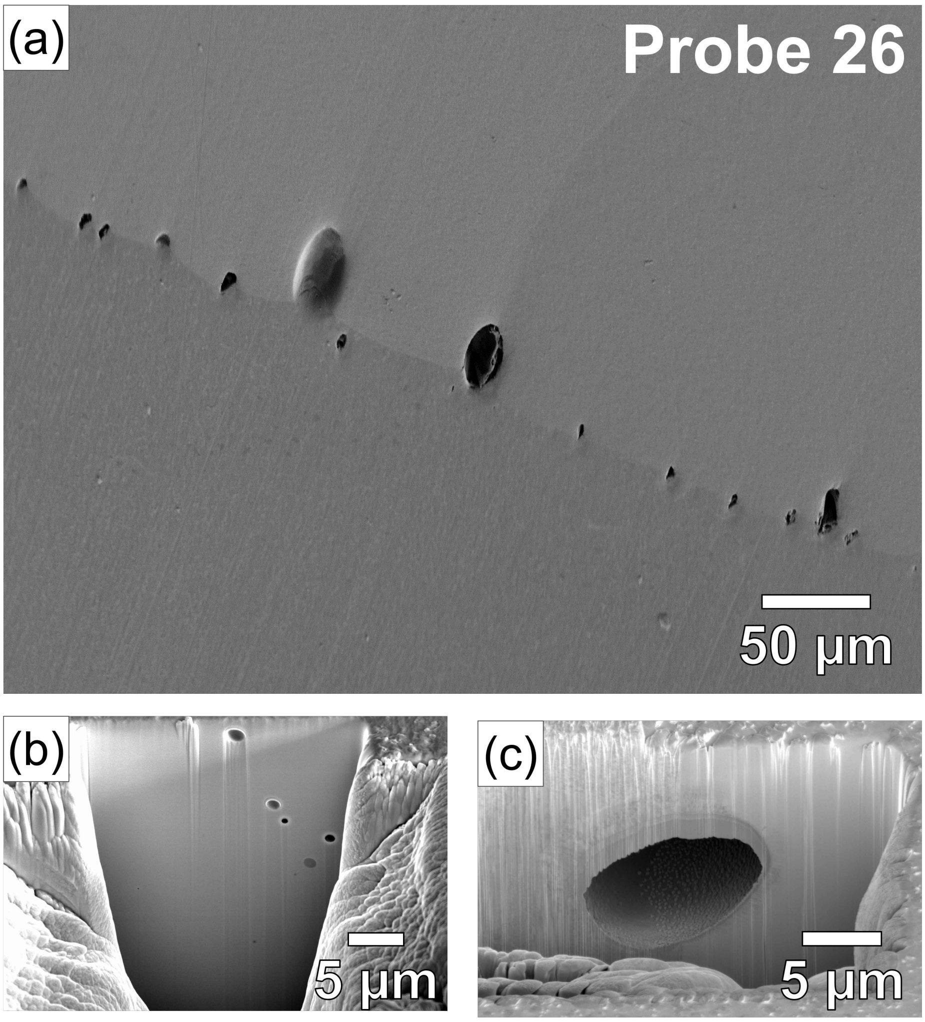

Figure 5.11: (a) SEM image of the voids on the cross-section of probe 26 and FIB trenches (b) and (c) showing subsurface voids in the vicinity of the GB.

Gas bubbles have been shown to form in fusion-relevant environments by high He fluences [29] and high-energy H ions [251]. Table 5.2 shows the number of H and He species injected into the JET vessel during ILW-1 and -2 as reported by L. Dittrich *et al.* [23]. He species were not injected into the vessel during ILW-1 and there were roughly 10,000 times more H species than He species injected during ILW-2. Although the average energies of the incident He ions were not known, they were thought to be lower than He implantation experiments [252][253]. Furthermore, only 8.45×10^{22} ^{3}He and ^{4}He atoms were injected into the entire vessel throughout ILW-2, while He implantation experiments generated He bubbles in W using doses of 3×10^{22} He per m^2, at 30 keV and much shorter timescales [254]. It was therefore assumed that the voids were not seeded by He bubbles. H and its isotopes (D and T) can create trapping sites in W at sufficient energies (38 eV) and fluences (>10^{22} ions/m^2) which can create stress-induced bubbles and voids when the solubility limit is reached [51][255]. Probe 26 made sufficient contact with the D plasma to cause melting and recrystallisation, so there was likely an abundance of D in the matrix to create bubbles.

Table 5.2: Injection data for various gases during ILW-1 and -2, recreated from the study by L. Dittrich *et al.* [23], where GIM is the Gas Introduction Module and DMV is the Disruption Mitigation Valve.

Gas	Injection Point	ILW-1	ILW-2
^{1}H	GIM, pellets DMV	2.5×10^{24} –	2.7×10^{25} 1.3×10^{24}
^{2}D	GIM, pellets DMV	9.1×10^{26} –	5.8×10^{26} 2.4×10^{26}
^{3}He	main chamber GIM	–	8.2×10^{22}
^{4}He	main chamber GIM	–	2.5×10^{21}

The fluence data recorded by the Langmuir probes in Table 5.3 could not help establish the origin of the voids. Probe 26 had a lower calculated fluence than probes 6 and 8, and these probes showed no sign of void formation. IR Camera data was unavailable for the positions of these probes but the different microstructures suggest that probe 26 reached the highest temperatures because it had partially melted and completely recrystallised. This was followed by probe 6 which was partially recrystallised and then probe 8 which did not visually differ from the as-received sample.

If probe 26 was exposed for longer in the JET divertor under prolonged stress and heating, the voids would likely continue to grow. This occurs when atoms diffuse from areas of high stress to the voids, particularly along GBs where the voids are situated. As a result, the voids are more likely to become sites for cracks to initiate and propagate, increasing the likelihood of component failure. Although these components were not designed to be armour materials, they were manufactured using standard W manufacturing processes for fusion components so voids could feasibly be observed in a future reactor such as ITER. Particularly considering the larger scale of ITER and the higher particle and heat loads that will be incident on its divertor components. Hence, it is crucial to understand the underlying mechanisms that lead to the formation of voids in W components especially since it was suspected that He was not involved. The two remaining hypotheses stem from impurity boiling and the saturation of D which are discussed in more detail in Section 5.8.

5.7 The Micromechanical Response of the JET Langmuir Probes

The significant grain growth shown in Fig. 5.10 (c) is typically accompanied by the removal of defects and a reduction in mechanical strength. It can potentially alter ductile-to-brittle transition temperature, surface roughness and power handling capabilities which have all been engineered to withstand specific conditions in the vessel [256]. Furthermore, the presence of trapped D could cause embrittlement which can lead to early component failure, particularly under cyclical loading. All Langmuir probe samples were indented with a Berkovich tip and the results were compared to the as-received data to discern how exposure to D plasma affects material hardness and elastic modulus.

Table 5.3: A comparison of the fluence, hardness and modulus values between the as-received Langmuir probe and probes 6, 8 and 26. The fluence values were calculated from the pulses with available data which included 59.7% of pulses for probe 26, 93.5% of pulses for probe 6 and 93.9% of pulses for probe 8.

iMicro				**Hardness (GPa)**		**Modulus (GPa)**	
Probe	Fluence (D/m^2)	Indented Region	Number of Indents	Mean	SD	Mean	SD
As-Received	N/A	Coarse Grains	19	**5.6**	0.1	**430**	10
26	1.3×10^{24}	RX (Site 1)	25	**5.8**	0.1	**450**	10
6	4.0×10^{24}	RX (Site 1)	19	**5.5**	0.1	**420**	10
		RX (Site 2)	16	**5.6**	0.1	**400**	10
		Coarse Grains (Site 3)	25	**5.7**	0.1	**430**	10
		Coarse Grains (Site 4)	46	**6.0**	0.2	**430**	10
8	2.8×10^{24}	Coarse Grains (Site 1)	34	**5.6**	0.2	**430**	10

The nanoindentation data is summarised in Table 5.3 and also shows the fluence incident on the Langmuir probes. The fluence data shows that the total number of incident particles increased between probe 26, probe 8 and probe 6 respectively. At the same time, the microstructural analysis in section 5.6.1 showed that surface temperatures increased between probe 8, probe 6 and probe 26 respectively. An initial comparison between the as-received Langmuir probe and probe 8, the sample that did not recrystallise in the reactor, showed extremely similar values for both hardness and modulus without too much scatter in the data, highlighted by the standard deviations. Since the grain size stayed roughly the same the contribution from GB hardening and the Hall-Petch effect should be the same between the two samples. The fact that the mechanical properties were unchanged after removal from JET suggests that particle fluence was not large enough for probe 8 to introduce sufficient defects into the lattice. Moreover, the surface temperatures were not sufficient to cause recrystallisation which is accompanied by annealing and the removal of defects, meaning these defects should still be present during indentation.

Probe 26, the sample that fully recrystallised and displayed significant grain growth, showed an increase in hardness of 0.2 GPa. This is approximately the size of the combined standard deviation of 0.2 GPa, calculated as the sum of the standard deviations of the mean values, suggesting that this could be a statistically significant increase. The modulus value also increased from the as-received sample by 20 GPa which was approximately the size of the combined standard deviation of 20 GPa. This appears to confirm that the mechanical properties were modified by exposure. An increase in grain size is typically associated with a decrease in sample hardness due to fewer boundaries which act as barriers to dislocation motion, making the sample easier to deform. The fact that both the hardness and modulus increased suggests that Hall-Petch was not the dominant mechanism. The increase in hardness can be explained by two potential mechanisms. The first mechanism involves the generation of vacancies and interstitials when incident ions displace W atoms in the lattice, these defects can cluster and impede dislocation motion. The incident particles are predominately D, and in the second mechanism this D becomes trapped, occupying interstitial sites and forming complexes with vacancies which causes embrittlement and an increase in hardness. Both mechanisms rely on defects forming after the recovery stage of recrystallisation which appears to contradict the fluence data.

Probe 8 was reportedly exposed to more incident particles than probe 26. Without recrystallisation, a significantly greater number of defects should be retained in probe 8 than in probe 26. The mechanical properties of probe 8 appear unchanged compared to the as-received probe while there was a significant increase in hardness in probe 26. Moreover, the heat loads on the divertor tiles are expected to scale with particle loads as both are influenced by the same energy transport processes and plasma-wall interactions. However, many factors could affect this correlation, including variations in energy per particle at constant flux, radiative cooling from impurities in the plasma, the shape and position of the magnetic field lines, plasma density and temperature gradient. Additionally, only 59.7% of the fluence data was available for probe 26, which could be attributed to the melting and warping of the probe tip. The fluence for probe 26 was likely higher than probe 8, as the melting observed in probe 26 suggests it was exposed to greater heat and particle loads. Overall, the microstructure and mechanical properties of the Langmuir probes suggest that the relative magnitudes of the calculated fluence may not be accurate enough to use as part of the analysis in this section.

Probe 6 had the most complex microstructure of the three exposed probes as the grain size increased in the hottest region of the tip and remained unchanged throughout the rest of the sample. The most significant change in hardness was found at site 4 which was next to the exposed surface where recrystallisation and therefore defect recovery had not occurred. There was an increase in hardness of 0.4 GPa with a combined standard deviation of 0.3 GPa at site 4 while the modulus appeared to be unchanged. The observed hardening can either be attributed to displacement damage or trapped D since site 4 was almost certainly affected by incident D^+ ions from the plasma. Site 3 was positioned on the other side of probe 6 to the exposed surface, where the grain size was still unchanged. The modulus in this region was approximately the same as the as-received probe and was therefore unchanged. The difference in hardness was 0.1 GPa with a combined standard deviation of 0.2 GPa, suggesting that the hardness in this region did not significantly differ from the as-received material.

Sites 1 and 2 were near the exposed surface but both hardness values were collected from the recrystallised region of the tip. The differences in hardness for these two sites compared to the as-received probe were well below one standard deviation so the hardness in the recrystallised region was essentially the same as the as-received probe. The defects that were originally present at sites 1 and 2 were believed to have annealed out during recrystallisation, meaning the mechanical properties recovered to how they were in the as-received state. The modulus value at site 1 was extremely close to the as-received probe while the value at site 2 appeared slightly lower than expected likely due to an inaccurate frame stiffness correction. Sites 1 and 2 were located in two neighbouring, recrystallised $\langle 101 \rangle$ grains, meaning the mechanical properties should essentially be the same from these two regions. The fact that the modulus was also unchanged at site 4 where the hardness was significantly altered, shows that there was no difference in modulus across the whole of probe 6.

In summary, initial comparisons between the as-received Langmuir probe and probe 8 indicated no significant changes in hardness or modulus, suggesting that particle fluence and surface temperatures were insufficient for recrystallisation or defect formation. Conversely, probe 26 fully recrystallised and showed a significant increase in hardness, despite an increase in grain size which is typically associated with Hall-Petch softening. Probe 6 exhibited significant hardening at site 4 which would have been subjected to a substantial fluence of D^+ ions with insufficient temperatures to cause recrystallisation, while other sites showed minimal changes. The observed increases in hardness in probes 6 and 26 were likely associated with the number of incident D^+ ions on the samples. Ion beam analysis (IBA) was carried out in the following section to determine whether the mechanical properties were augmented by displacement damage or trapped D.

5.8 Deuterium Retention in JET Langmuir Probes

The Microprobe data from a previous study is summarised in Fig. 5.12 [228] and the new results are shown in Fig. 5.13 with the reference sample in (a) showing how the NRA signal should look if D is detected. Fig. 5.13 (b) and (c) show three maps for both probe 26 and probe 8, respectively. No D was detected in these maps so probe 6 was not analysed using the Microprobe. Instead, all three probes were placed in the main NRA chamber, one after the other, where the larger beam sizes could ascertain if there was truly any D present. These results also came back negative which ruled out the possibility of D occupying interstitial sites or forming complexes with vacancies. Ultimately, there were no D atoms still retained in the probes that were responsible for causing the increase in hardness. The earlier Microprobe results from the exposed surfaces in Fig. 5.12, showed that some D had been retained after the initial removal of the probes from the vessel. The D had likely been removed due to H-D isotope exchange reactions when the sample was in contact with flowing water during cutting and polishing. The fact that D had previously been present in probe 26 appears to confirm that D bubbles could have seeded the void formation.

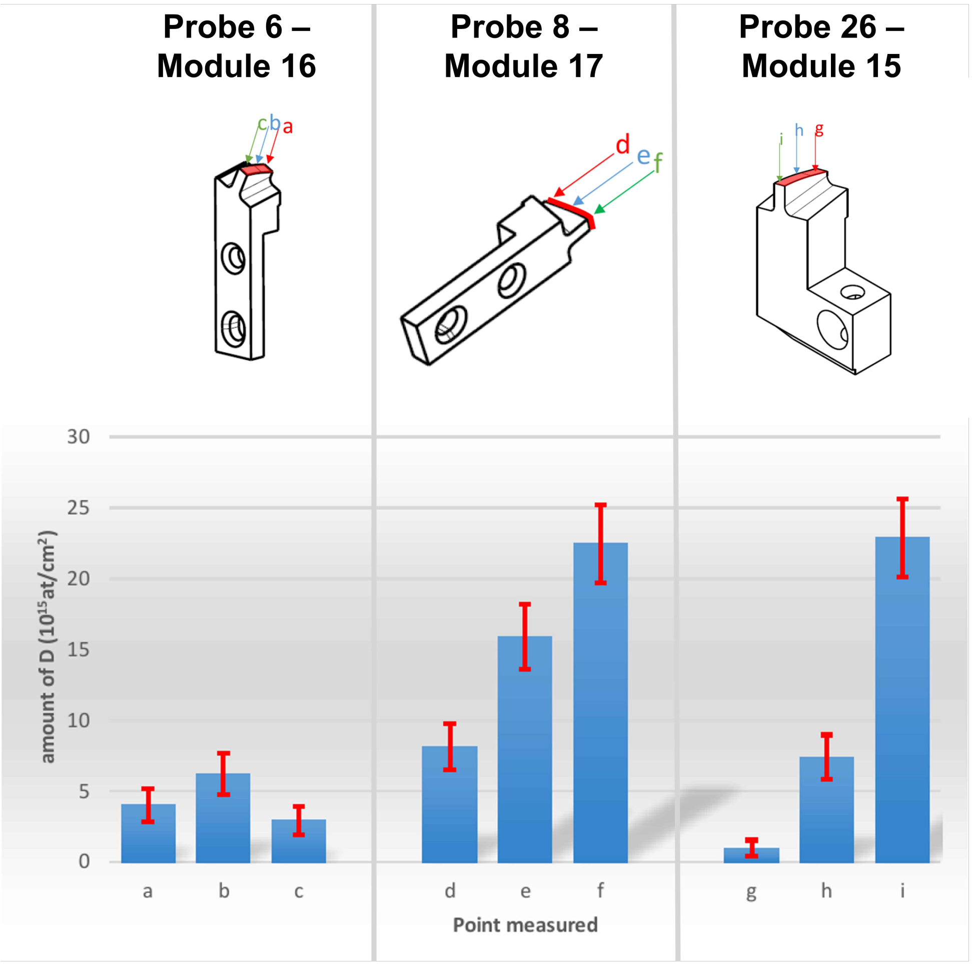

Figure 5.12: Previous results of the Microprobe experiment as IST, Lisbon on D retention at the exposed surface of Langmuir probes 6, 8 and 26, diagrams provided by N. Catarino [228].

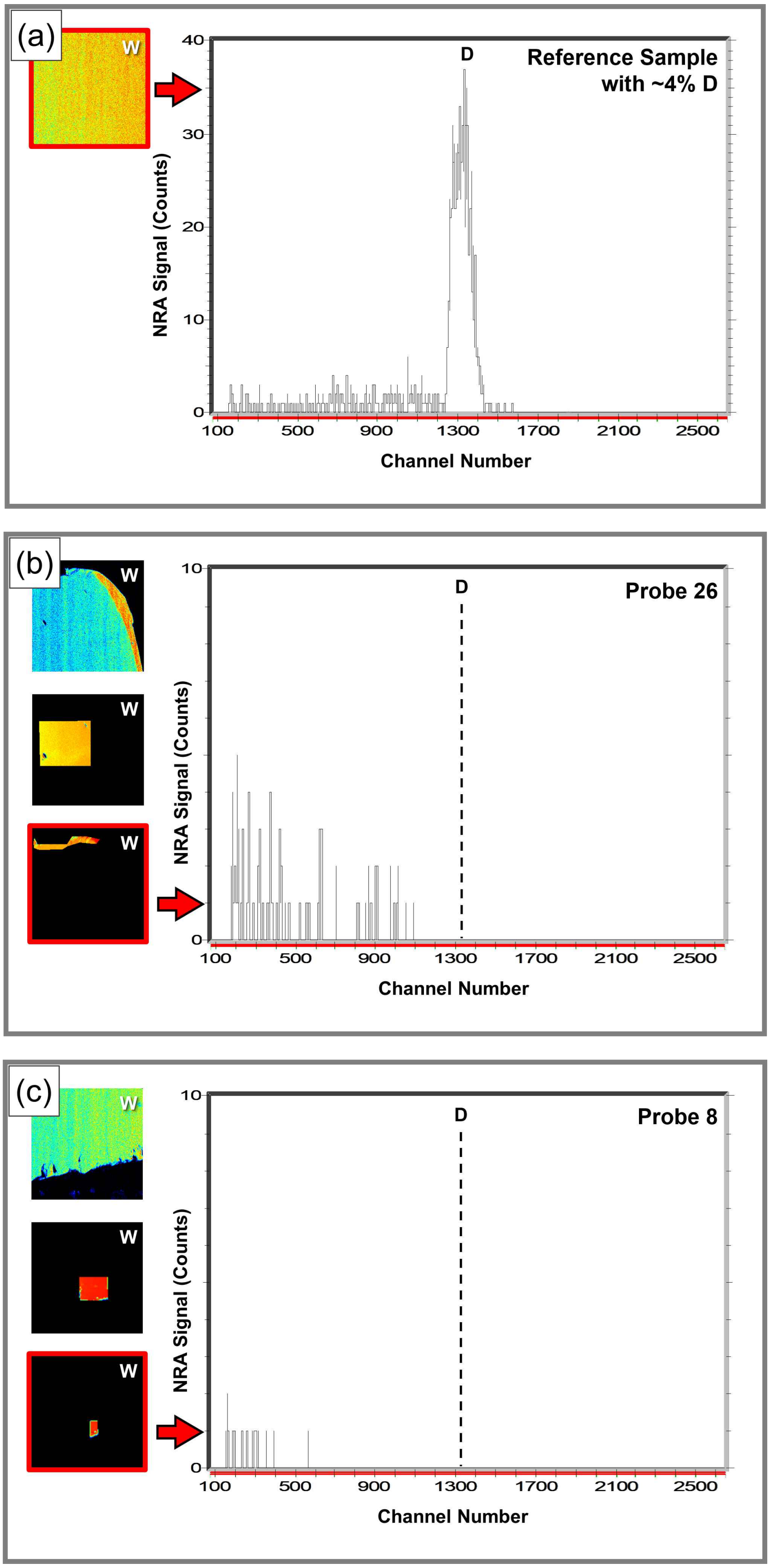

Figure 5.13: (a) A microbeam map from a ∼4% D reference Sample showing the standard D peak in the NRA signal (b) Three microbeam maps from probe 26 and (c) Three microbeam maps from probe 8 with an absence of a D peak.

5.9 Spherical Nanoindentation of Langmuir Probe 26 from Tile 6

Since retained D was not responsible for increasing the hardness of the probes, it was assumed that some sort of displacement damage was the underlying cause. In this mechanism, the incident D^+ ions would have enough energy to generate vacancies and interstitials which could go on to cluster and impede dislocation motion. Spherical nanoindentation was performed on probe 26 and the as-received probe to try and build a clearer picture of how these defects were affecting mechanical properties. The technique was selected because the spherical indenter tip produces an evolving stress state, providing a fast, non-destructive method for obtaining stress-strain curves. The spherical indents were all placed in ⟨101⟩ grains in the as-received Langmuir probe and the ⟨101⟩ grain at site 2 of probe 26 in Fig. 5.10 (c). The symmetry of the spherical indenter tip and the consistent crystal orientations should counteract the effects of any radiation-induced anisotropy that might have arisen. Berkovich indents were also placed at site 2 of probe 26, combined with the previous as-received indentation data to contextualise the results from the spherical tip.

Table 5.4: A table showing the mechanical properties of the as-received Langmuir probe and the ⟨101⟩ grain in probe 26 collected using a Berkovich tip and the Keysight G200 Nanoindenter.

G200			**Hardness (GPa)**		**Modulus (GPa)**	
Probe	Indented Region	Number of Indents	Mean	SD	Mean	SD
As-Received	Coarse Grains	15	**5.3**	0.1	**390**	10
26	RX (Site 2)	35	**5.7**	0.1	**410**	20

The ⟨101⟩ grain at site 2 of probe 26 showed an increase in hardness of 0.4 GPa from the as-received (an increase of ∼8%) while the ⟨111⟩ grain at site 1 showed an increase of 0.20 GPa. The slightly larger hardness value from site 2 was believed to be due to increased cascade damage caused by a greater particle flux since the grain was located next to the exposed surface. This was compared to site 1 which did not neighbour the exposed surface and was on the opposite side of site 2. However, a study by C. Yin *et al.* [257] found that anisotropy was responsible for a scatter of ∼8% in their hardness data after W samples were exposed to large fluences of 1 MeV neutrons. The types of defects and resulting damage profiles in W are expected to differ between neutron irradiation and D plasma exposure due to the distinct mechanisms involved. However, some hardening mechanisms, such as defect pinning and dislocation interactions, may share similarities. Perhaps anisotropy has more of an influence than anticipated, although its effects are minimised in the spherical indentation data. If radiation-induced anisotropy had been the focus of the project it would have been interesting to perform more indentation experiments looking at its effect on hardness compared to the distance from the exposed surface. This type of analysis could also involve SRIM-style calculations to estimate the damage profile in the sample.

A difference of 0.4 GPa is approximately the same increase in hardness that was measured in the coarse grains at site 4 of probe 6 and appears to be the maximum increase in hardness of all the samples that were exposed in JET during the ILW campaigns. A study by M. Spychalski *et al.* [109] also attempted to indent Langmuir probes from tile 3 and tile 6 and reported tip softening of 3.3 GPa in the tile 3 probe which they attributed to recrystallisation. However, these probes were indented on the unpolished component to quite shallow depths, invalidating any comparison with the probes analysed in this thesis. Surface roughness and deposition from plasma-surface interactions and residual plastic deformation from component machining would modify the hardness values compared to a sample that had been polished.

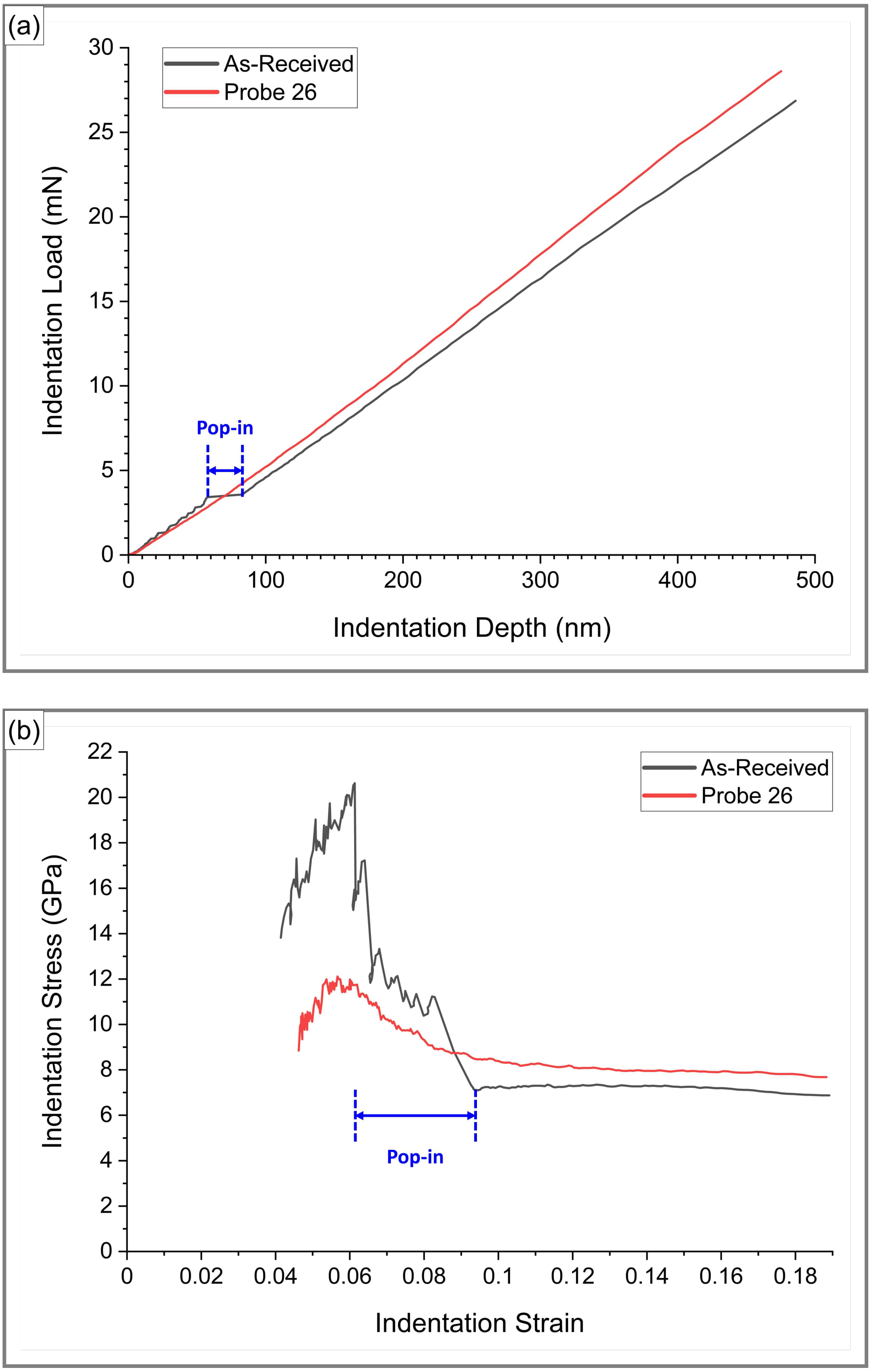

Figure 5.14: (a) Load-depth curves and (b) Stress-strain curves obtained from two spherical indents, test 21 on the as-received sample and test 2 on probe 26 with the effects of a pop-in highlighted in blue.

An overview of the spherical indentation results is presented in Fig. 5.14 where two individual indents, test 21 in the as-received Langmuir probe and test 2 in probe 26, were selected to represent the trends in the data. The stress-strain curves for all the indents for the as-received Langmuir probe and probe 26 can be seen in APPENDIX A. In theory, the stress-strain curves can be used to derive quantities such as the elastic modulus, yield strength and strain-hardening exponent. These quantities were not calculated for a few reasons. There was a large amount of scatter in the data at low indentation depths due to the small contact area. Any effects from surface roughness or deviations from the ideal spherical tip shape would be greatly exaggerated at these depths. It is also hard to detect the exact point of initial contact with a rounded tip compared to a sharp Berkovich tip. While calibration errors and experimental noise become more significant at small loads and displacements. A large proportion of the elastic region was therefore unusable and the elastic modulus could not be calculated reliably. Additionally, the elastic modulus is typically required in the calculation of the yield strength and the presence of large pop-ins visually obscured the yield point in the stress-strain curves of the as-received sample.

Another limitation originated from the complex exposure conditions of the samples which included varying gas compositions, particle energies and fluxes. This is highlighted in the discrepancy between the calculated fluence values and the observed microstructures for the probes in Section 5.7. The observed changes in mechanical properties were attributed to residual cascade damage caused by exposure in the ILW campaigns. However, the exact nature of the damage such as the proportion of vacancies and interstitials to defect clusters and dislocation loops, can alter the stress-strain response of the sample. For example, a high concentration of vacancies may lead to lower yield strengths and elastic modulus while lowering resistance to plastic deformation [258]. Conversely, a high concentration of dislocation loops could result in higher yield strengths and greater strain hardening [259]. The stress-strain curve integrates all of these effects which can be difficult to deconvolute without precise knowledge of the defect populations. Valuable insights could have been gained through an extensive high-resolution TEM study, involving the preparation of multiple TEM samples from each probe, but this was not feasible due to time constraints.

The first key observation from the stress-strain curves in Fig. 5.14 (b) can be seen between 0.1 and 0.18 indentation strain. At a given strain the stress values in this region are consistently higher for probe 26 than the as-received probe and so exposure in JET has increased resistance to deformation in the probes. The average stress values in this range are 8.0 GPa for probe 26 and 7.2 GPa for the as-received probe with a total difference of 0.8 GPa. This resistance to deformation post-irradiation can also be seen in the Berkovich indentation data in Table 5.4 from the same area of the sample. The difference in hardness of 0.4 GPa was likely caused by the same microstructural features. Irradiation-induced hardening likely stems from cascade damage in the probe where the collision of high energy particles with atoms in the lattice produces significant quantities of atomic displacements namely, interstitials and vacancies. These point defects then act as nucleation sites for dislocations, forming dislocation loops and networks. Point defects, dislocation loops and defect clusters can act as obstacles to dislocation motion, pinning them which increases the stress required to overcome the the obstacle.

Most metals also exhibit strain hardening, as plastic deformation continues there is an increase in dislocation density. Dislocations start to entangle, creating internal stress fields which oppose the applied stress. Greater applied stress is therefore required to increase the mobility of the dislocations. As a result, the gradient of the stress-strain curve increases beyond the point of ultimate tensile strength (UTS). Conversely, W has previously been shown to have a relatively low strain hardening exponent at room temperature [260][261] which can be seen between 0.1 and 0.15 in Fig. 5.14 (b). The low strain hardening exponent of W is primarily due to the BCC crystal structure [262]. In this structure, dislocation motion is predominantly hindered by the Peierls stress, which must be overcome for a dislocation to move across the glide plane. The Peierls stress remains largely unaffected by strain and dislocation density, thereby limiting the buildup of strain hardening. At room temperature, the relatively low level of thermal energy restricts dislocation activity and dynamic recovery mechanisms, further contributing to the subdued strain hardening behaviour observed in W. The stress-strain curves appear to curve down slightly between 0.15 and 0.18, this lowering in stress is most likely due to the tip deviating marginally from the assumed spherical shape at large displacements, which is where the usable spherical geometry of the tip starts to turn conical [187].

The second key observation is the presence of pop-ins in the as-received probe which were consistent for all indents performed in this sample, highlighted in blue in Fig. 5.14 (a) and (b). A pop-in is a sudden increase in indentation depth and strain during which the applied load remains relatively constant [263]. They occur when the elastic contact stress reaches a critical value required to nucleate dislocations within the plastic zone. Once the dislocations have been nucleated, the contact stress drops to the flow stress required to propagate the dislocations, facilitating further plastic deformation. The presence of pop-ins in the as-received probe indicates that the material within the plastic zone is initially defect-free, and higher stress is required to initiate plasticity in this sample.

Conversely, the absence of pop-ins in probe 26 suggests the presence of a high density of pre-existing defects within the plastic zone, likely resulting from cascade damage caused by incident D^+ ions. Defects such as vacancies, interstitials, clusters, and dislocation loops create localised stress fields that lower the energy barrier for dislocation nucleation. As a result, dislocations were nucleated more gradually without a sudden release of stress. Additionally, any immobile dislocations present before indentation would negate the need for new dislocations to be nucleated at the onset of plastic deformation, causing the contact stress to approximately equal the flow stress required to propagate dislocations.

5.10 Conclusions

Four lamellae were removed from the JET divertor including: C4 – ILW-3, C12 – ILW-1 & 3, C13 – ILW-3 and D12 – ILW-3. EBSD mapping indicated no detectable change in grain size in the exposed lamellae compared to the as-received sample. The surface temperatures of the lamellae were estimated using IR cameras and showed that each sample only exceeded 1000 °C for a few seconds, which was not high enough to cause recrystallisation, see Fig. 5.6 and Fig. 5.7. The plasma control system in JET was therefore successful at maintaining tile 5 surface temperatures and protecting the lamellae from high heat loads. Nanoindentation also showed minimal variance in mechanical properties post-exposure, implying no significant changes in hardness or modulus across the lamellae. The exposure period and location of the lamellae across tile 5 did not appear to have an effect and the microstructures of the exposed lamellae were essentially identical to that of the as-received sample. However, this is not always the case, as under different conditions, lamella C23 was found to develop deeper surface cracks after ILW-1 [10].

Three Langmuir probes, probes 6 and 8 from tile 3 and probe 26 from tile 6 had been exposed to D plasma in JET during ILW-1 & -2 and were then studied for changes in microstructure and mechanical properties, see Figs. 5.8–5.10. Probe 8 was the least damaged, showing a similar grain size and distribution to the as-received Langmuir probe. However, the EDM-induced surface cracks appeared wider and propagated a maximum of 20 times further into the bulk than the as-received sample. This indicates that thermal stresses were still significant even below recrystallisation temperatures. Probes 6 and 26 exhibited varying degrees of recrystallisation, suggesting higher exposure temperatures than probe 8. Probe 26 showed extensive grain growth and melt damage due to sustained high heat loads. Void formation also occurred near GBs in probe 26 which was attributed to bubbles of D gas in the molten parts of the component. The formation of He bubbles was ruled out due to the composition of gases pumped into the vessel.

Initial comparisons between the as-received Langmuir probe and probe 8 in Table 5.3 indicated no significant changes in hardness or modulus, suggesting insufficient particle fluence to cause defect formation. Probe 26 was fully recrystallised and exhibited an increase in hardness of 0.4 GPa, in contrast to the expected Hall-Petch softening. Subsequent IBA showed that any retained D had been removed after the initial Microprobe experiments on the exposed surfaces of the Langmuir probes, most likely due to sample preparation. D retention was therefore ruled out as the cause of hardening which pointed instead to displacement damage. Probe 6 showed significant hardening of 0.4 GPa near the exposed surface, similarly attributed to the cascade damage caused by the substantial fluence of D^+ ions. Spherical nanoindentation on probe 26 in Fig. 5.14 confirmed these findings, showing the suppression of pop-ins and increased resistance to deformation after exposure due to cascade damage.

The levels of heat exposure and damage, shown by the exposed Langmuir probes in the EBSD and hardness data, did not directly line up with the fluence values which called into question the validity of the fluence calculations. The main sources of error, particularly for probe 26, appeared to stem from a significant proportion of pulses that were missing data and from changes to the surface area of the tip, which was assumed to be constant in the calculations. This highlights the need for more robust diagnostic data collection and analysis methods, which can lead to more accurate predictions of material behaviour in future fusion devices. The fluence values were not needed to contextualise the nanoindentation data across the four lamellae. However, they were not reliable enough to compare to the hardness values of the three Langmuir probes. Ultimately, the strike point time, which is shown in Fig. 5.15, can be a good indicator of heat and particle loading.

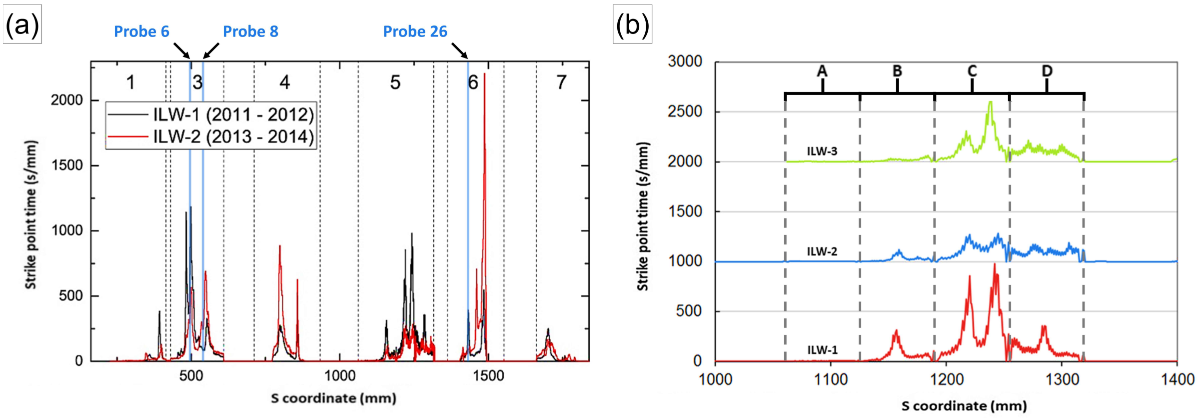

Figure 5.15: (a) The inner and outer strike point location on divertor tiles 1-7 during ILW-1 and -2 and the position of probes 6, 8 and 26 [18] (b) the outer strike point location on stacks A-D of tile 5 during ILW-1, -2 and -3 with each campaign offset on the Y-axis [10].

The strike point position suggests that particle loading on tile 3 near probes 6 and 8 was higher than on tile 6 near probe 26. However, the minimally damaged microstructures of probes 6 and 8 compared to probe 26 indicate that the inner strike point avoided prolonged contact with these probes. In contrast, the outer strike point likely remained in direct contact with probe 26 for a significant duration. The outer strike point position in Fig. 5.15 (b) also shows that the particle loading on the stack C lamellae during ILW-3 (only lamella C12 was exposed for ILW-1 & 3) was quite similar to that of tile 6 at the location of probe 26 during ILW-1 & -2. The significant hardening of probe 26 compared to the unchanged mechanical properties of the lamellae is most likely due to the probe tip protruding deeper into the plasma than the surface of the lamellae.

The starting microstructure of the components could also have a significant effect. The lamellae had a more typical rolled structure with the majority of the sample containing fine grains around 2 μm in diameter. Conversely, the Langmuir probe had some fine-grained regions but contained mostly coarser 30 μm grains. The lamellae would therefore contain a far greater density of GBs which act as sinks for the point defects generated by cascade damage. GBs can also dissipate the energy of dislocations, even promoting their recombination and annihilation, so a high number of GBs reduces the accumulation of dislocation networks which typically form during hardening. Moreover, a significant amount of strain hardening may have already occurred in the rolled lamellae microstructure, causing additional hardening from cascade damage to be less pronounced.

The fine grains may also be responsible for the thermal stability of the lamellae in contrast to probe 26 which suffered significant recrystallisation and grain growth. Smaller grains have higher energy barriers for nucleation and growth which slows down the recrystallisation process. If there is also a high number of dislocations already present then they are more likely to annihilate or rearrange at high temperatures than form new grains which reduces the overall driving force behind recrystallisation. However, the IR camera data suggest that the lamellae were not in the recrystallisation temperature range for a significant amount of time which may have ultimately been the reason for their apparent thermal stability. Unfortunately, the IR cameras were not directed towards the Langmuir probes that were investigated so their exact exposure conditions remain unknown.

These findings provide insights into the effects of microstructural design when developing W components for the divertor. The rolled and fine-grained structure of the lamellae appeared to be stable under thermal loading in the JET divertor and mitigated the effects of cascade damage without a significant change in mechanical properties. Conversely, the Langmuir probes sustained significant hardening and grain growth which were potentially exacerbated by the coarser grain size. The Langmuir probes were directly inserted into the plasma for ILW-1 and -2. They, therefore, demonstrate what the upper limit of damage can look like for a W component in a tokamak that is operated with D. ILW-1 and -2 had an average input power of 2.2 and 2.9 MW [226], respectively, while ITER is predicted to have an auxiliary heating power of 50 MW [225]. Although the W monoblocks in the ITER design will not be inserted into the plasma in the same manner as a Langmuir probe, surface temperatures are far more likely to be in the range of recrystallisation for a significant period compared to the JET lamellae. If the ITER monoblocks experience substantial grain growth there will be fewer sinks for radiation-induced defects, the DBTT will start to increase and they are more likely to fail via brittle fracture.

Probes 6 and 26 showed a hardening of $\sim$0.4 GPa after ILW-1 and -2 while ITER is projected to generate an integrated target flux up to 40 times greater than that of JET [5]. The two ILW campaigns consisted of 26.38 hours of divertor operation while the first ITER divertor is predicted to withstand 2500 hours of operation [5][264], a factor of approximately 95 greater than the two JET campaigns. The total integrated divertor ion fluence for the first fusion power operation phase of ITER is estimated to be $\sim$(1.6–3.2) $\times$ 10^{31} ions [5]. From cascade damage alone hardening of the W components may become an issue for ITER without the effects of He bubble formation and neutron damage which are also anticipated. In a recent study, M. Lloyd *et al.* irradiated a pure W sample with neutrons at the High Flux Reactor at Petten, Netherlands to 1.67 dpa for over 2900 hours [265]. This resulted in transmutation to 1.3% Re and 0.1% Os and an increase in hardness of 2.7 GPa. This degree of hardening is typically accompanied by severe embrittlement which makes the component far more susceptible to failure via cracking, particularly from the extreme thermal stresses that are present in the fusion environment. Further investigation is required to effectively estimate component lifetimes in future fusion devices. This will ultimately be achieved when W samples from D-T campaigns become available and the unique microstructures can be studied. However, a clearer picture of what extensive divertor operation can do to W components is starting to come into focus with reactor-based experiments such as the neutron-irradiation study and this study on JET components.

Chapter 6

High-Resolution Characterisation of Deposits in the JET Divertor

6.1 Introduction

This chapter focuses on one bulk lamella that was removed from the third row of stack C after a total of 12.62 hours of divertor operation in ILW-1 [264], shown in Fig. 6.1. The machine was operated with mainly pure D fuel and some ^{1}H fuel while N, Ne and Ar were the only other elements to be injected into the vessel [23]. The outer strike point remained on tile 5 for the majority of ILW-1 [114][266] and it was confirmed by IBA that tile 5 was a region of net erosion during this campaign [113]. Contrary to this, the first three lamellae of each module are slightly lowered to prevent component melting. This shadowing resulted in the preservation of deposits on the plasma-facing surface of lamella C3.

Deposits form when atoms, droplets, or solid fragments in the plasma, are directed onto material surfaces in the machine. Many of the deposit structures examined in this chapter contained significant amounts of Be. These types of deposits could form in ITER if the design continues with the inclusion of a Be first wall [14][267][268]. Moreover, Be poses a significant safety risk through the inhalation of toxic material [13] so it is important to understand how and where it is stored within the vessel.

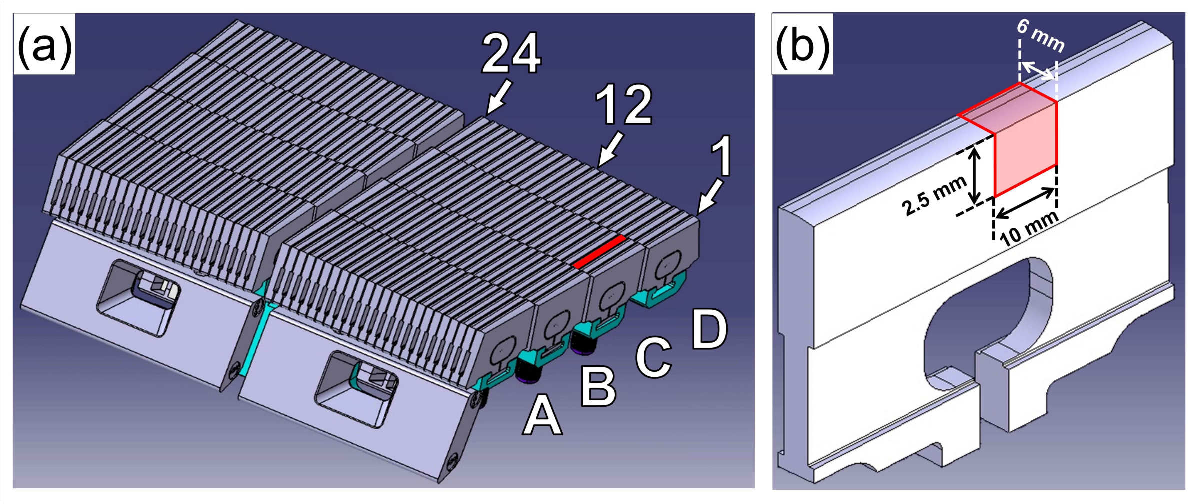

Figure 6.1: Schematic of (a) two tile 5 modules with lamella C3 highlighted in red (c) lamella C3 with the location of the studied sample highlighted in red.

Deposits are generally undesirable because they can form uneven layers of mixed materials that differ from the original surfaces in their physical properties. The weak adhesion of these deposits, combined with discrepancies in thermal expansion, can introduce additional impurity sources and lead to the continuous redistribution of material around the machine. Accumulated material may also form dust, which poses several risks, including plasma disruptions, interference with diagnostics and cooling systems, and increased retention of radioactive isotopes, all of which raise safety concerns.

There has been a range of studies on the composition of JET ILW deposits which have primarily used EDX and ion beam techniques [110–122]. These works have shown that the main types of deposition can be separated into mixed material layers (stratified deposits) that originate from the continual erosion of plasma-facing materials and metal droplets (mainly W, Ni and Be) that form during the melting of wall materials. The mixed material layers have also been shown to drive up T retention [126–128].

Be droplets, splashes and flakes likely come from Be components in the main chamber and Be-rich co-deposits that migrate around the divertor. W-rich droplets likely originated from the W-coated CFCs or Langmuir probes over the lamellae due to increased chances of melting. It is assumed that Ni-rich droplets were derived from Inconel components in the main chamber such as the tiles in the lower heat flux regions which contained a substrate of Inconel 625 and a 7-–9 μm thick Be coating [124]. Another source of Ni is the ion cyclotron resonance heating (ICRH) antennas where the central conductors and the antenna housing are both coated in Ni

[125].

This chapter investigates the structure of these deposits at the nanoscale, using high-resolution techniques such as TEM, TEM-EDX, EELS and TKD. Additionally, it examines how the various types of deposition interact with the microstructural features that were observed in the as-received lamella discussed in Chapter 4. Ultimately, these findings are evaluated concerning their impact on dust formation, a significant issue for the operation and maintenance of a device such as ITER.

6.2 Experimental Details

Lamella C3 was cut to a suitable size for characterisation, with dimensions of 2.5×6×10 mm. The sample was primarily imaged using a TESCAN Mira3 XMH SEM at 20 kV and a JEOL ARM 200F (S)TEM at 200 kV. All TEM samples and most FIB cross-sections in the bulk sample were prepared using an FEI Helios NanoLab FIB.

The length of lamella C3 was surveyed using six FIB cross-sections, examining the subsurface region for obvious changes in microstructure caused by plasma interaction. A TEM sample was produced from one of these cross-sections due to the formation of a layered structure on the surface and was studied using a JEOL Centurio high solid-angle EDX detector and a Gatan Quantum EELS detector.

Droplets of solidified material were observed on the surface of lamella C3, three of these droplets were cross-sectioned in the FIB and analysed by SEM with an Oxford Instruments X-Max 80 detector for EDX characterisation. For adequate statistics 48 spectra were taken from the region below the droplet and 30 spectra were taken from the droplet itself.

TEM samples were prepared from another four droplets, in addition to an area where the droplet had detached from the surface. They were analysed using STEM mode, EDX and EELS to correlate microstructural features with composition. One of these samples was also selected for TKD analysis using a Bruker Quantax EBSD system in a ZEISS Merlin FE-SEM.

To better understand the origin of some of these features a Tescan Amber X, Xe PFIB was used to perform tomography over the length of another droplet. A single crystal Si mask of dimensions 150×50×100 μm was applied on top of the droplet using the micromanipulator needle and was adhered with Pt to reduce ion beam-induced artefacts. A trench of 500×450 μm was milled at 100 nA to a depth of 200 μm which surrounded the droplet and reduced the amount of redeposited material that could interfere with the imaging. The droplet was then milled to a depth of 200 μm in successive slices of 30 nm for a total length of 100 μm, with a beam current of 30 nA and a voltage of 30 kV. A micrograph of 30×25 μm with a pixel size of 6 nm was collected for each of these slices at a voltage of 10 kV, beam current of 1 nA and a dwell time of 1 μs. The micrographs included a field of view larger than the area of interest to account for drift, the most representative images were cropped and are discussed in Section 6.5.2.

The microstructural features under the surface of lamella C3 were compared to the features that were characterised in the as-received lamella in Chapter 4. The code designed to process the IR camera data used in Chapter 5 was also used here to calculate the surface temperatures of lamella C3.

6.3 Surface Temperature and Microstructure

The IR camera data showed that the outer strike point was not close enough to the sample to produce temperatures above 400 °C for roughly 97.9% of ILW-1 pulses. The temperature distribution for the remaining 2.1% of pulses is shown in a histogram in Fig. 6.2, where the temperature data is separated into bins of 20 °C. Lamella C3 reached a maximum temperature of 1263 °C and spent a total of 2.4 s above 1100 °C, with only 0.1 s of that above 1200 °C. The sample therefore did not spend enough time in the temperature range for melting, recrystallisation or grain growth to occur [256][269].

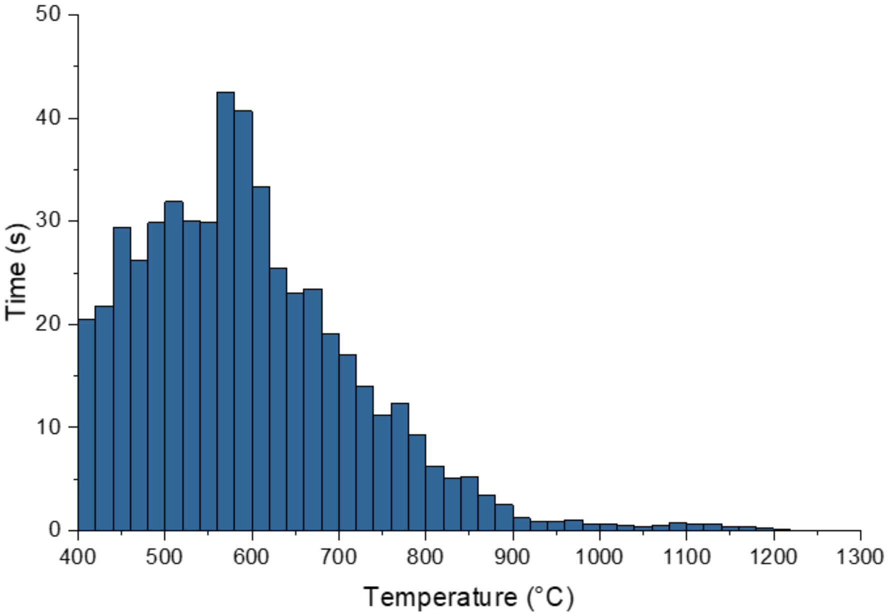

Figure 6.2: Histogram of the surface temperature distribution for lamella C3 during ILW-1 pulses that exceeded 400 °C.

Oxidation is more likely to be an issue at these temperatures since W can oxidise at 300 °C [99] with substantial rates above 600 °C [100]. After oxide formation, WO_3 starts to evaporate above 900 °C which could facilitate material loss from the surface [222]. The sample spent 302.7 s above 400 °C, 221.0 s above 600 °C. and 10.1 s above 900 °C. These timescales are unlikely to have caused a detectable amount of sublimation but may have produced enough WO_3 to significantly increase erosion of the exposed surface.

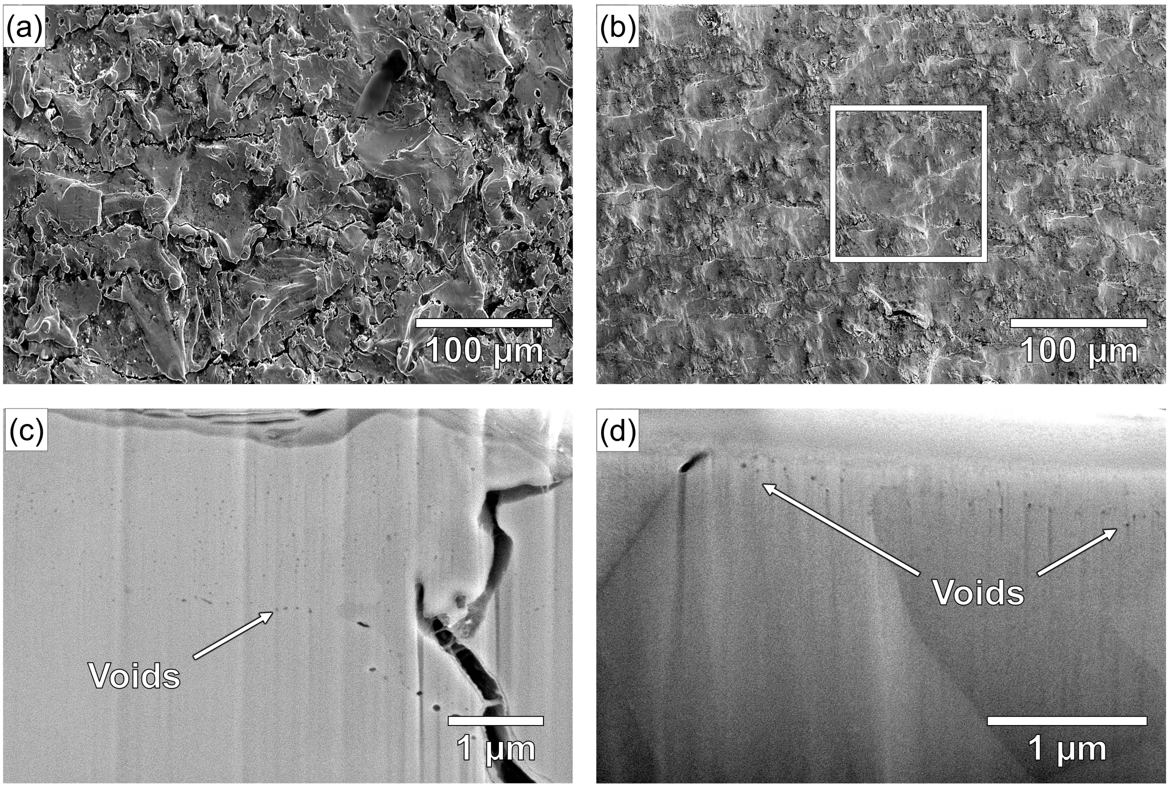

Figure 6.3: SE images showing the top EDM-ed surface of the (a) as-received lamella and (b) lamella C3 and a cross-sectional view of the voids in the (c) as-received lamella and (d) lamella C3.

Fig. 6.3 (a) shows the EDM-ed, plasma-facing surface of the as-received lamella and Fig. 6.3 (b) shows the same surface of lamella C3 after ILW-1. The surface appears smoother after exposure, with most peaks, valleys and particles no longer visible, particularly in the white box of Fig. 6.3 (b). A similar study also looking at lamellae from ILW-1 showed a 30% reduction in surface roughness and an increase in EDM crack length of 150 μm for lamella C23. These effects were attributed to higher power loads at that lamella position which caused increased erosion and melt formation [10]. The same study looked at lamellae A23 which was not exposed to the strike point and C14, both of which showed no changes in surface roughness. The lower temperatures shown in Fig. 6.2 highlight that the surface of lamella C3 did not melt during ILW-1. These lower temperatures indicate that if the plasma was responsible for smoothing the surface then the mechanism was more likely to be erosion than melt damage. Since lamella C3 was shadowed by the preceding module it is surprising that the surface appeared smoother and potentially could have been an artefact from cutting the sample which typically involves a water coolant. Despite this, the results from C3 are just a visual observation and no physical roughness measurements were taken. Fig. 6.3 (c) and (d) also confirm that the voids created by EDM, as studied in Chapter 4, were still present after exposure.

6.4 Stratified Deposits

Six FIB tranches were milled in the plasma-facing surface of lamella C3, sampling along the width of the lamella. Three of these trenches (see APPENDIX B) revealed a layered structure akin to the stratified deposits seen in other studies [18][110][111][118][119][121]. Fig. 6.4 shows one cross-section which was lifted out into a TEM sample so the structure of the layers could be studied with EDX and EELS.

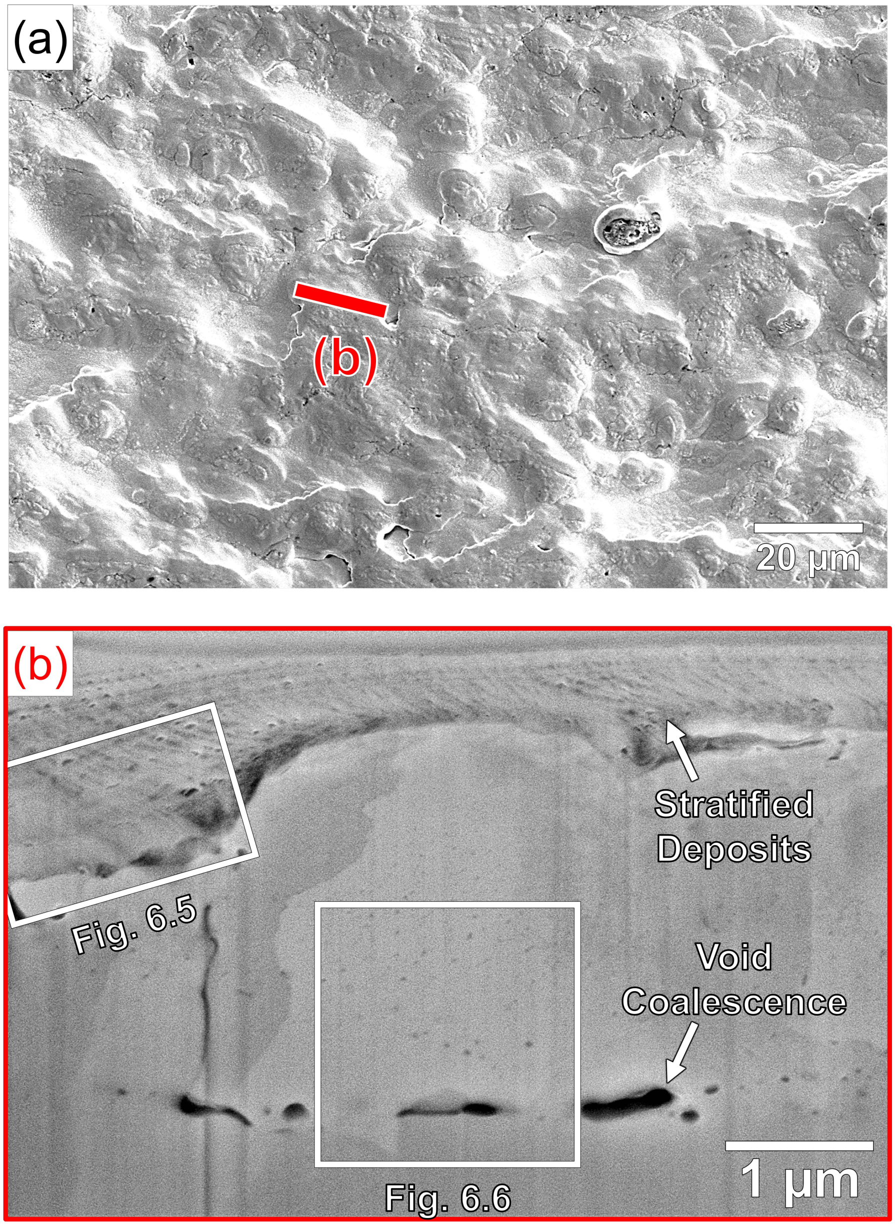

Figure 6.4: (a) SE image of the lamella surface showing the location of the FIB cross-section (b) SE image of the FIB cross-section showing the stratified co-deposits at the top, many voids have formed underneath these layers and have coalesced at a terminal depth from the surface.

The STEM HAADF image in Fig. 6.5 shows that the layered structure appears sponge-like with bright and dark regions. The EDX maps showed that the bright areas were mainly comprised of W, originating from other divertor components. There was also a single layer of Mo with a thickness of up to ∼50 nm, most likely from a single erosion event from a diagnostic in the main chamber. The darker regions in the STEM HAADF image were shown to contain O in the EDX maps.

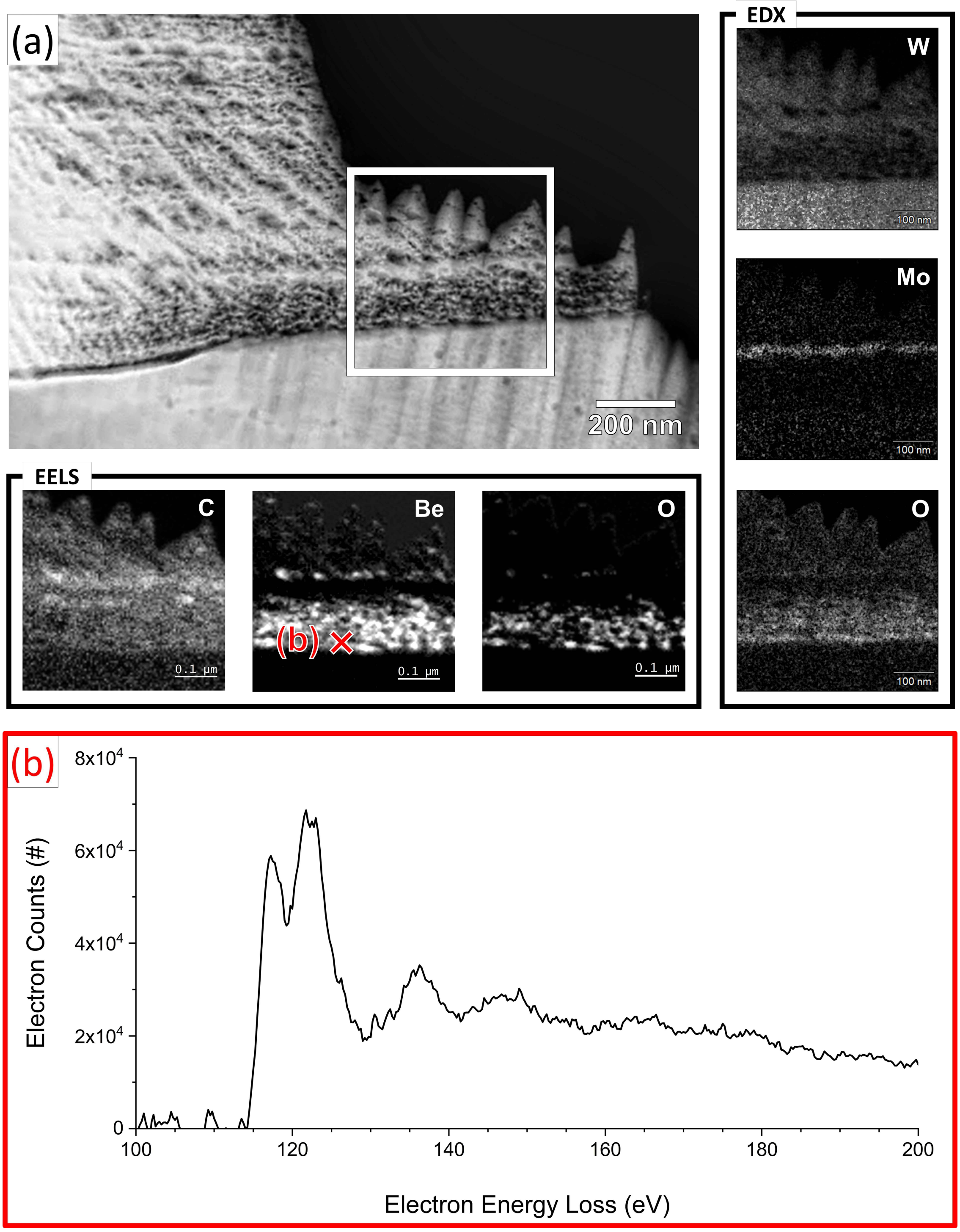

Figure 6.5: (a) STEM HAADF micrograph of deposited layers, EDX maps for W, Mo and O and EELS maps for C, Be and O (b) EELS spectrum showing the K-edge of BeO at 120 eV.

Five EELS maps were collected from the deposited layers across this TEM sample (see APPENDIX B) and the results from one such map are presented in Fig. 6.5 (a). The EELS data shows a correlation between the O K-edge at 532 eV [270] and the Be K-edge at 120 eV [271] in the dark regions of the layers. The fine structures of these Be peaks were missing an edge at 112 eV which is typical of metallic Be, as highlighted in Fig. 6.5 (b) and confirms the formation of BeO [272]. Be has most likely come from the tiles in the main chamber which are continually eroded by the plasma, the Be atoms then migrate downstream and are deposited onto the lamella surface by the magnetic field lines. It is possible for the O bound in BeO to have originated from exposure to the air after removal from the vessel. However, previous studies have shown that the ILW still operated with some O present at the plasma edge [24] and ion beam experiments showed similar depth profiles between Be and O [122]. These findings imply that O was either gettered by the Be or co-deposited during the operation of JET.

The EELS maps also revealed that the deposited layers contained significantly more C than the lamella underneath, with a prominent K-edge at 284 eV [169]. The sources of the C were likely the W-coated CFC tiles in the divertor which have been shown to flake off [121] or residual dust from the JET-C wall [122]. The fact that the distribution of C was not uniform throughout the EELS scan confirms that it originated from within JET and was not contaminated by the electron beam.

EDX analysis was also carried out on the voids underneath the deposited layers which showed O and a small C signal surrounding the larger cavities in Fig. 6.6. EELS was performed in this region to confirm that the O signal was not linked to BeO. There was no Be signal in any of the spectra and the O signal was therefore associated with the oxidation of W. This was likely caused by water vapour during the formation of the voids in EDM, as was shown for the as-received lamella in Chapter 4. However, TEM samples are prone to oxidation after thinning due to the high surface area-to-volume ratio and FIB damage has also been shown to exacerbate this effect [223]. Oxidation could have been localised at the edge of the cavity possibly because the sample was thinner in these regions [273]. The C EELS signal likely was not due to electron beam contamination, as it traced the edge of the cavity. The fact that C was seen at the same location as O suggests that the latter was present before sample preparation and was removing C impurities from the grain interiors as was proposed by J. Stephens [208].

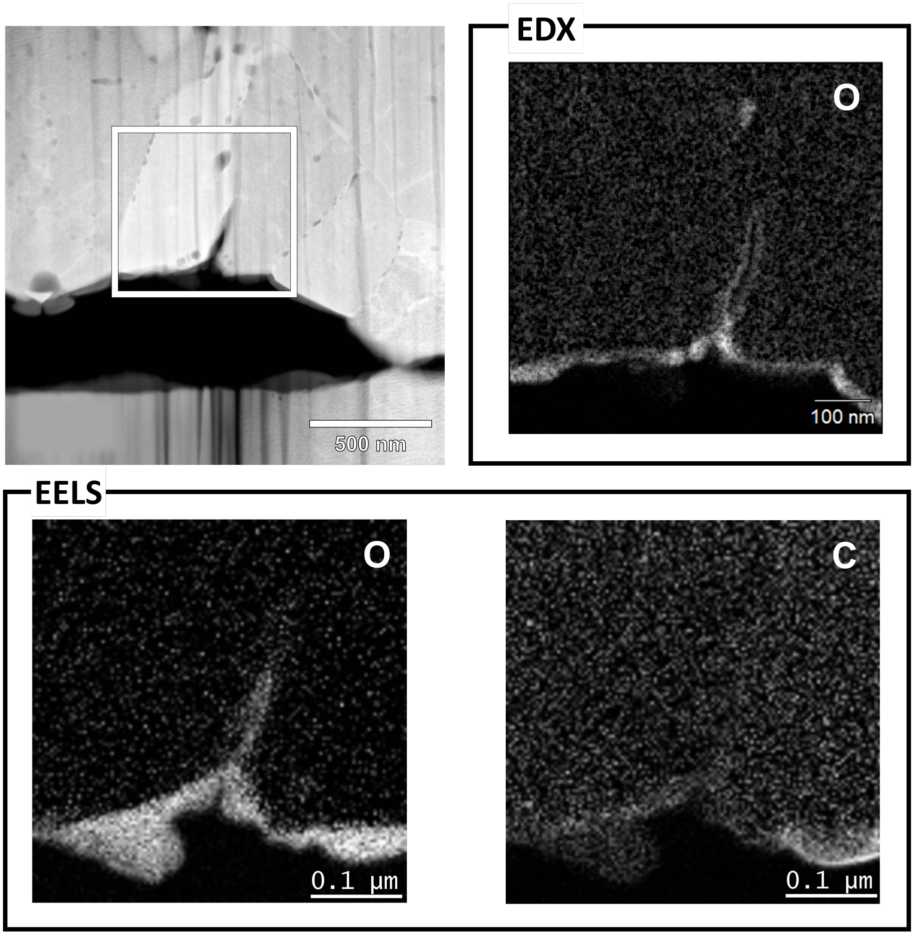

Figure 6.6: (a) STEM HAADF micrograph of voids underneath deposited layers, EDX map of O and EELS maps for O and C, with the mapped region highlighted in a white box.

6.5 Molten Droplets

6.5.1 Characterisation using SEM-EDX

The surface of lamella C3 is shown in Fig. 6.7 (a), with a large crack along the width of the sample. The crack extended only a few tens of microns into the surface in Fig. 6.7 (b), and since it could not be determined whether it formed during manufacturing, operation or sample preparation, it was not investigated further. The surface was also covered in 23 distinguishable droplets with an average length of 840 ± 110 μm, a maximum height and width of 65 μm and 72 μm respectively. These droplets all appeared to impact the surface at the same angle. This is likely due to material detaching from in-vessel components, melting and becoming charged in the plasma through collisions with high-energy electrons and ions. The Lorentz force then moves the droplets in a direction perpendicular to their velocity and the magnetic field lines. The droplet shape is governed by variables such as surface tension and solidification processes but the formation of a larger head with a smaller tail of material seems to be related to shear forces and adhesion in particular [274].

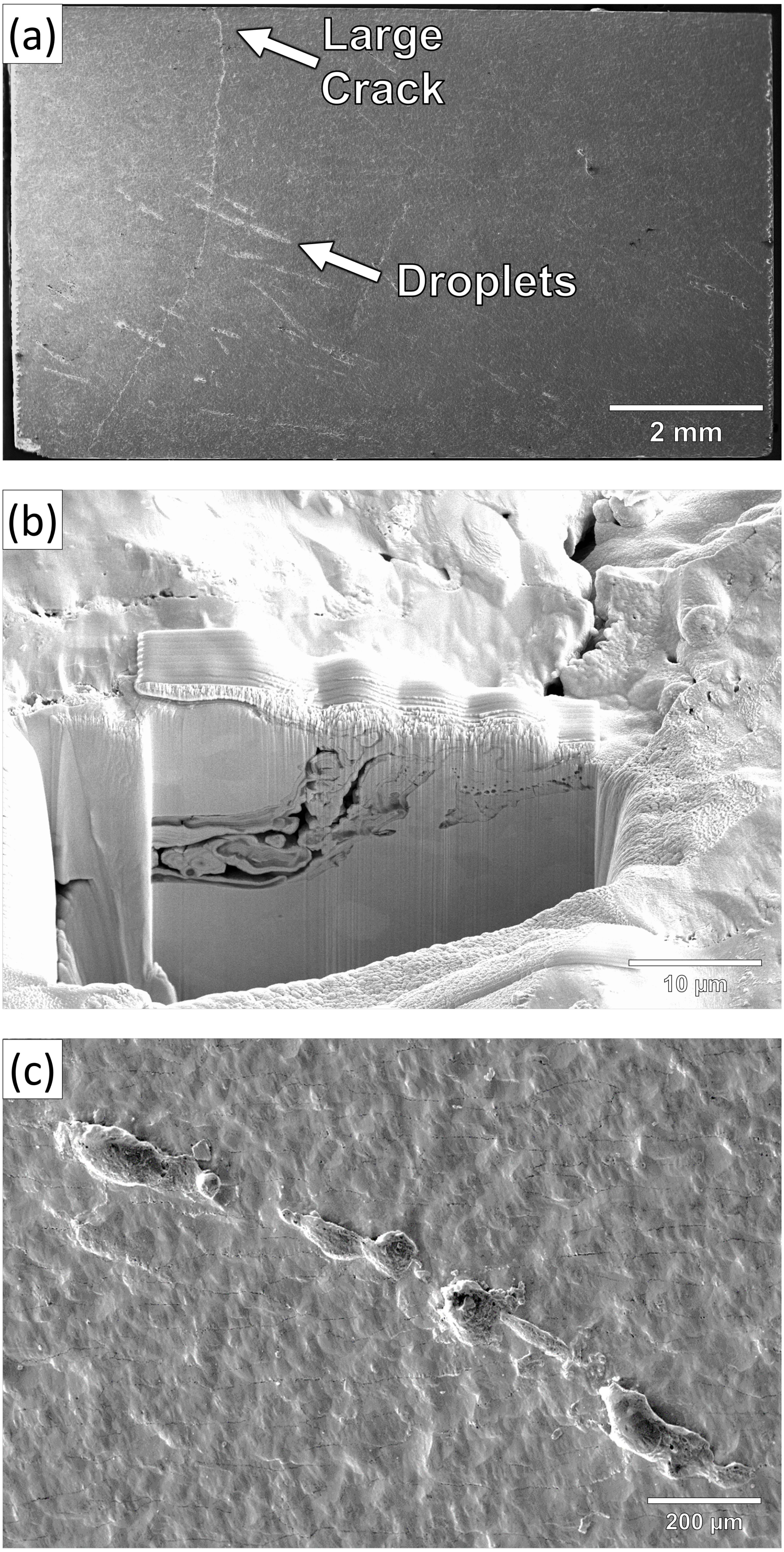

Figure 6.7: (a) SE image of the lamella C3 surface (b) FIB cross-section of the large crack (c) a typical W droplet.

Three droplets were cross-sectioned in the FIB and analysed using EDX. The spectra showed that the droplet primarily consisted of molten W. Langmuir probes are the most probable source since they protrude into the plasma itself, therefore experiencing the highest temperatures of all the W divertor material, as discussed in Chapter 5, and have been shown to crack and melt in the divertor [123]. These probes are also present in the main chamber but have only been shown to cause damage to neighbouring Be tiles. In general, the majority of eroded material from the main chamber is deposited on tile 0 (the High Field Gap Closure tile) and, to a lesser extent, on tile 1, making direct deposition on tile 5 unlikely [116]. Additionally, pieces of W that have delaminated from coated divertor tiles have previously been found in the outboard corner of the divertor and could therefore be another source of molten W [114][275].

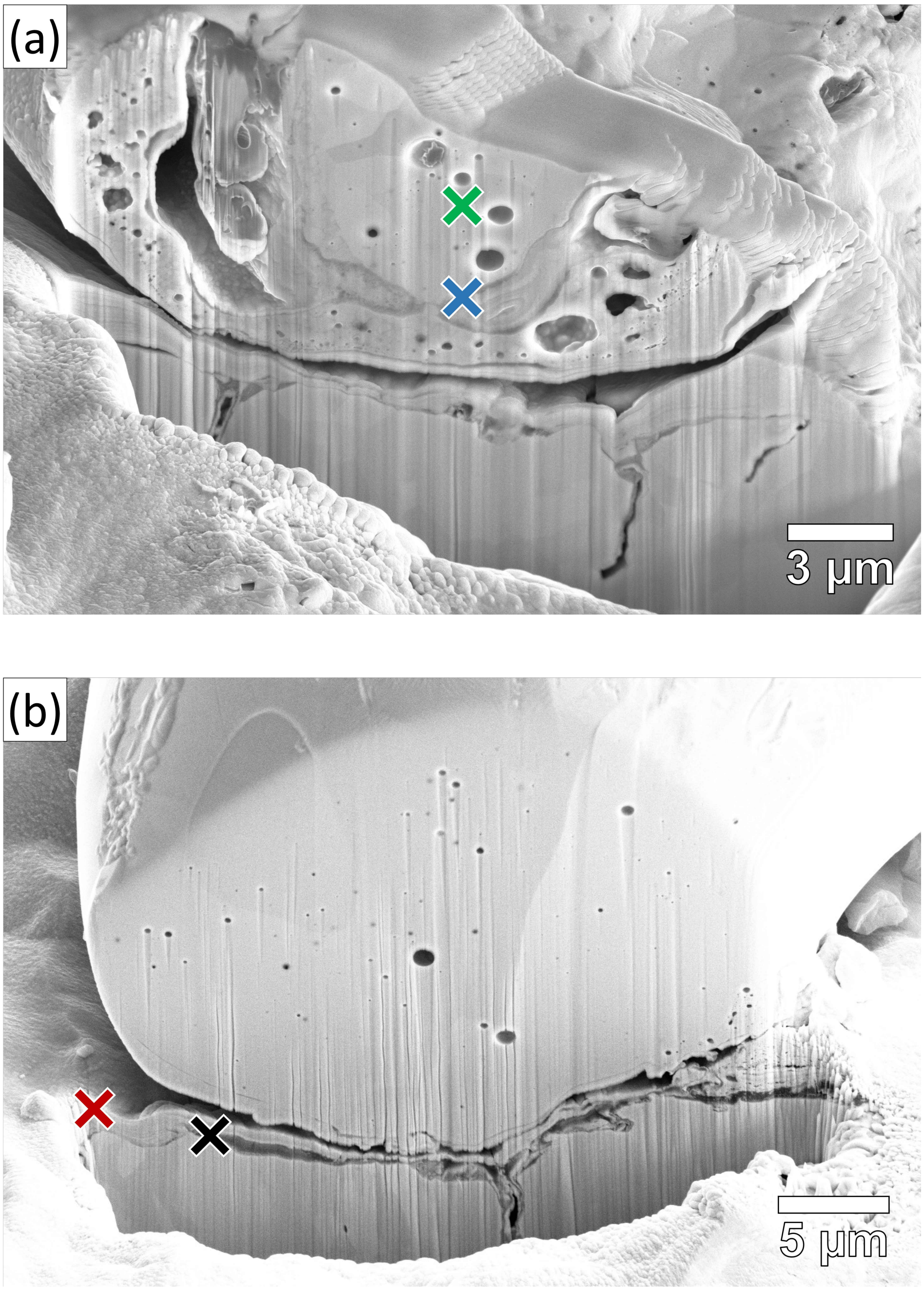

(a) SE micrographs from a droplet containing mixed material layers and (b) a droplet with mixed material layers underneath the surface

Figure 6.8: EDX Analysis of two W droplets in the SEM using a voltage of 10 kV with a spot size of 70 nm.

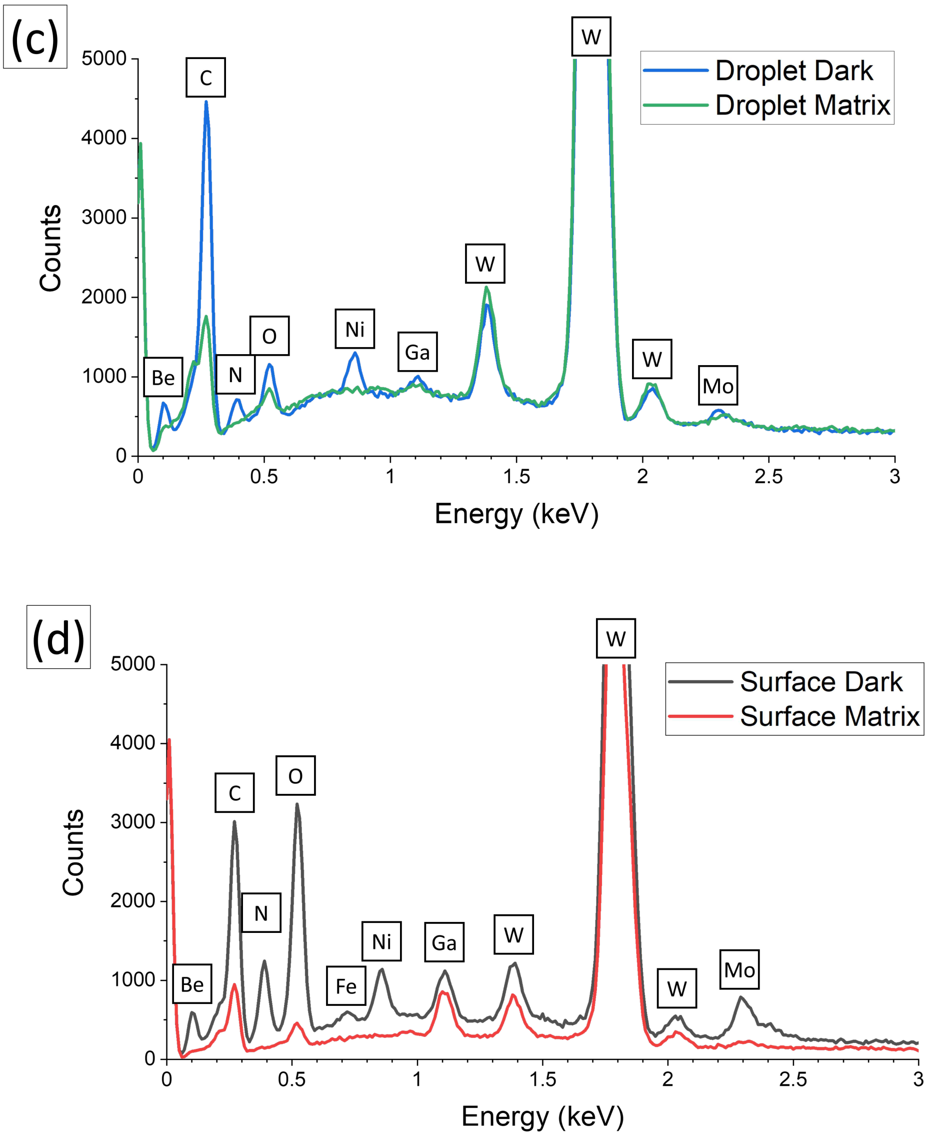

(c) EDX spectra from the different regions within the droplet and (d) underneath the droplet.

Figure 6.8: EDX Analysis of two W droplets in the SEM using a voltage of 10 kV with a spot size of 70 nm.

There were regions within the droplets and underneath the surface that appeared darker in the SE micrographs which were confirmed to be rich in impurities. The points marked with a cross in Fig. 6.8 (a) and (b) are the spectra that best highlight the differences in composition. Ga was present in all spectra due to cross-sectional milling with the FIB. The dark regions of the droplet shown in Fig. 6.8 (c), appeared to contain more C, N, O, Ni and Be than the light regions of the droplet.

The dark regions also appeared underneath the surface below the droplet, at the black cross in Fig. 6.8 (b). These regions could be debris from the divertor during operation or the same debris from the EDM process which was discussed in Chapter 4. They were observed directly underneath many of the droplets, which suggests the droplets might have been masking them from surface erosion. This also indicates that elsewhere the debris could have migrated into the plasma, radiating away some of the plasma power or creating contaminated dust.

The dark regions underneath the surface contained a large fraction of C and O, which is similar to the EDM debris in the as-received samples but could also stem from residual C dust from the JET-C campaigns. In addition to this, these dark regions contained detectable amounts of Be, N, Ni, Mo and Fe. These signals were absent from the W surface at the location of the red cross in Fig. 6.8 (d), suggesting that the debris, regardless of its origin, retains more of these elements than W. Be, Ni and Mo are primarily found in the main chamber and are continually eroded by the plasma during operation. Vaporised atoms or pieces of metallic Be, Ni and Mo will continually strike the surface of the divertor and any debris embedded in that surface. The dark regions also contained a small amount of Fe which could come from the Inconel components in the vessel or maintenance work during non-operational phases [17]. However, Fe may have been present before exposure, as it was a major impurity at the GBs of the as-received samples discussed in Chapter 4.

6.5.2 Characterisation using FIB Tomography

The formation of cracks and voids during EDM was discussed in Chapter 4. Void nucleation and coalescence appeared to be triggered by the creation of water vapour and H_2 gas bubbles in the molten surface during EDM. A total of seven droplets were cross-sectioned in the FIB for general imaging and EDX analysis. Voids were found near the surface underneath every droplet, suggesting that the presence of the droplet was also linked to void formation. The cross-section of another droplet was imaged in tomographic slices up to a length of 100 μm to discern whether the voids were introduced by the droplet during exposure in JET or if they had formed during manufacture. No He was introduced into the vessel during ILW-1 [23], and none was detected in the voids during the EELS analysis in this work. Therefore, He bubble formation is highly unlikely to have contributed to additional void formation.

The uneven surface and the presence of large cavities resulted in preferential milling in some areas, giving rise to the curtaining lines in Fig. 6.9 (b-e). This made it difficult to assemble a full tomographic reconstruction so a selection of frames was chosen to demonstrate the key findings. The darker layer beneath the Si mask, which covers the top of the droplet and is highlighted in Fig. 6.9(b), consists of a mixture of Pt and sputtered material redeposited during the mask application and trench milling.

Voids were consistently observed under the droplet for the entire examined length indicating that they may not have formed during EDM. There was also an absence of voids beyond the perimeter of the droplet on the right-hand side of Fig. 6.9 (c-e) which suggests that the droplets are indeed promoting void formation. This is likely due to the droplet introducing temperatures over 3422 °C, the melting point of W [66] and causing the top region of the surface to melt. Any species already present in the lamella or introduced by the droplet that can form gas bubbles at these temperatures could be responsible for the further void nucleation. Of the impurity elements in the droplet that were discussed in Section 6.5.1, including Be, Ni, N, O, C and Mo, the first four could feasibly vaporise at 3422 °C [66].

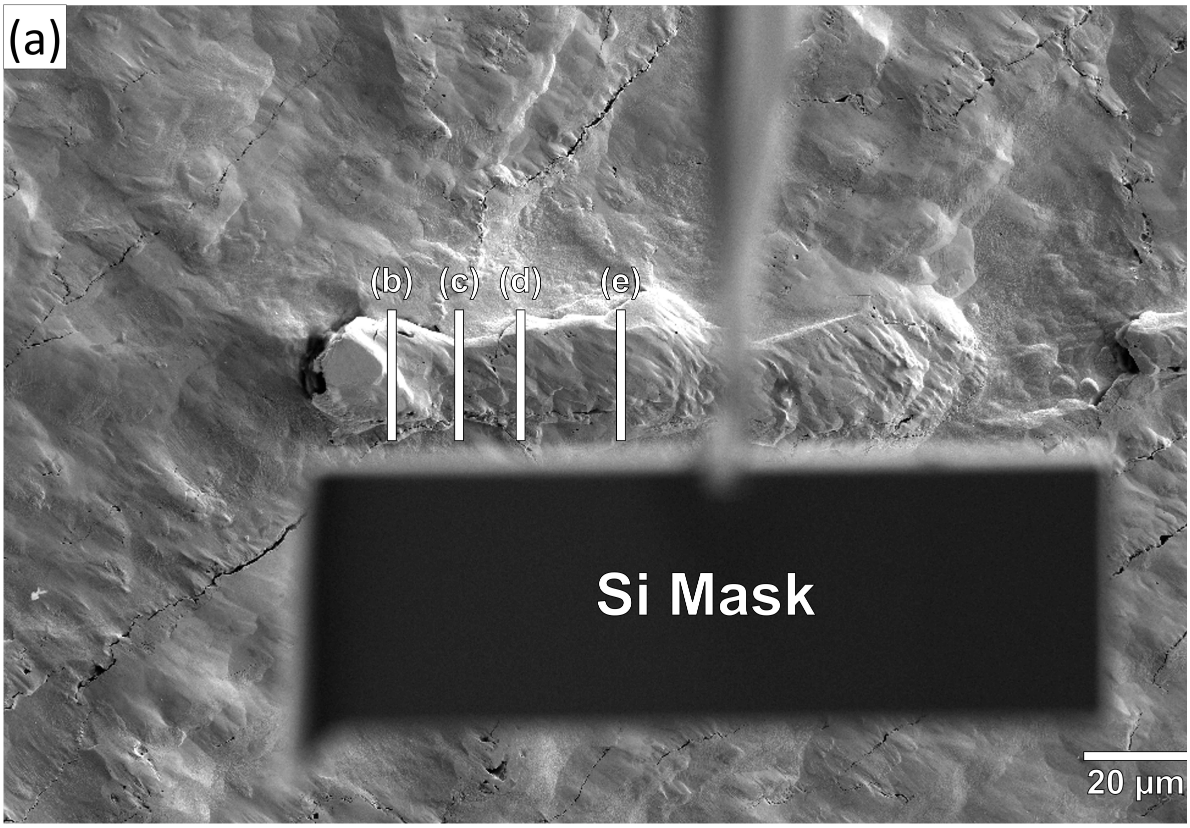

(a) SE micrograph of the droplet in the PFIB before the Si mask was applied and tomographic imaging was carried out.

Figure 6.9: SE micrographs from FIB tomography.

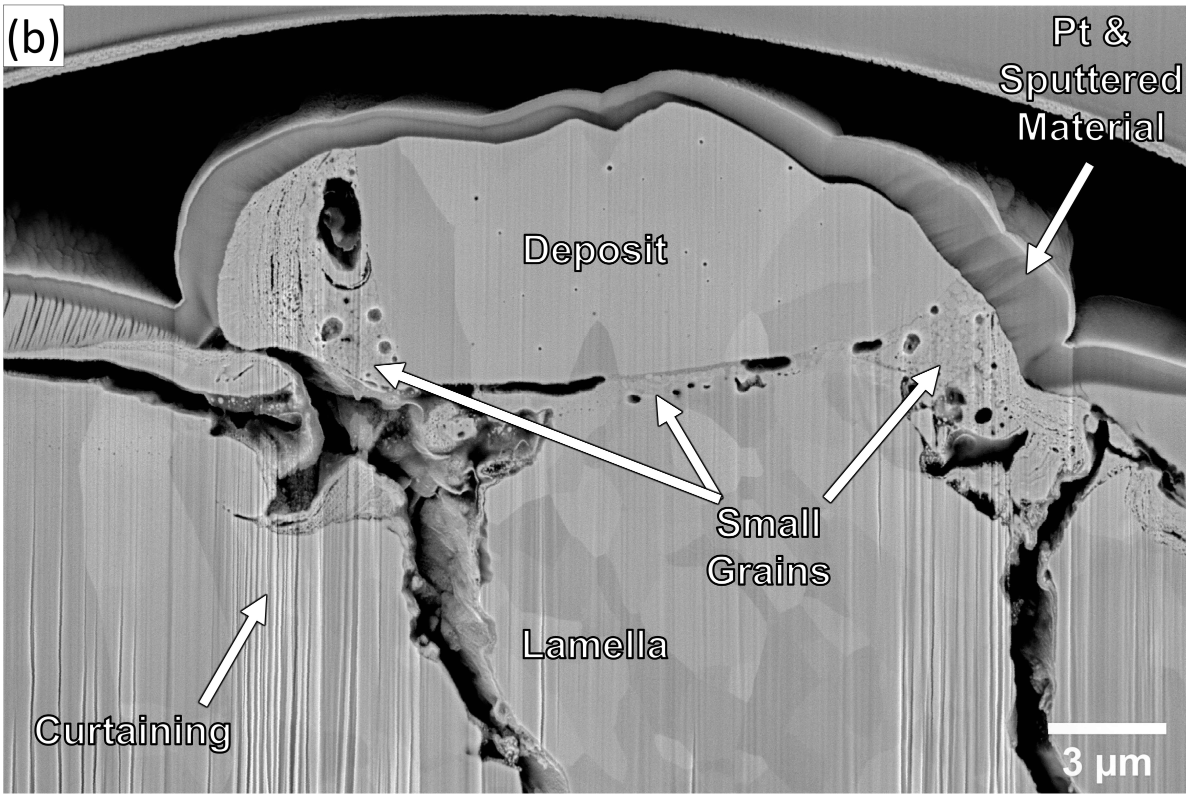

(b) SE micrograph of tomographic slice taken at 15.4 μm from the left-side edge of the droplet.

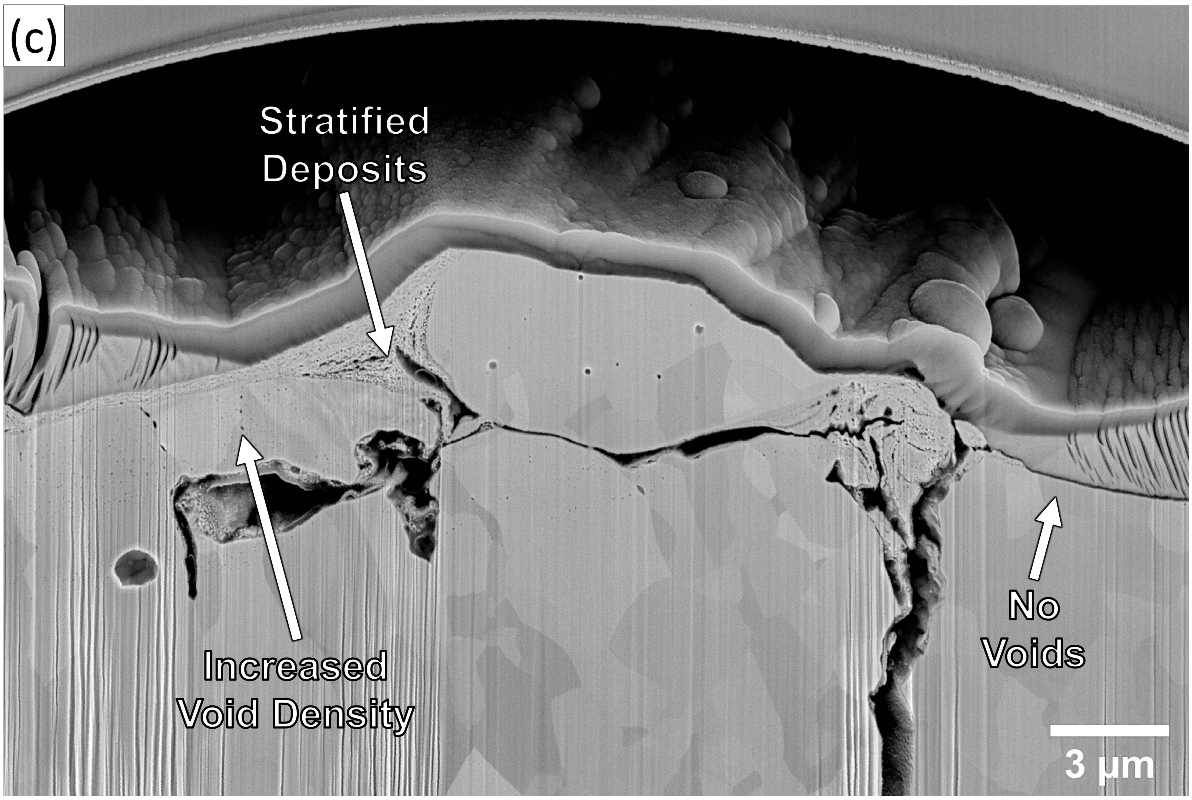

(c) SE micrograph of tomographic slice taken at 27.7 μm from the left-side edge of the droplet.

Figure 6.9: SE micrographs from FIB tomography.

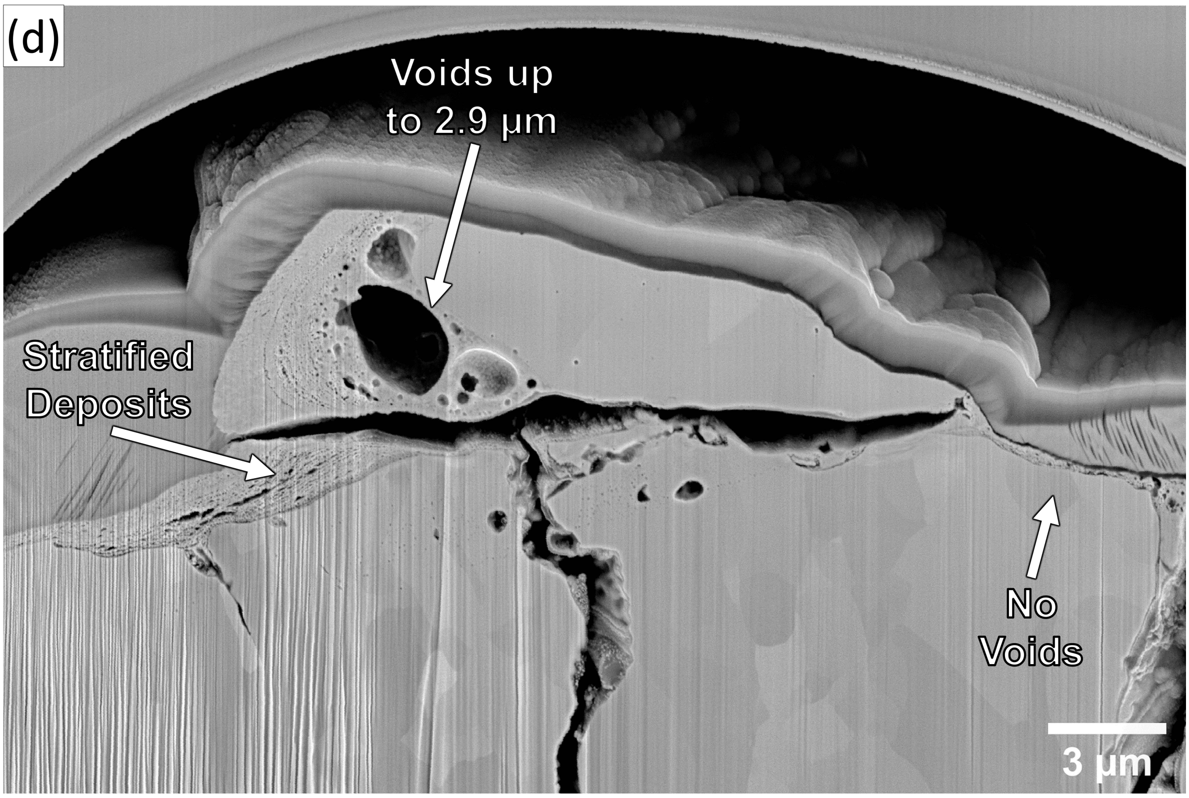

(d) SE micrograph of tomographic slice taken at 39.9 μm from the left-side edge of the droplet.

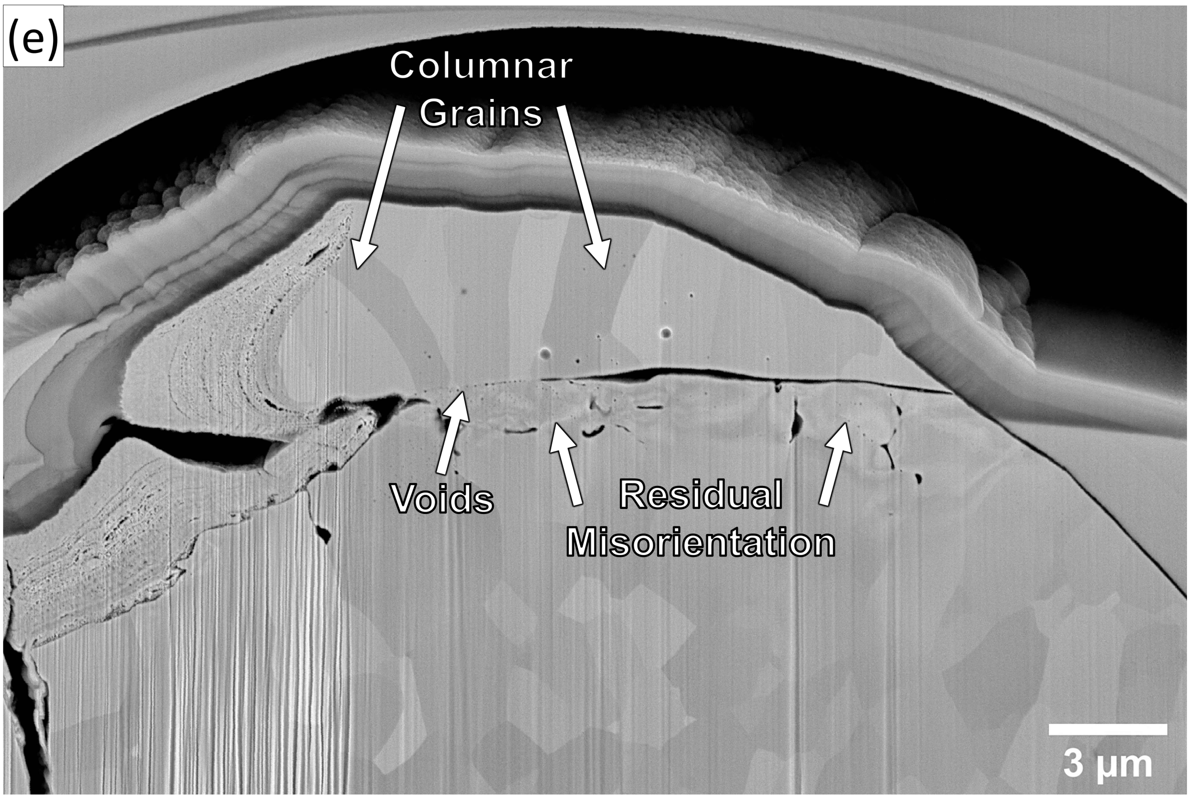

(e) SE micrograph of tomographic slice taken at 59.6 μm from the left-side edge of the droplet.

Figure 6.9: SE micrographs from FIB tomography.

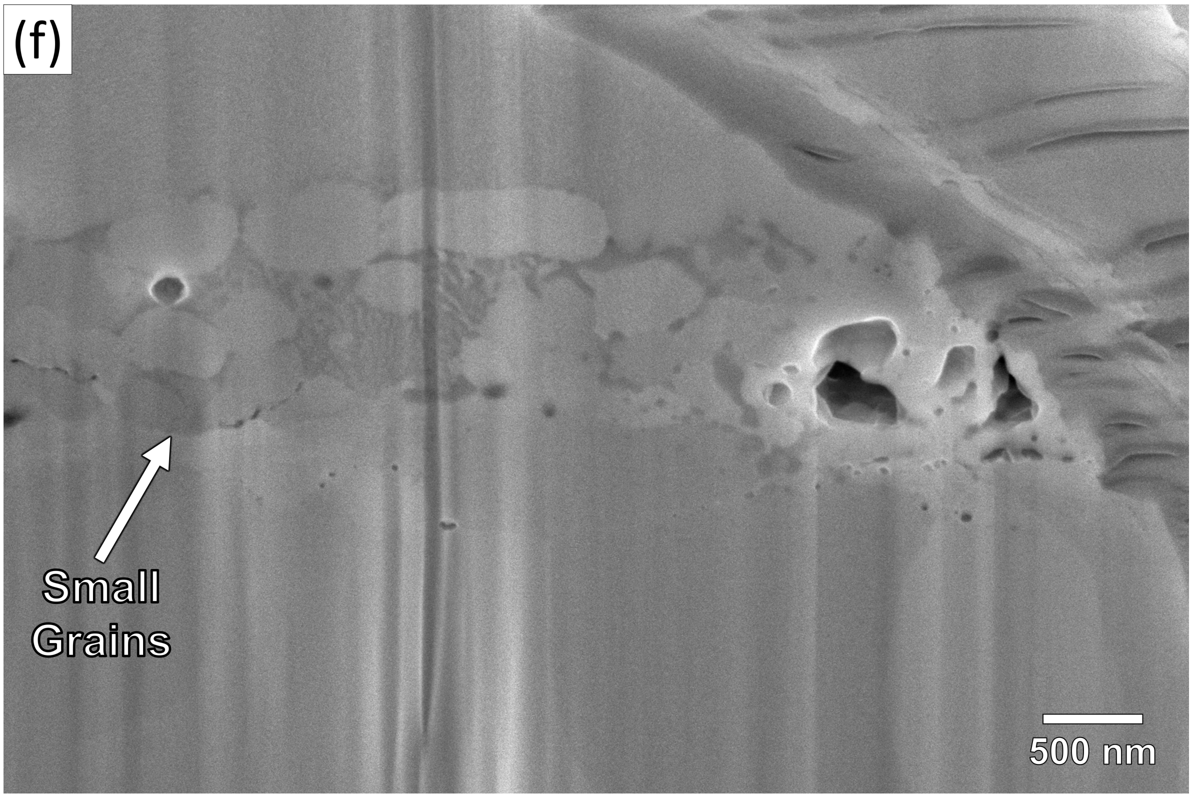

(f) High magnification SE micrograph of the small grains labelled in (b).

Figure 6.9: SE micrographs from FIB tomography.

The droplet, particularly in Fig. 6.9 (d) appeared to contain many small voids with some cavities up to 2.9 μm in diameter. The voids in the droplet were most likely driven by incident D flux and D_2 bubble formation while it was still molten. The largest cavities coincided with the location of the EDM cracks underneath the droplet. An increase in temperature and therefore void coalescence was potentially caused by the partial thermal isolation of the droplet [62]. Further discontinuities may have arisen due to rapid solidification from steep thermal gradients and pronounced volume contractions during cooling.

The left-hand side of the droplet in Fig. 6.9 (b-e) shows a layered structure akin to the stratified deposits in Section 6.4 which developed during and after solidification. A TEM sample from another droplet confirmed that this structure was indistinguishable from the one that formed on the lamella surface (see APPENDIX B). EDX also showed that W and Mo, N, C and O were all present in the layers. The TEM sample was slightly too thick for EELS analysis, but the O signal in the EDX map likely correlated with Be as was the case in Fig. 6.5.

Furthermore, there is a question of whether these layers are affixed on top of the original surface of the droplet or if the incident particles from the plasma are penetrating deeper into the droplet.

These layers appear to follow the shape of the droplet which suggests that the atoms had enough energy to become embedded in the surface. The increased impurity concentration and internal stress from material expansion could promote crack initiation in the deposited regions. There is then a higher probability of a crack propagating through the droplet. The adherence of the droplet to the surface would then weaken, increasing the production of dust in the divertor and driving up the T inventory.

In five out of seven cross-sectioned droplets in addition to that shown in Fig. 6.9, the deposited layers appeared to preferentially form along the sides of the droplets. This phenomenon may result from enhanced plasma erosion of the top surface, combined with an increased flux of ions incident on the sides of the droplets due to surface sputtering. The slight asymmetries in the shape of the droplet and the distribution of the deposited layers also highlight the importance of the magnetic field lines and therefore the incident angle of the D^+ ions.

In Fig. 6.9 (b) there are small grains on the order of 0.3 μm near the deposited layers where the differences in crystallographic orientation result in channelling contrast. These small grains were not observed without the droplet and were likely due to the increased impurity content which has been shown to decrease boundary migration rates during recrystallisation [276]. The combination of small grains and voids was also observed at the droplet-surface interface shown in Fig. 6.9 (b), suggesting that there is also a high impurity content in this region.

When molten, the droplet would be in continuous contact with the lamella surface so the cavity underneath the droplet must have developed during solidification. The lamellae are not actively cooled but should behave as a heat sink, making the thermal gradient normal to the surface. The droplet must impact the surface at temperatures exceeding the melting point of W which may also cause the lamella surface to locally melt. In Fig. 6.9 (e) the droplet-surface interface was also decorated with voids, indicating that impurity boiling and gas formation could initiate the formation of this cavity. Once voids have developed and there are discontinuities in the material, the droplet would become thermally isolated in some areas. Without somewhere for the heat to dissipate, it likely facilitated the coalescence of voids into a larger cavity.

The channelling contrast in Fig. 6.9 (e) was sufficient to see residual misorientation patterns below the droplet-lamella interface, which is further evidence of the lamella surface melting and rapidly solidifying [277–279]. The system can be compared to selective laser melting for additive manufacturing where the melt pool and the steep thermal gradient generated by the laser are analogous to the molten droplet on the surface [280]. In both cases, there should be a deposition zone on the surface, a remelting zone underneath, and a heat-affected zone which joins with the bulk material. The heat-affected zone surrounding the melt pool experiences thermal gradients which can result in high thermal stresses and can lead to the formation of dislocations and strain localisation [281]. Non-uniform cooling rates and variations in local composition can lead to misalignments of crystallographic planes within the affected regions [282]. Residual stresses can also be generated as a result of solidification-induced contraction of the melt pool [283].

Fig. 6.9 (e) also shows the formation of columnar grains within the droplet which typically form when solidification is directional and cooling rates are slow [284]. In this case, the cooling front slowly moves upwards, normal to the surface as heat is dissipated through contact with the lamella, providing the directionality for columnar grain growth. The columnar grain structure may influence erosion resistance, affecting the droplet response to temperature fluctuations, thermal stresses and its fatigue response to thermal cycling. Additionally, columnar grains can induce some anisotropy, particularly if these structures are irradiated with neutrons, causing embrittlement and potentially increased cracking at GBs under further loading.

6.5.3 Characterisation using TKD

TKD was performed at the droplet-lamella interface to help ascertain at what stage the cavity underneath the droplet formed. The uneven geometry of the lamella surface resulted in preferential milling during the thinning process. The formation of holes during FIB preparation can induce localised plastic deformation and strain relaxation at the edges of the holes, leading to misorientation in these regions. This artefact is reflected in the grain average misorientation (GAM) map in Fig. 6.10 (c), showing elevated misorientation within a few hundred nanometres of the hole perimeter, which does not represent the intrinsic microstructure of the sample.

There was less spread in the grain orientations in the lamella than in the droplet, which was likely a result of higher cooling rates in the lamella surface. Moreover, there was a greater amount of misorientation within the grain interiors in the lamella surface, which is likely residual stress from the solidification process. It is possible that meta-stable microstructures such as non-equilibrium GBs formed under rapid cooling, while impurities can also facilitate dislocation formation under steep thermal gradients. These factors in addition to the inconsistent geometry can result in inhomogeneous cooling rates that give rise to a large amount of misorientation within grains but a small spread in the orientation of neighbouring grains.

Conversely, the droplet contained a distinct spread of grain orientations, which suggests there is no preferred orientation for the grains to form. The long axis of columnar grains in BCC metals such as W is typically parallel to the <100> direction [285] but perhaps this behaviour is observed when the columnar growth is more pronounced. Furthermore, if the lamella surface was solid and behaved as a substrate, there would possibly be signs of epitaxial growth causing the grains in the molten droplet to have some relation to the grains in the lamella. Common epitaxial relationships in BCC materials include specific cube-on-cube or close-packed plane-on-plane alignments, resulting in low misorientation between the droplet and the lamella [286]. This does not appear to be the case, as there is a relatively large spread of orientations between the different grains in the droplet. If epitaxial growth had occurred, there may also be signs of localised strain in the droplet due to lattice mismatch. The GAM map in Fig. 6.10 (c) shows relatively low misorientation within individual grains of the droplet and no evidence of deformation. While a more detailed texture analysis would be necessary to completely rule out an epitaxial effect, these results suggest that it does not influence the final microstructure. Instead, the cavity likely formed through void coalescence while the W was still molten. This process would create thermally isolated regions, allowing grains to develop independently during solidification.

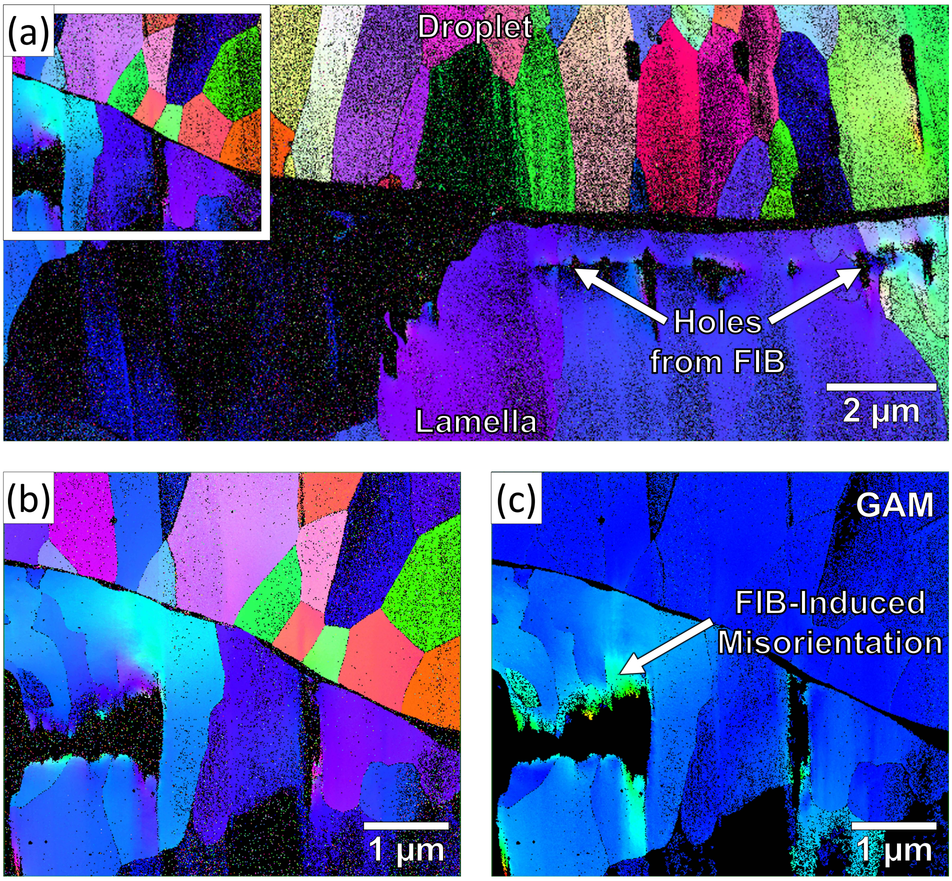

Figure 6.10: TKD data collected at the droplet-lamella interface, showing the inverse pole figures along the out-of-plane direction (IPF-Z) with a field of view of (a) 17.1 μm and (b) 5.4 μm and (c) a grain average misorientation (GAM) map at 5.4 μm.

6.6 The Interaction of Beryllium with Microstructural Features

An EELS map was collected from a TEM sample in a region where the droplet was still attached to the lamella surface to determine the elemental distribution during cavity formation. Small grains had formed at this interface, similar to Fig. 6.9 (b), and Be had segregated to the GBs, as shown in Fig. 6.11 (b). Impurities often segregate to GBs due to a higher concentration of lattice defects that can accommodate them and reduce the energy of the overall system. The fine structure of the Be K-edge in Fig. 6.11 (c) confirmed that Be remained in its metallic phase at the GBs, and BeO had formed at the cavity opening [271]. This suggests that there is increased availability of O at the edge of cavities and voids due to the formation of W oxide, which was hypothesised for the EDM-induced voids in Chapter 4.

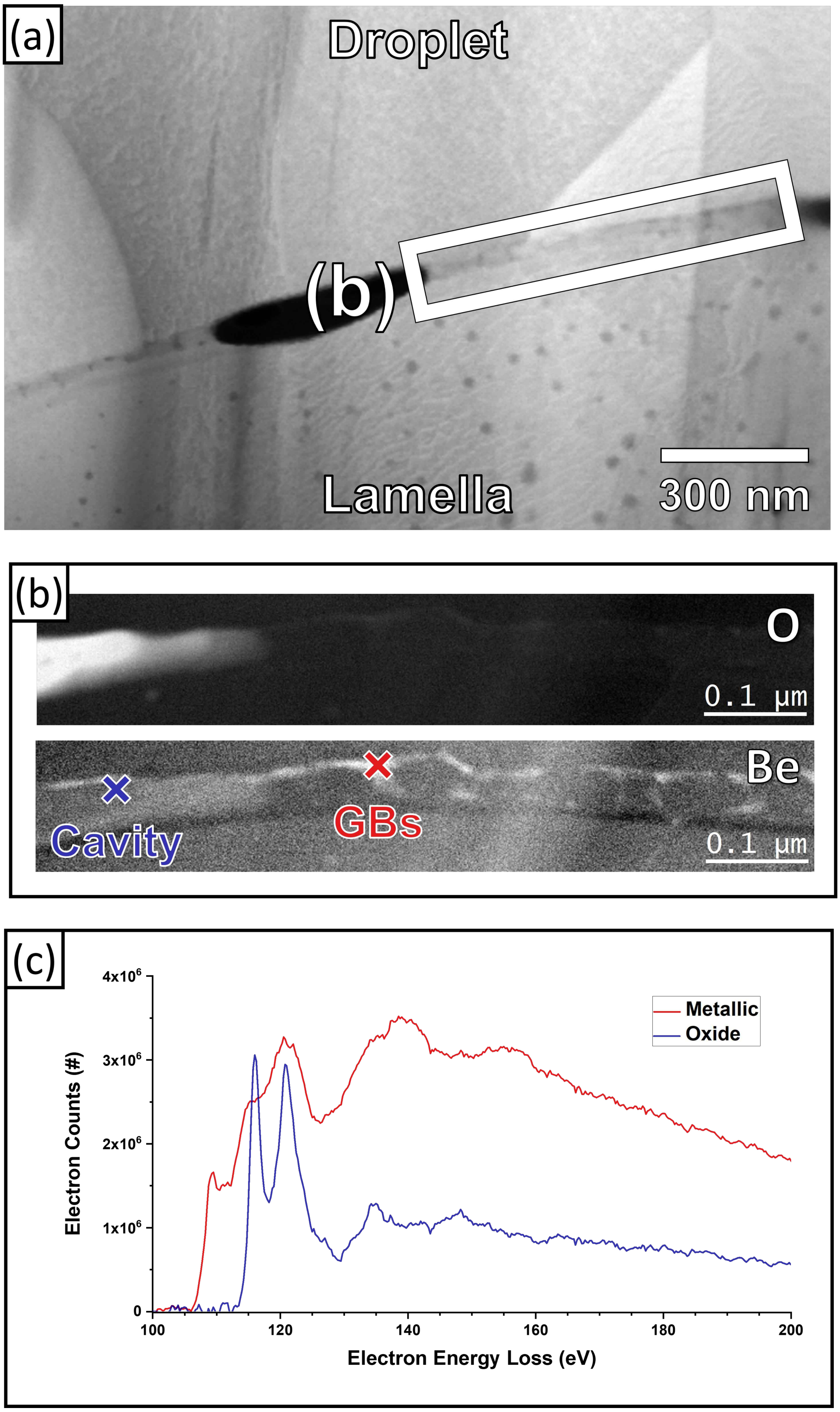

Figure 6.11: (a) STEM HAADF micrograph of the droplet-lamella interface, the white box is a representation of where the EELS map was collected and not the exact location (b) STEM EELS maps for O and Be (c) Difference in Be K-edge between metallic Be and BeO.

Assuming that the droplet was molten when it struck the surface, its temperature should be above 3422 °C which exceeds the boiling point of Be, 2468 °C [66]. The Be that has previously been deposited on the surface is then likely to boil which could facilitate the formation of more voids alongside other impurities. EELS was also performed underneath the cavity at the droplet-lamella interface of four different TEM samples which revealed many voids that contained BeO, as shown in Fig. 6.12. Be can form a solid solution in W or a Be-W alloy at elevated temperatures. However, as temperatures drop Be becomes less soluble in W and starts to favour segregation, which may drive Be to form a solid within the voids. An important question to consider is the role of O in this process. Was O already present at the edge of these voids, with Be becoming trapped due to its affinity for O? Alternatively, did the void initially contain Be vapour, which subsequently condensed and solidified as metallic Be before eventually reacting with oxygen? Further experimental work is necessary to clarify this mechanism and determine the precise sequence of events.

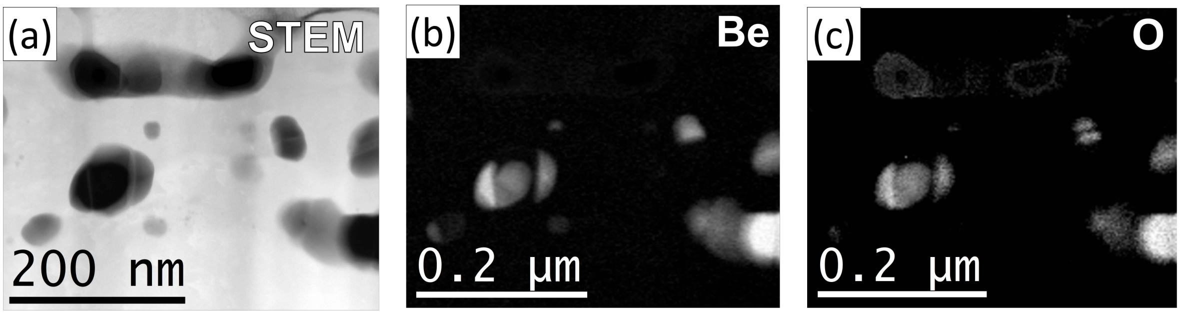

Figure 6.12: (a) STEM HAADF micrograph of voids underneath W droplet and EELS maps of (b) Be and (c) O.

At 20 °C, BeO has a slightly higher elastic modulus than metallic Be which increases the likelihood of it failing via brittle fracture [287]. However, it also has a slightly smaller thermal expansion coefficient which could reduce the amount of mechanical stress at higher temperatures compared to metallic Be. Regardless of the form Be takes, its segregation to specific areas such as voids and GBs is likely detrimental. These regions of high Be content are suspected to be potential sites for material detachment from the lamella, contributing to dust formation in the reactor. The trapped Be, the surrounding W and both of their oxides will have different rates of thermal expansion at elevated temperatures, which will undoubtedly produce internal stresses at these interfaces. In turn, this could initiate cracking, and cause interfacial delamination and fatigue failure if there are many cycles of rapid heating and cooling.

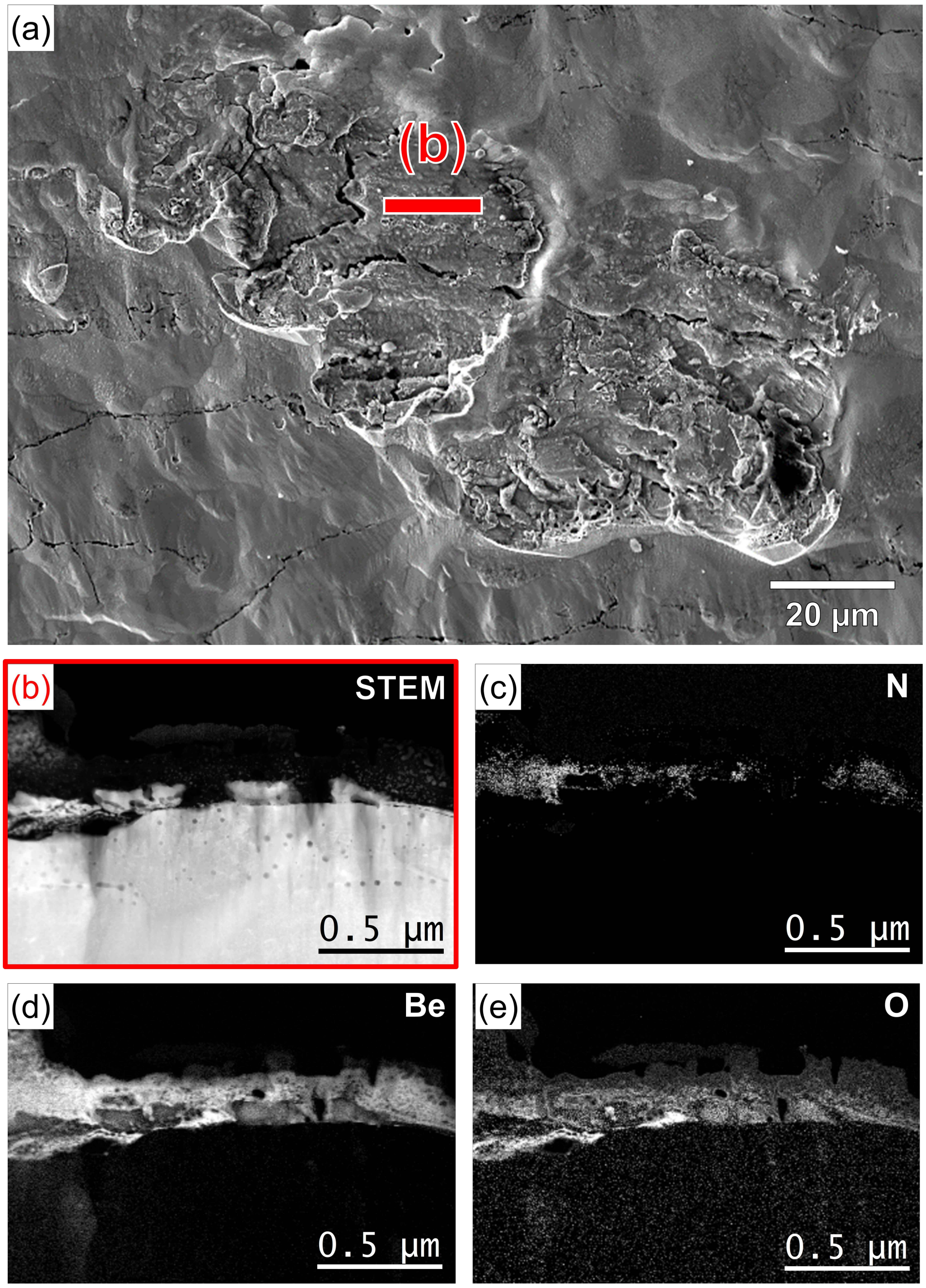

Figure 6.13: (a) SE image of the lamella surface where the droplet detached (b) STEM HAADF image of a cross-sectional TEM sample prepared from this region and EELS maps of (c) N, (d) Be and (e) O.

Fig. 6.13 highlights the significance of Be retention in W PFCs, showing the formation of a Be-rich layer up to 200 nm thick at the site where part of a droplet detached from the surface. The EELS maps in Fig. 6.13 (c-e) include the K-edge for N at 398 eV [272], showing a small region at the top of the Be layer that contains a significant amount of N while the rest appears to be BeO. N implantation in Be has been reported [288][289] but Be does not typically form stable compounds with N due to a large discrepancy in electronegativities. Perhaps the implantation of N within this layer and the unstable nature of Be_3N_2 led to the detachment of the droplet.

The droplets in the surrounding area remained intact, which suggests that detachment did not occur outside of the vessel or during sample preparation. If the droplet had been removed during handling the results still confirm that the Be-rich layer is still the weakest part of the structure. Under the assumption that this was a single event, then only one droplet detached out of a possible 23 during 12.62 hours of divertor operation [264][290]. The first ITER divertor is projected to have a total exposure period of 2500 hours [5]. That is ∼192 times greater than the exposure time of the lamella in JET which allows for many more cycles of heating and cooling and increases the likelihood for more droplets to detach. However, ITER is designed to operate with longer pulses than JET so the exact number of heating and cooling cycles may be more comparable and more droplets remain intact.

The lower bound estimate for the maximum temperature for lamella C3 throughout ILW-1 was 1263 °C, which is 310 °C below the temperature limit for the ITER divertor [155]. Although this may not appear to be a substantial difference, a temperature limit of 1573 °C exceeds the melting point of Be which is 1287 °C [66]. Furthermore, the most stable W oxide, WO_3, has a melting point of 1473 °C [66], while the W–Be alloys $Be_{22}W$ and $Be_{12}W$ have molten phases at 1327 and 1507 °C respectively [154]. These temperatures all fall within the temperature limit for ITER and it is, therefore, not unreasonable to expect some surface deposits to melt which could result in the detachment of more divertor material. Be layer growth is not anticipated at 1573 °C in the ITER divertor, due to sublimation [154]. However, these results show that even in typical regions of net erosion such as tile 5, not only is layer formation an issue but Be can diffuse into features such as GBs and voids and promote dust formation.

Beyond temperature, ITER is expected to have a maximum integrated target fluence 40 times greater than that of JET [5] and an auxiliary heating power of 50 MW [225] compared to an average input power of 2.2 MW for JET ILW-1 [226]. The enhanced particle loading will result in greater material erosion that can produce more deposits and impurities in the divertor. The larger input power of ITER will translate to approximately 16 MW m^{-2} of heat flux density on the divertor components [5]. The increased thermal loads can also lead to greater thermal stresses and localised hot spots which could create more molten droplets, uneven thermal expansion and cracking, particularly in the deposited regions. The larger scale of ITER will give rise to higher energy ELMs that may exacerbate material damage, including component melting, droplet ejection, and the generation of loose dust.

6.7 Conclusions

Lamella C3 was retrieved from a shadowed region of tile 5 after ILW-1 and a $2.5 \times 6 \times 10$ mm sample was cut from the centre of the component for post-mortem analysis. IR camera data indicated that surface temperatures likely remained below the threshold for melting or recrystallisation in the bulk sample. Its surface appeared smoother in SE images which was likely caused by erosion. FIB cross-sections made in the sample surface showed the deposition of mixed material layers in some areas. They primarily consisted of W, likely originating from other tiles in the divertor, with distinct layers of Mo and BeO from diagnostics and main chamber tiles respectively.

Droplets of W were also observed on the exposed surface which were thought to be caused by the melting of a Langmuir probe since there is evidence of this occurring during the ILW campaigns [123]. Many droplets were contaminated with Be, Ni, N, C, O and Mo while they were mobile in the vessel. These impurities were also retained underneath the droplets specifically in darker regions of the SE micrographs that resembled the trapped debris from EDM. It is possible that this debris originated from within the JET vessel but it is unclear how it could become trapped underneath the surface. Moreover, there was no evidence of this darker debris in the SE images of the surface, hence it was more likely to have been embedded during EDM. Finally, these regions of debris retained more impurities than the W matrix of the lamella, such as Be which poses a toxic safety risk.

If EDM continues to be used on plasma-facing surfaces in the divertor then more research should be done on how the process can be modified to produce a better surface finish. Ideally, the refinements should produce fewer and smaller cracks to reduce crack growth during operation. They should reduce the amount of debris and therefore the concentration of impurities that become trapped in the surface of the component. It would also be beneficial to understand the T retention properties of this debris using D implantation as a proxy and IBA techniques for compositional analysis.

FIB tomographic imaging of one droplet revealed that more layered structures had formed within the droplet once it had landed on the surface. This occurred particularly on its sides, where there could have been an increase in the capture of atoms that had been sputtered from the lamella surface. These mixed BeO layers, the formation of columnar grains and cavities up to 2.9 μm in diameter, also increase the risk of crack initiation within the droplet and therefore dust generation within the vessel. TKD showed that voids and cavities formed at the droplet-lamella interface during solidification, which resulted in thermally isolated regions with different grain structures.

The tomographic imaging also confirmed that the droplets were generating voids in the surface of the lamella, due to the introduction of large thermal gradients and impurities such as Be. EELS analysis confirmed that BeO had formed inside many of these voids and metallic Be was present at GBs near the droplet-lamella interface. There was also an occurrence of a droplet detaching from the lamella surface due to the presence of a 200 nm Be layer. The discrepancies in thermal expansion within the Be–W system were thought to introduce sufficient stresses under cyclical thermal loading to cause delamination.

ITER will likely operate with a Be main wall for the non-nuclear phase [5][14][15] which requires the careful handling of toxic components. It is therefore important to understand how a Be wall affects the longevity of a W divertor and dust production. These results show that deposits can build up on high-heat flux components in the divertor in addition to what has already been seen at tiles 0 and 1 on the inboard side of the divertor. Be in particular has been found in solid layers up to 200 nm thick, mixed material layers with W and Mo, trapped in subsurface debris and segregating to GBs and voids in W droplets. One benefit is that metallic Be and BeO have higher thermal conductivities than W so they will not exacerbate localised heating in regions that are already thermally isolated [98][287]. The main concern is a discrepancy in thermal expansion since metallic Be and BeO have larger expansion coefficients than W. This could produce compressive stresses in the W matrix under cyclic heating and cooling cycles, initiating crack growth and the detachment of material. This appears to have happened to a W droplet on the surface of lamella C3 where a Be layer remains at the site where the droplet detached. Loose material such as this is likely to be deposited on another surface or stay in the divertor as dust, increasing erosion and the T inventory.

Moreover, the ITER PFCs must endure transmutation and cascade damage from 14 MeV neutrons, incident He ions in addition to higher heat loads and higher particle fluxes than JET. This makes dust production a much greater issue for ITER than a machine like JET, both from the perspective of safety and nuclear licensing. ITER hopes to be the first tokamak to breakeven, but if the maximum T inventory is exceeded it will likely influence the decisions of nuclear regulatory authorities going forward. Ultimately, the findings in this chapter support the decision of the ITER Organisation to transition to a W first wall for the fusion power operational phases of the device.

Chapter 7

Conclusions

7.1 Overview of Key Results

- The JET Langmuir probes and lamellae as-received from the manufacturer, MGS Precision Ltd., displayed different grain structures despite reportedly undergoing the same manufacturing process. The lamellae displayed a typical rolled microstructure engineered to withstand high-heat fluxes with fine grains on the order of 2 μm. The probes generally had larger equiaxed grains on the order of 30 μm with some smaller regions that contained fine grains. This suggested that the rolling or annealing parameters were slightly different between the two types of components.

- Before exposure in the JET divertor, the plasma-facing surface of both the lamellae and the probes had been cut using EDM which produced cracks and voids that penetrated up to 50 μm into the surface. These features were primarily localised to GBs but there were examples of both intragranular cracks and voids.

- APT was performed at the GBs of the as-received samples and showed significantly higher concentrations of impurities than what was reported by the manufacturer for the W powder before sintering. The concentrations for P and Fe were particularly high, diffusing to the GBs during manufacture or surface machining and likely causing embrittlement.

- A UHP W sample with a purity of 99.999% was also cut with EDM and still displayed void and crack formation, showing that the intrinsic impurities W were not driving the formation of these features.

- A mechanism was proposed for void formation which included the melting of the component surface and the formation of water vapour and H_2 gas-filled bubbles which were then expelled from the molten layers during EDM.

- O was observed at voids and GBs in both TEM and APT samples, suggesting that oxidation may contribute to crack propagation. However, oxidation could also result from sample preparation in the FIB, so further investigation is recommended to confirm its origin.

- EDM was shown to embed debris in the cracks that it produced, containing large quantities of C and O. Indentation showed that these regions were considerably softer than the W component and could therefore become dislodged during divertor operation in JET. Moreover, these regions could expand under intense thermal loads and widen the cracks.

- Four JET lamellae were exposed in the JET divertor during the ILW campaigns (C4 – ILW-3, C12 – ILW-1 & 3, C13 – ILW-3 and D12 – ILW-3) and showed no sign of melting, recrystallisation or changes in hardness.

- Three Langmuir probes were exposed in the divertor during ILW-1 & 2, probe 26 from tile 6 and probe 8 and 6 from tile 3. Probe 8 showed no change in hardness or grain structure, but did show that the EDM cracks had widened and propagated down to 1 mm from the surface. Probes 6 and 26 both recrystallised and showed an increase in hardness of 0.4 GPa.

- The exposed surface of probe 26 also appeared to have melted and voids up to 50 μm in diameter had formed at GBs near the exposed surface. The voids were hypothesised to form in the melted regions of the probe due to D_2 bubbles that were the result of large D^+ ion fluxes.

- IBA had previously shown that D was present on the exposed surface of each probe but no D was detected on the cross-sections in this work due to sample preparation. D was not trapped in the samples and was not responsible for the observed hardening, but spherical nanoindentation revealed that there were still defects present in the probes that were suppressing pop-ins. These defects were likely to be cascade damage generated by incident D^+ ions during divertor operation.

- Another lamella was exposed in JET during ILW-1, C3, where shadowing from the plasma had preserved stratified deposits and W droplets on the surface of the component. The stratified deposit contained alternating layers of BeO and sputtered W and less frequent occurrences of Mo. The W droplet contained traces of Be, Ni, N, C, O and Mo.

- Dark regions were found underneath the surface of lamella C3 that visually resembled the trapped debris from EDM, although the exact origin could not be confirmed. These regions appeared to be enriched with Be, Ni, N, C, O and Mo, clearly retaining more impurities than the W matrix.
- Mixed material layers also formed along the sides of the W droplets and were attributed to the sputtering of surface material. The droplets appeared to cause the formation of more voids and cavities in the area directly underneath it such that the parts of the droplet became thermally isolated during solidification.
- Metallic Be was found at the boundaries of small grains near the droplet-lamella interface which oxidised near large cavities. BeO also decorated the interior of many voids and formed layers up to 200 nm thick underneath the droplets. The areas where Be accumulated appeared to be the most likely sites for droplet detachment.

7.2 Conclusions

This investigation aimed to fully characterise W components before and after they were exposed in the JET divertor during the ILW campaigns. The experiments revealed the presence of cracks, voids and debris in the plasma-facing surface of the as-received material that formed as a result of EDM. These types of features have been studied in many materials but not to this level of detail in W with the use of extremely high-resolution techniques. The knowledge gained from assessing component manufacturing and processing was essential to discern what structures developed as a consequence of D plasma-surface interactions.

The debris trapped underneath the plasma-facing surface after EDM was thought to increase the retention of Be, Ni, N, C, O and Mo. This debris may also contribute to crack widening due to thermal expansion at elevated temperatures. Moreover, the retention of Be poses a safety risk through the inhalation of toxic material. The T retention properties of the debris are also unknown, which could result in increased safety risks and nuclear licensing issues. These properties should be determined using D implantation as a proxy for T, followed by IBA techniques for compositional analysis and thermal desorption spectroscopy to understand the energy distribution of trapping sites.

Mixed material layers and W droplets were deposited on the surface of a divertor component, lamella C3. Further void formation was observed which was attributed to the melting of W, impurities boiling and intense particle loads of D^+ ions. Metallic Be was discovered at GBs, BeO was found inside many voids and formed layers up to 200 nm underneath W droplets. The regions where Be accumulated were identified as the most probable sites for droplet detachment due to the heating and cooling cycles that occur in the reactor and discrepancies in thermal expansion with the surrounding W. The increased production of loose material will likely result in increased erosion rates, T inventory and occurrences of plasma disruptions. The findings reinforce the decision to transition to a W first wall for its fusion power operational phases.

The preparation and characterisation of these active samples is a significant achievement considering how few facilities have these capabilities and the initial challenges with surface finish. The comparison between the as-received and exposed samples showed that the lamella design was effective at handling plasma loading in JET with no sign of melting, recrystallisation or changes in hardness. Although the selected lamellae were only in the range of rows 4 to 13. Experiments concerning regions of higher heat flux, such as lamella C23, have shown slight crack propagation but no sign of recrystallisation.

Conversely, the Langmuir probes exhibited more extreme microstructures and represented the maximum potential heat damage that a W component could experience in JET due to regular contact with the D plasma. Probe 8 displayed no sign of recrystallisation or change in hardness, but had augmented the EDM crack which appeared wider and extended to a maximum depth of 1 mm. The presence of EDM cracks on the surface of PFCs has been shown to lead to the development of deeper cracks following plasma exposure. To address this issue, dedicated experiments should be conducted to evaluate the various parameters of EDM and identify the optimal setup that minimises cracking. Alternatively, post-EDM surface refinements may need to be implemented before components are installed in future reactors.

The other two Langmuir probes, 26 and 6, both displayed signs of recrystallisation and a hardness increase of 0.4 GPa. This hardening was attributed to the cascade damage caused by incident D^+ ions during divertor operation. Moreover, this ion fluence was also deemed responsible for the formation of large voids up to 50 μm in diameter, in the molten layers of probe 26. These voids were predominantly aligned along GBs which could act as sites for stress concentration and increase the likelihood of brittle fracture along the boundary.

The results presented in this thesis offer a range of insights which are both promising, regarding the structural integrity of the lamellae, and concerning, such as the exacerbation of EDM-cracking and the segregation of Be. PFCs in future devices will be subjected to longer pulses and campaign lengths with greater heat loads and particle fluxes compared to JET. They will also have to contend with cascade damage and transmutation from 14 MeV neutrons and bubble formation from He ions. Ultimately, additional data is necessary to fully understand the long-term effects of D-T plasma exposure on W components. These questions will start to be addressed when the PFCs from the recent JET D-T campaigns [9] and from ITER become available [5][14].

7.3 Future Work

In addition to the study of JET and ITER components during D-T operations, other areas within this research would benefit from further development. EDM is the leading choice for cutting bulk W components due to its cost-effectiveness, precision and efficiency. For fusion applications, it is essential to conduct an in-depth analysis of machining parameters such as dielectric fluid type, electrode material, discharge currents and voltages and assess their impact on surface quality. Diagnostics could be developed to measure the surface temperature of the workpiece in situ and a methodology could be designed to reduce the amount of contaminants in the EDM chamber. The process could also be modelled, showing how the temperature and thermal stresses are distributed and potentially minimised. Enhancements in surface finish could be achieved through the development of a specialised polishing technique for batch production of industrial components.

Future studies on PFCs should shift focus away from Be, given the plan for ITER to transition to a W first wall during its D-T operational phase. Instead, research should prioritise the effects of B incorporation into W, as recent studies have highlighted its potential to significantly enhance oxidation resistance, mechanical strength, and ductility [291][292]. Incorporating B into W could open new pathways for improving the performance and durability of PFCs under fusion-relevant conditions.

Further investigations are necessary to understand how temperature and plasma exposure affect the structural integrity of W components, particularly concerning surface cracking and void formation in a fusion environment. The thermal expansion and melting temperature of the EDM debris embedded in the surface of the as-received samples, and their effects on crack length and width, should be studied through heating in a vacuum furnace. As previously mentioned the T retention properties of the debris could estimated using D implantation as a stand-in for T, followed by microprobe analysis for precise elemental distribution and thermal desorption spectroscopy to investigate the trapping mechanisms. The contaminants in the surface of the component could become active during D-T operations due to neutron bombardment which could also be modelled. Moreover, the PFIB could be used to estimate how much debris is embedded after EDM and compare that to lamella C3 to see if a considerable amount of debris enters the plasma during operation.

Cross-sections in the PFIB could be applied to estimate the crack length in lamellae C3 and compare that to lamella C23 [10] and the as-received lamella. Additionally, more APT samples could be created from both fine- and coarse-grained regions of both probes and lamellae, to see if there is a difference in impurity concentration and build up a robust average. APT could also be used to calculate the average impurity concentration at the GBs of the UHP W sample. Building on this concept, TEM samples could be taken from GBs in the UHP sample and an as-received JET component to investigate whether differences in impurity content affect oxidation. Moreover, in-situ heating experiments could explore the effect of impurity concentrations and oxidation on cracking and sublimation.

In relation to the Langmuir probes, high-resolution TEM could be used for samples prepared from the hardened regions to investigate defects such as dislocation loops which are likely responsible for the observed increase in hardness. X-ray diffraction (XRD) could also provide insights into the types of defects present in the probes by analysing changes in peak broadening, shifts, and asymmetry, which reflect strain fields and lattice distortions caused by defects such as dislocations, vacancies, and interstitials. By correlating these features with models of defect-induced hardening, XRD enables the identification and characterisation of defect populations contributing to the increase in material hardness. This information could then be used to help derive quantities such as the elastic modulus, yield strength and strain-hardening exponent from the spherical indentation stress-strain curves. Furthermore, the as-received probe could be intentionally melted in a linear plasma device, such as Magnum-PSI in the Netherlands, using a D plasma to confirm the mechanism behind the void formation observed in probe 26. Lastly, the method of fluence calculations from the Langmuir probe measurements proved underdeveloped. It remains unclear whether this method alone can provide reliable data to contextualise material observations without support from additional diagnostics.

References

[1] R. Newell, D. Raimi, and G. Aldana, "Global energy outlook 2019: the next generation of energy," *Resources for the Future*, vol. 1, no. 8, 2019.

[2] M. Kikuchi, K. Lackner, and M. Tran, *Fusion Physics.* International Atomic Energy Agency, 2012.

[3] T. Tang, Z. Zhang, J.-B. Meng, and D.-L. Luo, "Synthesis and characterization of lithium silicate powders," *Fusion Engineering and Design*, vol. 84, no. 12, pp. 2124–2130, 2009.

[4] L. Boccaccini, F. Arbeiter, P. Arena, J. Aubert, L. Bühler, I. Cristescu, A. D. Nevo, M. Eboli, L. Forest, C. Harrington, F. Hernandez, R. Knitter, H. Neuberger, D. Rapisarda, P. Sardain, G. Spagnuolo, M. Utili, L. Vala, A. Venturini, P. Vladimirov, and G. Zhou, "Status of maturation of critical technologies and systems design: Breeding blanket," *Fusion Engineering and Design*, vol. 179, p. 113116, 2022.

[5] R. Pitts, X. Bonnin, F. Escourbiac, H. Frerichs, J. Gunn, T. Hirai, A. Kukushkin, E. Kaveeva, M. Miller, D. Moulton, V. Rozhansky, I. Senichenkov, E. Sytova, O. Schmitz, P. Stangeby, G. De Temmerman, I. Veselova, and S. Wiesen, "Physics basis for the first ITER tungsten divertor," *Nuclear Materials and Energy*, vol. 20, p. 100696, 2019.

[6] M. Keilhacker, A. Gibson, C. Gormezano, P. Lomas, P. Thomas, M. Watkins, P. Andrew, B. Balet, D. Borba, C. Challis, I. Coffey, G. Cottrell, H. D. Esch, N. Deliyanakis, A. Fasoli, C. Gowers, H. Guo, G. Huysmans, T. Jones, W. Kerner, R. König, M. Loughlin, A. Maas, F. Marcus, M. Nave, F. Rimini, G. Sadler, S. Sharapov, G. Sips, P. Smeulders, F. Söldner, A. Taroni, B. Tubbing, M. von Hellermann, D. Ward, and J. Team, "High fusion performance from deuterium-tritium plasmas in JET," *Nuclear Fusion*, vol. 39, no. 2, p. 209, 1999.

[7] F. Orsitto, R. Villari, F. Moro, T. Todd, S. Lilley, I. Jenkins, R. Felton, W. Biel, A. Silva, M. Scholz, J. Rzadkiewicz, I. Duran, M. Tardocchi, G. Gorini, C. Morlock, G. Federici, and A. Litnovsky, "Diagnostics and control for the steady state and pulsed tokamak DEMO," *Nuclear Fusion*, vol. 56, no. 2, p. 026009, 2016.

[8] N. Bonanomi, C. Angioni, U. Plank, P. A. Schneider, C. F. Maggi, A. U. Team, E. M. Team, and J. Contributors, "Edge turbulent transport toward the L–H transition in ASDEX Upgrade and JET-ILW," *Physics of Plasmas*, vol. 28, no. 5, p. 052504, 2021.

[9] M. Maslov, E. Lerche, F. Auriemma, E. Belli, C. Bourdelle, C. Challis, A. Chomiczewska, A. D. Molin, J. Eriksson, J. Garcia, J. Hobirk, I. Ivanova-Stanik, P. Jacquet, A. Kappatou, Y. Kazakov, D. Keeling, D. King, V. Kiptily, K. Kirov, D. Kos, R. Lorenzini, E. D. L. Luna, C. Maggi, J. Mailloux, P. Mantica, M. Marin, G. Matthews, I. Monakhov, M. Nocente, G. Pucella, D. Rigamonti, F. Rimini, S. Saarelma, M. Salewski, E. Solano, Štancar, G. Stankunas, H. Sun, M. Tardocchi, D. V. Eester, and J. Contributors, "JET D-T scenario with optimized non-thermal fusion," *Nuclear Fusion*, vol. 63, no. 11, p. 112002, 2023.

[10] G. Pintsuk, S. Brezinsek, J. W. Coenen, A. Huber, M. Rubel, A. Widdowson, and J. Contributors, "Metallography and mechanical parameters of plasma-exposed plasma-facing materials and components," *Physica Scripta*, vol. 2020, no. T171, p. 014042, 2020.

[11] V. Philipps, P. Mertens, G. Matthews, and H. Maier, "Overview of the JET ITER-like wall project," *Fusion Engineering and Design*, vol. 85, no. 7, pp. 1581–1586, 2010.

[12] G. F. Matthews, M. Beurskens, S. Brezinsek, M. Groth, E. Joffrin, A. Loving, and et al., "JET ITER-like wall—overview and experimental programme*," *Physica Scripta*, vol. 2011, no. T145, p. 014001, 2011.

[13] X. Litaudon, S. Abduallev, M. Abhangi, P. Abreu, M. Afzal, K. Aggarwal, and et al., "Overview of the JET results in support to ITER," *Nuclear Fusion*, vol. 57, no. 10, p. 102001, 2017.

[14] ITER Organisation, "32nd ITER council: A focus on updating the baseline." Press Release, 2023.

[15] A. Loarte, R. Pitts, T. Wauters, I. Nunes, F. Köchl, A. Polevoi, S. Kim, M. Lehnen, J. Artola, L. Chen, *et al.*, "Initial evaluations in support of the new ITER baseline and research plan," *Technical Report No. ITR-24-004*, 2024.

[16] M. Rubel, P. Petersson, E. Alves, S. Brezinsek, J. P. Coad, K. Heinola, M. Mayer, and A. Widdowson, "The role and application of ion beam analysis for studies of plasma-facing components in controlled fusion devices," *Nuclear Instruments and Methods in Physics Research Section B: Beam Interactions with Materials and Atoms*, vol. 371, pp. 4–11, 2016.

[17] J. Mailloux, N. Abid, K. Abraham, P. Abreu, O. Adabonyan, P. Adrich, and et al., "Overview of JET results for optimising ITER operation," *Nuclear Fusion*, vol. 62, no. 4, p. 042026, 2022.

[18] M. Mayer, S. Krat, A. Baron-Wiechec, Y. Gasparyan, K. Heinola, S. Koivuranta, J. Likonen, C. Ruset, G. de Saint-Aubin, A. Widdowson, and J. Contributors, "Erosion and deposition in the JET divertor during the second ITER-like wall campaign," *Physica Scripta*, vol. 2017, no. T170, p. 014058, 2017.

[19] A. Widdowson, S. Aleiferis, E. Alves, L. Avotina, A. Baron-Wiechec, N. Catarino, J. P. Coad, V. Corregidor, K. Heinola, I. Jepu, C. Makepeace, and J. Contributors, "Fuel inventory and material migration of JET main chamber plasma facing components compared over three operational periods," *Physica Scripta*, vol. 2020, no. T171, p. 014051, 2020.

[20] S. Krat, M. Mayer, A. Baron-Wiechec, S. Brezinsek, P. Coad, Y. Gasparyan, K. Heinola, I. Jepu, J. Likonen, P. Petersson, C. Ruset, G. de Saint-Aubin, A. Widdowson, and J. contributors, "Comparison of erosion and deposition in JET divertor during the first three ITER-like wall campaigns," *Physica Scripta*, vol. 2020, no. T171, p. 014059, 2020.

[21] S. Lee, Y. Hatano, M. Tokitani, S. Masuzaki, Y. Oya, T. Otsuka, N. Ashikawa, Y. Torikai, N. Asakura, H. Nakamura, K. Isobe, H. Kurotaki, D. Hamaguchi, T. Hayashi, A. Widdowson, S. Jachmich, J. Likonen, and M. Rubel, "Global distribution of tritium in JET with the ITER-like wall," *Nuclear Materials and Energy*, vol. 26, p. 100930, 2021.

[22] S. Krat, M. Mayer, J. Coad, C. Lungu, K. Heinola, A. Baron-Wiechec, I. Jepu, and A. Widdowson, "Comparison of JET inner wall erosion in the first three ITER-like wall campaigns," *Nuclear Materials and Energy*, vol. 29, p. 101072, 2021.

[23] L. Dittrich, P. Petersson, S. Moon, M. Rubel, T. T. Tran, and A. Widdowson, "Retention of noble and rare isotope gases in plasma-facing components – experience from the JET tokamak with the ITER-like wall," *Fusion Engineering and Design*, vol. 192, p. 113620, 2023.

[24] S. Brezinsek, "Plasma-surface interaction in the Be/W environment: Conclusions drawn from the JET-ILW for ITER," *Journal of Nuclear Materials*, vol. 463, pp. 11–21, 2015.

[25] D. Segal, A. Cerfon, and J. Freidberg, "Steady state versus pulsed tokamak reactors," *Nuclear Fusion*, vol. 61, no. 4, p. 045001, 2021.

[26] B. Martin, *Nuclear and Particle Physics: An Introduction.* John Wiley & Sons, Ltd, 2006.

[27] L. Torrisi, S. Cavallaro, M. Cutroneo, L. Giuffrida, J. Krasa, D. Margarone, A. Velyhan, J. Kravarik, J. Ullschmied, J. Wolowski, A. Szydlowski, and M. Rosinski, "Deuterium–deuterium nuclear reaction induced by high intensity laser pulses," *Applied Surface Science*, vol. 272, pp. 42–45, 2013.

[28] EUROfusion, "Breaking new ground: JET tokamak's latest fusion energy record shows mastery of fusion processes.." `https://euro-fusion.org/eurofusion-news/dte3record/`, 2024.

[29] S. Das, "Recent advances in characterising irradiation damage in tungsten for fusion power," *SN Applied Sciences*, vol. 1, no. 12, p. 1614, 2019.

[30] J. Linke, J. Du, T. Loewenhoff, G. Pintsuk, B. Spilker, I. Steudel, and M. Wirtz, "Challenges for plasma-facing components in nuclear fusion," *Matter and Radiation at Extremes*, vol. 4, no. 5, p. 056201, 2019.

[31] D. E. J. Armstrong, P. D. Edmondson, and S. G. Roberts, "Effects of sequential tungsten and helium ion implantation on nano-indentation hardness of tungsten," *Applied Physics Letters*, vol. 102, no. 25, p. 251901, 2013.

[32] S. Gonderman, J. Tripathi, T. Sizyuk, and A. Hassanein, "Suppression of surface microstructure evolution in W and W–Ta alloys during simultaneous and sequential He and D ion irradiation in fusion relevant conditions," *Nuclear Fusion*, vol. 57, no. 8, p. 086001, 2017.

[33] M. Gilbert and J.-C. Sublet, "Neutron-induced transmutation effects in W and W-alloys in a fusion environment," *Nuclear Fusion*, vol. 51, no. 4, p. 043005, 2011.

[34] M. Gilbert, S. Dudarev, S. Zheng, L. Packer, and J.-C. Sublet, "An integrated model for materials in a fusion power plant: transmutation, gas production, and helium embrittlement under neutron irradiation," *Nuclear Fusion*, vol. 52, no. 8, p. 083019, 2012.

[35] M. R. Gilbert, J.-C. Sublet, and R. A. Forrest, *Handbook of activation, transmutation, and radiation damage properties of the elements simulated using FISPACT-II & TENDL-2014; Magnetic Fusion Plants.* Culham Centre for Fusion Energy, 2015.

[36] M. Gilbert, J.-C. Sublet, and S. Dudarev, "Spatial heterogeneity of tungsten transmutation in a fusion device," *Nuclear Fusion*, vol. 57, no. 4, p. 044002, 2017.

[37] C. E. Beck, S. G. Roberts, P. D. Edmondson, and D. E. J. Armstrong, "Effect of alloy composition & helium ion-irradiation on the mechanical properties of tungsten, Tungsten-Tantalum & Tungsten-Rhenium for fusion power applications," *MRS Online Proceedings Library*, vol. 1514, no. 1, p. 99, 2013.

[38] S. Gonderman, J. Tripathi, T. Novakowski, T. Sizyuk, and A. Hassanein, "The effect of low energy helium ion irradiation on tungsten-tantalum (W-Ta) alloys under fusion relevant conditions," *Journal of Nuclear Materials*, vol. 491, pp. 199–205, 2017.

[39] V. Barabash, G. Federici, M. Rödig, L. Snead, and C. Wu, "Neutron irradiation effects on plasma facing materials," *Journal of Nuclear Materials*, vol. 283-287, pp. 138–146, 2000.

[40] X. Yi, M. Jenkins, M. Briceno, S. Roberts, Z. Zhou, and M. Kirk, "In situ study of self-ion irradiation damage in W and W–5Re at 500°C," *Philosophical Magazine*, vol. 93, no. 14, pp. 1715–1738, 2013.

[41] V. Philipps, "Tungsten as material for plasma-facing components in fusion devices," *Journal of Nuclear Materials*, vol. 415, no. 1, Supplement, pp. S2–S9, 2011.

[42] M. Gilbert and J.-C. Sublet, "Differential dpa calculations with spectra-pka," *Journal of Nuclear Materials*, vol. 504, pp. 101–108, 2018.

[43] J. Matolich, H. Nahm, and J. Moteff, "Swelling in neutron irradiated tungsten and tungsten-25 percent rhenium," *Scripta Metallurgica*, vol. 8, no. 7, pp. 837–841, 1974.

[44] B. Khripunov, V. Koidan, A. Ryazanov, V. Gureev, S. Latushkin, E. Semenov, and V. Stolyarova, "Impact of deuterium plasma flux on fusion reactor materials: radiation damage, surface modification, erosion," *Physics of Atomic Nuclei*, vol. 84, no. 7, pp. 1252–1258, 2021.

[45] S. Zinkle and G. Was, "Materials challenges in nuclear energy," *Acta Materialia*, vol. 61, no. 3, pp. 735–758, 2013.

[46] I. de Broglie, C. Beck, W. Liu, and F. Hofmann, "Temperature dependence of helium-implantation-induced lattice swelling in polycrystalline tungsten: X-ray micro-diffraction and eigenstrain modelling," *Scripta Materialia*, vol. 107, pp. 96–99, 2015.

[47] X. Fang, A. Kreter, M. Rasinski, C. Kirchlechner, S. Brinckmann, C. Linsmeier, and G. Dehm, "Hydrogen embrittlement of tungsten induced by deuterium plasma: Insights from nanoindentation tests," *Journal of Materials Research*, vol. 33, pp. 3530–3536, 2018.

[48] P. Lhuillier, T. Belhabib, P. Desgardin, B. Courtois, T. Sauvage, M. Barthe, A. Thomann, P. Brault, and Y. Tessier, "Trapping and release of helium in tungsten," *Journal of Nuclear Materials*, vol. 416, no. 1, pp. 13–17, 2011.

[49] J. S.-L. Gibson, S. G. Roberts, and D. E. Armstrong, "High temperature indentation of helium-implanted tungsten," *Materials Science and Engineering: A*, vol. 625, pp. 380–384, 2015.

[50] C. Becquart and C. Domain, "Solute–point defect interactions in bcc systems: Focus on first principles modelling in W and RPV steels," *Current Opinion in Solid State and Materials Science*, vol. 16, no. 3, pp. 115–125, 2012.

[51] T. Tanabe, "Review of hydrogen retention in tungsten," *Physica Scripta*, vol. 2014, no. T159, p. 014044, 2014.

[52] S. Sharafat, A. Takahashi, K. Nagasawa, and N. Ghoniem, "A description of stress driven bubble growth of helium implanted tungsten," *Journal of Nuclear Materials*, vol. 389, no. 2, pp. 203–212, 2009.

[53] Y. Zayachuk, M. 't Hoen, P. Z. van Emmichoven, D. Terentyev, I. Uytdenhouwen, and G. van Oost, "Surface modification of tungsten and tungsten–tantalum alloys exposed to high-flux deuterium plasma and its impact on deuterium retention," *Nuclear Fusion*, vol. 53, no. 1, p. 013013, 2013.

[54] K. Wang, R. Doerner, M. J. Baldwin, F. W. Meyer, M. E. Bannister, A. Darbal, R. Stroud, and C. M. Parish, "Morphologies of tungsten nanotendrils grown under helium exposure," *Scientific reports*, vol. 7, no. 1, p. 42315, 2017.

[55] D. Nishijima, R. Doerner, D. Iwamoto, Y. Kikuchi, M. Miyamoto, M. Nagata, I. Sakuma, K. Shoda, and Y. Ueda, "Response of fuzzy tungsten surfaces to pulsed plasma bombardment," *Journal of Nuclear Materials*, vol. 434, no. 1, pp. 230–234, 2013.

[56] S. Kajita, G. D. Temmerman, T. Morgan, S. van Eden, T. de Kruif, and N. Ohno, “Thermal response of nanostructured tungsten,” *Nuclear Fusion*, vol. 54, no. 3, p. 033005, 2014.

[57] J. Gunn, S. Carpentier-Chouchana, F. Escourbiac, T. Hirai, S. Panayotis, R. Pitts, Y. Corre, R. Dejarnac, M. Firdaouss, M. Kočan, M. Komm, A. Kukushkin, P. Languille, M. Missirlian, W. Zhao, and G. Zhong, “Surface heat loads on the ITER divertor vertical targets,” *Nuclear Fusion*, vol. 57, no. 4, p. 046025, 2017.

[58] T. Evans, “ELM mitigation techniques,” *Journal of Nuclear Materials*, vol. 438, pp. S11–S18, 2013.

[59] T. Eich, B. Sieglin, A. Scarabosio, A. Herrmann, A. Kallenbach, G. Matthews, S. Jachmich, S. Brezinsek, M. Rack, and R. Goldston, “Empiricial scaling of inter-ELM power widths in ASDEX Upgrade and JET,” *Journal of Nuclear Materials*, vol. 438, pp. S72–S77, 2013.

[60] M. Wirtz, J. Linke, T. Loewenhoff, G. Pintsuk, and I. Uytdenhouwen, “Transient heat load challenges for plasma-facing materials during long-term operation,” *Nuclear Materials and Energy*, vol. 12, pp. 148–155, 2017.

[61] J. Gunn, S. Carpentier-Chouchana, R. Dejarnac, F. Escourbiac, T. Hirai, M. Komm, A. Kukushkin, S. Panayotis, and R. Pitts, “Ion orbit modelling of ELM heat loads on ITER divertor vertical targets,” *Nuclear Materials and Energy*, vol. 12, pp. 75–83, 2017.

[62] G. Pintsuk, M. Bednarek, P. Gavila, S. Gerzoskovitz, J. Linke, P. Lorenzetto, B. Riccardi, and F. Escourbiac, “Characterization of ITER tungsten qualification mock-ups exposed to high cyclic thermal loads,” *Fusion Engineering and Design*, vol. 98-99, pp. 1384–1388, 2015.

[63] M. T. L. W. Sergey Smolentsev, Thomas Rognlien and C. Kessel, “Integrated liquid metal flowing first wall and open-surface divertor for fusion nuclear science facility: Concept, design, and analysis,” *Fusion Science and Technology*, vol. 75, no. 8, pp. 939–958, 2019.

[64] C. Kessel, D. Andruczyk, J. Blanchard, T. Bohm, A. Davis, K. Hollis, P. Humrickhouse, M. Hvasta, M. Jaworski, J. Jun, *et al.*, “Critical exploration of liquid metal plasma-facing components in a fusion nuclear science facility,” *Fusion Science and Technology*, vol. 75, no. 8, pp. 886–917, 2019.

[65] C. Linsmeier, B. Unterberg, J. Coenen, R. Doerner, H. Greuner, A. Kreter, J. Linke, and H. Maier, “Material testing facilities and programs for plasma-facing component testing,” *Nuclear Fusion*, vol. 57, no. 9, p. 092012, 2017.

[66] W. Haynes, *CRC Handbook of Chemistry and Physics*. CRC Handbook of Chemistry and Physics, CRC Press, 2014.

[67] B. Spilker, *The Impact of Transient Thermal Loads on Beryllium as Plasma Facing Material*. Dr., RWTH Aachen, Jülich, 2017.

[68] A. Herrmann, I. Zammuto, M. Balden, H. Greuner, N. Jaksic, A. Kallenbach, M. Li, R. Neu, and V. Rohde, “Experiences with a solid tungsten divertor in ASDEX Upgrade,” *Nuclear Materials and Energy*, vol. 12, p. 205–209, 2017.

[69] T. Hino and M. Akiba, “Japanese developments of fusion reactor plasma facing components,” *Fusion Engineering and Design*, vol. 49-50, pp. 97–105, 2000.

[70] T. Hirai, K. Ezato, and P. Majerus, “ITER relevant high heat flux testing on plasma facing surfaces,” *MATERIALS TRANSACTIONS*, vol. 46, no. 3, p. 412–424, 2005.

[71] J. Bonal and C. Wu, "Neutron irradiation effects on the thermal conductivity and dimensional stability of carbon fiber composites at divertor conditions," *Journal of Nuclear Materials*, vol. 228, no. 2, pp. 155–161, 1996.

[72] T. Loarer, C. Brosset, J. Bucalossi, P. Coad, G. Esser, J. Hogan, J. Likonen, M. Mayer, P. Morgan, V. Philipps, V. Rohde, J. Roth, M. Rubel, E. Tsitrone, and A. Widdowson, "Gas balance and fuel retention in fusion devices," *Nuclear Fusion*, vol. 47, no. 9, p. 1112–1120, 2007.

[73] G. Matthews, "Plasma operation with an all metal first-wall: Comparison of an ITER-like wall with a carbon wall in JET," *Journal of Nuclear Materials*, vol. 438, pp. S2–S10, 2013.

[74] T. Loarer, S. Brezinsek, V. Philipps, J. Bucalossi, D. Douai, H. Esser, S. Grunhagen, J. Hobirk, S. Jachmich, E. Joffrin, U. Kruezi, C. Lowry, G. Matthews, R. Smith, E. Tsitrone, and S. Vartanian, "Comparison of long term fuel retention in JET between carbon and the ITER-Like Wall," *Journal of Nuclear Materials*, vol. 438, pp. S108–S113, 2013.

[75] D. Yao, G. Luo, S. Du, L. Cao, Z. Zhou, T. Xu, X. Ji, C. Liu, C. Liang, Q. Li, W. Wang, S. Zhao, Y. Xu, L. Li, Z. Wang, X. X. M. Qi, S. Wang, and J. Li, "Overview of the EAST in-vessel components upgrade," *Fusion Engineering and Design*, vol. 98–99, p. 1692–1695, 2015.

[76] M. Missirlian, J. Bucalossi, Y. Corre, F. Ferlay, M. Firdaouss, P. Garin, A. Grosman, D. Guilhem, J. Gunn, P. Languille, *et al.*, "The WEST project: Current status of the ITER-like tungsten divertor," *Fusion Engineering and Design*, vol. 89, no. 7-8, pp. 1048–1053, 2014.

[77] J. Likonen, J. Coad, E. Alves, N. Catarino, I. Coffey, S. Krat, M. Mayer, K. Mizohata, and A. Widdowson, "Material transport from marker tiles in the JET divertor," *Nuclear Materials and Energy*, vol. 36, p. 101505, 2023.

[78] E. Pajuste, A. S. Teimane, G. Kizane, L. Avotina, M. Halitovs, A. Lescinskis, A. Vitins, P. Kalnina, E. Lagzdina, R. J. Zabolockis, and J. Contributors, "Tritium in plasma-facing components of JET with the ITER-like-wall," *Physica Scripta*, vol. 96, no. 12, p. 124050, 2021.

[79] M. Jahan, M. Rahman, and Y. Wong, "A review on the conventional and micro-electrodischarge machining of tungsten carbide," *International Journal of Machine Tools and Manufacture*, vol. 51, no. 12, pp. 837–858, 2011.

[80] S. Omole, A. Lunt, S. Kirk, and A. Shokrani, "Advanced processing and machining of tungsten and its alloys," *Journal of Manufacturing and Materials Processing*, vol. 6, no. 1, 2022.

[81] H. Liu, Y. Oshida, S. University, and L. R. Center, *Literature Survey on Oxidations and Fatigue Lives at Elevated Temperatures.* NASA contractor report, Syracuse University, 1984.

[82] R. Mohan, R. Manivannan, V. Kaviarasan, S. Sangeetha, and S. Prabakar, "Experimental investigation in EDM by using brass electrode with Inconel 690 materials in mixed dielectric medium," *Materials Today: Proceedings*, vol. 37, pp. 3747–3754, 2021.

[83] T. Kawakami and M. Kunieda, "Study on factors determining limits of minimum machinable size in micro EDM," *CIRP Annals*, vol. 54, no. 1, pp. 167–170, 2005.

[84] Z. Chen, J. Moverare, R. L. Peng, and S. Johansson, "Surface integrity and fatigue performance of Inconel 718 in wire electrical discharge machining," *Procedia CIRP*, vol. 45, pp. 307–310, 2016.

[85] P. Govindan and S. S. Joshi, "Analysis of micro-cracks on machined surfaces in dry electrical discharge machining," *Journal of Manufacturing Processes*, vol. 14, no. 3, pp. 277–288, 2012.

[86] A. Mamalis, G. Vosniakos, N. Vaxevanidis, and J. Prohászka, "Macroscopic and microscopic phenomena of electro-discharge machined steel surfaces: An experimental investigation," *Journal of Mechanical Working Technology*, vol. 15, no. 3, pp. 335–356, 1987.

[87] H. Lee and T. Tai, "Relationship between EDM parameters and surface crack formation," *Journal of Materials Processing Technology*, vol. 142, no. 3, pp. 676–683, 2003.

[88] Y. Guu, "AFM surface imaging of AISI D2 tool steel machined by the EDM process," *Applied Surface Science*, vol. 242, no. 3, pp. 245–250, 2005.

[89] Y. Guu and M. T.-K. Hou, "Effect of machining parameters on surface textures in EDM of Fe-Mn-Al alloy," *Materials Science and Engineering: A*, vol. 466, no. 1, pp. 61–67, 2007.

[90] Y. Zhang, Y. Liu, R. Ji, and B. Cai, "Study of the recast layer of a surface machined by sinking electrical discharge machining using water-in-oil emulsion as dielectric," *Applied Surface Science*, vol. 257, no. 14, pp. 5989–5997, 2011.

[91] G. L. Krasko, "Effect of impurities on the electronic structure of grain boundaries and intergranular cohesion in tungsten," *International Journal of Refractory Metals and Hard Materials*, vol. 12, no. 5, pp. 251–260, 1993.

[92] P. A. Olsson and J. Blomqvist, "Intergranular fracture of tungsten containing phosphorus impurities: A first principles investigation," *Computational Materials Science*, vol. 139, pp. 368–378, 2017.

[93] P. A. Olsson, P. Hiremath, and S. Melin, "Atomistic investigation of the impact of phosphorus impurities on the tungsten grain boundary decohesion," *Computational Materials Science*, vol. 219, p. 112017, 2023.

[94] B. Gludovatz, S. Wurster, A. Hoffmann, and R. Pippan, "Fracture toughness of polycrystalline tungsten alloys," *International Journal of Refractory Metals and Hard Materials*, vol. 28, no. 6, pp. 674–678, 2010.

[95] B. Gludovatz, S. Wurster, T. Weingärtner, A. Hoffmann, and R. Pippan, "Influence of impurities on the fracture behaviour of tungsten," *Philosophical Magazine*, vol. 91, no. 22, pp. 3006–3020, 2011.

[96] Tran-Huu-Loi, J. P. Morniroli, M. Gantois, and M. Lahaye, "Brittle fracture of polycrystalline tungsten," 1985.

[97] G. Pintsuk, S. Antusch, T. Weingaertner, and M. Wirtz, "Recrystallization and composition dependent thermal fatigue response of different tungsten grades," *International Journal of Refractory Metals and Hard Materials*, vol. 72, pp. 97–103, 2018.

[98] E. Lassner and W.-D. Schubert, *Tungsten: Properties, Chemistry, Technology of the Elements, Alloys, and Chemical Compounds.* Springer Science & Business Media, 1999.

[99] A. Warren, A. Nylund, and I. Olefjord, "Oxidation of tungsten and tungsten carbide in dry and humid atmospheres," *International Journal of Refractory Metals and Hard Materials*, vol. 14, no. 5, pp. 345–353, 1996.

[100] J. Habainy, S. Iyengar, K. B. Surreddi, Y. Lee, and Y. Dai, "Formation of oxide layers on tungsten at low oxygen partial pressures," *Journal of Nuclear Materials*, vol. 506, pp. 26–34, 2018.

[101] A. Babak and E. Uskov, "Problem of high temperature embrittlement of tungsten," *Probl. Proch.;(Ukrainian SSR)*, vol. 5, 1983.

[102] D. Rupp and S. M. Weygand, "Experimental investigation of the fracture toughness of polycrystalline tungsten in the brittle and semi-brittle regime," *Journal of Nuclear Materials*, vol. 386-388, pp. 591–593, 2009.

[103] K. Wang, D. Ren, X. Zan, L. Luo, X. Zhu, and Y. Wu, "Recrystallization behavior of pure tungsten hot-rolled with high accumulated strain during annealing at 1250 °C–1350 °C," *Materials Science and Engineering: A*, vol. 806, p. 140828, 2021.

[104] C. Ren, Z. Fang, M. Koopman, B. Butler, J. Paramore, and S. Middlemas, "Methods for improving ductility of tungsten - a review," *International Journal of Refractory Metals and Hard Materials*, vol. 75, pp. 170–183, 2018.

[105] K. Farrell, A. Schaffhauser, and J. Stiegler, "Recrystallization, grain growth and the ductile-brittle transition in tungsten sheet," *Journal of the Less Common Metals*, vol. 13, no. 2, pp. 141–155, 1967.

[106] J. W. Coenen, V. Philipps, S. Brezinsek, G. Pintsuk, T. Tanabe, Y. Ueda, U. Samm, and the TEXTOR team, "Analysis of structural changes and high-heat-flux tests on pre-damaged tungsten from tokamak melt experiments," *Physica Scripta*, vol. 2011, no. T145, p. 014066, 2011.

[107] J. Coenen, V. Philipps, S. Brezinsek, G. Pintsuk, I. Uytdenhouwen, M. Wirtz, A. Kreter, K. Sugiyama, H. Kurishita, Y. Torikai, Y. Ueda, U. Samm, and the TEXTOR-Team, "Melt-layer ejection and material changes of three different tungsten materials under high heat-flux conditions in the tokamak edge plasma of TEXTOR," *Nuclear Fusion*, vol. 51, no. 11, p. 113020, 2011.

[108] J. Coenen, B. Bazylev, S. Brezinsek, V. Philipps, T. Hirai, A. Kreter, J. Linke, G. Sergienko, A. Pospieszczyk, T. Tanabe, Y. Ueda, and U. Samm, "Tungsten melt layer motion and splashing on castellated tungsten surfaces at the tokamak TEXTOR," *Journal of Nuclear Materials*, vol. 415, no. 1, Supplement, pp. S78–S82, 2011.

[109] M. Spychalski, E. Fortuna-Zalesna, J. Zdunek, M. Rubel, A. Widdowson, S. Aleiferis, B. Thomas, and J. Contributors, "Tungsten Langmuir probes from JET-with the ITER-like wall: Assessment of mechanical properties by nano-indentation," *Physica Scripta*, vol. 96, no. 12, p. 124072, 2021.

[110] M. Mayer, S. Krat, W. V. Renterghem, A. Baron-Wiechec, S. Brezinsek, I. Bykov, P. Coad, Y. Gasparyan, K. Heinola, J. Likonen, A. Pisarev, C. Ruset, G. de Saint-Aubin, A. Widdowson, and J. Contributors, "Erosion and deposition in the JET divertor during the first ILW campaign," *Physica Scripta*, vol. 2016, no. T167, p. 014051, 2016.

[111] M. Tokitani, M. Miyamoto, S. Masuzaki, Y. Fujii, R. Sakamoto, Y. Oya, Y. Hatano, T. Otsuka, M. Oyaidzu, H. Kurotaki, T. Suzuki, D. Hamaguchi, K. Isobe, N. Asakura, A. Widdowson, and M. Rubel, "Micro-/nano-characterization of the surface structures on the divertor tiles from JET ITER-like wall," *Fusion Engineering and Design*, vol. 116, pp. 1–4, 2017.

[112] E. Fortuna-Zaleśna, J. Grzonka, M. Rubel, A. Garcia-Carrasco, A. Widdowson, A. Baron-Wiechec, L. Ciupiński, and JET Contributors, "Studies of dust from JET with the ITER-like wall: Composition and internal structure," *Nuclear Materials and Energy*, vol. 12, pp. 582–587, 2017.

[113] A. Widdowson, J. Coad, E. Alves, A. Baron-Wiechec, N. Barradas, S. Brezinsek, N. Catarino, V. Corregidor, K. Heinola, S. Koivuranta, S. Krat, A. Lahtinen, J. Likonen, G. Matthews, M. Mayer, P. Petersson, M. Rubel, and J. Contributors, "Overview of fuel inventory in JET with the ITER-like wall," *Nuclear Fusion*, vol. 57, no. 8, p. 086045, 2017.

[114] A. Widdowson, E. Alves, A. Baron-Wiechec, N. Barradas, N. Catarino, J. Coad, V. Corregidor, A. Garcia-Carrasco, K. Heinola, S. Koivuranta, S. Krat, A. Lahtinen, J. Likonen, M. Mayer, P. Petersson, M. Rubel, and S. Van Boxel, "Overview of the JET ITER-like wall divertor," *Nuclear Materials and Energy*, vol. 12, pp. 499–505, 2017.

[115] E. Fortuna-Zaleśna, J. Grzonka, S. Moon, M. Rubel, P. Petersson, A. Widdowson, and J. Contributors, "Fine metal dust particles on the wall probes from JET-ILW," *Physica Scripta*, vol. 2017, no. T170, p. 014038, 2017.

[116] S. Fazinić, T. Tadić, M. Vukšić, M. Rubel, P. Petersson, E. Fortuna-Zaleśna, and A. Widdowson, "Ion microbeam analyses of dust particles and codeposits from JET with the ITER-like wall," *Analytical Chemistry*, vol. 90, no. 9, pp. 5744–5752, 2018.

[117] M. Rubel, A. Widdowson, J. Grzonka, E. Fortuna-Zalesna, S. Moon, P. Petersson, N. Ashikawa, N. Asakura, D. Hamaguchi, Y. Hatano, K. Isobe, S. Masuzaki, H. Kurotaki, Y. Oya, M. Oyaidzu, and M. Tokitani, "Dust generation in tokamaks: Overview of beryllium and tungsten dust characterisation in JET with the ITER-like wall," *Fusion Engineering and Design*, vol. 136, pp. 579–586, 2018.

[118] M. Tokitani, M. Miyamoto, S. Masuzaki, R. Sakamoto, Y. Oya, Y. Hatano, T. Otsuka, M. Oyaidzu, H. Kurotaki, T. Suzuki, D. Hamaguchi, K. Isobe, N. Asakura, A. Widdowson, K. Heinola, and M. Rubel, "Plasma-wall interaction on the divertor tiles of JET ITER-like wall from the viewpoint of micro/nanoscopic observations," *Fusion Engineering and Design*, vol. 136, pp. 199–204, 2018.

[119] P. Ström, P. Petersson, M. Rubel, E. Fortuna-Zaleśna, A. Widdowson, and G. Sergienko, "Analysis of deposited layers with deuterium and impurity elements on samples from the divertor of JET with ITER-like wall," *Journal of Nuclear Materials*, vol. 516, pp. 202–213, 2019.

[120] S. Fazinić, I. Božičević-Mihalić, G. Provatas, T. Tadić, M. Rubel, E. Fortuna-Zaleśna, A. Widdowson, and J. contributors, "Micro-analyses of dust particles generated in the JET tokamak with the ITER-like wall," *Nuclear Fusion*, vol. 60, no. 12, p. 126031, 2020.

[121] E. Fortuna-Zaleśna, T. Plociński, S. W. Moon, P. Petersson, M. Rubel, A. Widdowson, and J. Contributors, "Dust generation and accumulation in JET-ILW: morphology and stability of co-deposits on main plasma-facing components and wall probes," *Physica Scripta*, vol. 96, no. 12, p. 124038, 2021.

[122] S. Fazinić, G. Provatas, I. Božičević Mihalić, T. Tadić, M. Rubel, J. Grzonka, P. Petersson, A. Widdowson, S. Moon, and E. Fortuna-Zaleśna, "Dust monitors in JET with ITER-like wall for diagnosis of mobilized particles and co-deposited layers," *Materials*, vol. 15, no. 23, p. 8353, 2022.

[123] V. Riccardo, G. Arnoux, S. Collins, P. Lomas, G. Matthews, N. Pace, and V. Thompson, "Operational impact on the JET ITER-like wall in-vessel components," *Fusion Engineering and Design*, vol. 89, no. 7, pp. 1059–1063, 2014.

[124] C. Thomser, V. Bailescu, S. Brezinsek, J. Coenen, H. Greuner, T. Hirai, J. Linke, C. Lungu, H. Maier, G. Matthews, *et al.*, "Plasma facing materials for the JET ITER-like wall," *Fusion Science and Technology*, vol. 62, no. 1, pp. 1–8, 2012.

[125] A. Czarnecka, V. Bobkov, I. H. Coffey, L. Colas, P. Jacquet, K. D. Lawson, E. Lerche, C. Maggi, M.-L. Mayoral, T. Pütterich, D. Van Eester, and J.-E. contributors, “Spectroscopic investigation of heavy impurity behaviour during ICRH with the JET ITER-like wall,” *AIP Conference Proceedings*, vol. 1580, no. 1, pp. 227–230, 2014.

[126] S. Brezinsek, T. Loarer, V. Philipps, H. Esser, S. Grünhagen, R. Smith, R. Felton, J. Banks, P. Belo, A. Boboc, *et al.*, “Fuel retention studies with the ITER-like wall in JET,” *Nuclear Fusion*, vol. 53, no. 8, p. 083023, 2013.

[127] J. Romazanov, S. Brezinsek, D. Borodin, M. Groth, S. Wiesen, A. Kirschner, A. Huber, A. Widdowson, M. Airila, A. Eksaeva, *et al.*, “Beryllium global erosion and deposition at JET-ILW simulated with ERO2. 0,” *Nuclear materials and energy*, vol. 18, pp. 331–338, 2019.

[128] K. Soni, L. Moser, C. Porosnicu, R. Antunes, R. Arredondo, P. Dinca, R. Steiner, L. Marot, and E. Meyer, “Deuterium plasma sputtering of mixed Be-W layers,” *Journal of Nuclear Materials*, vol. 564, p. 153671, 2022.

[129] D. Ivanova, M. Rubel, A. Widdowson, P. Petersson, J. Likonen, L. Marot, E. Alves, A. Garcia-Carrasco, G. Pintsuk, and J.-E. Contributors, “An overview of the comprehensive first mirror test in JET with ITER-like wall,” *Physica Scripta*, vol. 2014, no. T159, p. 014011, 2014.

[130] M. Sertoli, J. Flanagan, M. Bacharis, O. Kardaun, A. Jarvinen, G. Matthews, S. Brezinsek, D. Harting, A. Cackett, E. Hodille, I. Coffey, E. Lazzaro, and T. Pütterich, “Impact of W events and dust on JET-ILW operation,” *Journal of Nuclear Materials*, vol. 463, pp. 837–841, 2015.

[131] A. Baron-Wiechec, E. Fortuna-Zaleśna, J. Grzonka, M. Rubel, A. Widdowson, C. Ayres, J. P. Coad, C. Hardie, K. Heinola, G. F. Matthews, and J. Contributors, “First dust study in JET with the ITER-like wall: sampling, analysis and classification,” *Nuclear Fusion*, vol. 55, no. 11, p. 113033, 2015.

[132] Z. He, H. He, J. Chen, R. Ding, and B. Pan, “Accumulation of beryllium and its effects on hydrogen retention in tungsten divertor,” *Nuclear Fusion*, vol. 58, no. 10, p. 106015, 2018.

[133] A. Lasa, D. Dasgupta, M. J. Baldwin, M. A. Cusentino, P. Hatton, D. Perez, B. P. Uberuaga, L. Yang, and B. D. Wirth, “Assessment of the literature about Be-W mixed material layer formation in the fusion reactor environment,” *Materials Research Express*, vol. 11, no. 3, p. 032002, 2024.

[134] H. Okamoto and L. Tanner, “The Be-W (Beryllium-Tungsten) system,” *Bulletin of Alloy Phase Diagrams*, vol. 7, no. 4, pp. 356–358, 1986.

[135] H. Goldschmidt and W. Ham, “The tungsten-rich end of the tungsten-beryllium system,” *Journal of the Less Common Metals*, vol. 10, no. 1, pp. 57–65, 1966.

[136] A. Allouche and C. Linsmeier, “Quantum study of tungsten interaction with beryllium (0001),” *Journal of Physics: Conference Series*, vol. 117, p. 012002, 2008.

[137] A. Wiltner and C. Linsmeier, “Formation of a surface alloy in the beryllium–tungsten system,” *Journal of Nuclear Materials*, vol. 337-339, pp. 951–955, 2005.

[138] A. Wiltner and C. Linsmeier, “Surface alloying of thin beryllium films on tungsten,” *New Journal of Physics*, vol. 8, no. 9, p. 181, 2006.

[139] C. Linsmeier, K. Ertl, J. Roth, A. Wiltner, K. Schmid, F. Kost, S. Bhattacharyya, M. Baldwin, and R. Doerner, "Binary beryllium–tungsten mixed materials," *Journal of Nuclear Materials*, vol. 363-365, pp. 1129–1137, 2007.

[140] A. Wiltner, F. Kost, S. Lindig, and C. Linsmeier, "Structural investigation of the Be–W intermetallic system," *Physica Scripta*, vol. 2007, pp. 133 – 136, 2007.

[141] A. Allouche, "Electronic aspects of beryllium–tungsten surface alloying, a density functional approach," *Chemical Physics Letters*, vol. 470, no. 1, pp. 119–122, 2009.

[142] A. Allouche, A. Wiltner, and C. Linsmeier, "Quantum modeling (DFT) and experimental investigation of beryllium–tungsten alloy formation," *Journal of Physics: Condensed Matter*, vol. 21, no. 35, p. 355011, 2009.

[143] M. Köppen, J. Riesch, A. Vollmer, and C. Linsmeier, "Interaction of energetic oxygen ions with the beryllium tungsten alloy Be_2W," *Physica Scripta*, vol. 2011, no. T145, p. 014015, 2011.

[144] M. Köppen, "Comparative Study of the Reactivity of the Tungsten Oxides WO_2 and WO_3 with Beryllium at Temperatures up to 1273 K," *Condensed Matter*, 2019.

[145] M. Köppen, M. Oberkofler, J. Riesch, K. Schmid, A. Vollmer, and C. Linsmeier, "Quantitative depth-resolved photoelectron spectroscopy analysis of the interaction of energetic oxygen ions with the beryllium–tungsten alloy Be_2W," *Journal of Nuclear Materials*, vol. 438, pp. S766–S770, 2013.

[146] K. Schmid, M. Baldwin, R. Doerner, and D. Nishijima, "Beryllium layer deposition on carbon and tungsten from beryllium-seeded plasmas," *Nuclear Technology*, vol. 159, no. 3, pp. 238–244, 2007.

[147] R. W. Conn, R. P. Doerner, and J. Won, "Beryllium as the plasma-facing material in fusion energy systems—experiments, evaluation, and comparison with alternative materials," *Fusion Engineering and Design*, vol. 37, no. 4, pp. 481–513, 1997.

[148] M. Cusentino, M. Wood, and A. Thompson, "Suppression of helium bubble nucleation in beryllium exposed tungsten surfaces," *Nuclear Fusion*, vol. 60, no. 12, p. 126018, 2020.

[149] M. Baldwin, R. Doerner, D. Nishijima, K. Tokunaga, and Y. Ueda, "The effects of high fluence mixed-species (deuterium, helium, beryllium) plasma interactions with tungsten," *Journal of Nuclear Materials*, vol. 390-391, pp. 886–890, 2009.

[150] R. Doerner, M. Baldwin, D. Nishijima, J. Roth, and K. Schmid, "Impact of beryllium surface layers on deuterium retention in tungsten," *Journal of Nuclear Materials*, vol. 415, no. 1, Supplement, pp. S717–S720, 2011.

[151] A. Allouche, N. Fernandez, and Y. Ferro, "Hydrogen retention and diffusion in tungsten beryllide," *Journal of Physics: Condensed Matter*, vol. 26, no. 31, p. 315012, 2014.

[152] A. Lasa, K. Heinola, and K. Nordlund, "The effect of beryllium on deuterium implantation in tungsten by atomistic simulations," *Nuclear Fusion*, vol. 54, no. 12, p. 123021, 2014.

[153] H.-B. Zhou, N. K. Momanyi, Y.-H. Li, W. Jiang, and X.-C. Li, "Paving a way to suppress hydrogen blistering by investigating the hydrogen–beryllium interaction in tungsten," *RSC Adv.*, vol. 6, pp. 103622–103631, 2016.

[154] M. Baldwin, R. Doerner, D. Nishijima, D. Buchenauer, W. Clift, R. Causey, and K. Schmid, "Be–W alloy formation in static and divertor-plasma simulator experiments," *Journal of Nuclear Materials*, vol. 363-365, pp. 1179–1183, 2007.

[155] G. Federici, R. Anderl, P. Andrew, J. Brooks, R. Causey, J. Coad, D. Cowgill, R. Doerner, A. Haasz, G. Janeschitz, W. Jacob, G. Longhurst, R. Nygren, A. Peacock, M. Pick, V. Philipps, J. Roth, C. Skinner, and W. Wampler, "In-vessel tritium retention and removal in ITER," *Journal of Nuclear Materials*, vol. 266-269, pp. 14–29, 1999.

[156] A. Widdowson, E. Alves, C. F. Ayres, A. Baron-Wiechec, S. Brezinsek, N. Catarino, J. P. Coad, K. Heinola, J. Likonen, G. F. Matthews, M. Mayer, M. Rubel, and J.-E. Contributors, "Material migration patterns and overview of first surface analysis of the JET ITER-like wall," *Physica Scripta*, vol. 2014, no. T159, p. 014010, 2014.

[157] R. Reichle, P. Andrew, P. Bates, O. Bede, N. Casal, C. Choi, R. Barnsley, C. Damiani, L. Bertalot, G. Dubus, J. Ferreol, G. Jagannathan, M. Kocan, F. Leipold, S. Lisgo, V. Martin, J. Palmer, R. Pearce, V. Philipps, R. Pitts, R. Pampin, G. Passedat, A. Puiu, A. Suarez, P. Shigin, W. Shu, G. Vayakis, E. Veshchev, and M. Walsh, "Review of the ITER diagnostics suite for erosion, deposition, dust and tritium measurements," *Journal of Nuclear Materials*, vol. 463, pp. 180–184, 2015.

[158] J. I. Goldstein, D. E. Newbury, J. R. Michael, N. W. M. Ritchie, J. H. J. Scott, and D. C. Joy, *Scanning Electron Microscopy and X-Ray Microanalysis.* New York, NY: Springer Nature, fourth edition. ed., 2018.

[159] C. A. Volkert and A. M. Minor, "Focused ion beam microscopy and micromachining," *MRS bulletin*, vol. 32, no. 5, pp. 389–399, 2007.

[160] J. Mayer, L. A. Giannuzzi, T. Kamino, and J. Michael, "TEM sample preparation and FIB-induced damage," *MRS bulletin*, vol. 32, no. 5, pp. 400–407, 2007.

[161] T. Burnett, R. Kelley, B. Winiarski, L. Contreras, M. Daly, A. Gholinia, M. Burke, and P. Withers, "Large volume serial section tomography by Xe Plasma FIB dual beam microscopy," *Ultramicroscopy*, vol. 161, pp. 119–129, 2016.

[162] M. Miller, K. Russell, and G. Thompson, "Strategies for fabricating atom probe specimens with a dual beam FIB," *Ultramicroscopy*, vol. 102, no. 4, pp. 287–298, 2005.

[163] K. Thompson, D. Lawrence, D. Larson, J. Olson, T. Kelly, and B. Gorman, "In situ site-specific specimen preparation for atom probe tomography," *Ultramicroscopy*, vol. 107, no. 2-3, pp. 131–139, 2007.

[164] D. Blavette, A. Bostel, J.-M. Sarrau, B. Deconihout, and A. Menand, "An atom probe for three-dimensional tomography," *Nature*, vol. 363, no. 6428, pp. 432–435, 1993.

[165] T. F. Kelly and M. K. Miller, "Atom probe tomography," *Review of scientific instruments*, vol. 78, no. 3, 2007.

[166] A. Cerezo, T. Godfrey, and G. Smith, "Application of a position-sensitive detector to atom probe microanalysis," *Review of Scientific Instruments*, vol. 59, no. 6, pp. 862–866, 1988.

[167] L. A. Giannuzzi and F. A. Stevie, "A review of focused ion beam milling techniques for TEM specimen preparation," *Micron*, vol. 30, no. 3, pp. 197–204, 1999.

[168] A. Aitkaliyeva, J. W. Madden, B. D. Miller, J. I. Cole, and J. Gan, "Comparison of preparation techniques for nuclear materials for transmission electron microscopy (TEM)," *Journal of Nuclear Materials*, vol. 459, pp. 241–246, 2015.

[169] D. Williams and C. Carter, *Transmission Electron Microscopy: A Textbook for Materials Science.* No. v. 1 in Cambridge library collection, Springer, 2009.

[170] R. Brydson, *Aberration-corrected analytical transmission electron microscopy*, vol. 280. Wiley Online Library, 2011.

[171] P. W. Trimby, Y. Cao, Z. Chen, S. Han, K. J. Hemker, J. Lian, X. Liao, P. Rottmann, S. Samudrala, J. Sun, *et al.*, "Characterizing deformed ultrafine-grained and nanocrystalline materials using transmission Kikuchi diffraction in a scanning electron microscope," *Acta materialia*, vol. 62, pp. 69–80, 2014.

[172] W. C. Oliver and G. M. Pharr, "An improved technique for determining hardness and elastic modulus using load and displacement sensing indentation experiments," *Journal of Materials Research*, vol. 7, no. 6, pp. 1564–1583, 1992.

[173] W. Oliver and G. Pharr, "Measurement of hardness and elastic modulus by instrumented indentation: Advances in understanding and refinements to methodology," *Journal of materials research*, vol. 19, no. 1, 2004-01.

[174] W. D. Nix and H. Gao, "Indentation size effects in crystalline materials: A law for strain gradient plasticity," *Journal of the Mechanics and Physics of Solids*, vol. 46, no. 3, pp. 411–425, 1998.

[175] M. Rester, C. Motz, and R. Pippan, "Indentation across size scales – a survey of indentation-induced plastic zones in copper 111 single crystals," *Scripta Materialia*, vol. 59, no. 7, pp. 742–745, 2008.

[176] L. Chen, A. Ahadi, J. Zhou, and J.-E. Ståhl, "Modeling effect of surface roughness on nanoindentation tests," *Procedia CIRP*, vol. 8, pp. 334–339, 2013.

[177] J. Čech, P. Haušild, O. Kovářík, and A. Materna, "Examination of Berkovich indenter tip bluntness," *Materials Design*, vol. 109, pp. 347–353, 2016.

[178] D. Roundy, C. Krenn, M. L. Cohen, and J. Morris Jr, "The ideal strength of tungsten," *Philosophical Magazine A*, vol. 81, no. 7, pp. 1725–1747, 2001.

[179] A. Atkins and D. Tabor, "Plastic indentation in metals with cones," *Journal of the Mechanics and Physics of Solids*, vol. 13, no. 3, pp. 149–164, 1965.

[180] D. Tabor, *The hardness of metals.* Oxford university press, 2000.

[181] J.-L. Bucaille, S. Stauss, E. Felder, and J. Michler, "Determination of plastic properties of metals by instrumented indentation using different sharp indenters," *Acta materialia*, vol. 51, no. 6, pp. 1663–1678, 2003.

[182] S. Shim, J.-i. Jang, and G. M. Pharr, "Extraction of flow properties of single-crystal silicon carbide by nanoindentation and finite-element simulation," *Acta Materialia*, vol. 56, no. 15, pp. 3824–3832, 2008.

[183] A. Leitner, V. Maier-Kiener, and D. Kiener, "Extraction of flow behavior and Hall–Petch parameters using a nanoindentation multiple sharp tip approach," *Advanced engineering materials*, vol. 19, no. 4, p. 1600669, 2017.

[184] Y.-T. Cheng and C.-M. Cheng, "Can stress–strain relationships be obtained from indentation curves using conical and pyramidal indenters?," *Journal of Materials Research*, vol. 14, pp. 3493–3496, 1999.

[185] A. J. Cackett, C. D. Hardie, J. J. Lim, and E. Tarleton, "Spherical indentation of copper: Crystal plasticity vs experiment," *Materialia*, vol. 7, p. 100368, 2019.

[186] S. Jakob, *Investigation into the mechanical character of grain boundaries in technically pure and micro-doped molybdenum.* PhD thesis, Montanuniversitaet Leoben (000), 2021.

[187] A. Leitner, V. Maier-Kiener, and D. Kiener, “Essential refinements of spherical nanoindentation protocols for the reliable determination of mechanical flow curves,” *Materials Design*, vol. 146, pp. 69–80, 2018.

[188] S. Pathak, D. Stojakovic, and S. R. Kalidindi, “Measurement of the local mechanical properties in polycrystalline samples using spherical nanoindentation and orientation imaging microscopy,” *Acta Materialia*, vol. 57, no. 10, pp. 3020–3028, 2009.

[189] N. Catarino, “Van de graaff manual de operaÇÃo,” 2023. Available at: http://www.se.ctn.tecnico.ulisboa.pt/FisNuclear/LATR/Manuais/Manual_VG.pdf.

[190] V. Foteinou, F. Maragkos, H.-W. Becker, L. Hess, K. Ivanković, M. Kokkoris, M. Mayer, G. Provatas, and D. Rogalla, “Differential cross-section measurements for the ^{9}Be(^{3}He,^{3}He$_0$)^{9}Be elastic scattering and the ^{9}Be(^{3}He,p$_x$)^{11}B reactions,” *Nuclear Instruments and Methods in Physics Research Section B: Beam Interactions with Materials and Atoms*, vol. 542, pp. 158–175, 2023.

[191] M. Rieth, S. Dudarev, S. Gonzalez de Vicente, J. Aktaa, T. Ahlgren, S. Antusch, D. Armstrong, M. Balden, N. Baluc, M.-F. Barthe, *et al.*, “Recent progress in research on tungsten materials for nuclear fusion applications in europe,” *Journal of Nuclear Materials*, vol. 432, no. 1, pp. 482–500, 2013.

[192] R. Hill, *The mathematical theory of plasticity*, vol. 11. Oxford university press, 1998.

[193] K. Johnson, “The correlation of indentation experiments,” *Journal of the Mechanics and Physics of Solids*, vol. 18, no. 2, pp. 115–126, 1970.

[194] K. L. Johnson, *Contact Mechanics*. Cambridge University Press, 1985.

[195] C. Robertson, S. Poissonnet, and L. Boulanger, “Plasticity in ion-irradiated austenitic stainless steels,” *Journal of Materials Research*, vol. 13, no. 8, p. 2123–2131, 1998.

[196] P. Lied, W. Pantleon, C. Bonnekoh, S. Bonk, A. Hoffmann, J. Reiser, and M. Rieth, “Comparison of K-doped and pure cold-rolled tungsten sheets: Tensile properties and brittle-to-ductile transition temperatures,” *Journal of Nuclear Materials*, vol. 544, p. 152664, 2021.

[197] A. Alfonso, *Thermal stability of warm-rolled tungsten*. PhD thesis, DTU Mechanical Engineering, 2015.

[198] B. S. Kong, J. H. Shin, T. An, C. Jang, and H. C. Kim, “Strain-rate dependence of tensile behavior in commercial-grade tungsten—effect of recrystallization condition,” *Materials*, vol. 15, no. 17, 2022.

[199] A. Manhard, K. Schmid, M. Balden, and W. Jacob, “Influence of the microstructure on the deuterium retention in tungsten,” *Journal of Nuclear Materials*, vol. 415, no. 1, Supplement, pp. S632–S635, 2011.

[200] Y. Zayachuk, D. Armstrong, K. Bystrov, S. Van Boxel, T. Morgan, and S. Roberts, “Nanoindentation study of the combined effects of crystallography, heat treatment and exposure to high-flux deuterium plasma in tungsten,” *Journal of Nuclear Materials*, vol. 486, pp. 183–190, 2017.

[201] D. Armstrong, X. Yi, E. Marquis, and S. Roberts, “Hardening of self ion implanted tungsten and tungsten 5-wt% rhenium,” *Journal of Nuclear Materials*, vol. 432, no. 1, pp. 428–436, 2013.

[202] T. Hirai, S. Panayotis, V. Barabash, C. Amzallag, F. Escourbiac, A. Durocher, and et al., “Use of tungsten material for the ITER divertor,” *Nuclear Materials and Energy*, vol. 9, pp. 616–622, 2016.

[203] Y. Seki, K. Ezato, S. Suzuki, K. Yokoyama, H. Yamada, and T. Hirayama, “A study of plasma facing tungsten components with electrical discharge machined surface exposed to cyclic thermal loads,” *Fusion Engineering and Design*, vol. 109-111, pp. 1148–1152, 2016.

[204] Y. Hao, C. Tan, X. Yu, R. Chen, Z. Nie, Y. Ren, S. Yang, Y. Li, and F. Wang, “Effect of grain boundary misorientation angle on diffusion behavior in molybdenum-tungsten systems,” *Journal of Alloys and Compounds*, vol. 819, p. 152975, 2020.

[205] P. Díaz-Rodríguez, M. Panizo-Laiz, C. González, R. Iglesias, I. Martín-Bragado, R. González-Arrabal, J. M. Perlado, O. Peña-Rodríguez, and A. Rivera, “Direct observation of hydrogen permeation through grain boundaries in tungsten,” *Emergent Materials*, vol. 5, no. 4, pp. 1075–1087, 2022.

[206] B. Fu, M. Qiu, J. Cui, J. Wang, and Q. Hou, “Diffusion, trapping, and dissociation behaviours of helium at the 5 grain boundary in tungsten: A molecular dynamics study,” *Journal of Nuclear Materials*, vol. 543, p. 152599, 2021.

[207] B. Gault, F. Danoix, K. Hoummada, D. Mangelinck, and H. Leitner, “Impact of directional walk on atom probe microanalysis,” *Ultramicroscopy*, vol. 113, pp. 182–191, 2012.

[208] J. R. Stephens, *Effect of oxygen on mechanical properties of tungsten.* National Aeronautics and Space Administration, 1963.

[209] S. Tian, X. Li, A. Wang, Y. Chen, H. Li, and Y. Hu, “Hydrodenitrogenation of quinoline and decahydroquinoline over a surface nickel phosphosulfide phase,” *Catalysis Letters*, vol. 148, 2018.

[210] S. Oyama, P. Clark, X. Wang, T. Shido, Y. Iwasawa, S. Hayashi, and et al., “Structural characterization of tungsten phosphide (WP) hydrotreating catalysts by X-ray absorption spectroscopy and nuclear magnetic resonance spectroscopy,” *Journal of Physical Chemistry B - J PHYS CHEM B*, vol. 106, 2002.

[211] X.-J. Xiang, G.-Z. Song, X.-F. Zhou, H. Liang, Y. Xu, S.-J. Qin, and et al., “Congruent melting of tungsten phosphide at 5 GPa and 3200 °C for growing its large single crystals,” *Chinese Physics B*, vol. 29, no. 8, p. 088202, 2020.

[212] K. Gingerich, “Vaporization behavior and phosphorus decomposition pressures of tungsten monophosphide,” *The Journal of Physical Chemistry*, vol. 68, no. 4, pp. 768–772, 1964.

[213] J. Sun, B. Li, Q. Wang, P. Zhang, Y. Zhang, L. Gao, and X. Li, “Preparation of phosphorus-doped tungsten trioxide nanomaterials and their photocatalytic performances,” *Environmental Technology*, vol. 42, no. 26, pp. 4104–4114, 2021.

[214] W. Shu, E. Wakai, and T. Yamanishi, “Blister bursting and deuterium bursting release from tungsten exposed to high fluences of high flux and low energy deuterium plasma,” *Nuclear Fusion*, vol. 47, no. 3, p. 201, 2007.

[215] W. M. Shu, A. Kawasuso, Y. Miwa, E. Wakai, G.-N. Luo, and T. Yamanishi, “Microstructure dependence of deuterium retention and blistering in the near-surface region of tungsten exposed to high flux deuterium plasmas of 38 eV at 315 K,” *Physica Scripta*, vol. 2007, no. T128, p. 96, 2007.

[216] W. M. Shu, “High-dome blisters formed by deuterium-induced local superplasticity,” *Applied Physics Letters*, vol. 92, no. 21, p. 211904, 2008.

[217] W. Shu, A. Kawasuso, and T. Yamanishi, “Recent findings on blistering and deuterium retention in tungsten exposed to high-fluence deuterium plasma,” *Journal of Nuclear Materials*, vol. 386-388, pp. 356–359, 2009.

[218] W. Shu, M. Nakamichi, V. Alimov, G.-N. Luo, K. Isobe, and T. Yamanishi, “Deuterium retention, blistering and local melting at tungsten exposed to high-fluence deuterium plasma,” *Journal of Nuclear Materials*, vol. 390-391, pp. 1017–1021, 2009.

[219] B. Huang, B. He, Y. Xiao, R. Ang, J. Yang, J. Liao, Y. Yang, N. Liu, D. Pan, and J. Tang, “Microstructure and bubble formation of Al–K–Si doped tungsten prepared by spark plasma sintering,” *International Journal of Refractory Metals and Hard Materials*, vol. 54, pp. 335–341, 2016.

[220] C. Nowak, G. Schmitz, and R. Kirchheim, “Electric field effect on low temperature nanoscale oxidation,” *Surface Science*, vol. 604, no. 7, pp. 641–648, 2010.

[221] S. Cifuentes, M. Monge, and P. Pérez, “On the oxidation mechanism of pure tungsten in the temperature range 600–800°C,” *Corrosion Science*, vol. 57, pp. 114–121, 2012.

[222] V. Ivanov, *High Temperature Oxidation Protection of Tungsten.* NASA TT, National Aeronautics and Space Administration, 1969.

[223] M. Togaru, R. Sainju, L. Zhang, W. Jiang, and Y. Zhu, “Direct observation of tungsten oxidation studied by in situ environmental TEM,” *Materials Characterization*, vol. 174, p. 111016, 2021.

[224] J. Wendel, “Thermodynamics and kinetics of tungsten oxidation and tungsten oxide sublimation in the temperature interval 200–1100°C,” Master’s thesis, Lund University, 2014.

[225] A. Sips, J. Schweinzer, T. Luce, S. Wolfe, H. Urano, J. Hobirk, S. Ide, E. Joffrin, C. Kessel, S. Kim, P. Lomas, I. Nunes, T. Pütterich, F. Rimini, W. Solomon, J. Stober, F. Turco, P. de Vries, J. Contributors, T. A. U. team, T. D. team, T. C.-M. team, T. J.-U. team, I.-I. T. members, and experts, “Assessment of the baseline scenario at q95 $\sim$3 for ITER,” *Nuclear Fusion*, vol. 58, no. 12, p. 126010, 2018.

[226] C. Ruset, E. Grigore, M. Mayer, F. Baiasu, C. Porosnicu, S. Krat, A. Widdowson, J. Likonen, M. Analytis, and R. Meihsner, “Deuterium and beryllium depth profiles into the W-coated JET divertor tiles after ITER-like wall campaigns,” *Nuclear Materials and Energy*, vol. 30, p. 101151, 2022.

[227] J.-M. Collin, G. Mauvoisin, and R. El Abdi, “An experimental method to determine the contact radius changes during a spherical instrumented indentation,” *Mechanics of Materials*, vol. 40, no. 4, pp. 401–406, 2008.

[228] R. Kerr, Y. Zayachuk, A. Widdowson, E. Alves, N. Catarino, S. Lozano-Perez, and D. Armstrong, “Mechanical and microstructural analysis of tungsten exposed in JET deuterium plasmas,” *Nuclear Materials and Energy*, vol. 35, p. 101420, 2023.

[229] G. Grime and M. Dawson, “Recent developments in data acquisition and processing on the Oxford scanning proton microprobe,” *Nuclear Instruments and Methods in Physics Research Section B: Beam Interactions with Materials and Atoms*, vol. 104, no. 1, pp. 107–113, 1995.

[230] N. Catarino, A. Widdowson, A. Baron-Wiechec, J. P. Coad, K. Heinola, M. Rubel, N. P. Barradas, E. Alves, and J. Contributors, “Deposition in the tungsten divertor during the 2011–2016 campaigns in JET with ITER-like wall,” *Physica Scripta*, vol. 2020, no. T171, p. 014044, 2020.

[231] N. Barradas and C. Jeynes, "Advanced physics and algorithms in the IBA DataFurnace," *Nuclear Instruments and Methods in Physics Research Section B: Beam Interactions with Materials and Atoms*, vol. 266, no. 8, pp. 1875–1879, 2008.

[232] R. Sedláček, W. Blum, J. Kratochvil, and S. Forest, "Subgrain formation during deformation: physical origin and consequences," *Metallurgical and Materials Transactions A*, vol. 33, pp. 319–327, 2002.

[233] F. Ostermann, "Dislocation cell formation and recrystallization in tungsten," *Metallurgical Transactions*, vol. 2, no. 9, pp. 2737–2740, 1971.

[234] H. Wang, Z. Xie, M. Yu, B. Zhao, R. Liu, Q. Fang, X. Wang, C. Liu, and X. Wu, "Ultrafine-grained surface layer of tungsten via a simple two-step microstructure modulation," *International Journal of Refractory Metals and Hard Materials*, vol. 121, p. 106675, 2024.

[235] I. Balboa, G. Arnoux, T. Eich, B. Sieglin, S. Devaux, W. Zeidner, C. Morlock, U. Kruezi, G. Sergienko, D. Kinna, P. D. Thomas, M. Rack, and J. E. Contributors, "Upgrade of the infrared camera diagnostics for the JET ITER-like wall divertor," *Review of Scientific Instruments*, vol. 83, no. 10, p. 10D530, 2012.

[236] I. Balboa, S. Silburn, P. Drewelow, V. Huber, A. Huber, D. Kinna, M. Price, G. F. Matthews, S. Collins, J. Fessey, M. Rack, P. Trimble, and K.-D. Zastrow, "Recent developments of in-vessel calibration of mid-IR cameras at JET," *Review of Scientific Instruments*, vol. 87, no. 11, p. 11D419, 2016.

[237] M.-H. Aumeunier and J.-M. Travere, "Development of a realistic photonic modeling for the evaluation of infrared reflections in the metallic environment of ITER," *Review of Scientific Instruments*, vol. 81, no. 10, p. 10E524, 2010.

[238] R. Reichle, J.-P. Lasserre, F. Oelhoffen, C. Desgranges, F. Faisse, L. Eupherte, C. Pocheau, and M. Todeschini, "Infrared reflection properties and modelling of in situ reflection measurements on plasma-facing materials in Tore Supra," *Physica Scripta*, vol. 2009, no. T138, p. 014029, 2009.

[239] R. Reichle, P. Andrew, G. Counsell, J.-M. Drevon, A. Encheva, G. Janeschitz, D. Johnson, Y. Kusama, B. Levesy, A. Martin, C. S. Pitcher, R. Pitts, D. Thomas, G. Vayakis, and M. Walsh, "Defining the infrared systems for ITER," *Review of Scientific Instruments*, vol. 81, no. 10, p. 10E135, 2010.

[240] M.-H. Aumeunier, J.-M. Travere, R. Reichle, T. Loarer, E. Gauthier, D. Chabaud, and E. Humbert, "Simulation of the infrared views of the upper port VIS/IR imaging system of ITER," *IEEE Transactions on Plasma Science*, vol. 40, no. 3, pp. 753–760, 2012.

[241] J. Beal, *Erosion, deposition and material migration in the JET divertor with carbon and ITER-like walls.* PhD thesis, University of York, 2016.

[242] M. Brix, N. C. Hawkes, A. Boboc, V. Drozdov, S. E. Sharapov, and J.-E. Contributors, "Accuracy of EFIT equilibrium reconstruction with internal diagnostic information at JET," *Review of Scientific Instruments*, vol. 79, no. 10, p. 10F325, 2008.

[243] P. Mertens, H. Altmann, T. Hirai, M. Knaup, O. Neubauer, V. Philipps, J. Rapp, V. Riccardo, S. Sadakov, B. Schweer, A. Terra, I. Uytdenhouwen, and U. Samm, "A bulk tungsten divertor row for the outer strike point in JET," *Fusion Engineering and Design*, vol. 84, no. 7, pp. 1289–1293, 2009.

[244] Y. Corre, P. Bunting, J. Coenen, J. Gaspar, D. Iglesias, G. Matthews, I. Balboa, I. Coffey, R. Dejarnac, M. Firdaouss, E. Gauthier, S. Jachmich, K. Krieger, R. Pitts, M. Rack, S. Silburn, and J. Contributors, "Thermal analysis of protruding surfaces in the JET divertor," *Nuclear Fusion*, vol. 57, no. 6, p. 066009, 2017.

[245] K. Tsuchida, T. Miyazawa, A. Hasegawa, S. Nogami, and M. Fukuda, "Recrystallization behavior of hot-rolled pure tungsten and its alloy plates during high-temperature annealing," *Nuclear Materials and Energy*, vol. 15, pp. 158–163, 2018.

[246] A. Huber, D. Kinna, V. Huber, G. Arnoux, G. Sergienko, I. Balboa, C. Balorin, P. Carman, P. Carvalho, S. Collins, N. Conway, P. McCullen, A. Drenik, S. Jachmich, M. Jouve, C. Linsmeier, B. Lomanowski, P. Lomas, C. Lowry, C. Maggi, G. Matthews, A. Meigs, P. Mertens, I. Nunes, M. Price, P. Puglia, V. Riccardo, F. Rimini, A. Widdowson, K.-D. Zastrow, and J. contributors, "Real-time protection of the JET ITER-like wall based on near infrared imaging diagnostic systems," *Nuclear Fusion*, vol. 58, no. 10, p. 106021, 2018.

[247] L. Dittrich, S. Moon, P. Petersson, M. Rubel, A. Widdowson, and J. Contributors, "Deuterium retention and depth profiling of co-deposits on bulk beryllium and tungsten tiles from JET-ILW," in *47th EPS Conference on Plasma Physics, EPS 2021, 21 June 2021 through 25 June 2021*, pp. 1–4, European Physical Society (EPS), 2021.

[248] C. Guillemaut, M. Lennholm, J. Harrison, I. Carvalho, D. Valcarcel, R. Felton, S. Griph, C. Hogben, R. Lucock, G. F. Matthews, C. P. V. Thun, R. A. Pitts, S. Wiesen, and JET contributors, "Real-time control of divertor detachment in H-mode with impurity seeding using Langmuir probe feedback in JET-ITER-like wall," *Plasma Physics and Controlled Fusion*, vol. 59, no. 4, p. 045001, 2017.

[249] J. W. Coenen, G. F. Matthews, K. Krieger, D. Iglesias, P. Bunting, Y. Corre, S. Silburn, I. Balboa, B. Bazylev, N. Conway, I. Coffey, R. Dejarnac, E. Gauthier, J. Gaspar, S. Jachmich, I. Jepu, C. Makepeace, R. Scannell, M. Stamp, P. Petersson, R. A. Pitts, S. Wiesen, A. Widdowson, K. Heinola, A. Baron-Wiechec, and J. Contributors, "Transient induced tungsten melting at the Joint European Torus (JET)," *Physica Scripta*, vol. 2017, no. T170, p. 014013, 2017.

[250] K. Heinola, A. Widdowson, J. Likonen, T. Ahlgren, E. Alves, C. F. Ayres, A. Baron-Wiechec, N. Barradas, S. Brezinsek, N. Catarino, P. Coad, C. Guillemaut, I. Jepu, S. Krat, A. Lahtinen, G. F. Matthews, M. Mayer, and JET Contributors, "Experience on divertor fuel retention after two ITER-like wall campaigns," *Physica Scripta*, vol. 2017, no. T170, p. 014063, 2017.

[251] I. Ipatova, R. Harrison, S. Donnelly, M. Rushton, S. Middleburgh, and E. Jimenez-Melero, "Void evolution in tungsten and tungsten-5wt.% tantalum under in-situ proton irradiation at 800 and 1000 °C," *Journal of Nuclear Materials*, vol. 526, p. 151730, 2019.

[252] H. Iwakiri, K. Morishita, and N. Yoshida, "Effects of helium bombardment on the deuterium behavior in tungsten," *Journal of Nuclear Materials*, vol. 307–311, no. 1 SUPPL., p. 135–138, 2002.

[253] H. Lee, A. Haasz, J. Davis, R. Macaulay-Newcombe, D. Whyte, and G. Wright, "Hydrogen and helium trapping in tungsten under simultaneous irradiations," *Journal of Nuclear Materials*, vol. 363-365, pp. 898–903, 2007.

[254] B. Cipiti and G. Kulcinski, "Helium and deuterium implantation in tungsten at elevated temperatures," *Journal of Nuclear Materials*, vol. 347, no. 3, pp. 298–306, 2005.

[255] J. Roth and K. Schmid, "Hydrogen in tungsten as plasma-facing material," *Physica Scripta*, vol. 2011, no. T145, p. 014031, 2011.

[256] A. Suslova, O. El-Atwani, D. Sagapuram, S. Harilal, and A. Hassanein, "Recrystallization and grain growth induced by ELMs-like transient heat loads in deformed tungsten samples," *Scientific reports*, vol. 4, no. 1, p. 6845, 2014.

[257] C. Yin, G. Bonny, and D. Terentyev, "Anisotropy in the hardness of single crystal tungsten before and after neutron irradiation," *Journal of Nuclear Materials*, vol. 546, p. 152759, 2021.

[258] M. Yuasa, H. Matsumoto, M. Hakamada, and M. Mabuchi, "Effects of vacancies on deformation behavior in nanocrystalline nickel," *Materials transactions*, vol. 49, no. 10, pp. 2315–2321, 2008.

[259] H. M. Zbib, T. Dıaz de la Rubia, M. Rhee, and J. P. Hirth, "3D dislocation dynamics: stress–strain behavior and hardening mechanisms in fcc and bcc metals," *Journal of Nuclear Materials*, vol. 276, no. 1, pp. 154–165, 2000.

[260] Q. Wei and L. Kecskes, "Effect of low-temperature rolling on the tensile behavior of commercially pure tungsten," *Materials Science and Engineering: A*, vol. 491, no. 1-2, pp. 62–69, 2008.

[261] M. Scapin, L. Peroni, C. Torregrosa, A. Perillo-Marcone, and M. Calviani, "Effect of strain-rate and temperature on mechanical response of pure tungsten," *Journal of Dynamic Behavior of Materials*, vol. 5, pp. 296–308, 2019.

[262] M. Hokka, *Dynamic Behavior of Materials: Fundamentals, Material Models, and Microstructure Effects*. Elsevier, 2023.

[263] S. Pathak and S. R. Kalidindi, "Spherical nanoindentation stress–strain curves," *Materials Science and Engineering: R: Reports*, vol. 91, pp. 1–36, 2015.

[264] S. Lee, Y. Hatano, M. Hara, S. Masuzaki, M. Tokitani, M. Oyaizu, H. Kurotaki, D. Hamaguchi, H. Nakamura, N. Asakura, Y. Oya, J. Likonen, A. Widdowson, S. Jachmich, K. Helariutta, and M. Rubel, "Tritium distribution analysis of Be limiter tiles from JET-ITER like wall campaigns using imaging plate technique and β-ray induced X-ray spectrometry," *Fusion Engineering and Design*, vol. 160, p. 111959, 2020.

[265] M. J. Lloyd, J. Haley, B. Jim, R. Abernethy, M. R. Gilbert, E. Martinez, K. Hattar, O. El-Atwani, D. Nguyen-Manh, M. P. Moody, P. A. Bagot, and D. E. Armstrong, "Microstructural evolution and transmutation in tungsten under ion and neutron irradiation," *Materialia*, vol. 33, p. 101991, 2024.

[266] F. Romanelli and on behalf of JET Contributors, "Overview of the JET results," *Nuclear Fusion*, vol. 55, no. 10, p. 104001, 2015.

[267] M. Rubel, J. Coad, A. Widdowson, G. Matthews, H. Esser, T. Hirai, J. Likonen, J. Linke, C. Lungu, M. Mayer, L. Pedrick, and C. Ruset, "Overview of erosion–deposition diagnostic tools for the ITER-like wall in the JET tokamak," *Journal of Nuclear Materials*, vol. 438, pp. S1204–S1207, 2013.

[268] S. A. Silburn, G. F. Matthews, C. D. Challis, D. Frigione, J. P. Graves, M. J. Mantsinen, E. Belonohy, J. Hobirk, D. Iglesias, D. L. Keeling, D. King, K. Kirov, M. Lennholm, P. J. Lomas, S. Moradi, A. C. C. Sips, M. Tsalas, and J. Contributors, "Mitigation of divertor heat loads by strike point sweeping in high power JET discharges," *Physica Scripta*, vol. 2017, no. T170, p. 014040, 2017.

[269] M. Richou, A. Durif, M. Lenci, M. Mondon, M. Minissale, L. Gallais, G. Kermouche, and G. De Temmerman, "Recrystallization at high temperature of two tungsten materials

complying with the ITER specifications," *Journal of Nuclear Materials*, vol. 542, p. 152418, 2020.

[270] J. G. Chen, "NEXAFS investigations of transition metal oxides, nitrides, carbides, sulfides and other interstitial compounds," *Surface Science Reports*, vol. 30, pp. 1–152, 1998.

[271] C. Makepeace, C. Pardanaud, P. Roubin, I. Borodkina, C. Ayres, P. Coad, A. Baron-Wiechec, I. Jepu, K. Heinola, A. Widdowson, S. Lozano-Perez, and J.E.T. Contributors, "The effect of beryllium oxide on retention in JET ITER-like wall tiles," *Nuclear Materials and Energy*, vol. 19, pp. 346–351, 2019.

[272] J. Moulder and J. Chastain, *Handbook of X-ray Photoelectron Spectroscopy: A Reference Book of Standard Spectra for Identification and Interpretation of XPS Data*. Physical Electronics Division, Perkin-Elmer Corporation, 1992.

[273] S. Abolhassani and P. Gasser, "Preparation of TEM samples of metal–oxide interface by the focused ion beam technique," *Journal of Microscopy*, vol. 223, no. 1, pp. 73–82, 2006.

[274] S. Jung, M. K. Tiwari, N. V. Doan, and D. Poulikakos, "Mechanism of supercooled droplet freezing on surfaces," *Nature communications*, vol. 3, no. 1, p. 615, 2012.

[275] A. Widdowson, J. Coad, E. Alves, A. Baron-Wiechec, N. Catarino, V. Corregidor, K. Heinola, S. Krat, C. Makepeace, G. Matthews, M. Mayer, K. Mizohata, and M. Sertoli, "Deposition of impurity metals during campaigns with the JET ITER-like wall," *Nuclear Materials and Energy*, vol. 19, pp. 218–224, 2019.

[276] W. D. Klopp and P. L. Raffo, *Effects of purity and structure on recrystallization, grain growth, ductility, tensile, and creep properties of arc-melted tungsten*, vol. 2503. National Aeronautics and Space Administration, 1964.

[277] J. Toman, D. C. Pagan, P. Müllner, and M. Chmielus, "Epitaxial re-solidification of laser-melted Ni-Mn-Ga single crystal," *Acta Materialia*, vol. 219, p. 117236, 2021.

[278] L. Gomell, S.-P. Tsai, M. Roscher, R. Bueno Villoro, P. Konijnenberg, S. Zaefferer, C. Scheu, and B. Gault, "In situ nitriding of Fe_2VAl during laser surface remelting to manipulate microstructure and crystalline defects," *Phys. Rev. Mater.*, vol. 6, p. 085405, 2022.

[279] P. Biswas and J. Ma, "Development of crystallographic misorientation in laser powder bed fusion 316L stainless steel," *Additive Manufacturing*, vol. 80, p. 103951, 2024.

[280] J. Wang, R. Zhu, Y. Liu, and L. Zhang, "Understanding melt pool characteristics in laser powder bed fusion: An overview of single- and multi-track melt pools for process optimization," *Advanced Powder Materials*, vol. 2, no. 4, p. 100137, 2023.

[281] H. Zhang, P. R. Carriere, E. D. Amoako, C. D. Rock, S. U. Thielk, C. G. Fletcher, and T. J. Horn, "Microstructure and elevated temperature flexure testing of tungsten produced by electron beam additive manufacturing," *Journal of the Minerals, Metals Materials Society*, vol. 75, no. 10, 2023.

[282] P. Jreidini, T. Pinomaa, J. M. K. Wiezorek, J. T. McKeown, A. Laukkanen, and N. Provatas, "Orientation gradients in rapidly solidified pure aluminum thin films: Comparison of experiments and phase-field crystal simulations," *Phys. Rev. Lett.*, vol. 127, p. 205701, 2021.

[283] P. Mercelis and J. P. Kruth, "Residual stresses in selective laser sintering and selective laser melting," *Rapid Prototyping Journal*, vol. 12, pp. 254–265, 2006.

[284] H. Kotadia, G. Gibbons, A. Das, and P. Howes, "A review of laser powder bed fusion additive manufacturing of aluminium alloys: Microstructure and properties," *Additive Manufacturing*, vol. 46, p. 102155, 2021.

[285] H. Hu, "Texture of metals," *Texture*, vol. 1, 1974.

[286] U. Dahmen, "Orientation relationships in precipitation systems," *Acta Metallurgica*, vol. 30, no. 1, pp. 63–73, 1982.

[287] B. Sharma, "Nuclear reactors: Moderator and reflector materials," in *Encyclopedia of Materials: Science and Technology* (K. J. Buschow, R. W. Cahn, M. C. Flemings, B. Ilschner, E. J. Kramer, S. Mahajan, and P. Veyssière, eds.), pp. 6365–6369, Oxford: Elsevier, 2001.

[288] K. Dobes, M. Köppen, M. Oberkofler, C. P. Lungu, C. Porosnicu, T. Höschen, G. Meisl, C. Linsmeier, and F. Aumayr, "Interaction of nitrogen ions with beryllium surfaces," *Nuclear Instruments and Methods in Physics Research Section B: Beam Interactions with Materials and Atoms*, vol. 340, pp. 34–38, 2014.

[289] M. Oberkofler, G. Meisl, A. Hakola, A. Drenik, D. Alegre, S. Brezinsek, R. Craven, T. Dittmar, T. Keenan, S. G. Romanelli, R. Smith, D. Douai, A. Herrmann, K. Krieger, U. Kruezi, G. Liang, C. Linsmeier, M. Mozetic, V. Rohde, the ASDEX Upgrade team, the EUROfusion MST1 Team, and J. Contributors, "Nitrogen retention mechanisms in tokamaks with beryllium and tungsten plasma-facing surfaces," *Physica Scripta*, vol. 2016, no. T167, p. 014077, 2016.

[290] A. Lahtinen, J. Likonen, S. Koivuranta, A. Hakola, K. Heinola, C. Ayres, A. Baron-Wiechec, J. Coad, A. Widdowson, and J. Räisänen, "Deuterium retention in the divertor tiles of JET ITER-like wall," *Nuclear Materials and Energy*, vol. 12, pp. 655–661, 2017.

[291] Y. Lin, C. McFadzean, and S. A. Humphry-Baker, "Oxidation resistance of WB and W_2B-W neutron shields," *Journal of Nuclear Materials*, vol. 565, p. 153762, 2022.

[292] M. Wurmshuber, S. Doppermann, S. Wurster, S. Jakob, M. Balooch, M. Alfreider, K. Schmuck, R. Bodlos, L. Romaner, P. Hosemann, H. Clemens, V. Maier-Kiener, and D. Kiener, "Enhancing mechanical properties of ultrafine-grained tungsten for fusion applications," *International Journal of Refractory Metals and Hard Materials*, vol. 111, p. 106125, 2023.

List of Figures and Tables

List of Figures

List of Tables

APPENDIX A

Error in Frame Stiffness Correction for Lamella D12

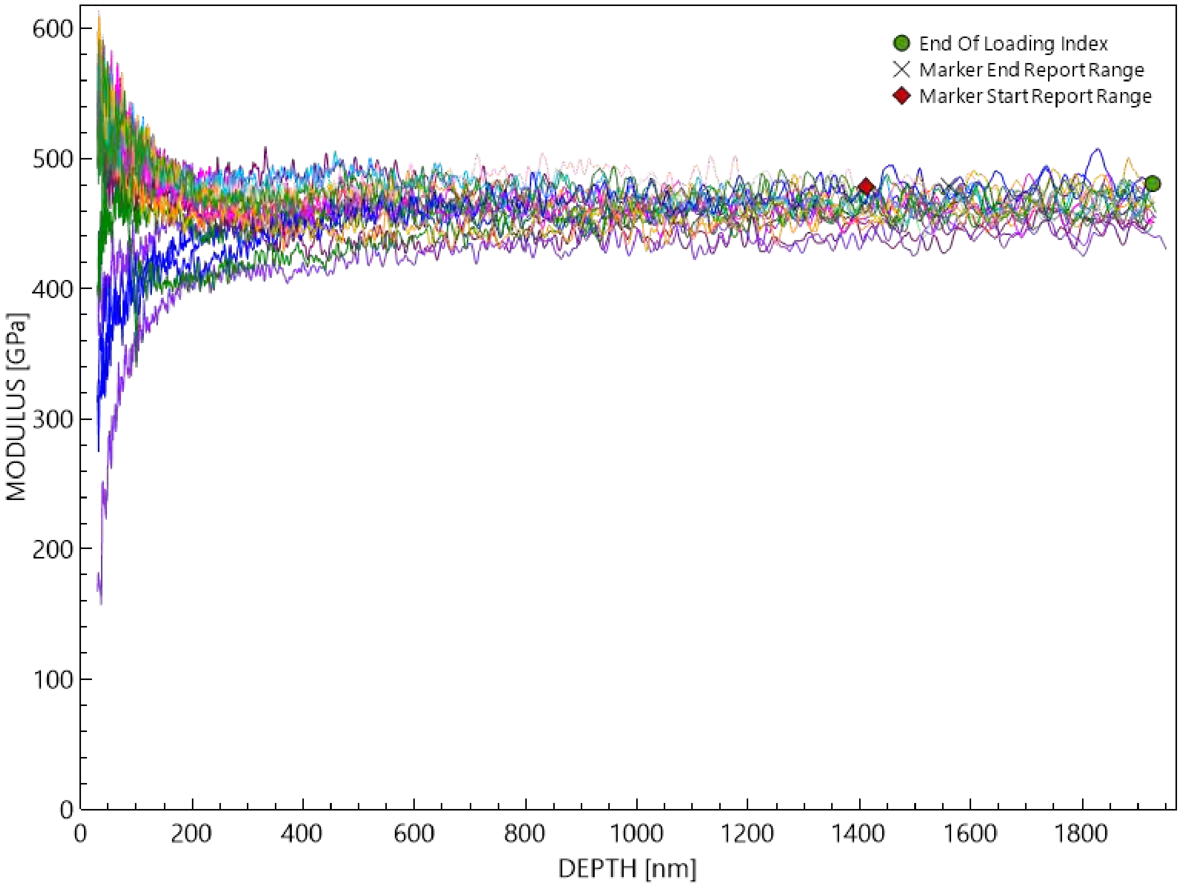

Eastic modulus against indentation depth curves for lamellae D12, highlighting possible issues with the frame stiffness correction.

All Stress-Strain Curves from the Spherical Indentation

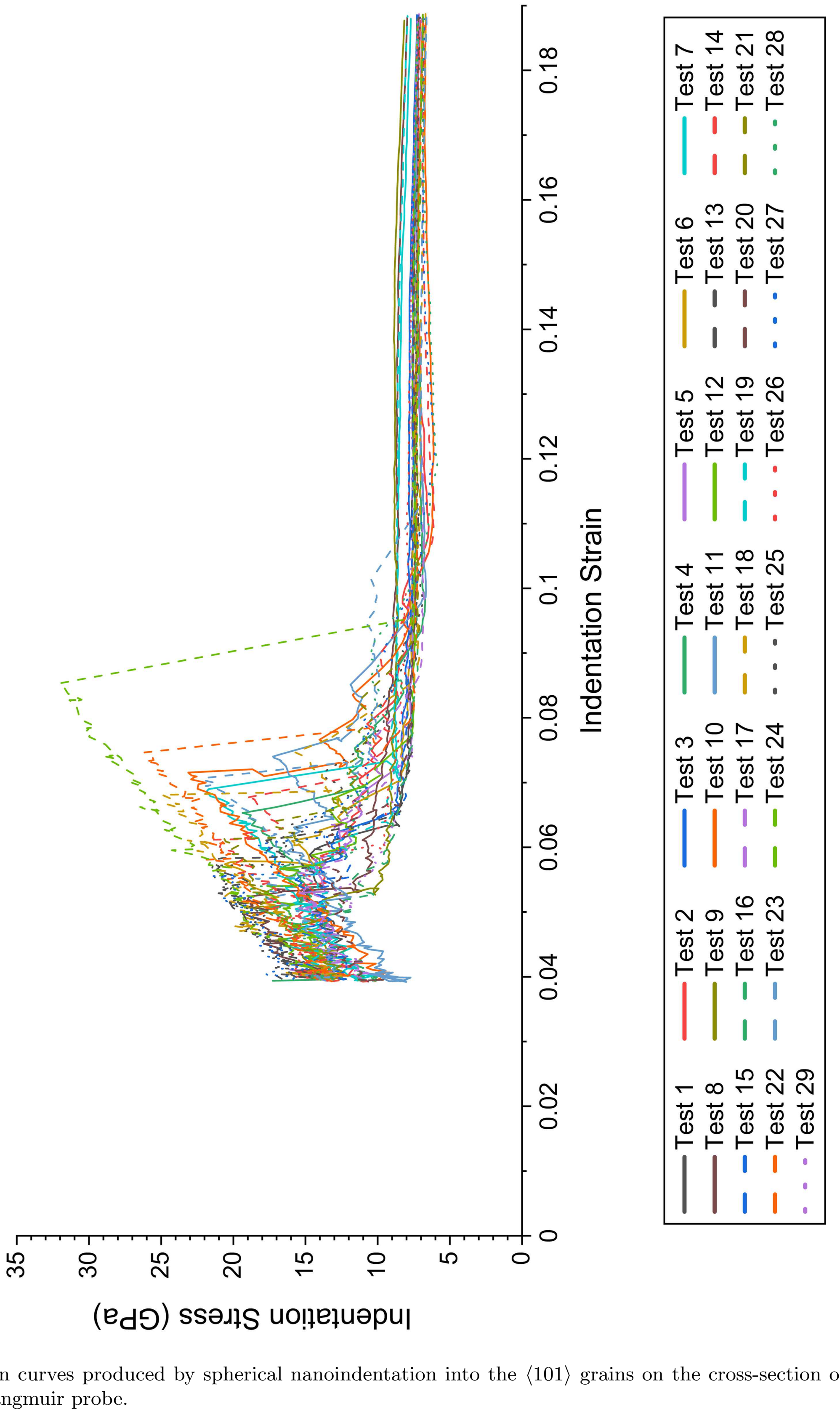

Stress-strain curves produced by spherical nanoindentation into the ⟨101⟩ grains on the cross-section of the as-received Langmuir probe.

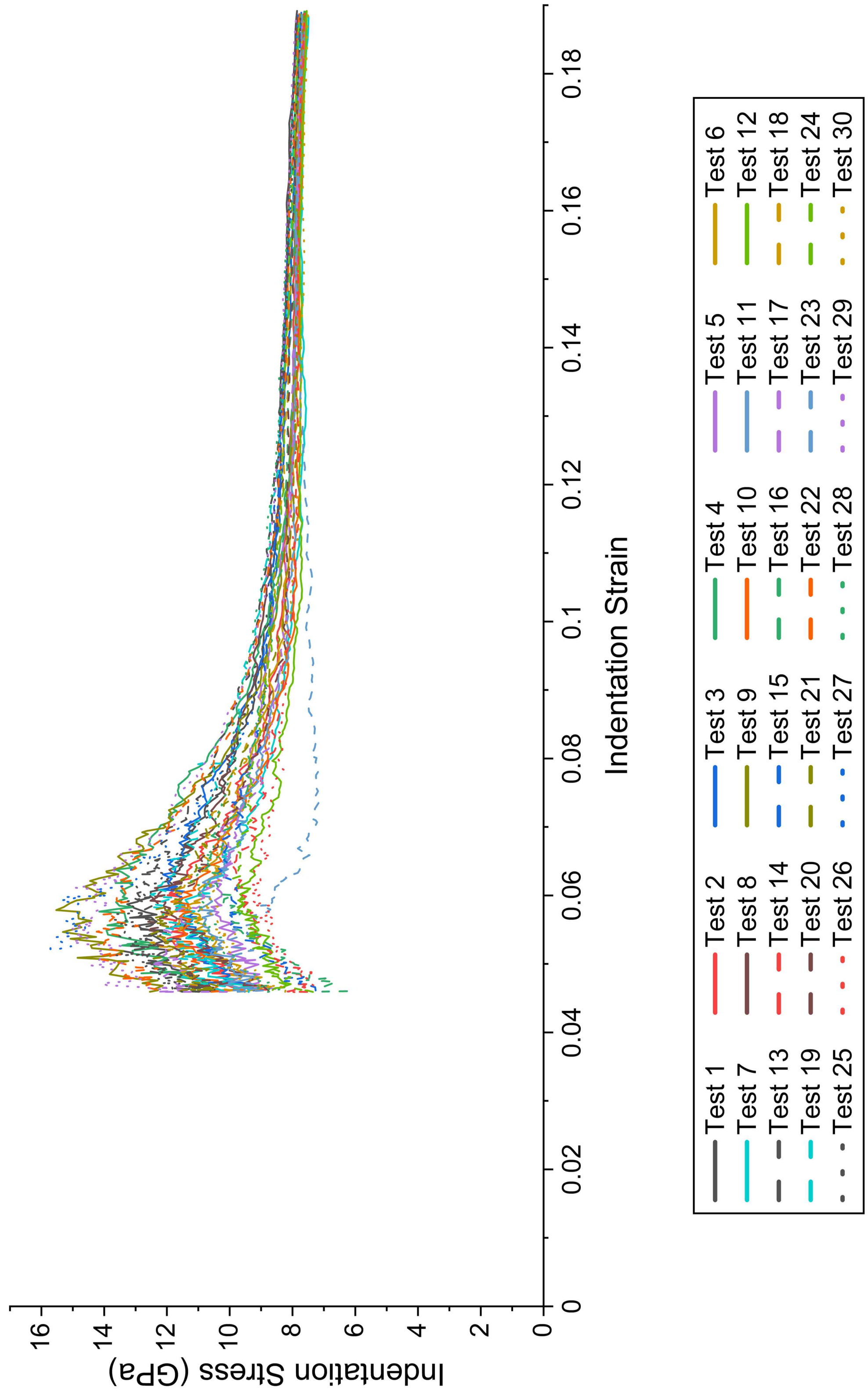

Stress-strain curves produced by spherical nanoindentation into the ⟨101⟩ grains on the cross-section of probe 26.

APPENDIX B

Locations of Stratified Deposits in Lamella C3

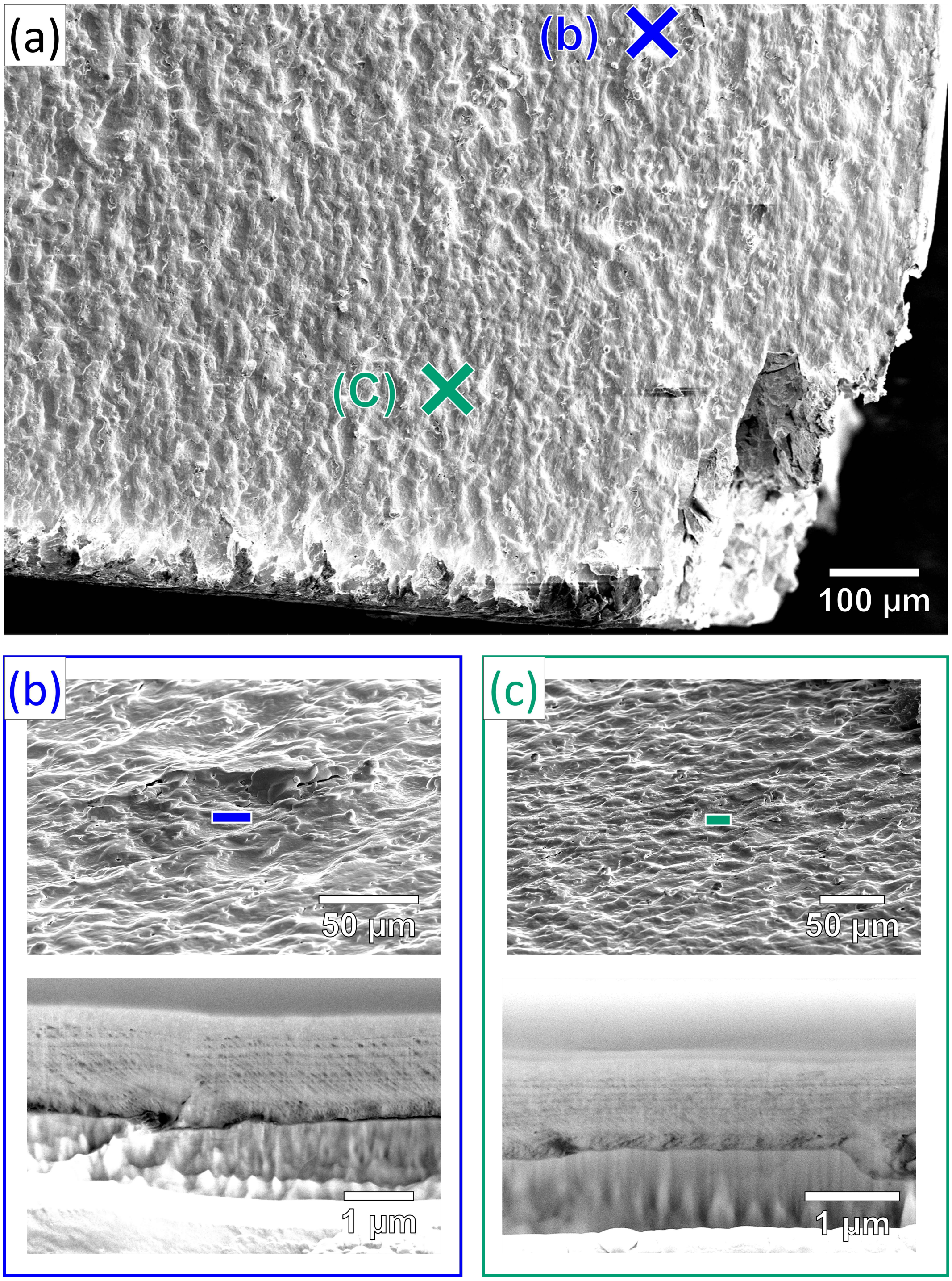

SE images from the surface of lamella C3 showing (a) the locations of the FIB cross-sections where the stratified deposits were found (b) the first cross-section (c) the second cross-section.

Be EELS Maps of Stratified Deposit in Lamella C3

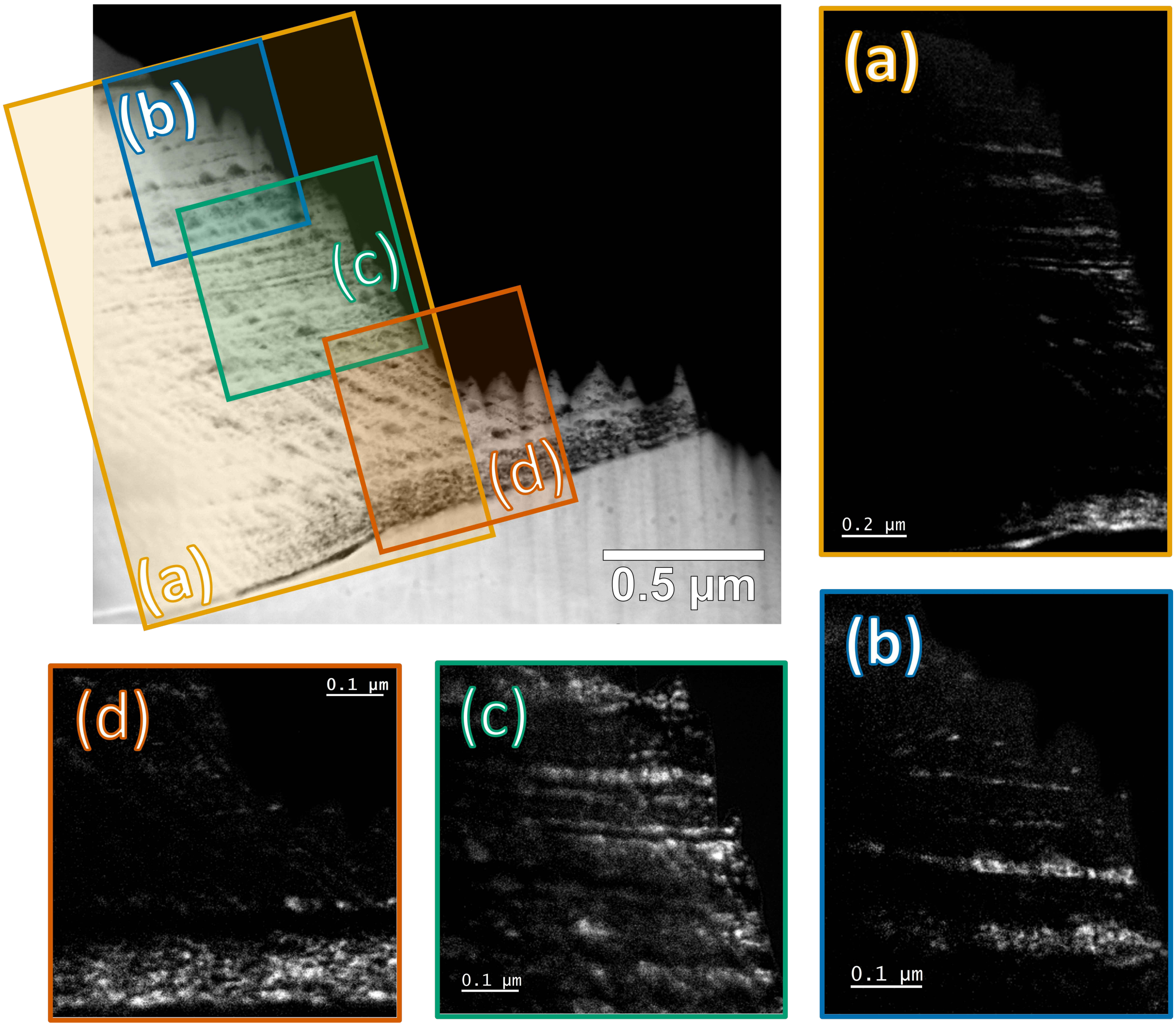

STEM HAADF image of the stratified deposits in Fig. 6.5 showing the Be EELS maps in (a) (b) (c) and (d).

EDX Maps of Stratified Deposit on W Droplet in Lamella C3

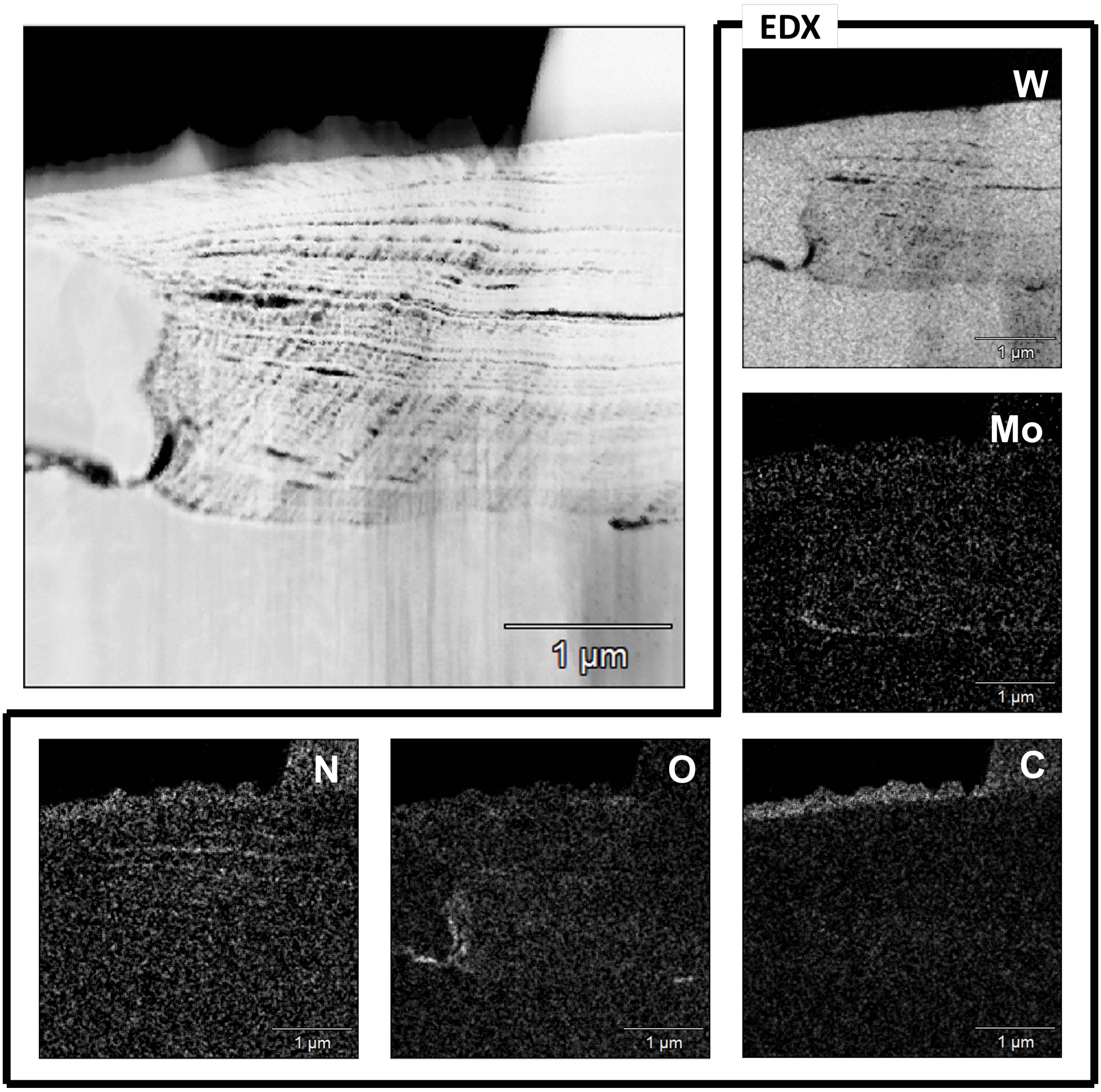

STEM HAADF image of stratified deposits that formed on a W droplet with EDX maps for W, Mo, C, N and O, where there was a strong C signal from the protective Pt layer and a weaker signal from the deposited layers.